Characterization of nanomechanical resonators based on silicon nanowires

Marc Sansa Perna

Memòria presentada per optar al
Grau de Doctor en Enginyeria Electrònica

Departament d'Enginyeria Electrònica
Universitat Autònoma de Barcelona

Realitzada sota la direcció de:
Prof. Francesc Pérez Murano

Tutor:
Prof. Núria Barniol Beumala

Juny 2013

En Francesc Pérez Murano, Professor d'investigació de l'Institut de Microelectrònica de Barcelona (IMB-CNM, CSIC),

CERTIFICA:

que la memòria titulada "Characterization of nanomechanical resonators based on silicon nanowires" que presenta en Marc Sansa Perna per a optar al grau de Doctor en Enginyeria Electrònica per la Universitat Autònoma de Barcelona ha estat realitzada sota la seva direcció.

Bellaterra, juny de 2013

Prof. Francesc Pérez Murano

Agraïments

El doctorat és una etapa de formació molt personal, i sovint viscuda molt intensament. Tot i així, regna un desconeixement general del significat d'aquest període, les seves implicacions i la importància que té per a nosaltres, els doctorands. És molt més que una feina, és un repte. En aquest sentit us vull agrair a tots, especialment els que esteu fora del camp de la recerca, la vostra comprensió durant aquests anys.

En primer lloc vull donar les gràcies a el Prof. Francesc Pérez, que m'ha introduït al món de la recerca, m'ha donat la oportunitat de realitzar la tesi doctoral al seu grup i m'ha guiat durant tots aquests anys. La seva direcció i la profunda implicació en aquesta feina han permès que aquesta tesi arribi a bon port. Vull agrair-li també el seu esforç per a formar un investigador, tasca que va molt més enllà de dirigir una tesi.

També vull donar les gràcies a el Dr. Álvaro San Paulo, amb qui vaig col·laborar estretament els primers anys de tesi. La seva experiència i entusiasme em van guiar durant els inicis del meu trajecte.

Aquesta feina tampoc hauria sigut possible sense l'ajuda d'un gran nombre de persones, el "personal del CNM"... Si us esmentés a tots la llista seria massa llarga, i segur que em deixaria algú. Tot i així, us vull donar a les gràcies a tots els que m'heu ajudat amb interès i ganes, i sovint amb un somriure. Aquesta feina ha sigut possible gràcies a vosaltres.

Les mesures dels ressonadors haurien segut impossibles sense l'ajuda de la Prof. Núria Barniol, que ens va fer un espai al grup ECAS del departament d'Enginyeria Electrònica: bona part dels resultats d'aquesta tesi han sortit del seu laboratori. També vull agrair la càlida acollida a la resta de personal del grup: l'Eloi, en Gabriel, en Miquel, en Jordi, en Joan, en José Luis, l'Arantxa, en Francesc, ... Us vull donar les gràcies per tot, tant a nivell professional com personal. He tingut una gran sort de poder treballar amb vosaltres.

També he tingut la sort de trobar bons amics entre la gent amb qui he viscut el dia a dia de la meva feina, la gent "del despatx". Amb la Marta hem compartit

moltes hores (i desesperacions) amb el CVD de creixement de nanofils, i alguna que altra "Eternal". En la Nerea i en Jordi he trobat dos bon companys de despatx, de doctorat i sobretot dos bons amics. I un agraïment també a la resta de gent del despatx: la Lorea, en Giordano, l'Iñigo, la Gemma, la Irene, en Dani, l'Yigezu i en Bergoi, amb qui ha sigut un pler passar totes aquestes hores.

Considero que tinc la sort també de tenir molts i bons amics, a qui no puc deixar d'agrair tot el suport durant aquests anys. Els castellers, els "blaus" i els "verds", que m'han mostrat el que són la colla i els castells. "Els de la uni", amb qui vaig compartir molts anys de carrera i encara compartim una gran amistat. Però sobretot vosaltres, els que sempre heu estat aquí i espero que sempre hi sigueu. Sembla que la situació ens escombra molt lluny els uns dels altres, però quan ens trobem és talment com si mai ens haguéssim separat. A dos de vosaltres us vull agrair en especial la vostra amistat i ajuda, les hores junts, la confiança: Eloi i Carme, gràcies per tot.

Un agraïment profund també per a la meva família, que em va inculcar la curiositat, les ganes de tirar endavant, la idea de que l'esforç és necessari i a la llarga dóna fruits. Que encara avui em dóna aquella empenta i ajuda que ho fa tot més fàcil. Gràcies, aquesta tesi és tant vostra com meva.

Per acabar, et vull donar les gràcies Irena per tot: per ser-hi, per compartir, per opinar, per divertir, per ajudar, per conviure, per comprendre, i per estimar.

Marc Sansa, Juny 2013

Resum

Els sensors de massa nanomecànics han atret un gran interès darrerament per la seva alta sensibilitat, que ve donada per les petites dimensions del ressonador que actua com a element sensor. Aquesta tesi tracta sobre la fabricació i caracterització de ressonadors nanomecànics per a aplicacions de sensat de massa. Aquest objectiu inclou diferents aspectes: 1) el desenvolupament d'una tecnologia de fabricació per a ressonadors nanomecànics basats en nanofils de silici, 2) la caracterització de la seva resposta freqüencial utilitzant mètodes elèctrics i 3) l'avaluació del seu rendiment com a sensors de massa.

Durant aquest treball hem fabricat ressonadors nanomecànics basats en nanofils de silici doblement fixats, utilitzant dues estratègies de fabricació diferents: els nanofils crescuts amb mètodes *bottom-up* ("de baix a dalt"), i els definits amb mètodes de litografia *top-down* ("de dalt a baix"). Aprofitant les característiques d'ambdues tècniques, hem fabricat nanofils amb dimensions laterals de fins a 50 nanòmetres, i amb un alt nombre de dispositius per xip, aconseguint un alt grau de rendiment per a estructures d'aquestes dimensions.

Hem aplicat esquemes avançats de detecció elèctrica basats en la mescla de senyals cap a freqüències baixes per tal de caracteritzar la resposta freqüencial dels ressonadors. Hem demostrat que el mètode de freqüència modulada (FM) proporciona la millor eficiència en la transducció de l'oscil·lació mecànica en una senyal elèctrica. Aquesta tècnica ha permès detectar múltiples modes de ressonància del ressonador, a freqüències de fins a 590 MHz. La detecció de modes de ressonància superiors és important per tal de solucionar una de les principals problemàtiques en el camp dels sensors de massa nanomecànics: desacoblar els efectes de la posició i la massa de partícules dipositades al sensor. També hem combinat la informació obtinguda de la caracterització elèctrica amb simulacions d'elements finits per tal de quantificar l'estrès acumulat als nanofils durant la seva fabricació.

Hem estudiat els sistemes de transducció electromecànica en ressonadors basats en nanofils de silici comparant l'eficiència de tres mètodes de detecció: el mètode FM ja esmentat i els mètodes de dos generadors, 1 i de dos generadors, 2 . D'aquesta manera hem demostrat que dos mecanismes de transducció diferents coexisteixen en els nanofils de silici *bottom-up*: el mecanisme lineal (en què la senyal transduïda

és proporcional al moviment del ressonador) i el quadràtic (en què la senyal transduïda és proporcional al quadrat del moviment del ressonador). Per altra banda, en els ressonadors *top-down* només és present el mecanisme de transducció lineal. Aquest mecanisme lineal és el que permet la gran eficiència del mètode FM per a la caracterització de la resposta freqüencial de ressonadors basats en nanofils de silici.

Per tal d'utilitzar els ressonadors nanomecànics com a sensors de massa, el seguiment de la freqüència de ressonància en temps real és indispensable. Hem dissenyat i implementat una configuració en llaç tancat basada en la caracterització FM i un algorisme de detecció de pendent. Aquest sistema permet el seguiment de canvis en la magnitud i freqüència de la resposta del ressonador, possibilitant la detecció de massa en temps real i la caracterització de l'estabilitat temporal del sistema. D'aquesta manera s'ha pogut avaluar l'eficiència del sistema per a aplicacions de sensat de massa. La sensibilitat en massa dels sensors de dimensions més reduïdes és de l'ordre de 6 Hz/zg (1 zg $= 6 \times 10^{-21} g$), i les mesures d'estabilitat en freqüència en llaç tancat mostren una resolució en massa de 6 zg a temperatura ambient.

Summary

Nanomechanical mass sensors have attracted interest during the last years thanks to their unprecedented sensitivities, which arise from the small dimensions of the resonator which comprises the sensing element. This thesis deals with the fabrication and characterization of nanomechanical resonators for mass sensing applications. This objective comprises three different aspects: 1) development of a fabrication technology of nanomechanical resonators based on silicon nanowires (SiNW), 2) characterization of their frequency response by electrical methods and 3) evaluation of their performance as mass sensors.

During this work, we have fabricated nanomechanical resonators based on SiNW clamped-clamped beams, using two different approaches: bottom-up growth of SiNW and top-down definition by lithography methods. By exploiting the advantages of each technique, we have succeeded in fabricating nanowires of small lateral dimensions, in the order of 50 nanometers, and with high number of devices per chip, achieving a high throughput for structures of these dimensions.

We have applied advanced electrical detection schemes based on frequency downmixing techniques for the characterization of the frequency response of the devices. We have found that the frequency modulation (FM) detection method provides the best efficiency in transducing the mechanical oscillation into an electrical signal. This technique has enabled the detection of multiple resonance modes of the resonator at frequencies up to 590 MHz. The detection of high modes of resonance is important to address one of the issues in nanomechanical mass sensing, decoupling the effects of the position and mass of the deposited species. Moreover, by combining the information obtained from the experimental characterization of the frequency response with FEM simulations, we have quantified the stress accumulated in the SiNWs during the fabrication.

We have studied the electromechanical transduction mechanisms in SiNW resonators by the comparative performance of three electrical detection methods: the aforementioned FM and two more detection techniques (namely the two-source, 1 and the two-source, 2). We have proved that two different transduction mechanisms co-exist in bottom-up grown SiNWs: linear (in which the transduced signal is proportional to the motion of the resonator) and quadratic (in which the transduced

signal is proportional to the square of the motion of the resonator). On the other hand, in the top-down nanowires only the linear transduction mechanism is present. It is this newly found linear transduction which enables the outstanding performance of the FM detection method when characterizing the frequency response of SiNW resonators.

For the use of nanomechanical resonators in mass sensing applications, the real-time tracking of their resonance frequency is needed. We have designed and implemented a novel closed-loop configuration, based on the FM detection technique and a slope detection algorithm. It allows the monitoring of changes in the magnitude and the frequency of the response of the resonator, enabling not only the real time detection of mass, but also the characterization of the temporal stability of the resonator. In this way, the overall performance of the system for mass sensing applications has been characterized. The mass sensitivity of the system for the smallest resonators stands in the range of 6 Hz/zg (1 zg = 6×10^{-21} g) and the frequency stability measurements in the closed loop configuration reveal a mass resolution of 6 zg at room temperature.

Contents

Thesis presentation

This thesis has been realized in the group of Nanofabrication and functional properties of nanostructures, of the Institut de Microelectrònica de Barcelona (IMB-CNM), which is part of the CSIC (Centro Superior de Investigaciones Científicas). This work has been supervised by Prof. Francesc Pérez Murano.

Introduction

This thesis deals with the study and application of nanoelectromechanical systems, that is, electromechanical systems of nanometric dimensions. First of all, a definition of an electromechanical system is in order: this term refers to a mechanical component coupled to electronic circuits via electromechanical transducers [1]. Therefore, an electromechanical system consists of different parts: 1) an input transducer, which receives electric signals from a circuit and transforms them to stimuli for the mechanical element; 2) the mechanical element itself; and 3) the detection transducer, which senses the state or stimuli provided by the mechanical element and transforms them to measurable electric signals.

This general description encompasses a large number of systems, in which the mechanical element is affected by different kinds of stimuli. Electromechanical systems have applications ranging from sensing (pressure, inertial, chemical sensors,...) to RF components, scanning probes, etc. This work is centered in the study of clamped-clamped beam structures, in which resonance states can be excited and detected using electrical methods. The resonance frequency of these structures is extremely sensitive to a number of parameters, and therefore its tracking can be used for sensing purposes.

Miniaturization in electromechanical systems: MEMS-NEMS

Over the last century, the evolution of electronics and more specifically, Integrated Circuits (ICs) has induced a revolution in the miniaturization and integration of electronic components. This has enabled consumer electronics and a breakthrough in information technologies. This technology is based in the fabrication of electronic

components using planar technologies, generally based on silicon wafers. Much effort has been put into the miniaturization of these components, mainly by improving the different technologies involved in their fabrication.

In parallel to the development of IC technologies, bulk Si micromachining techniques have been developed, adding the possibility of using a similar set of techniques to fabricate mechanical structures integrated in Si chips [2]. The combination of these mechanical parts with electronics quickly followed, giving birth to the field of Microelectromechanical Systems (MEMS) [3]. This term makes reference to mechanical elements of micrometric dimensions which are actuated or sensed electrically, by means of transduction mechanisms.

During the last three decades this field has evolved, taking advantage of the evolution of microelectronic technologies and using them to fabricate mechanical structures of increasingly small dimensions. As a result of this trend of miniaturization, eventually the fabrication technology allowed to fabricate structures of sub-micrometric dimensions, opening the field of the Nanoelectromechanical Systems (NEMS). NEMS are first, but not only, an evolution of MEMS in which one or more of its dimensions are in the sub-micron range. This miniaturization provides advantages in many applications, such as lower masses of the mechanical elements and higher resonance frequencies. Additionally, the evolution of the size of these structures towards the atomic range enables the exploration of quantum effects, which can be exploited to create new paradigms of sensing and electronics.

NEMS as mass sensors

One of the applications of NEMS–and, more specifically, the beam structures studied in this work–is their use in the field of mass sensing. Due to their small dimensions, nanomechanical resonators present exceptionally low masses and high resonance frequencies, which confer them outstanding qualities as mass sensors. For this reason, the field of mass sensing based on NEMS has been gathering interest in the last years, and recent works have reported unprecedented resolution in the yoctogram range [4] (1 yg is 1×10^{-24} g, or the mass of a proton) and real-time detection of single proteins [5].

Despite all of the developments of the last years in the field of mass sensing based on nanomechanical resonators, there are still challenges to be addressed. From the point of view of the resonators, their miniaturization in a controlled way implies technological difficulties that require improving the existing fabrication methods. Furthermore, the small dimensions that confer exceptional mass sensing performance also entail issues in the measurement of the resonators, such as transduction signals of small amplitude and high frequency, tendency to non-linear behaviours, etc. Therefore, high sensitivity mass sensing implies not only a challenge in the miniaturization of the sensors, but also in their measurement and characterization.

Fabrication methods

The fabrication of mass sensors based on nanomechanical resonators pushes the limits of existing fabrication technologies in order to build structures of the smallest possible dimensions. In general, two different approaches can be employed to fabricate micro- and nanostructures. 1) Top-down techniques, which start with a bulk material, and selectively remove certain regions to fabricate the structures [6], similarly to sculpturing a figure from a block of rock. This is the base of classical micromachining techniques, in which a mechanical structure is patterned in bulk Si using IC and microfabrication technologies. 2) Bottom-up techniques, in which the structures are fabricated from smaller building blocks by molecular recognition or self-assembly, similarly to building a structure from smaller bricks. These are the technologies used for the fabrication of Carbon Nanotubes (CNTs) or Silicon Nanowires (SiNWs) based devices, which are synthesized by chemical reactions favoured from a seed of catalyst.

Each of these general approaches presents advantages and disadvantages. Without entering into the particulars of each technique, many of the processes employed in top-down methods are also used in IC fabrication, and therefore are widely used and well controlled. This kind of techniques generally offer good resolution and repetitivity for relatively large structures, but they fail when resolutions below hundreds of nanometers are required. On the other hand, bottom-up methods are usually specific to one material or family of materials, as they rely on chemical reactions, but they can offer outstanding results when fabricating structures of small dimensions. These methods can be used to fabricate materials of the lowest possible dimensionality, like CNTs or graphene sheets, which are fabricated from a single atomic layer. However, the accurate positioning of the grown objects is usually difficult, which hinders the repetitive fabrication of devices based on these structures. In summary, top-down and bottom-up approaches can be considered to have complimentary advantages nowadays, which must be evaluated for each particular application.

Objectives

The general objective of this thesis is the study of nanomechanical resonators, and the evaluation of their application in mass sensing. This objective is approached as a means of exploring different challenges currently present in the field of mass sensing based on nanomechanical resonators. For this reason, special emphasis is put during each step into the study and application of different alternative solutions. The specific objectives of this thesis and their implications are:

Fabrication: Fabrication of nanomechanical resonators of small dimensions. In this

step, the advantages and limitations of bottom-up and top-down fabrication approaches are studied. With these objectives, two different fabrication processes are developed based on top-down and bottom-up approaches, in order to take advantage of their respective particularities.

Measurement: Characterization of nanomechanical resonators by using novel electrical measurement methods. This implies the comparison of different measurement techniques, addressing the issues related with the high frequencies and the low signal levels which are inherent to these devices. A comparative study of diverse electrical detection methods is performed.

Investigation of the properties of nanomechanical resonators: Study of the characteristics of the fabricated nanomechanical resonators from the characterization results. Several attributes of the resonators which are important for their application ass mass sensors can be investigated and disclosed with the help of experimental results and finite element simulations.

Application of the resonators as mass sensors: Integration of the resonators into a close-loop interface for their application as a mass sensors. This step involves the design and implementation of a close loop interface for the real time monitoring of the resonance frequency of nanomechanical resonators, adapted to the particular measurement method employed.

Structure

This document consists in 6 different chapters, comprising a theoretical introduction to NEMS resonators, followed by the fabrication and characterization of top-down and bottom-up nanowires and finally their application as mass sensors.

Chapter 1 is devoted to introducing the theory of nanoelectromechanical resonators, and it is divided in three sections. The first part comprises a study of the theory of resonating beams, which describes the behaviour of the mechanical structures studied throughout this work. The second section presents actuation methods for nanomechanical resonators, while the last one deals with different transduction mechanisms to electrically detect the motion of nanomechanical resonators.

Chapter 2 presents the fabrication of nanomechanical resonators based on bottom-up silicon nanowires. First, an introduction to bottom-up fabrication and its challenges is presented, centred in the specific issues particular of semiconductor nanowires. Afterwards an overview of different technologies used for the fabrication of this kind of devices is presented. The last section presents the actual fabrication

process for nanomechanical resonators based on bottom-up silicon nanowires, and an evaluation of the fabrication results.

Chapter 3 introduces several downmixing methods for the measurement of nanomechanical resonators, and their application for the measurement of bottom-up silicon nanowires. In the first section, three different downmixing methods are studied, namely the two-source, 1 , the two-source, 2 and the frequency modulation. In the next section the measurement of bottom-up nanowires with these different methods is presented, and afterwards the transduction mechanisms of the studied devices are discussed based on the experimental measurements. Next, the obtained results are compared with finite element simulations in order to obtain additional information about the resonators. Finally, the last section presents a small discussion of the mode-splitting effect encountered during the measurement of the resonators.

Chapter 4 presents the fabrication of nanomechanical resonators based on top-down nanowires. Analogously to chapter 2, first an overview of top-down fabrication technologies is presented, followed by the specific fabrication process for top-down nanomechanical resonators used in this work. Finally, the fabrication results are discussed.

Chapter 5 describes the measurement results of top-down nanomechanical resonators using the previously studied downmixing methods. First the measurement results are presented, and then the transduction mechanisms present in top-down nanowires are discussed based on the characterization results. Afterwards a study of the measurement results with finite elements simulations is performed. Finally, the last section presents a comparison and discussion of the measurement results of top-down and bottom-up nanowire resonators.

Chapter 6 studies the application of nanomechanical resonators as mass sensors. First an introduction to mass sensing is performed, starting with the state of the art and following with a study of the characteristics of nanomechanical resonators as mass sensors. Afterwards, a theoretical evaluation of the resolution of nanomechanical resonators as mass sensors is performed. Then, the building of a closed loop system for the real time frequency tracking of nanowire resonators is presented, allowing to characterize the frequency stability of the measured devices. This closed loop configuration is validated by tracking changes in the response of the resonator. Finally, an evaluation of the SiNW nanomechanical resonators as mass sensors is performed.

To finalize, some general conclusions are extracted from the different parts of the present work. Additionally, this document includes several appendices. The first two of them describe some additional work which has been performed as a part of this thesis, namely the evaporation of metal contacts employing Nanostencil Lithography and the implementation of software libraries and interfaces for the measurement

of the nanomechanical resonators. A third annex contains a list of peer-reviewed publications and contributions to scientific events that have been produced as a result of this work.

Projects and funding

The present thesis has been performed under the framework of the following projects:

- ATOMETER (Towards atomic resolution nanomechanical mass spectrometers based on Si nanowires), Ref. 2010503020. 2010-2012.
- NANOFUN (NEMS avanzados con aplicaciones a la detección biológica ultrasensible), Ref: TEC2009-14517-C02-01. 2012-2012.
- FORCE-for-FUTURE (Tecnologías de microscopía de fuerzas para aplicaciones en nanomecánica y nanomedicina), Ref: CSD2010-00024. 2011-2015.

The author acknowledges the financial support of the Spanish Ministry of Education via the "Formación de Profesorado Universitario (FPU)" grant, Ref: AP2008-03849.

References

[1] K. L. Ekinci, "Electromechanical transducers at the nanoscale: Actuation and sensing of motion in nanoelectromechanical systems (NEMS)," *Small*, vol. 1, no. 8-9, p. 786–797, 2005.

[2] K. Petersen, "Silicon as a mechanical material," *Proceedings of the IEEE*, vol. 70, pp. 420 – 457, May 1982.

[3] K. Gabriel, J. Jarvis, and W. Trimmer, "Small machines, large opportunities: a report on the emerging field of microdynamics," *National Science Foundation, AT&T Bell Laboratories, Murray Hill, New Jersey, USA*, 1988.

[4] J. Chaste, A. Eichler, J. Moser, G. Ceballos, R. Rurali, and A. Bachtold, "A nanomechanical mass sensor with yoctogram resolution," *Nature Nanotechnology*, vol. 7, pp. 301–304, Apr. 2012.

[5] M. S. Hanay, S. Kelber, A. K. Naik, D. Chi, S. Hentz, E. C. Bullard, E. Colinet, L. Duraffourg, and M. L. Roukes, "Single-protein nanomechanical mass spectrometry in real time," *Nature Nanotechnology*, vol. 7, pp. 602–608, Sept. 2012.

[6] B. Bhushan, *Springer Handbook of Nanotechnology*. Springer, 2004.

Chapter 1

Nanomechanical resonators with electrical transduction

Contents

Nanoelectromechanical systems are being used in many fields, from sensors to RF components. Their small dimensions also imply low masses, high surface-to-volume ratios and high resonance frequencies, which make them excellent candidates for many applications. In the case of mass sensors based on nanomechanical resonators, for example, the sensitivity is determined by the resonance frequency and the mass of the mechanical element. For this reason, the use of devices with small dimensions allows achieving excellent sensitivities, and even mass resolutions

down to the yoctogram range [1]. Furthermore, the employment of these resonators as sensors requires a good knowledge of their frequency response, which is indeed well known and studied by standard elasticity theory, which is valid even for small structures such as carbon nanotubes and graphene resonators [2].

However, an accurate modelling of the resonating element is not sufficient, as it is part of a wider system. An electromechanical system consists on the one side in the mechanical element, and on the other in the transducers, which allow to interact electrically with the former. The mechanical element, which is the central part of the system, is in our case the nanomechanical resonator. The actuation transducer is in charge of transforming electrical signals to mechanical stimuli to drive the mechanical element. Lastly, the detection transducer reads the state of the mechanical element and converts it to measurable electric signals. Therefore, the modelling of a nanoelectromechanical system includes the study of all of these parts.

This chapter deals with the basic modelling of the resonators and their transduction methods, with the objective to serve as a basis for the measurement and study of these devices. First, an overview of the dynamic response of the resonator is given, centered in the devices and phenomena which are afterwards studied during the measurements. Then some actuation methods are reviewed, and electrostatic actuation is studied in detail. Finally the basics of some detection mechanisms used for nanomechanical resonators are studied, focused in the study of piezoresistive transduction and conductance modulation due to induced charge in the resonator, which are commonly employed for the measurement of nanomechanical resonators.

1.1 Modelling of the response of nanomechanical resonators

Nanomechanical resonators are used as sensors in different fields, such as mass sensing or gas detection. One of the usual modes of operation of these sensors is the dynamic mode, in which the resonator is driven into resonance. Some of the parameters of this resonant response are tracked, and changes in this response are correlated with the sensed parameter (such as deposition of mass in the case of mass sensing). This kind of sensing requires a good knowledge of the frequency response of the resonator, in order to measure and predict its behaviour. This section is centered in the study of the dynamic response of beam resonators, focused in clamped-clamped beam (cc-beam) structures. Different models of the response are studied, with focus on some of the most common experimental conditions and phenomena (such as the driven response and non-linearities in the elastic constant).

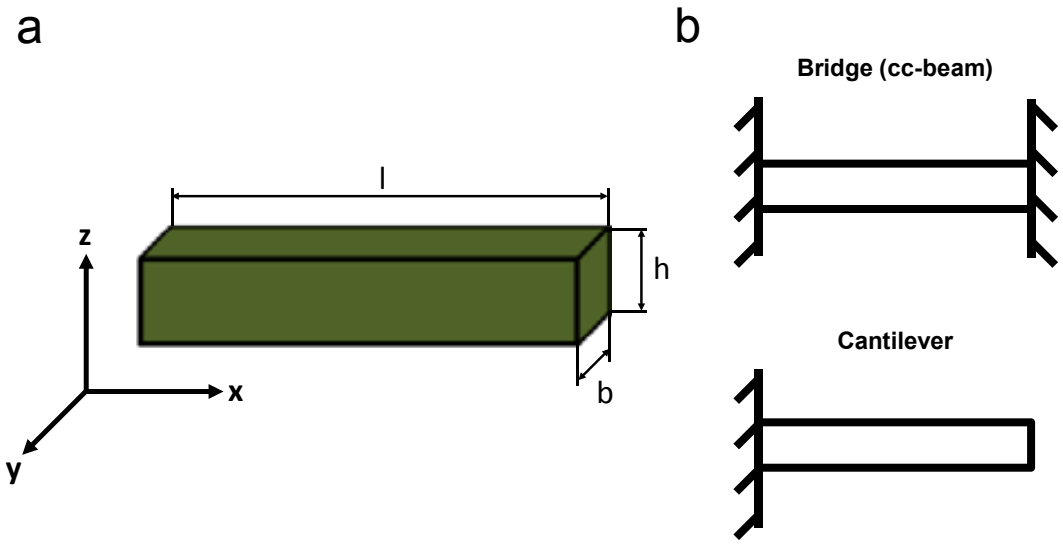

Figure 1.1: Geometry of the beam. a) Orientation and dimensions of the beam used throughout this study. b) Two different topologies of a beam resonator: clamped-clamped beam (bridge), in which both of the ends of the beam are clamped, and cantilever, in which only one of the ends is clamped.

1.1.1 Dynamic response of the resonator

The theory of elasticity describes the behaviour of homogeneous elastic materials. Elastic materials deform when a force is applied to them, but recover their shape when this force is removed. Crystalline silicon, which is a widely used material for nanomechanical resonators, fulfils this requirements for small deformations and a wide range of temperatures, so its behaviour can be studied in detail using this theory.

This section is centered in the study of the dynamic behaviour of beam resonators, with the objective of studying their frequency response. These resonators are formed by an homogeneous beam (Figure 1.1a), which has some or all its ends perfectly anchored to a side-wall (Figure 1.1b). These clampings of the beam fix the position and curvature at the clamped ends (i. e. its deformation and curvature are 0 at the clamped positions).

For the study we consider a homogeneous rectangular beam of width b, thickness h and length l, with its axis along the x direction (Figure 1.1a). When the beam is deformed, the displacement of a point of the beam at position x in the z direction is defined as $w(x)$. From the basics of the theory of elasticity, the differential equation describing the free behaviour of a beam (without applied forces) can be deduced [3] as:

$$EI\frac{^4w(x\ t)}{x^4} + \rho A\frac{^2w(x\ t)}{t^2} = 0 \tag{1.1}$$

where $w(x\ t)$ is the displacement of the beam at its longitudinal position x at time t, E is the Young's modulus of the material, ρ is the density of the material, A is the area of the cross-section of the beam ($b \times h$ in beam of rectangular cross-section) and I its moment of inertia, which for a rectangular beam moving in the z direction is defined as:

$$I = \int_{-h/2}^{h/2} z^2 b(z) dz \qquad I_{rectangular} = \frac{bh^3}{12} \tag{1.2}$$

As we observe, the thickness of the resonator in the direction of motion h has a strong influence in its moment of inertia. Equation (1.1) describes the unforced behaviour of the beam. By solving this equation we find that the resonator has a stable oscillating solution at determinate frequencies with certain associated mode shapes. In these conditions, the motion of the resonator $w(x\ t)$ can be described as the shape of the mode $w(x)$ oscillating at a determined frequency:

$$w(x\ t) = w(x)\cos(\ _n t + \theta) \tag{1.3}$$

By substituting this equation into (1.1) and derivating we obtain:

$$EI\frac{^4w(x)}{x^4} \pm \rho A\ \ ^2_n w(x) = 0 \tag{1.4}$$

We define $(k_n)^4 = \frac{\rho A}{EI}\ \ ^2_n$ and rewrite the expression as:

$$\frac{^4w(x)}{x^4} - k_n^4 w(x) = 0 \tag{1.5}$$

To solve this equation we use $w(x) = e^{\lambda x}$, obtaining:

$$\lambda^4 - (k_n)^4 = 0 \tag{1.6}$$

And therefore the solutions to this expression are:

$$\lambda = k_n \quad \lambda = -k_n \quad \lambda = jk_n \quad \lambda = -jk_n \tag{1.7}$$

From this solution, we determine that the shape of the mode $w(x)$ can be expressed as a sum of trigonometric functions:

$$w(x) = A_n \sin(k_n x) + B_n \cos(k_n x) + C_n \sinh(k_n x) + D_n \cosh(k_n x) \tag{1.8}$$

The coefficients A_n, B_n, C_n and D_n can be extracted from the contour conditions of the resonator, determined by the clampings. As an example, here equation (1.8) will be solved for a clamped-clamped beam, with perfect clampings at both sides, so the displacement of the beam and its curvature are null at both ends:

$$w(0) = 0 \quad w(l) = 0 \quad \frac{w(0)}{x} = 0 \quad \frac{w(l)}{x} = 0 \tag{1.9}$$

With these conditions, (1.8) is solved yielding:

$$A_n = -C_n \tag{1.10}$$

$$B_n = -D_n \tag{1.11}$$

$$\frac{A_n}{B_n} = \frac{\sin(k_n l) + \sinh(k_n l)}{\cos(k_n l) - \cosh(k_n l)} \tag{1.12}$$

$$\frac{A_n}{B_n} = -\frac{\cos(k_n l) - \cosh(k_n l)}{\sin(k_n l) - \sinh(k_n l)} \tag{1.13}$$

The parameter $k_n l$ is different for each mode of vibration. From the last two equations, the following equation is deduced:

$$\cosh(k_n l) \times \cos(k_n l) = 1 \tag{1.14}$$

This expression allows obtaining the values of $k_n l$, where each solution corresponds to a different vibration mode. For the particular case of a a cc-beam, the first four solutions are 4.73004, 7.8532, 10.9956 and 14.1372. The solution of the shape of the different modes of the resonator (1.8) can be written as:

$$w(x) = \cosh(k_n x) - \cos(k_n x) + \frac{\sin(k_n l) + \sinh(k_n l)}{\cos(k_n l) - \cosh(k_n l)}(\sinh(k_n x) - \sin(k_n x)) \tag{1.15}$$

Equations 1.14 and 1.15 allow determining the shape of the different vibration modes of vibration of the resonator. Substituting the first three solutions of $k_n l$ into the modeshape equation (1.8), the first three modeshapes of a cc-beam resonator are obtained and shown in Figure 1.2.

Finally, from the definition of $k_n l$, an expression of the resonance frequency is obtained:

$$_n = \frac{(k_n l)^2}{l^2} \quad \overline{\frac{EI}{\rho A}} \tag{1.16}$$

where the resonance frequency of the different modes is obtained from the different values of $k_n l$.

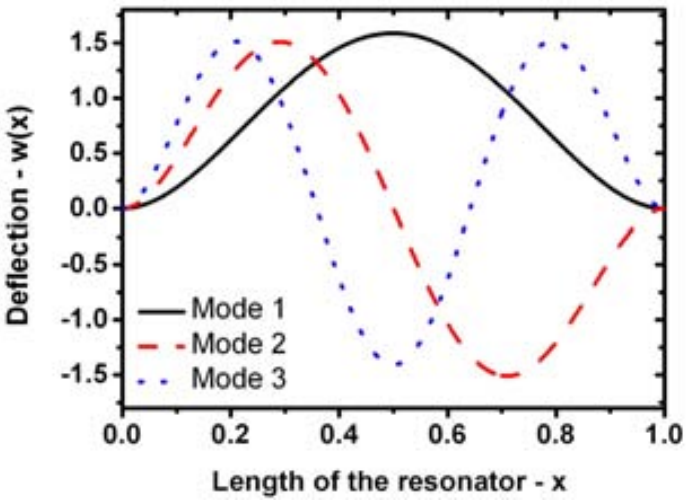

Figure 1.2: Shape of the first three resonance modes of a cc-beam resonator with unitary length.

This development can be easily applied to cantilever resonators by solving equation (1.8) with the appropriate contour conditions. Additionally, many of the measurement performed throughout this work are from bottom-up nanowires with hexagonal cross section, where the moment of inertia takes the form:

$$I_{hexagonal} = \frac{5\ \ \overline{3}d^4}{144} \tag{1.17}$$

where d is the distance between the parallel sides of the hexagon.

1.1.1.1 Mass-spring model

The vibration of a mechanical structure studied with the Euler-Bernoulli equation (1.1) can be simplified using a mass-spring model. Using this method, the motion of a particular point of the resonator is modelled as the movement of a mass attached to a spring (Figure 1.3). This simplified model provides no information of the resonance parameters for a determined physical structure, but has advantages in the study of complex resonating configurations, such as those containing multiple clampings or coupled resonators, which can be then modelled as series of springs and masses. This approximation and its related terminology are also used in the modelling of resonators for mass sensing applications (Section 6.2).

In a simple mass-spring model, the actuation of a force in the x direction which disturbs the mass from its balance position, provokes a recovery force $F = -kx$ where k is the elastic constant of the spring. In absence of a force, the equation of motion of the system is:

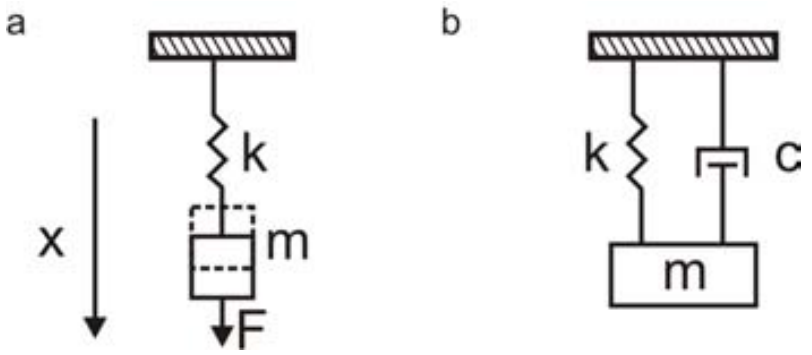

Figure 1.3: Mass-spring model. a) Simple mass-spring model: response of the system to an applied force. b) Mass-spring model with damping.

$$m\ddot{x} = -kx \qquad m\ddot{x} + xk = 0 \tag{1.18}$$

Where $\dot{x}$ denotes the derivative of x with respect to time. Defining the oscillation frequency $_n = \overline{k\ m}$ the equation of motion becomes:

$$\ddot{x} + \ {}^2_n x = 0 \tag{1.19}$$

The general solution for equation (1.19) is:

$$x(t) = A\sin(\ {}_n t + \alpha) \tag{1.20}$$

where the amplitude of motion (A) and the phase (α) are determined by the initial conditions.

In order to use this model, it is necessary to find equivalents between the physical parameters of the resonator, which have been studied using the Euler-Bernoulli method, and the ones from the mass-spring model. The natural oscillation frequency $_n$ corresponds to the resonance frequency of the resonator, which is found using the Euler-Bernoulli method. The spring constant k has a direct correspondence in the case of beams. When applying a punctual force to a beam (for example, to the center of a cc-beam) the beam deflects a certain amount. The constant which relates the displacement of the beam as a reaction to the deflection force is the spring constant, similarly to the mass-spring model. This parameter can be calculated by using the elasticity theory: for a cc-beam resonator, for a displacement of the center of the resonator provoked by a punctual perpendicular force, the elastic constant is defined as:

$$k_{cc-beam} = \frac{192EI}{l^3} \tag{1.21}$$

where I is the moment of inertia and E the young modulus of the material. On the contrary, the mass term m does not correspond to the real mass of the resonator.

It is a mathematical term, usually referred to as the effective mass of the resonator (m_{eff}). It can be found from the resonance frequency and the elastic constant as $m = k \quad ^2$. From the definition of the resonance frequency in equation (1.16) and the definition of the spring constant in equation (1.21), the effective mass of a cc-beam can be defined as:

$$m_{eff,cc-beam} = \frac{192 m_{beam}}{(k_n l)^4} = \alpha m_{beam} \tag{1.22}$$

where m_{beam} is the real mass of the resonator extracted from its dimensions and density.

The mass-spring model is a useful abstraction to study the behaviour of the resonator, although it does not give information of the resonance frequency or the modeshape. Until now, the analysis has been centred in a lossless resonator, where there is no dissipation of energy. In a real system dissipation is always present, and damping affects the motion of the oscillator. As a first order approximation, damping can be modelled with a damping force proportional to the speed of movement $F_d = -c\dot{x}$. In this case, the response of the system to a disturbance presents different solutions depending on the damping ratio, defined as $\zeta = c \ (2 \ _0 m)$. For slight damping $\zeta < 1$ the system oscillates with an exponentially decaying amplitude. In contrast, for $\zeta \geq 1$ the system does not oscillate at all. A complete development of the general response of a damped oscillator is found in [3].

During the operation of the resonator, a sinusoidal excitation force is generally supplied in order to overcome the damping and provoke the motion of the resonator. The force has the general form $F = F_0 \sin(\ \ t)$. In presence of these two additional terms, the differential equation describing the motion of the resonator becomes:

$$m\ddot{x} = -kx - c\dot{x} + F_0 \sin(\ \ t) \tag{1.23}$$

A detailed solution of this equation can be found in [3]. The response of the resonator contains two terms: the first one is important during the first cycles of the oscillation, and contains beats due to the forced oscillation and damping. The first transitory term vanishes quickly in most experimental conditions and the steady oscillating response dominates afterwards. Therefore, the analysis is centred in the stationary regime. In these conditions, the solution of equation (1.23) can be approximated as:

$$x(t) \approx \frac{F_0 \ \ m}{\sqrt{(\ \ _0^2 - \ \ ^2)^2 + 2c \ \ ^2 \ \ m}} \sin(\ \ t - \partial) \tag{1.24}$$

This equation shows that the amplitude of vibration is maximum when the frequency of the excitation signal equals the resonance frequency of the structure

(= $_0$). However, the damping of the system has an important effect on the shape of the frequency response of the resonator.

1.1.2 Quality factor and dissipation

The quality factor is a measure of the dissipation of energy in the resonator. The effects of this parameter are important for many applications: dissipation limits the sensitivity of the resonator to externally applied forces, it sets the level of fluctuations that degrade its spectral purity and determines the minimum intrinsic power levels at which the resonator can operate [4].

The quality factor Q is defined as the ratio between the total system energy and the average energy loss in one radian at resonance frequency:

$$Q = 2\pi \frac{E}{\Delta E} \tag{1.25}$$

where E is the total energy of the system and ΔE the energy dissipated by damping in one cycle. When studying the response of the resonator, a more useful expression of the quality factor can be defined from the damping ratio $\zeta = c\ (2\ _0 m)$:

$$Q = \frac{1}{2\zeta\ \sqrt{1-\zeta^2}} \qquad Q \approx \frac{1}{2\zeta} \tag{1.26}$$

Where the approximation is valid form for a small damping ratio. Returning to the equation of motion (1.24), the introduction of the quality factor yields:

$$x(t) = \frac{F_0\ m}{\sqrt{(\ _0^2 - \ ^2)^2 + \frac{\omega_0^2\omega^2}{Q}}} \sin(\ t - \partial) \tag{1.27}$$

$$\partial = atan\left(\frac{2n}{\ _0^2 - \ ^2}\right) \tag{1.28}$$

The frequency response of the resonator can be extracted from equation (1.27), and takes the form:

$$X(\ ) = \frac{F_0\ m}{\sqrt{(\ _0^2 - \ ^2)^2 + \frac{\omega_0^2\omega^2}{Q^2}}} \tag{1.29}$$

$$\angle X(\ ) = atan\left(\frac{_0\ Q}{\ _0^2 - \ ^2}\right) \tag{1.30}$$

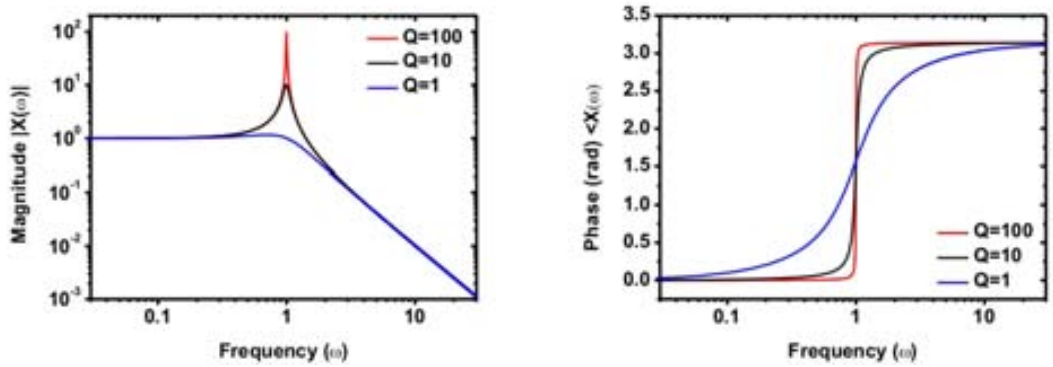

Figure 1.4: Frequency response of a resonator with unitary resonance frequency, for different quality factors.

These equations describe the amplitude of motion at the center of the resonator when the excitation force is a sinusoidal at frequency . A graphical representation of the equations near the resonance frequency is shown in Figure 1.4. The magnitude of the response has a resonance peak with its maximum at the resonance frequency, and its phase experiments a shift of π radians during resonance. In most experimental situations, the motion of the resonator is only detectable near the resonance frequency, where its amplitude is highest. From equation (1.29) the maximum oscillation amplitude of the resonator in resonance can be calculated:

$$X(\ _0)_{max} = \frac{F_0 Q}{m\ _0^2} \tag{1.31}$$

Figure 1.4 also shows the effect of the quality factor in the response of the resonator. With increased energy dissipation (lower quality factor) the resonance peak and the phase response widen, and the maximum oscillation amplitude decreases. In practice, this results in more uncertainty in the determination of the resonance frequency, due to lower signal-to-noise ratios and a smoother response.

Experimentally, the quality factor can be extracted from the bandwidth of the frequency response and the resonance frequency as shown in Figure 1.5:

$$Q = \frac{f_0}{\Delta f_{A/\sqrt{2}}} \tag{1.32}$$

The dissipation in nanomechanical resonators has different origins, both external to the resonator (such as the pressure of the gas surrounding the resonator) or relative to the resonator itself, such as defects in its structure. Due to the high quantity of effects which lead to energy dissipation, it is very difficult to predict the quality factor of a device, although some of its contributions can be studied. The

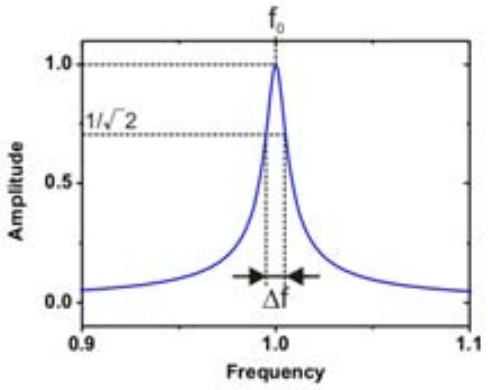

Figure 1.5: Determination of the quality factor from the response of the resonator.

total quality factor of the device Q_t can be calculated from the different contributions as:

$$Q_T^{-1} = Q_{gas}^{-1} + Q_{clampings}^{-1} + Q_{internal}^{-1} + \tag{1.33}$$

Therefore, when one of these factors dominates, its influence can be studied. Some of the sources of external damping which commonly affect nanomechanical resonators are losses due to gas damping and clamping losses at supports [4]. The losses due to gas damping are usually dominant when resonators are operated at ambient pressure, where there is a large number of collisions with gas molecules. When decreasing the gas pressure this effect becomes less important, which is why it is a usual practice to measure the resonators in vacuum conditions. Another source of damping which is more difficult to avoid arises from the clampings of the resonator with its supports, which introduce losses due to acoustic coupling. These are specially important in the case of cc-beams (which are supported at both of their ends). These losses increase when the clampings are of poor quality (compared to the ideal clamping defined during the Euler-Bernoulli development), such as in the cases where the clampings are not rigid or not completely immobile.

The sources of internal damping are relative to the material and structure of the resonator. Many resonators are fabricated from crystalline latices (such as Si resonators). Perfect crystal lattices have an intrinsic amount of damping, which represents the fundamental damping limit of the resonator. However, in practice the crystalline structure contains defects that add losses, which become higher than the intrinsic limit. More important in many cases is the damping at the surface of the resonator: native oxide, defects on the surface or adsorbates all contribute to generate damping in the resonator. These losses are specially important in small resonators, which present high surface-to-volume ratios: in general, this means that these resonators are more sensitive to surface effects. In practice, it is found that

smaller resonators tend to present lower quality factors, which confirms the increasing importance of surface effects when reducing the dimensions of the resonators [5, 4].

1.1.3 Non-linearities

One of the assumptions made during the analysis of the resonator is that the spring constant of the resonator remains constant for its whole range of operation (in other words, k does not depend on the motion of the resonator x). When this is not fulfilled and k can not be considered a constant, some corrections have to be applied to the equation of motion. This section presents an overview of the effects of non-linearities in the spring constant. The developments to find the studied expressions can be found at [6, 7].

When the spring constant is dependent on the amplitude of motion, it can be modelled with high order corrections, k_1 and k_2, which are included in the equation of motion:

$$m\ddot{x} + kx + c\dot{x} + k_1x^2 + k_2x^3 = F_0 \sin(\ t) \tag{1.34}$$

The solution of this equation yields a response very similar to equation (1.29), in which the resonance frequency $ {}'_0$ is not a constant, but a function of the amplitude of motion:

$$X(\ ) = \frac{F_0 \ m}{\sqrt{(\ {}'^2_0 - \ {}^2)^2 + \frac{\omega'^2_0\omega^2}{Q^2}}} \tag{1.35}$$

$$ {}'_0 = \ {}_0k' \ X(\ )^{\ 2} \tag{1.36}$$

$$k' = \frac{3k_2}{8k} \ {}_0 - \frac{5k_1^2}{12k^2} \ {}_0 \tag{1.37}$$

where $ {}_0$ and k are the resonance frequency and spring constant of the linear resonator. Figure 1.6a shows the evolution of the response of the resonator for an increasing excitation force (and hence, an increasing amplitude of motion), for different values of k'. When k' is positive, the resonance peak shifts to upper frequencies with an increasing amplitude of motion, while for negative k values it shifts towards lower frequencies. Another effect of non-linearities is shown in Figure 1.6b: after a certain critical amplitude $X_{crit}(\ )$, the response of the resonator presents hysteresis. The existence of multiple paths in the function entails issues with the use of the resonator as a sensor, due to the instability of part of the frequency response. For this reason, it is important to work in linear regime or develop strategies to deal with these non-linear effects [8].

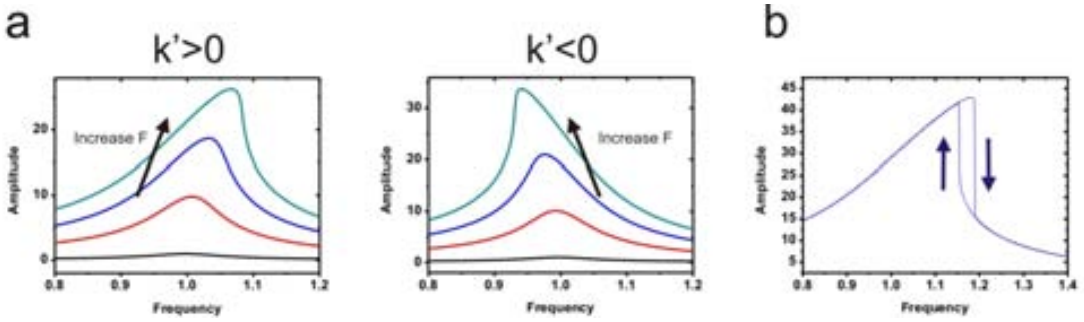

Figure 1.6: Effects of a nonlinear spring constant in the frequency response of the resonator. a) Evolution of the response with an increase of the amplitude of motion, for positive and negative values of k'. b) Hysteretic frequency response, which appears for high amplitudes of motion.

In practice, there are two main factors which modify the spring constant of the resonator: an increase of the rigidity of the beam due to its elongation (called spring hardening), and a decrease of its spring constant due to the gradient of the electric field when using electrostatic actuation (called spring softening).

The mechanical spring hardening effect occurs when the rigidity of the resonator is no longer constant relative to the elongation of the resonator. When the elongation of the resonator is sufficiently large, its rigidity (and its restoring force) increases. This effect is common in cc-beam resonators, in which their deflection also implies an elongation of the beam: for sufficiently large vibration amplitudes, the rigidity is higher when the beam is at its maximum deflection. This effect can be modelled with a positive value of k', representing a higher rigidity of the structure when the amplitude of motion increases.

The spring softening effect occurs for electrostatically actuated resonators. In this actuation method, which is treated in detail below, the motion is induced by an electric field between the resonator and an actuation electrode, which are separated by a gap. The attracting force from the electrode increases with a decreasing gap, but for small vibration amplitudes (amplitude of vibration much smaller than the gap) this effect can be neglected. However, for large vibrations, the electrostatic force over the resonator is stronger when the resonator is near the gap, and weaker when it is farther. This can be modelled with a negative values of k', representing a decrease of the rigidity of the structure with an increase of the amplitude of motion.

1.2 Actuation methods

The present section deals with the modelling of the actuation transducer, which is in charge of setting in motion the mechanical element using electric signals. In the case of nanomechanical resonators, the actuator drives the resonator into resonance and therefore has the particularity of dealing with high frequency signals, specially for

NEMS resonators. In order to generate this mechanical stimulus, several different actuation methods can be used [9]. This section provides a general description of some common actuation methods and a detailed description of the electrostatic actuation, which is employed in this work.

1.2.1 Electrostatic actuation

Electrostatic actuation, also called capacitive actuation, is probably the most extensively used method in the field of nanomechanical resonators. It relies in the attractive force which develops between the plates of a capacitor when they are charged. In most cases, either a driving electrode (also called gate) is fabricated near the resonator for actuation, or the substrate under the resonator is used. The main advantages of this technique is that it is integrable, and it works in a wide range of materials, as long as they are conductive. This actuation technique is effective at high frequencies, and has been used from low frequency resonators to those operating at tens of gigahertzs [10]. This section presents an analysis of electrostatic actuation of nanomechanical resonators.

In electrostatic actuation, the resonator and the driving electrode form a capacitor, with capacitance C_0 at rest. Several models for the calculation of this capacitance are discussed below, based on the geometry of the gate-resonator system. In this case, the electrostatic energy stored in the capacitance is:

$$W = \frac{1}{2}CV^2 \tag{1.38}$$

Where V is the voltage drop between the resonator and the electrode. The force between both elements is defined as the energy gradient:

$$F_e = -\frac{W}{x} = -\frac{1}{2}V^2\frac{C}{x} \tag{1.39}$$

The term C x depends on the geometry of the system. In general, the voltage V applied between the resonator and the driving electrode consists in a DC plus an AC term. The AC term is in charge of the high frequency excitation of the resonator, and in general its frequency is the resonance frequency of the resonator. Moreover, in general $V_{DC} \gg V_{AC}$, and in then in this case the voltage term in the equation can be written as:

$$\begin{aligned} V^2 &= (V_{DC} + V_{AC}\cos(\ t))^2 \\ &= V_{DC}^2 + \frac{1}{2}V_{AC}^2 + \frac{1}{2}V_{AC}^2\cos(2 \ t) + 2V_{DC}V_{AC}\cos(\ t) \end{aligned} \tag{1.40}$$

The voltage has three different contributions: a constant term, a high frequency term at twice the AC frequency (2) and a third term at the frequency of the AC

signal. This third term is the one used for excitation. With these contributions, the electrostatic force takes the form:

$$F_e = -\frac{1}{2}\frac{C}{x}\left(V_{DC}^2 + \frac{1}{2}V_{AC}^2 + \frac{1}{2}V_{AC}^2\cos(2\ \ t) + 2V_{DC}V_{AC}\cos(\ \ t)\right) \tag{1.41}$$

The particular expression of the excitation frequency depends on C x. However, in most cases, if the gap between the resonator and the actuation electrode g is much larger than the motion of the resonator at resonance x ($g \gg x$) the electrostatic force can be considered constant. In this case, the force term at the excitation frequency, which is the one that dominates when the resonator operates near its resonance frequency, is:

$$F_e = -\frac{C}{x}V_{DC}V_{AC}\cos(\ \ t) \tag{1.42}$$

This expression can be treated as a first approximation of the electrostatic force. However, a more accurate model of the capacitance has to be used to study the motion in each particular case.

1.2.1.1 Capacitance between the resonator and the actuation electrode

As it is shown in the last section, and specially in equation (1.42), a model of the capacitance between the resonator and the actuation electrode is important to evaluate the efficiency of the electrostatic actuation method. Here, several capacitance models are presented, which are applicable to different geometries of the resonator and actuation electrode. In this work, all the studied resonators have two features which are used to simplify the calculations: the gap between the resonator and driving electrode is large compared to the motion of the resonator x ($g \gg x$), and the gap is also much larger than the lateral dimensions of the resonator t ($g \gg t$). This second approximation is not as clear as the first one. However, we find that in most of the measured devices, $g > 10t$. Finally, the motion of the resonator with respect to the actuation electrode is modelled as a reduction of the gap between both elements. Figure 1.7 shows the different models of capacitance which are analysed in this section, and their associated dimensions.

The first model is the parallel plate capacitor, in which the electric field is generated between two parallel plates (Figure 1.7a). The motion of the resonator x reduces the gap:

$$C_{pp,0} = \epsilon\frac{lt}{g} \tag{1.43}$$

$$C_{pp} = \epsilon\frac{lt}{(g-x)} = C_{pp,0}\frac{g}{(g-x)} \tag{1.44}$$

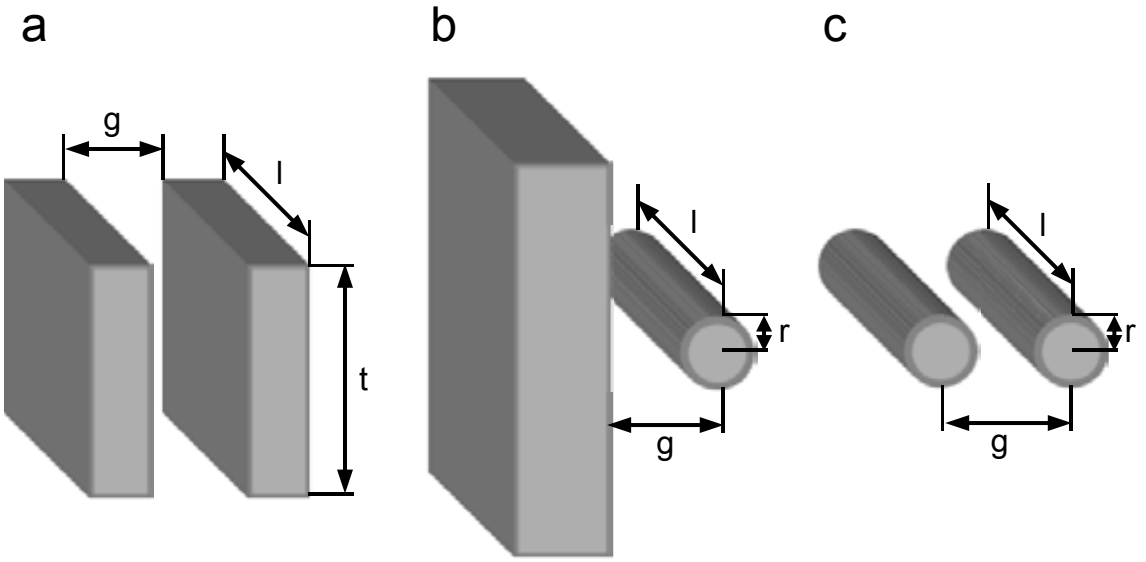

Figure 1.7: Capacitance between the resonator and the actuating electrode. a) Parallel plate capacitor: two parallel plates with dimensions $l \times t$. b) Wire of radius r and length l parallel to an infinite plane. c) Capacitance between two parallel wires with radius r and length l.

where ϵ is the permittivity of the medium which conforms the gap. With the expression of the capacitance, $\partial C/\partial x$ can be calculated. By expanding this expression and afterwards derivating we find:

$$C_{pp} = \frac{C_{pp\,0}}{1-\frac{x}{g}} \approx C_{pp\,0}\left(1+\frac{x}{g}+\frac{x^2}{g^2}+...\right) \tag{1.15}$$

$$\frac{\partial C_{pp}}{\partial x} = \frac{C_{pp\,0}}{g}\left(1+\frac{2x}{g}+...\right) \tag{1.16}$$

Finally, for $g \gg x$, we find:

$$\frac{\partial C_{pp}}{\partial x} \approx \frac{C_{pp\,0}}{g} \tag{1.17}$$

The second model is a wire parallel to an infinite plane (Figure 1.7b). In this case, the capacitance can be expressed as:

$$C_{pw\,0} = \frac{2\pi\epsilon l}{\ln\left(\frac{g}{r}+\sqrt{\frac{g^2}{r^2}-1}\right)} \approx \frac{2\pi\epsilon l}{\ln\left(2\frac{g}{r}\right)} \tag{1.18}$$

Considering that the motion of the resonator reduces the gap, and derivating:

$$C_{pw} = \frac{2\pi\epsilon l}{\ln\left(2\frac{g}{r}\left(1-\frac{x}{g}\right)\right)} \tag{1.49}$$

$$\frac{C_{pw}}{x} = \frac{2\pi\epsilon l}{(g-x)\ln\left(2\frac{g}{r}\left(1-\frac{x}{g}\right)\right)^2} \tag{1.50}$$

$$\tag{1.51}$$

Again, for $x \ll g$:

$$\frac{C_{pw}}{x} \approx \frac{C_{pw,0}}{g\ln\left(\frac{2g}{r}\right)} \tag{1.52}$$

The third considered model consists in two parallel wires (Figure 1.7c). The capacitance between the wires in this model is expressed as:

$$C_{ww,0} = \frac{\pi\epsilon l}{\ln\left(\frac{g}{2r}+\sqrt{\frac{g^2}{4r^2}-1}\right)} \approx \frac{\pi\epsilon l}{\ln\left(\frac{g}{r}\right)} \tag{1.53}$$

$$C_{ww} = \frac{\pi\epsilon l}{\ln\left(\frac{g-x}{r}\right)} \tag{1.54}$$

Similarly to the wire-plane model, the derivative considering $x \ll g$ yields:

$$\frac{C_{ww}}{x} \approx \frac{C_{ww,0}}{g\ln\left(\frac{g}{r}\right)} \tag{1.55}$$

In all three cases, as a first approximation, the derivative of the capacitance with respect to the motion of the nanowire can be considered a constant (independent of the amplitude of motion), as long as this amplitude of motion is sufficiently small compared to the gap.

1.2.2 Other actuation methods

Besides electrostatic actuation, other methods are employed to actuate nanomechanical resonators. In magnetomotive transduction [9, 11] the motion of the resonator is induced by the Lorentz force generated by a static magnetic field to a current-carrying conductor. The resonator is exposed to a strong magnetic field, and a current at the desired frequency of motion is passed through it in order to induce the actuation. The strong magnetic field is generated externally, and the direction of the actuation force can be controlled by the direction of the field. This technique

does not degrade at high frequencies [12], but it needs the external generation of strong magnetic fields (it is not integrated in the chip).

Another actuation mechanism is the use of thermal mechanisms to provoke the deflection of the mechanical structure. These thermal effects are generally applied using Joule heating originated from a current passing through the resonator or one of its elements. Different methods for thermal excitation exist. Rahafrooz et al. take advantage of the expansion of the material conforming the bulk of the resonator, which expands when heating [13]. By applying an AC current, the cycles of heating-cooling of the resonator induce their motion, which is further amplified at resonance. This is possible thanks to the small dimensions of the resonators, which allow fast cycling of the temperature. Another alternative is used by Bargatin et al. [14]. In their case the current is not supplied to the body of the resonator, but introduced through a metal loop located over the resonator. The difference in thermal expansion coefficients causes stress in the structure when the loop heats and induces the motion of the resonator.

Another actuation method consists in using piezoelectric elements to induce the motion of the resonator. A piezoelectric material responds to an external electric field by deforming, which can be used to actuate nanomechanical resonators. This can be accomplished, for example, by defining a loop of piezoresistive material over the resonator [15]. Piezoresistive actuation however relies on a reduced choice of materials which present piezoelectric properties. For high frequency applications, the material also needs to be able to react sufficiently fast to the applied voltages (i. e. its relaxation time must be sufficiently small).

1.3 Transduction mechanisms

The third part of a nanoelectromechanical system is the transducer in charge of transforming the response of the mechanical element to an electric signal. In the case of nanomechanical resonators, this implies obtaining a measurable electrical signal which provides information about the motion of the resonator. The most common approach in the field of NEMS resonators is electrical transduction, in which the motion of the resonator directly generates a measurable electric signal, and optical transduction, in which optical methods (such as interferometry) are used to detect the motion of the resonator. This section is focused in the study of electrical detection mechanisms, paying special attention the piezoresistive transduction mechanism and the conductance change due to charge modulation in the resonator, which are widely used for the detection of the motion of high frequency nanomechanical resonators.

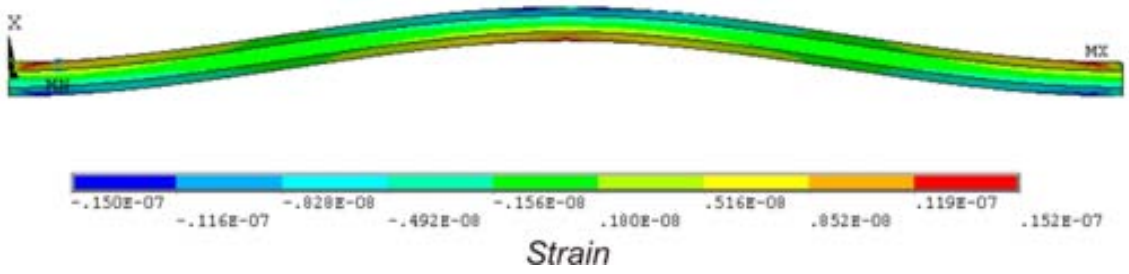

Figure 1.8: Simulation of the strain in a deformed clamped-clamped beam using the Ansys FEM software. The strain has opposite signs in the upper and lower sides of the neutral axis of the beam: it is compressive in the lower side of the resonator, and tensile in the upper side.

1.3.1 Piezoresistive transduction

The piezoresistance effect is the change of the electrical resistivity of a material upon the application of an external stress. In the case of a nanoelectromechanical resonator, the stresses generated by its motion change its resistance, which can be monitored electrically. Although this transduction mechanism is used in different topologies, this section is centered in the study of cc-beam resonators fabricated entirely from a piezoresistive material.

In the case of cc-beams, the internal stresses which occur in the different parts of the beam during its deflection balance each other, so that the total stress of the structure is null. This is shown in figure 1.8, where strains (and therefore, stresses) are tensile above the neutral axis and compressive below. Therefore, the total resistance change provoked by these stresses is null. However, the deformation of the beam also causes an elongation of the structure.This elongation provokes an overall tensile stress, which increases the resistance of the resonator. Considering a cc-beam resonator with length l_0 at rest, laying along the x direction (such as the one in Figure 1.1), when the deformation of the wire is $w(x)$, its elongation can be defined as:

$$l_{deformed} = l_0 + \Delta l = \int_0^{l_0} \sqrt{1 + \left(\frac{w(x)}{x}\right)^2}\, dx \approx \int_0^{l_0} \sqrt{\left(\frac{w(x)}{x}\right)^2}\, dx \qquad (1.56)$$

As a first approximation, the elongation of a wire with a displacement at its center can be found by supposing that the deformed center forms a triangle with its clampings, similarly to the deformation of a rubber. In this case, it is readily found that the elongation $\Delta l = (l_{deformed} - l_0)\ l_0$, when displacing the centre of the wire a longitude z is:

$$\frac{\Delta l}{l_0} \approx 2\frac{z^2}{l_0^2} \qquad (1.57)$$

A more accurate approximation can be obtained using equation (1.56) when using an appropriate equation describing $w(x)$. A more precise value for a deformed resonator with a punctual force applied to its centre is $\Delta l \ l_0 \approx 2\ 44(z^2 \ l_0)^2$.

A widely used parameter to quantify the piezoresistance effect in beam resonators is the gauge factor G_{PR}, which relates the elongation of the resonator with the resistance change due to its piezoresistance. It should be noted that, even without a piezoresistive effect, a deformed beam still increases its resistance due to the elongation and the related decrease of its cross-section when deformed. To rigorously determine the gauge factor, the geometric increase of resistance should be extracted when determining the resistance change from the elongation. In practice, however, when using a piezoresistive material with relatively high gauge factor (such as silicon), the geometric effect is generally low enough to be negligible [16]. In this case, the gauge factor for a resonator with a resistance at rest R_0 can be defined as:

$$G_{PR} = \frac{\Delta R \ R_0}{\Delta l \ l_0} \tag{1.58}$$

Combining equations (1.57) and (1.58), and defining the motion at the centre of the resonator as $x(t)$, the resistance change due to a deflection at the centre of the cc-beam can be written as:

$$\Delta R_{motion}(t) = R_0 G_{PR} \frac{\Delta l(t)}{l_0} \approx 2\ 44 R_0 G_{PR} \left(\frac{x(t)}{l_0}\right)^2 \tag{1.59}$$

1.3.2 Conductivity modulation by induced charge

It has been observed that the conductivity of certain types of nanowires and nanotubes can be modified by inducing charge in the structure. Under these conditions, a modulation of this charge leads to a modulation of the conductivity of the device [17]. This effect is used, for example, in the fabrication of Carbon Nanotube Field Effect Transistors (CNT-FETs) from semiconductor CNTs. This conductivity modulation is also used in the case of nanomechanical resonators, where the motion of the resonator modulates the capacitance with an actuation electrode, which in turn modulates the charge (and conductance) in the resonator [2]. Therefore, the conductance of the resonator $G(t)$ can be expressed as:

$$G(t) = \frac{G(t)}{q} q(t) \tag{1.60}$$

In the case of a nanomechanical resonator with electrostatic actuation, the resonator forms a capacitance with the actuation electrode. Considering the relation between capacitance C, charge q and tension V, $q = V \times C$, and that the motion of the resonator is induced by a voltage in the actuation electrode with frequency

($V_g(t) = V_{g,DC} + V_{g,AC}(t)$, where $V_{g,AC}(t) = V_{g,AC,0}\cos(\ \ t)$), the expression of the charge in the resonator is:

$$q(t) = C_g(t)V_{g,DC} + C_{g,0}V_{g,AC}(t) \tag{1.61}$$

where $C_{g,0}$ is the capacitance between the resonator and the actuation electrode at rest, and $C_g(t)$ is the capacitance due to the motion of the resonator. The first term describes the contribution of the motion of the resonator to the charge modulation, modelled as a capacitance which includes the motion of the resonator and its frequency response. The second term is the purely electrical contribution of the gate voltage at frequency which is used to actuate the resonator. We define the motion of the center of the resonator as $x(t)$, with an amplitude depending on its frequency response $X(\ \ )$. In this case the distance between the resonator and the gate $g(t)$ depends on the gap at rest g_0 and the motion of the resonator:

$$g(t) = g_0 - x(t) = g_0 - \ X(\ \ )\ \cos(\ \ t) \tag{1.62}$$

This motion induces a change in capacitance between the resonator and the gate:

$$C_g(t) = \frac{C_g}{x}x(t) \tag{1.63}$$

Therefore, the motion of the resonator induces a charge modulation of the form:

$$q_{motion}(t) = C_g(t)V_{g,DC} = \frac{C_g}{x}x(t)V_{g,DC} \tag{1.64}$$

and consequently a conductance modulation:

$$\Delta G_{motion}(t) = \frac{G}{q}q_{motion}(t) = \frac{G}{q}\frac{C_g}{x}x(t)V_{g,DC} \tag{1.65}$$

In practice however, the contribution of the second term of expression (1.61) is not negligible and will contribute with a parasitic signal of electrical origin, which interferes with the motional signal and hinders its detection.

1.3.3 Other transduction mechanisms

The piezoresistive effect and the conductivity change by charge modulation are common detection techniques for nanomechanical resonators, but there are other methods which are equally popular for the transduction of the motion of resonators, such as capacitive, magnetomotive and piezoelectric transduction.

Capacitive transduction is based in the modulation of the capacitance between the beam and a fixed detection electrode, which in turn modulates the charge in the readout electrode (originated by the relation $q = CV$). First, a biasing voltage

is applied between the resonator and the actuator electrode. When the capacitance is modulated by the motion of the resonator, the charge in the readout electrode is also modulated, generating a current which contains information about this motion. The main advantages of this method are its simplicity and the fact that it is integrated on chip. However, additional capacitances are present at the output of the resonator (called parasitic capacitances), which can absorb part of the output signal. When reducing the dimensions of the resonator, the capacitance of the resonator and the output signals become smaller, and additionally the resonance frequencies are generally higher. Because of these effects, care must be taken when scaling down this transduction mechanism. Some techniques are used to alleviate this issues, such as the use of integrated amplification circuitry at the output of the resonator or the reduction of the dimensions of the gap between the resonator and the actuation electrode to achieve a higher capacitance [18, 19].

The magnetomotive transduction mechanism is also employed to detect the motion of resonators. Similarly to the magnetomotive transduction, it relies in the effects of a strong magnetic field applied to a conductive resonator. When the resonator oscillates in a uniform constant magnetic field, a current is generated through the resonator. The detection of this current has constraints similar to those found in the capacitive method, namely small currents and the presence of parasitic capacitances.

Alternatively, the piezoelectric effect can also be used as a transduction mechanism. We have seen in previous sections that the motion of the resonator provokes stress in its structure. In a piezoelectric material, this stress in turn provokes a voltage drop in the structure, which can be monitored to obtain information about its motion.

References

[1] J. Chaste, A. Eichler, J. Moser, G. Ceballos, R. Rurali, and A. Bachtold, "A nanomechanical mass sensor with yoctogram resolution," *Nature Nanotechnology*, vol. 7, pp. 301–304, Apr. 2012.

[2] V. Sazonova, Y. Yaish, H. Üstünel, D. Roundy, T. A. Arias, and P. L. McEuen, "A tunable carbon nanotube electromechanical oscillator," *Nature*, vol. 431, pp. 284–287, Sept. 2004.

[3] M.-h. Bao, *Micro Mechanical Transducers: Pressure Sensors, Accelerometers and Gyroscopes*. Elsevier, Oct. 2000.

[4] K. L. Ekinci and M. L. Roukes, "Nanoelectromechanical systems," *Review of Scientific Instruments*, vol. 76, pp. 061101–061101–12, May 2005.

[5] P. Mohanty, D. A. Harrington, K. L. Ekinci, Y. T. Yang, M. J. Murphy, and M. L. Roukes, "Intrinsic dissipation in high-frequency micromechanical resonators," *Physical Review B*, vol. 66, p. 085416, Aug. 2002.

[6] V. Kaajakari, T. Mattila, A. Oja, and H. Seppa, "Nonlinear limits for single-crystal silicon microresonators," *Journal of Microelectromechanical Systems*, vol. 13, pp. 715 – 724, Oct. 2004.

[7] V. Kaajakari, "Ville kaajakari's MEMS tutorials."

[8] N. Kacem, J. Arcamone, F. Perez-Murano, and S. Hentz, "Dynamic range enhancement of nonlinear nanomechanical resonant cantilevers for highly sensitive NEMS gas/mass sensor applications," *Journal of Micromechanics and Microengineering*, vol. 20, p. 045023, Apr. 2010.

[9] K. L. Ekinci, "Electromechanical transducers at the nanoscale: Actuation and sensing of motion in nanoelectromechanical systems (NEMS)," *Small*, vol. 1, no. 8-9, p. 786–797, 2005.

[10] E. A. Laird, F. Pei, W. Tang, G. A. Steele, and L. P. Kouwenhoven, "A high quality factor carbon nanotube mechanical resonator at 39 GHz," *Nano Letters*, p. 111202105855000, Dec. 2011.

[11] X. L. Feng, R. He, P. Yang, and M. L. Roukes, "Very high frequency silicon nanowire electromechanical resonators," *Nano Letters*, vol. 7, pp. 1953–1959, July 2007.

[12] X. M. H. Huang, X. L. Feng, C. A. Zorman, M. Mehregany, and M. L. Roukes, "VHF, UHF and microwave frequency nanomechanical resonators," *New Journal of Physics*, vol. 7, pp. 247–247, Nov. 2005.

[13] A. Rahafrooz and S. Pourkamali, "High-frequency thermally actuated electromechanical resonators with piezoresistive readout," *IEEE Transactions on Electron Devices*, vol. 58, pp. 1205–1214, Apr. 2011.

[14] I. Bargatin, I. Kozinsky, and M. L. Roukes, "Efficient electrothermal actuation of multiple modes of high-frequency nanoelectromechanical resonators," *Applied Physics Letters*, vol. 90, pp. 093116–093116–3, Feb. 2007.

[15] L. G. Villanueva, R. B. Karabalin, M. H. Matheny, E. Kenig, M. C. Cross, and M. L. Roukes, "A nanoscale parametric feedback oscillator," *Nano Letters*, p. 111025132735008, Oct. 2011.

[16] R. He and P. Yang, "Giant piezoresistance effect in silicon nanowires," *Nature Nanotechnology*, vol. 1, no. 1, pp. 42–46, 2006.

[17] S. J. Tans, A. R. M. Verschueren, and C. Dekker, "Room-temperature transistor based on a single carbon nanotube," *Nature*, vol. 393, pp. 49–52, May 1998.

[18] J. Arcamone, M. A. F. van den Boogaart, F. Serra-Graells, J. Fraxedas, J. Brugger, and F. Pérez-Murano, "Full-wafer fabrication by nanostencil lithography of micro/nanomechanical mass sensors monolithically integrated with CMOS," *Nanotechnology*, vol. 19, p. 305302, July 2008.

[19] J. Verd, A. Uranga, G. Abadal, J. Teva, F. Torres, J. Lopez, E. Perez-Murano, J. Esteve, and N. Barniol, "Monolithic CMOS MEMS oscillator circuit for sensing in the attogram range," *IEEE Electron Device Letters*, vol. 29, pp. 146 –148, Feb. 2008.

Chapter 2

Fabrication of bottom-up silicon nanowire nanomechanical resonators

Contents

The fabrication of nanomechanical resonators with lateral dimensions in the nanometer scale poses a technological challenge. The scaling of classical top-down approaches involving photolithography is not effective at this range of dimensions, because their resolution is usually limited by the wavelength of the exposing light [1]. Smaller dimensions can be defined by using complex resolution-enhancing techniques or with other methods such as electron-beam (e-beam) lithography, which are able to reach dimensions down to 10 nm. Even with appropriate techniques, device size

fluctuations are important at this scale, and they can affect key characteristics of the nanostructures, such as their electrical properties [2] or resonance frequency.

The use of bottom-up methods alleviates some of the problems related with fabrication at the nanometer scale. These techniques consist in building structures by using nanoscale building blocks and placing them at the desired positions [1]. With this approach it is inherently easy to build structures of small dimensions because there are no photolithographic constraints, although a precise control of the dimensions of these structures is still challenging. In this sense, bottom-up nanowires are good candidates for the fabrication of nanomechanical resonators of small dimensions.

This chapter describes the fabrication process of nanomechanical resonators based on doubly-clamped bottom-up silicon nanowires. The objective is the fabrication of nanomechanical resonators of small dimensions, with lengths of micrometers and diameters of tens of nanometers. These resonators must have good electrical properties to allow electrical transduction in down-mixing electrical measurement methods. Moreover, the nanowires must be as close as possible to a side-gate for electrostatic actuation.

The first section of this chapter presents a short review of the state of the art and challenges in the field of bottom-up nanomechanical resonators based on nanowires. The next section reviews the different technological processes involved in the fabrication of the resonators, paying special attention to those specific to bottom-up techniques (such as nanowire synthesis). The last section presents the fabrication process which is used in this work.

2.1 Introduction to resonators based on bottom-up semiconductor nanowires

Bottom-up semiconductor nanowires present intrinsic properties that make them excellent candidates for nanomechanical resonators, thanks to their electric and material properties. For example, the synthesis of nanowires with small dimensions and diameters in the deep nanometer scale allows to reach high resonance frequencies. Moreover their lateral dimensions in the nanometer scale reveal properties which differ from that of bulk materials, such as the giant piezoresistive coefficients present in silicon nanowires [3]. In consequence these devices are outstanding candidates to study both the properties of nanomechanical resonators and material properties at the nanoscale.

This work is centred in electrically-transduced nanomechanical resonators, which is based in applying an electric signal to the nanoresonator and detecting changes in this signal produced by its motion. In this sense, a cc-beam connected to electrodes

which supply the electric signals is the most basic structure which allows this kind of transduction. The cantilever is another geometry suitable for the fabrication of electrically-transduced nanomechanical resonators: they can be sensed capacitively [4] or electrostatically [5]. However, this work is centred in the clamped-clamped beam topology.

Even if the technology allows for a feasible fabrication of nanowires with dimensions in the range of tens of nanometers, the integration of these devices as nanomechanical resonators is not straightforward. In order to have electrically transduced nanomechanical resonators, the nanowire needs to electrically connect two electrodes which are typically patterned using standard micromachining planar technologies. At this point, two different approaches exist: to grow the nanowires directly on the pre-patterned substrate, or to deposit previously grown nanowires in between the electrodes to connect them.

The growth of nanowires directly in the pre-patterned chips, in which they are welded to both sides of a trench, presents some advantages thanks to the epitaxial contacts formed between the nanowires and both side-walls [6]. However, the fabrication process usually involves placing catalyst particles at the desired growth position, that is, a localized position of the walls. This is challenging from a technological point of view, and different approaches to solve this problem are explained below.

The first attempts at growing nanowires in pre-patterned chips were performed in 2005 by the group of P. Yang [7, 8] and by R. S. Williams et al. [9]. In these works, Silicon Nanowires (SiNWs) are grown in trenches connecting two electrodes defined in the device layer of Silicon-on-Insulator (SOI) wafers (as seen in Figure 2.1), allowing to introduce and read electric signals through the wire. These structures permitted new approaches for the study of mechanical properties of this kind of nanowires, such as the determination of their elasticity using Atomic Force Microscopy (AFM) [10]. Also, these structures allowed to study electromechanical properties of bottom-up SiNW of small dimensions, such as their piezoresistive factors. A complete study of this parameter for nanowires of different diameters and conductivities was performed [3], finding that structures of small lateral dimensions present giant gauge factors. Later on, the same structures were used as nanomechanical resonators using magnetomotive [11, 12] (Figure 2.1) and piezoresistive [13] transduction. In these works, a dynamic characterization of nanowires with diameters down to 30 nm with resonance frequencies ranging up to 215 MHz was performed. Also, high quality factors arising from the crystalline structure of the nanowires and their epitaxial contacts were demonstrated.

An alternative to the epitaxial growth of nanowires in substrates is the synthesis of the nanowires followed by their deposition in pre-patterned substrates. An example of this technology can be seen in Figure 2.2, in which zinc oxide (ZnO)

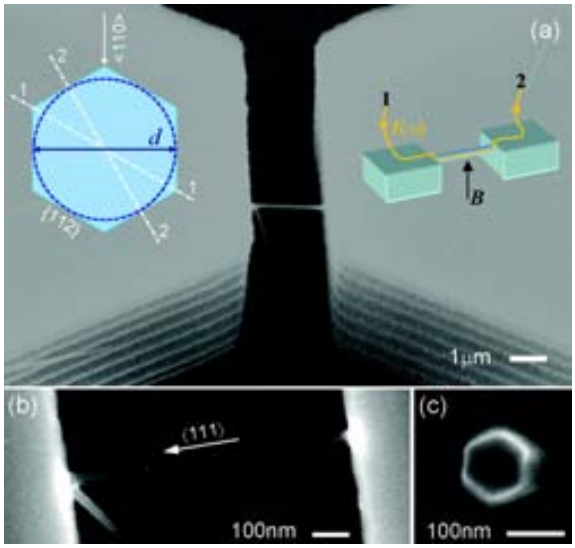

Figure 2.1: Silicon nanowire resonator transduced using magnetomotive transduction. Extracted from [11].

nanowires are deposited on top of pre-defined electrodes, and are subsequently used as nanomechanical resonators [14]. This approach has also been followed by Nelis et al. [15] to successfully characterize SiNW resonators using optical interferometry. The flexibility of this fabrication technique allows to use nanowires of a variety of materials, because there is no influence of the substrate in their synthesis. Several works use this approach to build nanomechanical resonators from a variety of materials such as the ZnO nanowires (shown above), tin oxide (SnO_2) [16], gallium nitride (GaN) [17] and indium arsenide (InAs) [18, 19]. In all these cases, the nanowires have diameters of 100 nm or more and the resonance frequencies are lower than 100 MHz.

Some works have also been performed with nanomechanical resonators based in bottom-up nanowires characterized with optical methods. Although they do not use electric transduction, these works provide insight into phenomena related to nanomechanical resonators, such as mode splitting. In this case, the nanowires do not need to be clamped to the side-walls by both ends, as no electric signal is required to pass through the wire. Examples of such devices can be found both for in-chip grown [20, 21] and deposited [22] nanowires.

2.1.1 Challenges in the fabrication of bottom-up nanomechanical resonators

As it is pointed above, there are several difficulties in the use of bottom-up nanowires as nanomechanical resonators. A complete NEMS device typically comprises

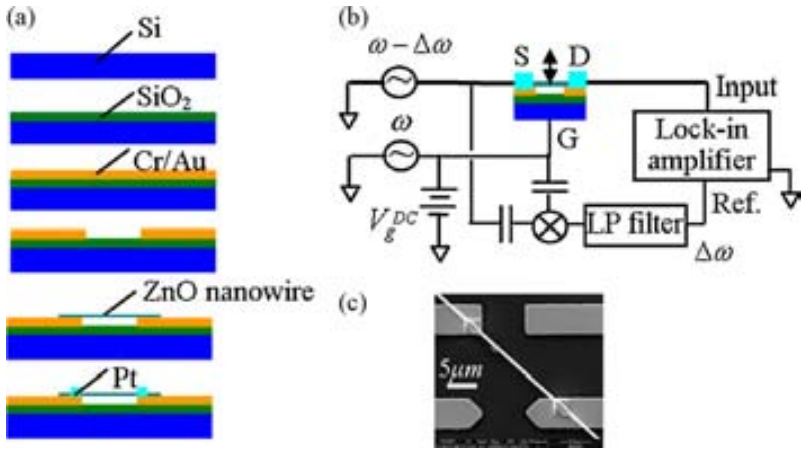

Figure 2.2: Fabrication of nanomechanical resonators based on ZnO nanowires.Extracted from [14].

the mechanical element (in this case, the resonator) as a part of a larger system which includes electrical connections, actuation electrodes, etc. In the case of the studied nanomechanical resonators, the bottom-up element is placed within larger structures defined by top-down methods. Nowadays the limiting technological step is the placement of the bottom-up elements in specific positions of these top-down structures. The proper placement of the nanowire is crucial, as it affects some of the properties of the resonator: as an example, in the case of electrically actuated nanowires, the position of the nanowire with respect to the actuation electrode greatly affects its behaviour. Therefore the precise and repetitive placement of the nanostructures is a key issue to ensure device reliability and fabrication throughput. This is specially important if batch manufacturing is desired.

The fabrication approach which generally yields the best qualities for nanomechanical resonators is the growth of the nanowires directly in a pre-patterned substrate, so that the nanowire is welded by both ends to the top-down structures. In this sense, it is important to develop techniques to ensure the proper placement of the catalyst particles which determine the growth position and the diameter of the nanowire in most bottom-up techniques.

On the other hand, in the case of the deposition of previously synthesised nanowires, the critical step is the placement of the nanowire at a desired position with respect to the pre-patterned structures. It is crucial to develop methods which address this issue, and some works have made advances in this sense [22, 23]. Alternatively, methods such as e-beam or FIB techniques can be used to place the readout electrodes and other structures at the position of a pre-deposited nanowire [18]. However, this approach is not feasible for batch fabrication for two reasons: it requires a particular treatment of each device and it uses beam-lithography techniques, which are slow and expensive.

2.2 Fabrication technologies for bottom-up nanomechanical resonators

This section provides an overview of different technologies involved in the fabrication of nanomechanical resonators based on bottom-up silicon nanowires grown in pre-patterned chips. The critical steps of the fabrication process are studied, and different alternatives are explored for each step. The contents of this section are sorted by technologies: the nanowire synthesis method, the deposition of the catalyst, the doping of the nanowires and the structuring of the substrates.

2.2.1 Growth of silicon nanowires

This section presents an overview of three different growth mechanisms for SiNWs. Special attention is paid to the Vapor-Liquid-Solid (VLS) mechanism, which is one of the most studied and also the one which we employ to fabricate the nanowires. More thorough reviews about the growth of semiconductor nanowires, which also include other growth mechanisms and methods, can be found at references [1, 24, 2, 25, 26].

2.2.1.1 Vapor-Liquid-Solid mechanism

The vapor-liquid-solid mechanism for the growth of nanowires is one of the most deeply studied, and it is widely employed for the synthesis of semiconductor nanowires [2]. In this growth mechanism, which was first reported by Wagner et al. in 1964 [27], the nanowire grows from a catalyst particle deposited in a crystalline substrate. Using the VLS growth mechanism, nanowires with diameters from hundreds of microns to 3 nm [28] have been synthesised, and lengths up to millimetres [29] have been achieved with guided-growth techniques.

The main advantage of this method is that the diameter of the nanowire is determined by that of the catalyst particle, and its direction by the crystalline structure of the substrate. Furthermore, the nanowire and the substrate form an epitaxial union, which has good electrical and mechanical properties [6]. Therefore, nanowires grown in a substrate using this method are outstanding candidates to be used as nanomechanical resonators with electrical transduction. The name of the growth mechanism makes reference to the phases of precursor silicon during the growth process, which starts in gas phase, then moves to a liquid droplet and finally to the solid nanowire.

The VLS process usually takes place in a Chemical-Vapor-Deposition (CVD) system in which the temperature, the gases and sometimes the pressure of the process are controlled. The growth process for SiNWs starts on a crystalline Si substrate. Catalyst particles–usually gold (Au)–of small dimensions are deposited on the substrate, which is then heated until the particles dissolve with the silicon and melt.

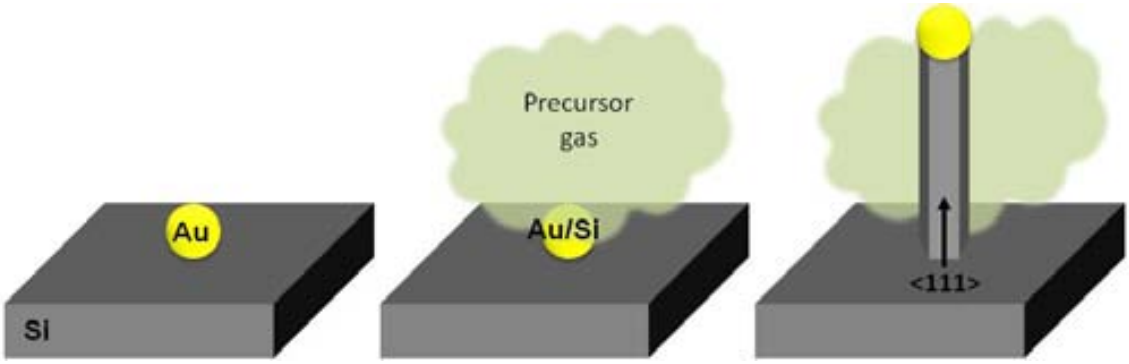

Figure 2.3: Growth process of SiNWs using the VLS mechanism.

The temperature range for this process depends on the catalyst material, but it is above the eutectic temperature of Si and the catalyst (in the case of SiNWs with Au catalyst, this temperature is above 363 °C [2]). Then a gas containing the precursor is introduced into the chamber, providing silicon which dissolves in the liquid droplet. When sufficient precursor is introduced into the droplet the mixture supersaturates, and as a consequence the precursor precipitates to the base of the droplet (which is in contact with the substrate). In this way, the silicon starts depositing at the substrate below the Au-Si droplet and the growth of the nanowire begins. The growth direction of the nanowire follows the crystalline structure of the substrate with a given direction which depends on the material and the size of the nanowire [28].

The VLS method has been used to grow nanowires from a number of semiconductors [30], most notably silicon and germanium, but also gallium arsenide (GaAs), indium phosphide (InP) or zinc oxide (ZnO) [1]. In the particular case of silicon nanowires, they are usually grown in a CVD system (the so-called VLS-CVD method) with Au as a catalyst. However, Au is known to affect the electrical properties of the nanowire and is also incompatible with CMOS processes, so a number of other metal catalysts have been studied. SiNWs have been successfully grown using Au, silver (Ag), platinum (Pt) [1], copper (Cu) [31], or aluminum (Al) [32], the two last ones being compatible with CMOS processes. Nevertheless, Au still remains the most widely used material. The precursor gases used for the growth of SiNW are silane (SiH_4) and silicon tetrachloride ($SiCl_4$). The growth temperature for SiH_4 is lower than for $SiCl_4$, but the process takes place at low pressure, whereas with the latter the growth process is performed at atmospheric pressure.

2.2.1.2 Vapor-Solid mechanism

The vapor-solid mechanism is based on the thermal evaporation of the source material and its subsequent condensation under certain conditions of temperature, pres-

sure, substrate, etc. [33]. This method does not rely on liquid droplets of catalyst on the substrate (and hence the name Vapor-Solid, in contrast to the VLS mechanism which relies on a liquid intermediate step), but instead the nanowires self-organize covering the surface of the substrate material. It is possible to control the diameter and length of the nanowires by varying the parameters of the growth process (temperature, pressure, time, etc.) although a control of the spacial density of nanowires is difficult to achieve. Although this method is usually employed for metal oxide nanowires (such as ZnO or Ga_2O_3) it is also possible to use it to grow SiNW [34]. The absence of a localized catalyst particle makes this method poorly suitable for the fabrication of single NWs, although a posterior deposition of the grown nanowires intro pre-patterned substrates is still possible.

2.2.1.3 Solution growth

The Solution-Liquid-Solid (SLS) growth mechanism is similar to the VLS mechanism, but in this case the precursor is in a liquid solution instead of a vapour phase. This mechanism was first reported in 1995 by Buhro et al. [35], and consists in growing the nanowires in a solution containing both the catalyst particles and the precursor. Similarly to the VLS mechanism, under certain conditions of temperature and pressure the nanowires grow on the substrate at a position defined by the catalyst particles. The main advantage of this mechanism with respect to the VLS method is the possibility to operate at lower temperatures, which allow to use a large range of different substrates [1].

2.2.2 Deposition of catalyst for nanowire growth

One of the key issues in the fabrication of bottom-up SiNW resonators is the placement of the catalyst. The position and diameter of the nanomechanical resonator is fixed by the particle which catalyses its growth, and therefore it is important to control both parameters. In the case of nanomechanical resonators additional difficulties arise, because the catalyst must be placed in vertical side-walls (i. e. side-walls perpendicular to the planar substrate). In this section different catalyst deposition techniques are presented, with particular emphasis to the particular problematic of nanomechanical resonators.

2.2.2.1 Thin film deposition

One of the most common techniques to deposit catalyst material on the substrates to grow nanowires is the selective deposition of thin films using lithographic techniques. The Figure 2.4 shows an example of a process using this technique: a metal film is deposited on a substrate, followed by a lithography step and a selective etch of the

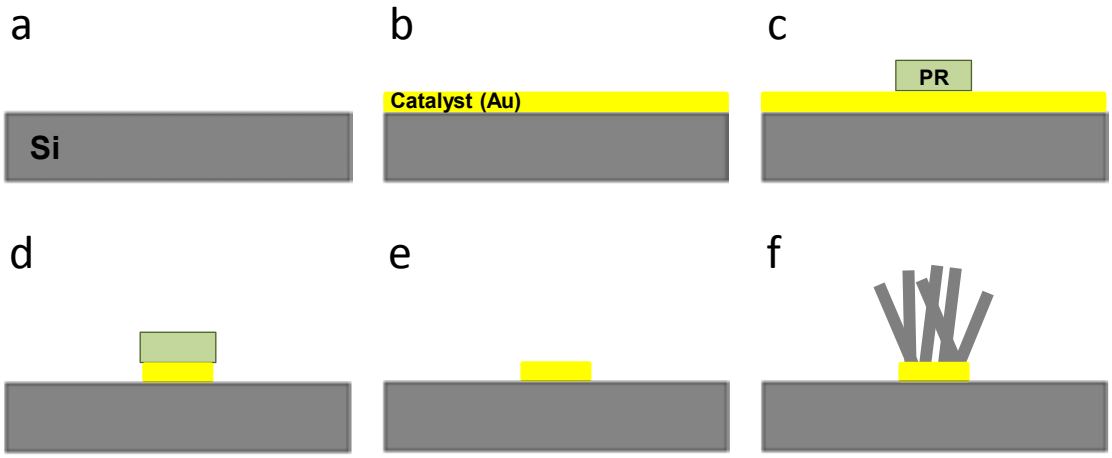

Figure 2.4: Example of deposition of the catalyst and synthesis of NWs using photolithography and thin film deposition. a) Silicon substrate. b) Deposition of a thin catalyst layer, such as gold. c) Deposition of photoresist (PR) and photolithography. d) Etching of the gold layer. e) Strip of the photoresist. f) Growth of the nanowires.

metal. Then the metal remaining on the substrate acts as a catalyst for the growth of the nanowires.

The resolution of this method is limited by the lithographic technique: from hundredths of microns when using optical photolithography, to tens of nanometers when using e-beam lithography. Furthermore, besides traditional lithographic techniques, other technologies such as nanosphere lithography, nanoimprint lithography [1] or nanostencil lithography [26] can also be used to selectively deposit the metal layers.

The main problem with these techniques in the case of nanomechanical resonators is that the nanowires generally grow connecting two vertical walls, and therefore the catalyst must be deposited in one of them. With most techniques it is really complex or impossible to pattern vertical side-walls, so this approach is of limited use in this case.

2.2.2.2 Colloidal nanoparticles

Another widely used catalyst deposition technique is the use of suspensions of catalyst nanocrystals. In the case of gold, for example, there are a number of providers which offer solutions of gold colloids with diameters ranging from hundreds of nanometers to 2 nanometers. Furthermore, the size distribution of these particles is quite good, resulting in nanowires with a low dispersion of diameters.

The process of deposition of the nanoparticles starts with a clean, crystalline Si substrate. The colloidal suspension is put in contact with the chip, in such a way that some of the colloids adhere to the substrate. This adhesion can be precipitated

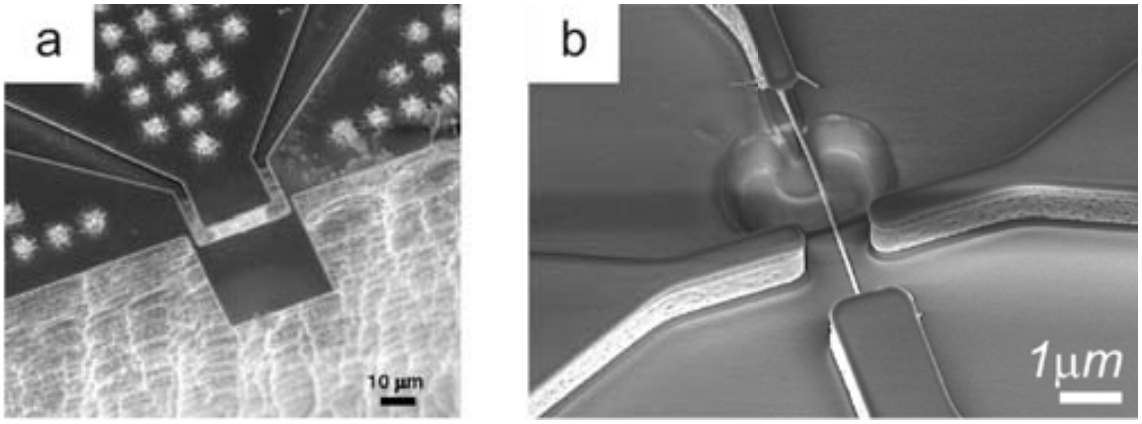

Figure 2.5: Fabrication of bottom-up nanowires using galvanic displacement techniques to deposit the catalyst particles. (a) Fabrication of a SiNW array as the transducing element of piezoresistive cantilevers. Extracted from [36]. (b) Fabrication of mechanical resonators based on bottom-up SiNWs. Extracted from [41].

ly using intermediate substances, like Poly-L-Lysine, which charges the substrate positively while the colloids are charged negatively. After the colloids are deposited, the nanowires are grown with the desired technology, for example using a VLS-CVD method.

The main drawback of this method is that catalyst particles land in random positions, so it is not possible to control the exact position of the nanowire. However, some parts of the substrate can be covered (for example, by SiO_2) such that, even if the colloids are deposited there, no nanowires will grow in that position. Besides, the catalyst deposition using this technique is independent of the orientation of the surface which acts as a substrate, so that it can be used to grow nanowires in vertical side-walls.

2.2.2.3 Galvanic displacement

The galvanic displacement technique is based on selective deposition of thin metal films in oxidizable substrates, such as Si or Ge. Galvanic displacement growth methods usually consist in covering the substrate in SiO_2 except for certain areas where nanowire growth is desired. This method allows to deposit gold nanoparticles only in these areas [37]. Gao and co-workers reported the selective growth of SiNW arrays with controlled diameter by combining the galvanic displacement deposition technique with the employ of microemulsions containing gold nanoclusters of controlled diameter [38]. This same method has been used to fabricate arrays of double clamped beams which have been used to study mechanical properties of SiNWs [7]. More recently, these NW arrays have been applied as the transduction element of piezoresistive cantilevers [36] (Figure 2.5a) and for energy harvesting devices [40].

An evolution of this method consists in using the galvanic displacement technique in sufficiently small deposition areas (i. e. areas with exposed silicon), so that a single nanowire is grown. This approach is based on the deposition of a thin film of gold in the deposition area. When heated above the Au/Si eutectic temperature, this film forms droplets and, if the film is sufficiently small and thin, it forms a single droplet. Afterwards, a single nanowire can be grown from this catalyst particle using CVD-VLS techniques. This approach has been used to fabricate single-nanowire bottom-up resonators [41], which are shown in Figure 2.5b. Compared to the colloidal nanoparticles deposition method, this technique provides a precise control over the position of catalyst, and therefore over that of the nanomechanical resonator.

2.2.3 Doping of bottom-up nanowires

This section deals with the doping process of bottom-up nanowires. Also, the doping and conductivity of electrically transduced resonators have an important effect on their properties, such as their transduction efficiency. The doping of semiconductor nanowires is a much-studied issue, given the interest of using these nanowires as electronic components such as transistors and interconnections. It is known that the dopant profile differs from that of bulk materials specially for nanowires of small dimensions [42, 25], and there is an ongoing related discussion about how this profile can affect their properties. In the field of SiNW resonators, for example, it has been proposed that the dopant profile has some effect in the giant piezoresistive properties of these devices.

This section discusses the different doping approaches for bottom-up SiNWs: the in-situ approach, in which the nanowires are doped at the same time as they grow; and the ex-situ approach, in which they are doped afterwards, so the doping process is independent of the synthesis of the nanostructure.

2.2.3.1 In-situ doping

One of most common techniques to dope bottom-up nanowires fabricated by VLS techniques is the in-situ approach. With this method the nanowires are doped at the same time that they are synthesized, by introducing a dopant gas in the reaction chamber together with the precursor [43]. By adjusting the flow of the doping gas, the dopant concentration can be varied and consequently the conductivity of the nanowire controlled. The dopant profile for VLS-grown Ge nanowires using this doping technique has been studied, and it has been found that this profile consists in a heavily doped shell and a much less doped core [42]. This raises questions about how this profile can affect the electrical properties of the nanowires. The main advantages of this technique are that the doping level is controllable and it

does not require additional fabrication steps. Also, under most circumstances the doping process does not heavily affect the growth process of the nanowires [43].

This technique has been successfully used to fabricate several functional devices, such as electrically transduced resonators based on Si [13] and InAs nanowires [19], and Indium Phosphide transistors [44].

2.2.3.2 Ex-situ doping

The second approach for the doping of bottom-up nanowires is the ex-situ, in which the devices are doped after the growth process. This approach provides additional control over the doping process, as it is independent of the growth process, but also requires additional fabrication steps, namely the implantation and high-temperature annealing of dopant species.

In general, this process consists in the following steps: first, the nanowires are grown in a supporting substrate. Afterwards this substrate is annealed at high temperatures while providing a source of dopant species, so that the doping molecules diffuse into the nanowire [45]. The annealing to activate this dopant can be the same as the diffusion one, or a separate process.

Different alternatives can be used as the source of dopant species. One option is to use a CVD method, where the dopant is introduced in gas phase with a controlled flow while the samples are annealed at high temperature. This approach has been reported with SiNWs doped with Boron Tribromide (BBr_3) [46]. Another option is to introduce the dopant in powder form, along with the chips carrying nanowires, into a sealed ampoule, and to anneal it so that the dopant diffuses into the nanowires [47]. Also, spin-on doping has been used in top-down fabricated nanowires [48], in which the dopant is provided by a solution which is spin-coated over a chip containing the nanowires and afterwards annealed.

An alternative doping procedure is to place a source of dopant in close proximity to the nanowires, and then anneal them in a CVD while providing a mild flow of inert gas to allow the dopants to diffuse to the nanowires (Figure 2.6). This method has been reported by Ingole et al. [45], using a chip with spin-on dopant as the boron source. This method does not require a dedicated CVD or spin-coating the doping substance directly over the nanowires, which can lead to contamination issues. One variation of this method is to use a dopant wafer fragment (for example, a boron nitride wafer) as a source of the doping species. We have successfully applied the latter alternative to dope bottom-up and top-down SiNWs [49], as it is explained in detail below.

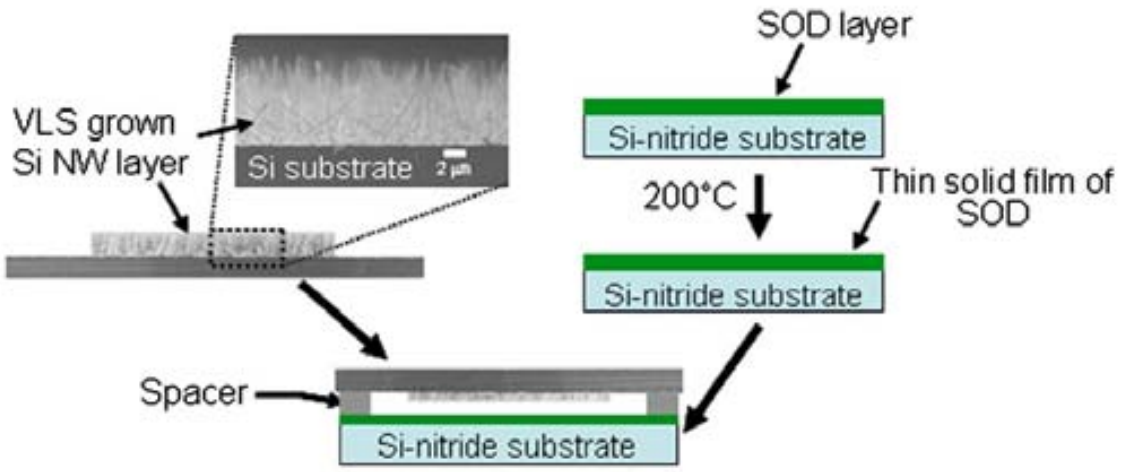

Figure 2.6: Ex-situ deposition using a dopant source in close proximity to the nanowires. Extracted from [45].

2.2.4 Structuring of the substrates

The top-down structuring of the substrates where the nanowires are grown is usually performed using IC and micromachining technologies. This kind of structures are typically of hundreds of micrometers or larger, and can be defined using optical photolithography, which is widely used in IC fabrication and therefore well studied. This section presents an overview of two steps in the definition of structures in the substrate, the lithography and the etching processes.

2.2.4.1 Photolithography

The definition of structures in the substrate requires a means of transferring some computer-generated patterns into the substrate, what is called the lithography process. This is performed by selectively covering some areas of the substrate, in order to process only the uncovered ones. Lithographic techniques can be divided into two families: parallel lithographic techniques–in which the substrate is treated as a whole or in regions–and series techniques, in which the patterns are "drawn" one by one.

Many of the lithographic techniques are based in different types of resists which are sensitive to UV light, electron beams, X rays or similar sources. This photoresists are polymeric materials which are spun onto the substrates in liquid form, covering it with a homogeneous layer. These materials change their properties after an exposition of a determined light source: the exposed areas are dissolved in a subsequent development step (for "positive" photoresists) or they remain intact after the exposition, whereas the non-exposed areas dissolve (in the case of "negative"

photoresists). This leaves a selectively covered substrate, which can be treated with a variety of processes afterwards. Once the selective processing of the substrate is performed, the photoresist is completely stripped.

The most common lithographic technique, photolithography, is a parallel technique which relies on selectively exposing photosensitive resists usually using ultraviolet light. This selective exposition is performed by placing a photomask, or mask with clear and covered areas, between the substrate and the light source. Photolithography is widely used by the microelectronic industry, and its resolution is limited by that of the exposing light source. The highest resolutions are achieved with extreme UV, with a wavelength of 10-14 nm. However, reaching this level of detail is complex and expensive, and requires taking into account interference effects when designing the photomasks, making it exclusive to only a few foundries worldwide. Most common photolithographic equipments use UV sources like high pressure mercury lamps (for example, the i-line with a wavelength of 365 nm) or deep UV sources like excimer lasers (with lengths of 248 nm for KrF and 193 nm for ArF), with more modest resolutions [24]. In spite of its relatively low resolutions, photolithography allows parallel processing, and patterns of different sizes can be defined in the same exposition.

Another family of lithography techniques rely on defining the patterns in a sequential manner, by "drawing" them in the resist or directly on the structure. This is the case of e-beam lithography, which relies on an electron beam of small wavelength (around 1 Å) to draw patterns on a resist sensitive to this kind of radiation. The resolution of this technique is limited by the scattering of the electrons in the resist, but it can achieve resolutions of around 10 nm. Nevertheless, this is a slow technique, and the patterning of large areas is long and expensive. Therefore, it is usually reserved for the fabrication of photomasks (which require high resolution), or used in conjunction with conventional photolithograpy. Other techniques similar to e-beam lithography are laser lithography (which relies on a laser source) or focused ion beam lithography (in which the patterns are defined using an ion beam). Some of these high-resolution lithographic techniques are covered in more detail in section 4.2.2.

2.2.4.2 Micromachining using reactive ion etching

The micromachining of silicon can be performed using two different kinds of etchings: wet, in which the etchant is in liquid phase; and dry etching, which usually relies on plasma-based techniques. In general, dry etching techniques achieve better resolution and higher anisotropy, allowing to fabricate high aspect ratio structures [24]. This section is centred in the use of dry etching techniques for the structuring of the substrates, and in particular in the Reactive Ion Etching (RIE) technique. A more detailed study of RIE can be found at references [24, 50].

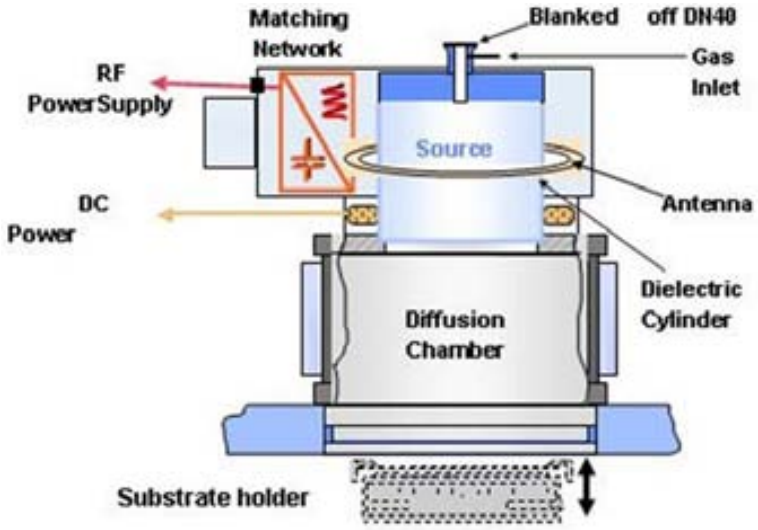

Figure 2.7: Schematic of a Reactive Ion Etching processing chamber (Center of Micronanotechnology, EPFL).

The reactive ion etching is a dry etching method which is based in attacking the substrate with chemically reactive ions. The ions are generated at low pressure by an electromagnetic field which creates plasma from gas species, and then they are accelerated towards the substrate. The Figure 2.7 shows a schematic of a RIE processing chamber. The top antenna is used to generate the plasma from the incoming gas, using a high-frequency signal. The substrate holder is also connected to an RF source of lower frequency, which is used to bias it and control the energy of the incoming ions.

The main advantage of RIE compared to other etch methods is its high directionality, which is independent of the crystalline orientation of the substrate, and provides the ability to faithfully transfer photolithographically defined patterns to the underlying substrate. Moreover, RIE can achieve relatively high etching rates, which is important in bulk micromachining. This process has been widely studied and optimized, and nowadays is an important part of micro and nanofabrication processes. The fabrication of substrates for the growth of silicon nanowires requires a good control of the RIE process, as high aspect ratio structures are needed. Some of the parameters and effects which can become an issue for the fabrication and must be carefully controlled are listed below.

Aspect ratio: One of the main advantages of the RIE is its high anisotropy. The aspect ratio of the etching is defined as the relation of the etch rate in the direction of interest to that in other directions. The fabrication of nanostructures requires a good control of the process parameters to achieve a very low lateral attack. Moreover, these structures also present the particularity that

this etching must be done at the nanoscale, i. e. with depths of micrometers and lateral attacks in the orders of tens on nanometers (Figure 2.8b). While high aspect ratio etchings are well controlled for structures in the orders of micrometers or hundreds of micrometers (the Deep RIE process), they are not so studied for nanostructures, which require different RIE conditions.

Scalloping: Some RIE processes present a characteristic profile of the walls, which contain scallops due to the cycles of passivating and etching gases which occur during the process (Figure 2.8a). This scallops determine the morphology and verticality of the walls and may affect the growth of the nanowires or the colloid deposition. The shape (depth and width) of the scallops can be controlled by tuning the etch parameters, such as the length of the gas pulses or its flow rate.

Notching: Notching is a phenomenon which occurs during time-multiplexed etchings when silicon is located over a layer of dielectric material (for example, the oxide layer of SOI substrates). When the etch reaches the boundary of the two layers, a characteristic lateral etch occurs due to charge accumulation. When the RIE is performed at wafer level on SOI wafers, due to the desuniformity of the etching, some zones must be over-etched in order to completely etch all the silicon and reach the oxide layer in the whole wafer (figure 2.8a). These over-etched zones will present notching on the lower zones of the silicon layer. Some special processes can reduce or eliminate the notching effect. For example, by applying a pulsed RF power to the cathode, the charge at the silicon dioxide boundary has time to dissipate in between pulses, and thus the notching effect is attenuated.

Selectivity: The selectivity of an etching is defined as the relationship of the etch rate of the silicon to that of the mask (usually photoresist or silicon dioxide). In general, the photolithography of high resolution patterns requires very thin layers of photoresist, making selectivity an important parameter of the etching, specially for that of deep silicon layers (in this case, deep means in the order of micrometers). The etch rate of the photoresist can be decreased by baking it prior to the etch process, but this also causes a deformation of the resist and a loss of resolution of its features. Also, if the width of the photoresist is insufficient, an additional layer may be put on the silicon to be used as an additional mask, such as silicon dioxide.

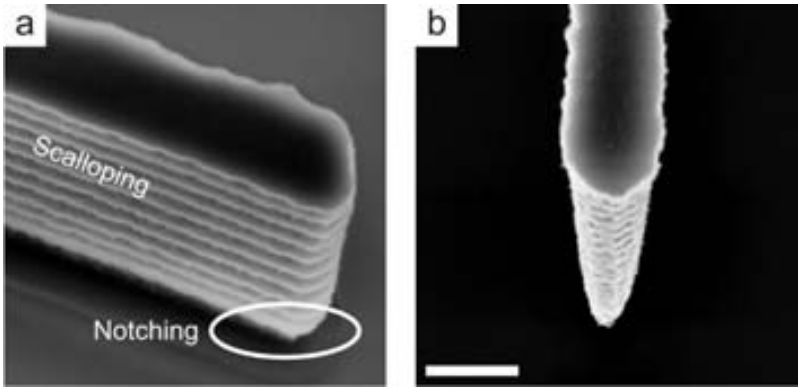

Figure 2.8: Effects of the RIE process during the patterning of substrates. a) Scalloping and notching effects in a SOI wafer using a time-multiplexed etching. b) Effect of high lateral etching in narrow electrodes (scale bar: 400 nm).

2.3 Fabrication of bottom-up nanomechanical resonators

The fabrication method of bottom-up SiNW resonators used in this work is based on several of the fabrication steps which are presented above. The process is based on the use of colloidal solutions to deposit the catalyst particles, and a CVD-VLS process is employed to grow the SiNWs. This section presents the complete fabrication process of nanomechanical resonators based on bottom-up silicon nanowires. The different fabrication steps and equipments are discussed, and afterwards the results of the fabrication process are shown. The whole fabrication process was carried out at the clean room facilities of the Institut de Microelectrònica de Barcelona, IMB-CNM (CSIC).

2.3.1 Fabrication process

An overview of the fabrication process is shown in Figure 2.9. The process is carried out in SOI wafers, in which a thin SiO_2 layer acts as an insulator between the electrical contacts and the substrate (Figure 2.9a). First, the electrical contacts and trenches are patterned in the device layer using photolithography and dry etching (Figure 2.9b). Then, the wafers are cut into chips and catalyst particles are randomly deposited in them using a gold colloid solution (Figure 2.9c). Afterwards, the nanowires are grown in the substrates using a VLS method in an atmospheric CVD (Figures 2.9d-e). Finally, the nanowires are doped using an ex-situ process, by annealing the chips with NWs in close proximity to a wafer containing boron.

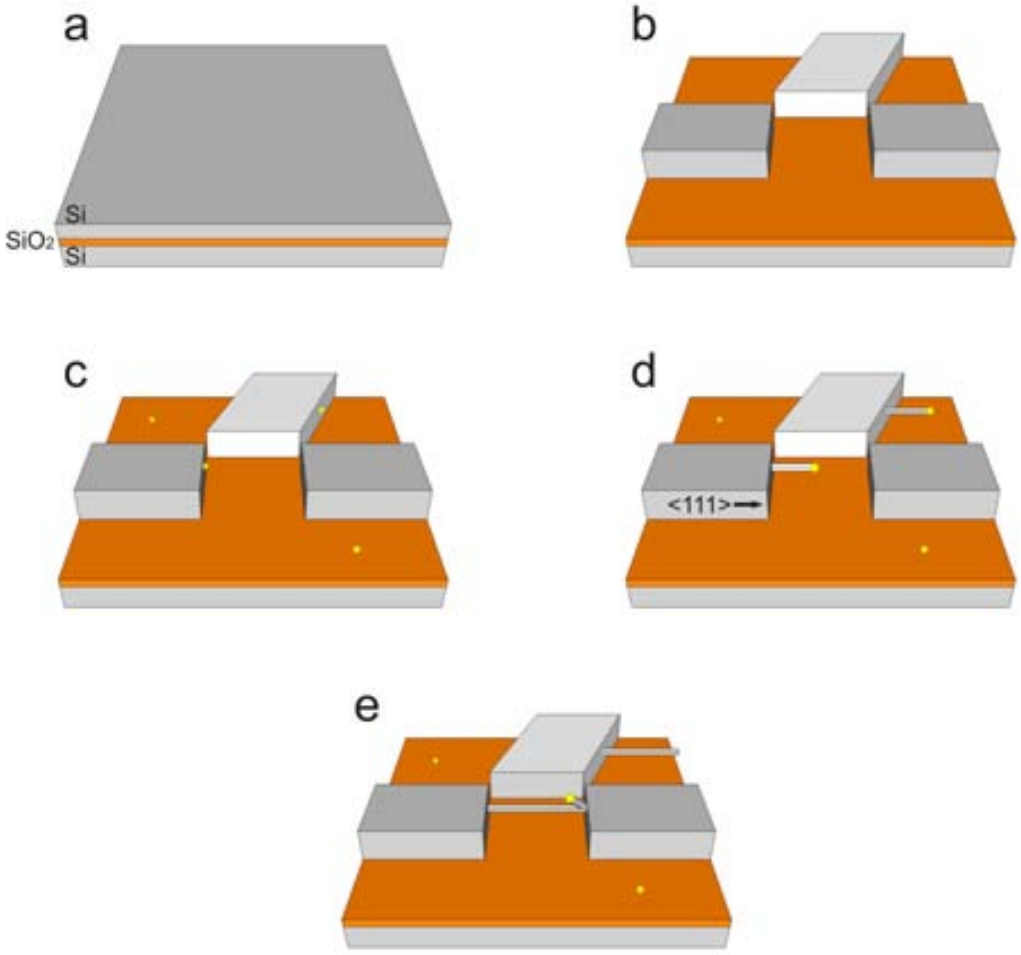

Figure 2.9: Fabrication process for nanomechanical resonators based on bottom-up SiNWs. a) SOI wafers are used as a substrate. b) The top-down structures are defined using photolithography and RIE. c) Gold colloids are deposited on the substrate. d) SiNWs are grown using a CVD-VLS process. e) Once the nanowires are grown, they are doped using an ex-situ process.

2.3.1.1 Patterning of the substrates

The first step in the fabrication process is the definition of the microstructures where the nanowires will grow and that will be used as electrical contacts. Due to the randomness of the deposition of the catalyst particles, substrates with a high number of structures are designed, in order to account for the low yield of the fabrication process. In addition, the width of the trenches in the substrate determines the length of the resonator, so different chips aimed at different lengths of the resonator are designed. Additionally, each of these different chips has small design variations: different width of the side-walls and different dimensions of the side-gates. These variations are aimed at finding adequate conditions for the whole fabrication process.

The fabrication process starts with the selection of the substrate wafers. The crystallographic direction of the top silicon layer is one of the important parameters during this step, because the bottom-up nanowires grown using the VLS method grow preferentially along the <111> direction of the crystalline structure. The SOI wafers and the orientation of the top-down patterns must be chosen so that this direction is perpendicular to the trenches where the nanowires will grow.

The substrates which are employed for the fabrication process are 4-inch SOI wafers from Ultrasil Corporation. Table 2.1 shows some of their specifications. The top silicon layer (device layer) has <110> orientation–so that the <111> direction is horizontal (i. e. in-plane) with respect to the wafer–and it is heavily doped with boron to obtain low-resistivity contacts. Note the high dispersion of the device layer, of about a 25% of the total: this causes issues during the dry etching step (leading to over-etch some of the regions of the wafer) as well as uncertainty regarding the final dimensions of the side-walls where the nanowires grow.

The next step of the fabrication process is the patterning of the structures in the device layer: the electric contacts and the trenches which will be connected by the nanowires. This process is carried out using photolithography and dry etching. Two different kinds of substrates are fabricated, which differ in the employed photolithography equipment, which conditions the resolution of the designs: the first iteration of the substrates is fabricated with the stepper NIKON i12D, which has a resolution of 0.5 μm, while the second iteration is fabricated with the stepper NIKON NSR 1505-G7 with a resolution of 0.35 μm. Another difference between these two processes is the photoresist that they use: the lower resolution 0.5 μm patterns are fabricated using 1.2 μm of HIPR-6512, while the 0.35 μm process uses 0.6 μm of OiD-650 photoresist. The dry etching step is identical for both of them.

The 0.35 μm resolution photolithography step was carried out for the first time in the facilities of the IMB-CNM, and a calibration step was necessary to adjust the proper exposition time during the photolithography. This calibration was performed by exposing different areas of a Si wafer with different parameters, and then choosing

Device Layer	
Orientation	<110>
Thickness	2 ± 0.5 μm
Dopant	P/Boron
Resistivity	0.07-0.14 ohm × cm
Buried oxide (BOX)	
Thickness	0.5 μm
Handle Wafer	
Dopant	P/Boron
Resistivity	1-10 ohm × cm

Table 2.1: Specifications of the SOI wafers used during the fabrication (source: Ultrasil Corporation [51]).

RIE Recipe	
Parameter	Value
SF_6 flow (sccm)	150 (pulsed 2.5 s)
C_4F_8 flow (sccm)	100 (pulsed 2 s)
ICP RF power (W)	1500
Plate LF power (W)	13
Pressure (mbar)	1.4-2.8 × 10^{-2}
Time (s)	90

Table 2.2: Conditions of the optimized RIE process.

the best results using SEM inspection (Figure 2.10). To avoid a loss of resolution, the photoresist is not baked after exposition, which also causes its selectivity during the dry etching to be a little lower.

The silicon dry etching process in the IMB-CNM is performed using an Alcatel P-601 RIE equipment. The fabrication of the electrodes requires an optimization of the existing RIE recipes to adapt them to the stringent requirements described above. The objective of the optimization is to correctly fabricate electrodes for the growth of silicon nanowires, which have dimensions as low as 350 nm of width and 2.5 μm of depth in the case of the high-resolution photolithography process. The RIE process which has been chosen as a base for the optimization is a pulsed method, which consists in cycles of C_4F_8 and SF_6 acting as passivating and etching agents respectively.

The optimization of the process is performed by varying some of the parameters

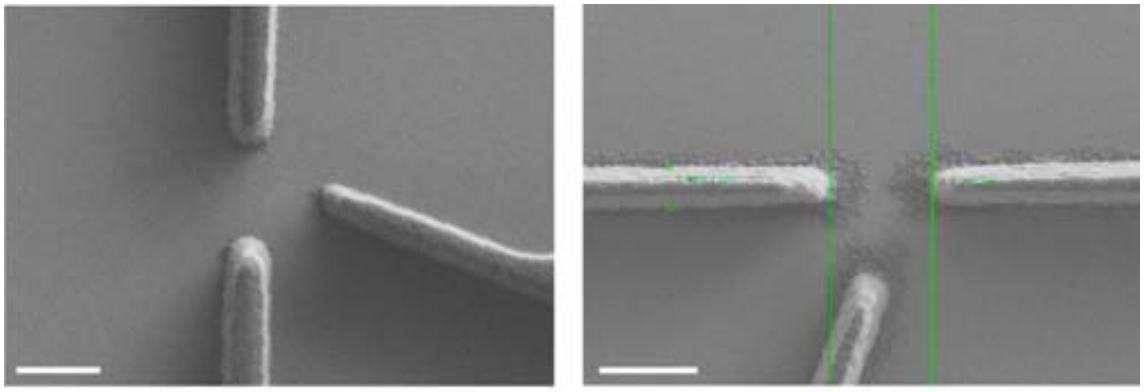

Figure 2.10: Characterization of the photolithography expositions. Photoresist structures over SiO_2 substrates. Scale bar: 1 μm.

of the base recipe at full wafer scale. The results are examined by SEM after the photoresist stripping. Figure 2.11a shows an etching using the base conditions, which presents a high level of lateral attack (about 60 nm for each 1000 nm of depth). This excessive lateral attack may be due to a lack of passivating layer on the sidewalls. This can be solved by lengthening the passivating gas cycles or increasing its flow. Moreover, we found that increasing the passivating gas using either method also leads to improved surface quality in the sidewalls. The next tests were aimed at optimizing these parameters. Figure 2.11b shows a detail of one structure after the optimization process, with little lateral attack and a good quality of the side-walls. The conditions of the optimized recipe are shown in Table 2.2.

The recipe obtained from the optimization process has been used for the fabrication of all the chips used to grow bottom-up SiNWs. Even though the wafers containing 0.35 μm patterns have a thinner layer of photoresist, the selectivity of the recipe is high enough to withhold the process. However, due to the desuniformity of the thickness of the device layer, some areas of the wafer have to be over-etched in order for the etching to finish in other areas. This causes damaged structures and underetching in some regions of the wafer. Figure 2.12 shows a full wafer of patterned chips. Different regions of the wafer contain chips with different lengths.

2.3.1.2 Deposition of the catalyst

The process employed to deposit the catalyst particles in this work is based in the use of gold colloid solutions. Although this method lacks control of the position of the nanowires, it provides an accurate control of their diameter, thanks to the low dispersion of the size of the catalyst particles. This absence of control on the position of the particles (which entails a decrease of the fabrication yield) can be compensated by having a large number of potential devices per chip. In addition, the

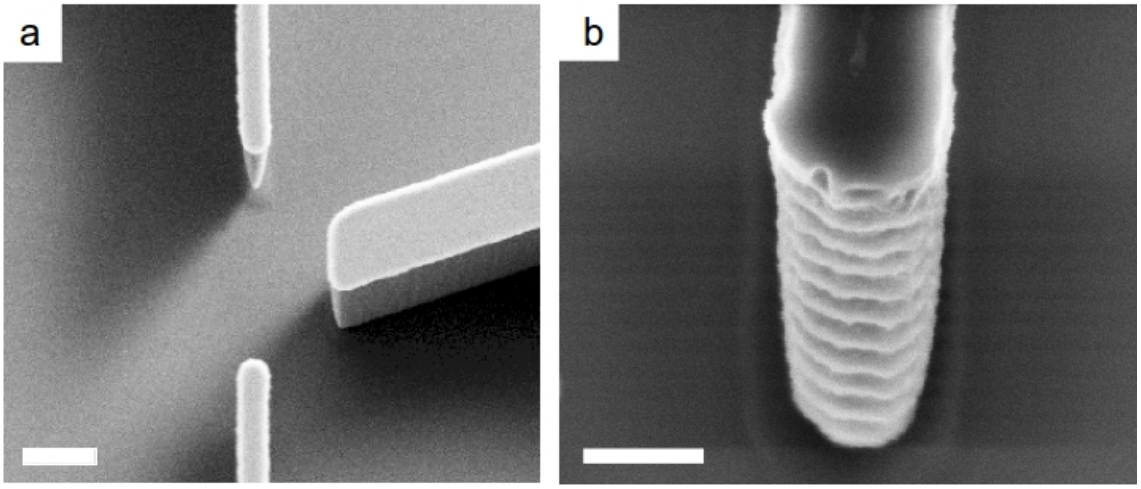

Figure 2.11: Results of the different RIE tests. a) Recipe without optimization. The width of the electrode is 5000 Å approximately. Scale bar: 1 μm. b) Results after the optimization process. The lateral attack is reduced, and the walls present a smooth surface. Scale bar: 400 nm.

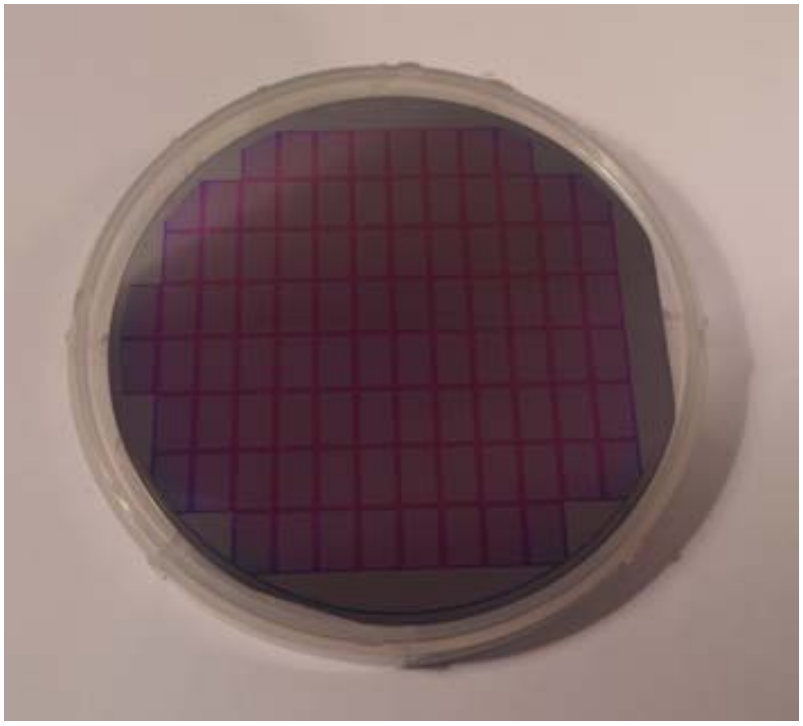

Figure 2.12: Four-inch SOI wafer with patterned chips.

number of functional devices can be maximized by adjusting the density of colloids, in order to obtain the maximum value of devices with a single nanowire in between the electrodes.

Gold colloid solutions of different diameters are commercially available from BBInternational. For the growth of nanomechanical resonators, the chosen diameters are 30 and 50 nm. In order to achieve the correct density of colloids (and, consequently, nanowires), the solution containing gold colloids is diluted in deionized (DI) water prior to its deposition in the chip. Additionally, poly-L-lysine is used to propitiate the deposition of the gold particles on the chips by charging its surface.

After the RIE process and the stripping of the photoresist, the pre-patterned wafers are cut into chips. These chips are then cleaned by dipping them in acetone for four minutes and then in isopropanol for two more minutes, and afterwards they are dried under a flow of nitrogen. Immediately before the deposition of the colloids, a short HF attack is performed on the chips to eliminate the native oxide layer in the silicon, which can interfere with the growth process of the nanowires. This attack is performed using an HF solution (Sioetch MT 06/01 VLSI selectipur, from Basf) for ten seconds, followed by a rinse with DI water and a drying in a flow of nitrogen. Then, the chips are dipped for 60 seconds in a poly-L-lysine solution, and then rinsed with DI water. Finally the chips are dipped into a mixture containing DI water and the gold colloid solution for 30 seconds, rinsed in DI water and then dried using a flow of nitrogen.

2.3.1.3 VLS-CVD growth of silicon nanowires

The silicon nanowires are grown by a VLS mechanism using an atmospheric CVD equipment, using silicon tetrachloride ($SiCl_4$) as a precursor gas. This section describes the SiNW growth method in detail, as well as the optimization process to control the growth of SiNWs.

The atmospheric CVD used to grow the SiNWs is located in the clean room facilities of the IMB-CNM, and it was designed by Dr. Álvaro San Paulo. The system uses $SiCl_4$ as a precursor and Ar with 15% H_2 as both the reaction and carrier gas. The precursor is supplied by a bubbler located in the same system (Figure 2.13b). During the growth process the carrier gas passes through the bubbler, which is held at a constant temperature of 0 °C to have a constant vapour pressure, and it drags some precursor into the reaction chamber. The same gas is introduced directly to the camber during the reaction. The CVD works at temperatures up to 1100 °C. The base conditions for the growth process are similar to those found in reference [52]: the process takes place at a temperature of 800 °C, with a direct flow of Ar/H_2 of 270 sccm and a precursor flow of 50 sccm.

It is necessary to perform a fine optimisation of the growth parameters to adapt

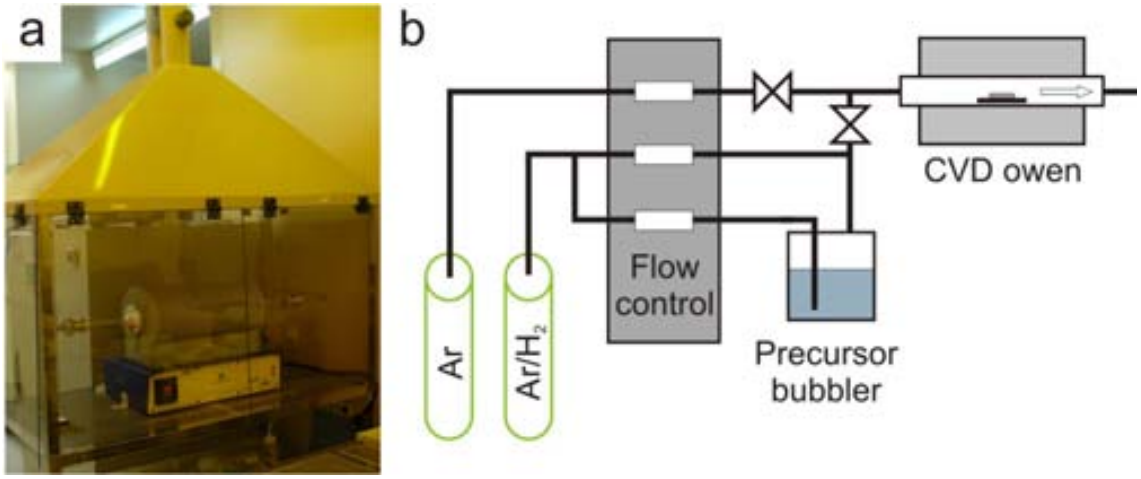

Figure 2.13: CVD equipment for the growth of VLS silicon nanowires. a) Image of the atmospheric CVD owen in the clean room facilities of the IMB-CNM. b) Simplified schematic of the bubbler and the flow control system.

them to the specific nanowire density and diameter. The optimization process consists in a series of growths in unpatterned <111> chips varying some of the parameters (mainly the process temperature and the precursor gas flow), followed by a fine-tuning of the conditions in patterned chips. In these substrates the growth direction lies perpendicular to surface, so the results of these growths are arrays of vertical nanowires. The optimisation process has to be performed for each diameter, because the density of nanowires and growth conditions are slightly different. In addition to obtaining optimal growth conditions, this process allows to study the dependence of the nanowire morphology on the synthesis parameters.

The first parameter which has been studied is the flow rate of the precursor gas, $SiCl_4$, while the temperature and other parameters are held constant. The temperature of the growth process is fixed at 800 ^{o}C, and gold colloids of 50 nm are used for this test. The results of the sweep of this parameter are shown in Figure 2.14a-c. The precursor flow has a clear effect on the density and morphology of the nanowires. It is readily observed that the optimal density appears for the precursor flow of 50 sccm, specially for vertical nanowires (which follow the <111> direction of the substrate).

For a low precursor flow several effects are observed in the morphology of the nanowires: the apparition of amorphous silicon at the base of the nanowires, a loss of directionality (i. e. the NWs are not vertical) and a high conification of the structures. The conification effect is due to the VS deposition of silicon in the side-walls of the nanowire during the growth process, which competes with the VLS longitudinal growth. This layer of silicon is thicker at the base of the wire, which has been exposed for a longer time. The conification can be reduced by adjusting the

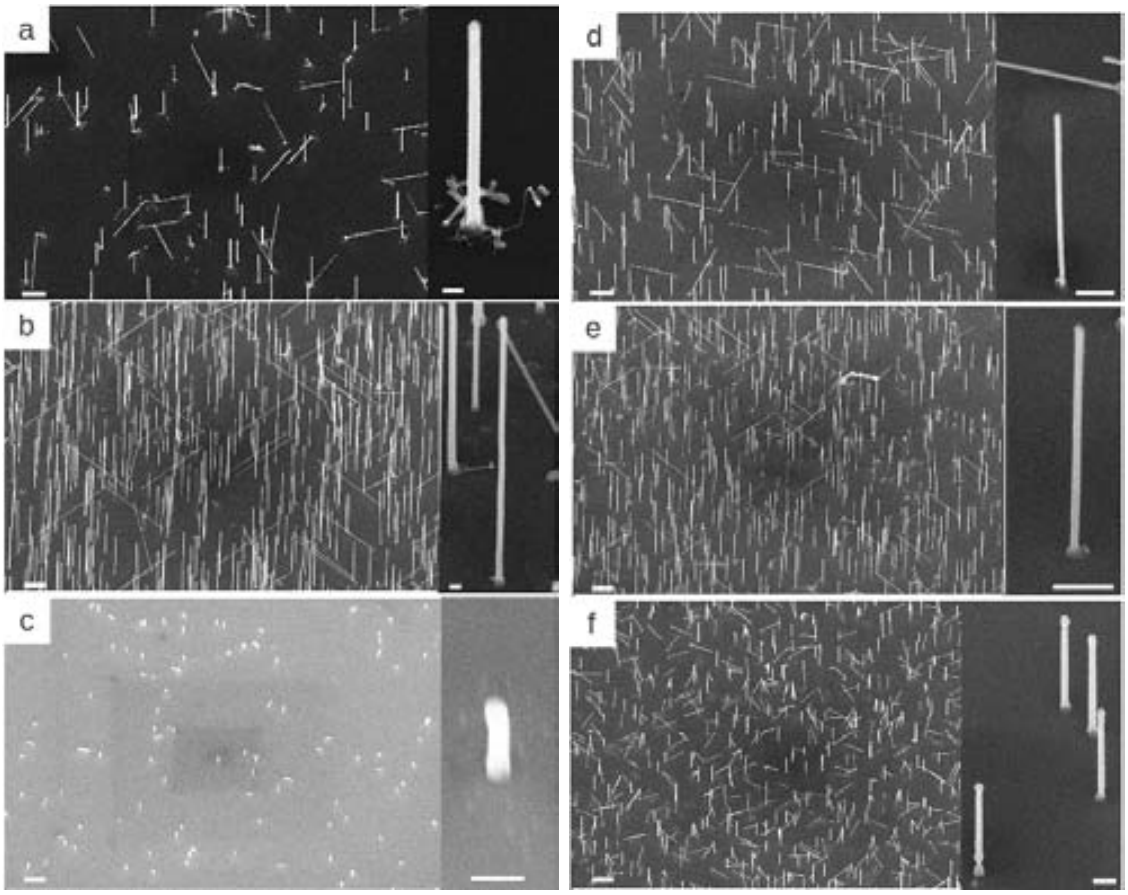

Figure 2.14: SEM images of the optimization of the growth of 50-nanometer SiNWs. Left column: sweep of the $SiCl_4$ flow, for a process temperature of 800 °C. a) Flow of 45 sccm. b) Flow of 50 sccm. c) Flow of 80 sccm. The scale bar of the left images is 2 μm, and of the right images is 200 nm. Right column: sweep of the process temperature, for a precursor flow of 50 sccm. d) Temperature of 785 °C. e) Temperature of 800 °C. f) Temperature of 845 °C. The scale bar of the large images is 2 μm, and of the small images is 500 nm.

growth conditions, but it is nonetheless present in some grade in all the structures which have been fabricated. The best results are found with a flow of 50 sccm of precursor, with a high density of directional nanowires, good morphology and length. When further augmenting the flow of precursor the length and density of the nanowires decrease (Figure 2.14c).

The second parameter which has been studied is the temperature of the process. In this case, the flow of precursor gas is fixed at the optimum value found during the first tests, at 50 sccm, while the temperature is varied from 785 °C to 845 °C. Some results from these tests are shown in Figure 2.14d-f. In this case we observe an evolution analogous to that found by varying the flow os $SiCl_4$. This is due to the fact that both parameters have the effect of increasing the reaction rate, whether by supplying a greater amount of precursor or a higher process temperature.

For low temperatures less density of NWs is observed, as well as an apparition of amorphous silicon at the base of the wires. The best results are found at temperatures around 800-815 °C. For high temperatures, a loss of quality in the surface of the nanowires is observed, together with localized defects (Figure 2.14f). Both effects are due to the generation of HCl during the reaction, which etches the silicon surface of the nanowires when its concentration is high enough [53].

The length of the nanowires is consistently controlled by the reaction time. The growth speed varies with the density and diameter of the nanowires, but it is found to be around 0.5 μm per second for the 50 nm nanowires. The diameter of the nanowires is affected by the conification and the size of the catalyst particle. However, it should be noted that the diameter of the nanowire does not correspond to the diameter of the solid catalyst particle in the solution: during the growth process, the gold colloid mixes with silicon and forms a liquid droplet in the substrate. It is the contact surface between this droplet and the substrate which defines the growth area and the initial diameter of the nanowires. Additionally, the conification effect is always present in the grown wires: when it is provoked by VS deposition it can be alleviated by choosing optimal growth conditions, but in some cases there is also a migration of the gold from the droplet along the nanowire [54] o towards other nanowires [55] which affects the final shape of the structure. In practice, we find the nanowires grown from 50-nanometer colloids to have a diameter of around 80 nm, and those grown from 30-nanometer colloids have diameters around 50 nm. The influence of these phenomena on individual nanowires is further discussed in section 2.3.2.1.

2.3.1.4 Doping of silicon nanowires

The doping of the silicon nanowires fabricated in pre-patterned chips is performed ex-situ, after the growth process. The process is similar to the work of Ingole et al. [45], but using a different dopant source. This doping process is flexible and offers a good control of the doping level of the nanowires.

Typical annealing conditions	
Parameter	Value
Nitrogen flow	50 sccm
Ascending ramp temperature	850 - 1000 °C
Ascending ramp time	30 min
Descending ramp temperature	1000 - 850 °C
Descending ramp time	30 min

Table 2.3: Typical conditions of the ex-situ doping of SiNWs.

The doping process consists in an annealing of the chips with NWs in close proximity to a wafer containing boron, while subject to a mild flow of N_2. Commercial boron nitride wafers are used (BN-1250 from Saint-Gobain Advanced Ceramics), containg 40 % of boron nitride and 60 % of SiO_2. The level of doping is controlled by varying the annealing temperature and time.

The objective of the doping is to obtain an optimal nanowire conductivity for electrical transduction. A high level of doping is needed so that the structures exhibit high conductivity and a metallic behaviour [43]. In order to find the correct doping conditions, some undoped resonators are located in different chips and electrically characterized using a probe station. The undoped nanowires present non metallic behaviour, consistent with that observed in previous works [43] (Figure 2.15a). Afterwards, the chips are doped using different annealing times, and the devices are characterized again both electrically and by scanning electronic microscope. The doping conditions that fulfil our requirements, and which have been used to dope the resonators used throughout this work, are summarized in Table 2.3. Under standard doping conditions no damage of the surface of the nanowires is observed from SEM images. However, during the tests we observed that a high level of doping can indeed damage and etch the nanowires (Figure 2.15b).

Under the right doping conditions, the nanowires present a a metallic electric response with conductivities around 1×10^{-4} Ω·m. The doping level is found to be quite consistent, both in the same chip and under different doping processes. However, due to constrictions arising from the layout it is not possible to perform 4-probe measurements, and therefore a detailed analysis of the repetitivity of the doping process of the nanowires is difficult to perform.

2.3.1.5 Packaging of the chips

After the chips are fabricated, a wire bonding step is performed in order to be able to connect individual nanowires to the measurement systems. The first step is the localization of functional devices: it is done with a combination of optical and SEM

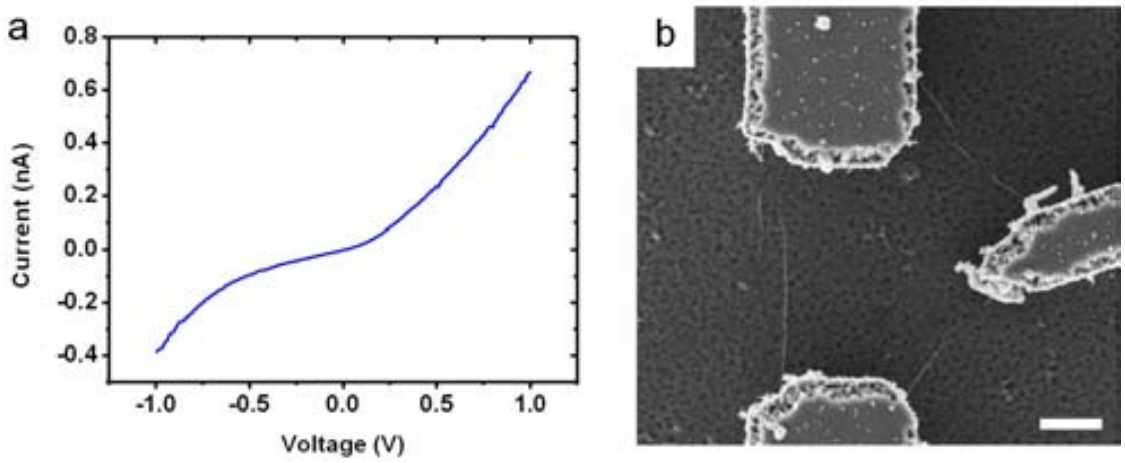

Figure 2.15: Ex-situ doping of SiNWs. a) i-V characteristic of a SiNW prior to the doping. It it presents a non-resistive behaviour. b) SEM image of the effect of high doping level on the surface of a SiNW. The wires present a diameter of few nanometers, when initially it was of 70 nm. Scale bar: 1 μm.

microscopy, the first one to locate candidates of functional devices and the second one to characterize their geometry with precision. After the devices are located, the chips are glued to a PCB with conductive silver paste. Then, a wire-bonding step is used to connect the electrodes contacted with a single nanowire to the PCB for electrical measurement (Figure 2.16). After the wire-bonding, nanowires are extremely sensitive to electrostatic discharge issues, so this last step must be done immediately before the measurements and using a series of anti-static measures to avoid destroying the devices.

2.3.2 Results

The fabrication process has provided a high number of patterned substrates for the growth of SiNWs with different lengths. Depending on the chip design (different designs are used for the two different photolithography equipments), each chip contains between 392 and 480 device candidates. For their use as nanomechanical resonators, we consider that a device is functional when it contains only one nanowire between the electrical contacts, and there are no nanowires short-circuiting the side-gate. After the growth step usually around 20 functional devices per chip (out of 392 devices) are located and characterized by SEM, which represents a yield of roughly 5%. Although this fabrication method is not suitable for batch production due to its low repetitivity and yield, it is more than appropriate for the study of the properties of individual resonators.

Some of the resulting nanomechanical resonators obtained using this fabrication

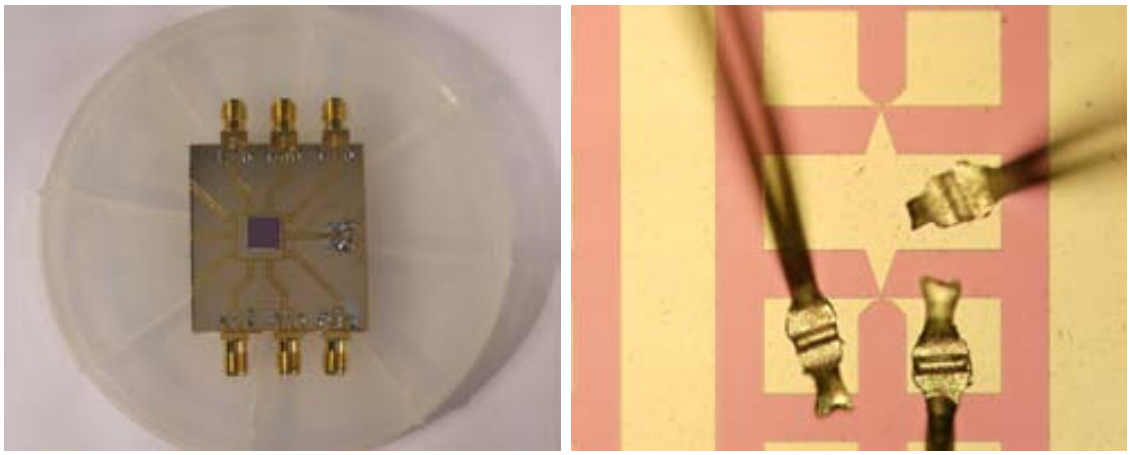

Figure 2.16: Wire-bonding of the functional resonators. Left: PCB with a wire-bonded device. Right: Detail of a wire-bonded nanowire with a side-gate.

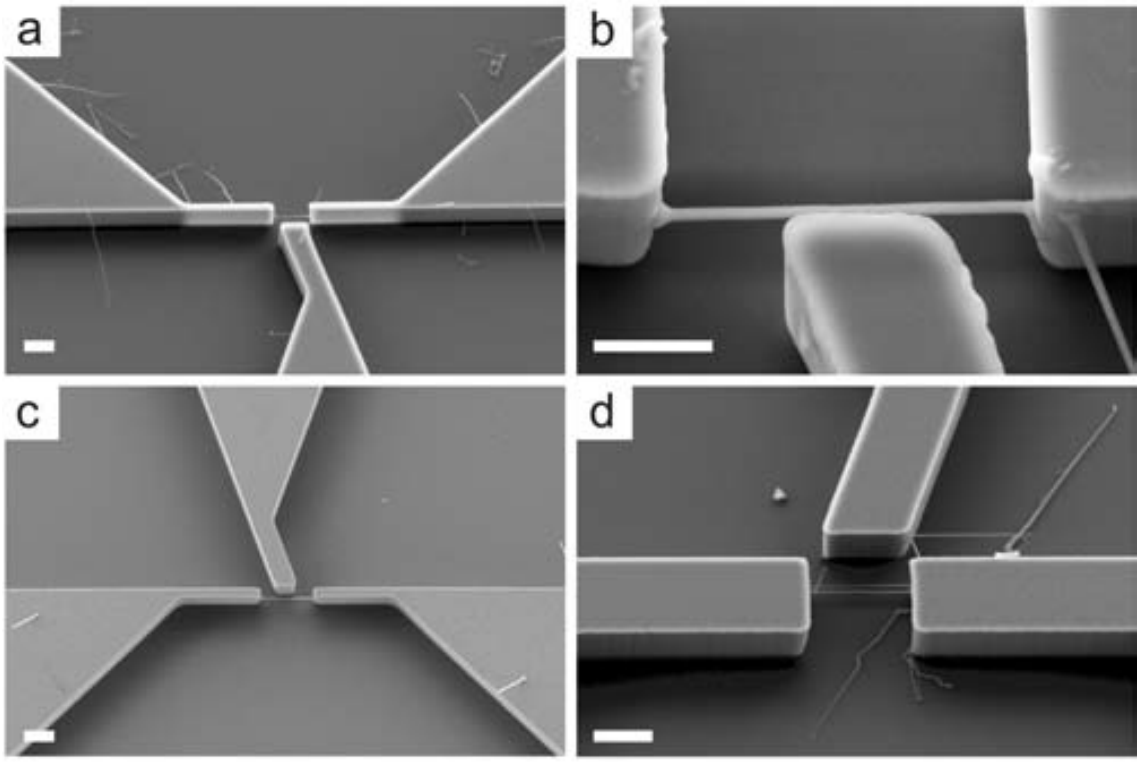

Figure 2.17: Fabrication results of nanomechanical resonators. The lower-right image shows a non-functional device, with multiple wires between the electrodes and a nanowire short-circuiting the side-gate. The diameters of these particular devices range from 70 to 100 nm. Scale bar: 2 μm.

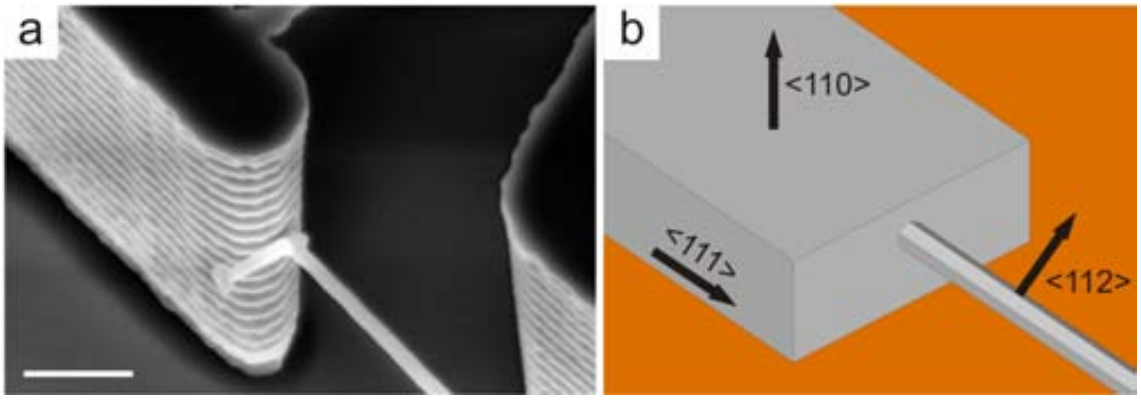

Figure 2.18: Morphology of a resonator based in VLS-grown silicon nanowires. a) SEM image of a nanowire and an electrode. Scale bar: 400 nm. b) Schematic of the geometry of the nanowire, in the same orientation as a).

technology are shown in Figure 2.17. The fabricated resonators have diameters from 50 to 100 nanometers, and lengths ranging from 1 to 3 micrometers. They have a lateral electrode for electrostatic actuation, which in some cases is as close to the nanowire as 300 nanometers. Additionally, the nanowires can be electrostatically actuated using the substrate, although it is farther than the side gate, so the actuation efficiency is lower. One particularity of the fabrication process is the minimum distance between the nanowire and the side-gate to the nanowire as a function of its length. Due to the resolution of the photolithograpy step, the side-gate can be placed closer to the trenches where the nanowires grow only for the lengths greater that 3 μm. In the lengths of 2 and 1 μm this side-gate is located farther from the trench which results in lower electrostatic coupling to the nanowire, thus leading to a lower actuation efficiency. In practice, it means that nanowires with a length of 3 μm can potentially be located as close as necessary to the side gate, while those with lengths of 2 and 1 μm have a minimum distance of around 200 and 400 nanometers respectively.

2.3.2.1 Morphology of the resonators

The nanowires fabricated using the VLS method follow the <111> direction of the silicon device layer. Another particularity of this type of nanowires is that their section is hexagonal, and their surfaces lie along the {112} plane. Moreover, they present a edge facing upwards, so an untilted image of the nanowire using SEM provides the side-to-side diameter as illustrated in Figure 2.18. This geometry is typical from bottom-up nanowires with this range of diameters grown from VLS techniques [11].

The use of bottom-up nanowires as nanomechanical resonators provides a series

of advantages in terms of the morphology of the resonator: they are formed by crystalline silicon, they present epitaxial contacts to the top-down structures, and they have a high quality surface. However, they can also present some defects which affect their performance. These defects are mainly conification, which has been already discussed above, and buckling.

Tapering or conification is a phenomenon which occurs frequently during the bottom-up growth of nanowires, and consists in the nanowires having a difference in diameter between their ends (as can be observed in Figure 2.19a). This phenomenon is observed in the nanowires grown during this work, with differences in diameter of a 25% in the worst cases (characterized by SEM). The conification effect can have different origins: it can be caused by a change of the size of the catalyst particle during the growth, or due to the deposition of silicon in the side-walls of the nanowire caused by a VS process.

The size of the catalyst particle can change during the growth process for different causes. For instance, it is known that during nanowire growth part of the gold of the colloid is introduced into the structure and surface of the nanowire [54]. This can cause a modification of the size of the droplet, and it has caused some concern over the uncertainty of the effect that this gold can have over the electric properties of the nanowires. Alternatively, it has also been reported that the gold can migrate from one colloid to another, or even to different chips [55]. In these cases, the diameter of the nanowire becomes thinner than it should be according to the diameter of the gold colloid, because the process begins with a larger volume of catalyst which decreases during the growth process. The second mechanism causing tapering is the VS deposition of silicon during the growth of the nanowire: in addition to the growth process catalysed by the colloid, there is an incorporation of silicon directly from the precursor to the surface of the nanowire. In this case, the nanowire is thicker than it should be according to the catalyst particle diameter.

The latter is indeed our case: the nanowires have diameters thicker than expected from the diameter of the employed gold colloids. As an example, the nanowires grown from 50 nm colloids have lower diameters of around 70 nm, and higher diameters of up to 100 nm. R. He made an estimation of the relationship between the diameter of the gold colloids (d_{Au}) and that of the nanowires (d_{NW}) for a growth temperature of 800 °C [53]. He found that for colloids of 30 nm or more the following relation holds $d_{NW} = 1\ 16 d_{Au}$, and verified it for different diameters. This means that 50 nm colloids should yield 58 nm nanowires, while 30 nm colloids should yield 35 nm nanowires. Moreover, we examined the catalyst particles by SEM before the growth of the nanowire and we found their diameter to be in concordance with the specifications, of around 50 nm. Also, the diameter of the nanowires varies a little between different growth processes, presumably because of slightly different growth conditions which favour one growth mechanism over the other. This leads us to

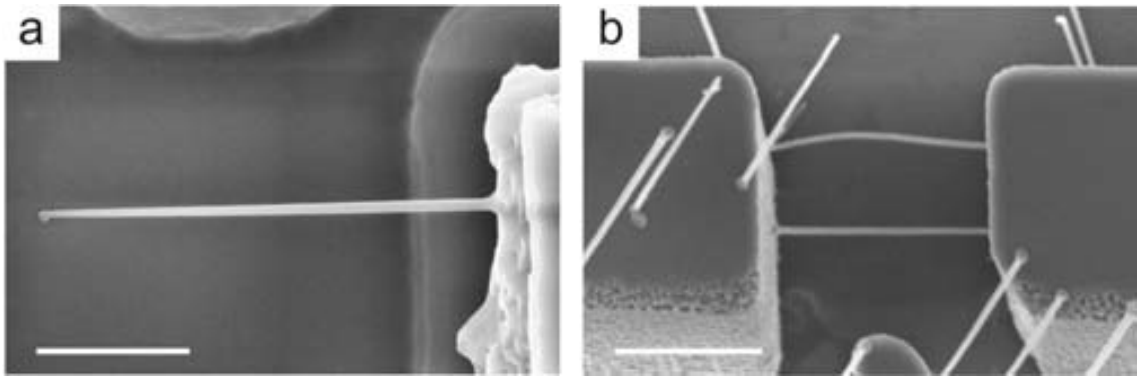

Figure 2.19: Effects of the conification and buckling in resonators based on bottom-up nanowires. a) SEM image of a conificated nanowire. In this case the nanowire is too short to contact both electrodes. Scale bar: 1μm. b) SEM image of a conificated nanowire resonator. Scale bar: 2μm.

conclude that the VS deposition is the cause of conification in our case.

Another phenomena that we observed in the resonators is buckling. This effect is caused when the nanowire reaches the opposite side-wall during the growth process. Usually the nanowire "bounces" and continues its growth along another <111> direction. In some cases, however, the nanowire continues growing "against" the wall for a period of time, introducing compressive stress into the structure. This effect is difficult to quantify using SEM characterization: in order to correctly measure the deflection caused by the buckling it should occur perpendicular to the image, and this is not generally the case. However we observed this phenomena in repeated occasions, such as in Figure 2.19b. Even though this effect has not been characterized in depth during this work, we observe that it is more common for the thinner nanowires grown from 30 nm colloids.

In the next chapter, devices fabricated with this technology are electrically characterized. From these measurements, several characteristics of the nanowires are studied, including the stress accumulated during the fabrication process.

References

[1] H. J. Fan, P. Werner, and M. Zacharias, "Semiconductor nanowires: From self-organization to patterned growth," *Small*, vol. 2, no. 6, pp. 700–717, 2006.

[2] W. Lu and C. M. Lieber, "Semiconductor nanowires," *Journal of Physics D: Applied Physics*, vol. 39, pp. R387–R406, Nov. 2006.

[3] R. He and P. Yang, "Giant piezoresistance effect in silicon nanowires," *Nature Nanotechnology*, vol. 1, no. 1, pp. 42–46, 2006.

[4] J. Arcamone, G. Rius, G. Abadal, J. Teva, N. Barniol, and F. Pérez-Murano, "Micro/nanomechanical resonators for distributed mass sensing with capacitive detection," *Microelectronic Engineering*, vol. 83, pp. 1216–1220, Apr. 2006.

[5] K. Jensen, J. Weldon, H. Garcia, and A. Zettl, "Nanotube radio," *Nano Letters*, vol. 7, no. 11, pp. 3508–3511, 2007.

[6] A. Chaudhry, V. Ramamurthi, E. Fong, and M. S. Islam, "Ultra-low contact resistance of epitaxially interfaced bridged silicon nanowires," *Nano Letters*, vol. 7, pp. 1536–1541, June 2007.

[7] R. He, D. Gao, R. Fan, A. I. Hochbaum, C. Carraro, R. Maboudian, and P. Yang, "Si nanowire bridges in microtrenches: Integration of growth into device fabrication," *Advanced Materials*, vol. 17, no. 17, pp. 2098–2102, 2005.

[8] A. I. Hochbaum, R. Fan, R. He, and P. Yang, "Controlled growth of si nanowire arrays for device integration," *Nano Letters*, vol. 5, no. 3, pp. 457–460, 2005.

[9] M. Tabib-Azar, M. Nassirou, R. Wang, S. Sharma, T. I. Kamins, M. S. Islam, and R. S. Williams, "Mechanical properties of self-welded silicon nanobridges," *Applied Physics Letters*, vol. 87, no. 11, p. 113102, 2005.

[10] A. San Paulo, J. Bokor, R. T. Howe, R. He, P. Yang, D. Gao, C. Carraro, and R. Maboudian, "Mechanical elasticity of single and double clamped silicon nanobeams fabricated by the vapor-liquid-solid method," *Applied Physics Letters*, vol. 87, p. 053111, July 2005.

[11] X. L. Feng, R. He, P. Yang, and M. L. Roukes, "Very high frequency silicon nanowire electromechanical resonators," *Nano Letters*, vol. 7, pp. 1953–1959, July 2007.

[12] X. Feng, R. He, P. Yang, and M. Roukes, "Quality factors and energy losses of single-crystal silicon nanowire electromechanical resonators," pp. 1325–1326, IEEE, 2007.

[13] R. He, X. L. Feng, M. L. Roukes, and P. Yang, "Self-transducing silicon nanowire electromechanical systems at room temperature," *Nano Letters*, vol. 8, pp. 1756–1761, June 2008.

[14] R. Zhu, D. Wang, S. Xiang, Z. Zhou, and X. Ye, "Zinc oxide nanowire electromechanical oscillator," *Sensors and Actuators A: Physical*, vol. 154, pp. 224–228, Sept. 2009.

[15] M. R. Nelis, L. Yu, W. Zhang, Y. Zhao, C. Yang, A. Raman, S. Mohammadi, and J. F. Rhoads, "Sources and implications of resonant mode splitting in silicon nanowire devices," *Nanotechnology*, vol. 22, p. 455502, Nov. 2011.

[16] W. Y. Fung, E. N. Dattoli, and W. Lu, "Radio frequency nanowire resonators and in situ frequency tuning," *Applied Physics Letters*, vol. 94, pp. 203104–203104–3, May 2009.

[17] J. M. Gray, C. T. Rogers, K. A. Bertness, and N. A. Sanford, "Gallium nitride nanowire electromechanical resonators with piezoresistive readout," *Journal of Vacuum Science & Technology B: Microelectronics and Nanometer Structures*, vol. 29, no. 5, p. 052001, 2011.

[18] T. S. Abhilash, J. P. Mathew, S. Sengupta, M. R. Gokhale, A. Bhattacharya, and M. M. Deshmukh, "Wide bandwidth nanowire electromechanics on insulating substrates at room temperature," *Nano Letters*, vol. 12, pp. 6432–6435, Dec. 2012.

[19] H. S. Solanki, S. Sengupta, S. Dhara, V. Singh, S. Patil, R. Dhall, J. Parpia, A. Bhattacharya, and M. M. Deshmukh, "Tuning mechanical modes and influence of charge screening in nanowire resonators," *Physical Review B*, vol. 81, p. 115459, Mar. 2010.

[20] E. Gil-Santos, D. Ramos, J. Martínez, M. Fernández-Regúlez, R. García, l. S. Paulo, M. Calleja, and J. Tamayo, "Nanomechanical mass sensing and stiffness spectrometry based on two-dimensional vibrations of resonant nanowires," *Nature Nanotechnology*, vol. 5, no. 9, pp. 641–645, 2010.

[21] D. Ramos, E. Gil-Santos, V. Pini, J. M. Llorens, M. Fernández-Regúlez, l. San Paulo, M. Calleja, and J. Tamayo, "Optomechanics with silicon nanowires by harnessing confined electromagnetic modes," *Nano Letters*, vol. 12, pp. 932–937, Feb. 2012.

[22] M. Li, R. B. Bhiladvala, T. J. Morrow, J. A. Sioss, K.-K. Lew, J. M. Redwing, C. D. Keating, and T. S. Mayer, "Bottom-up assembly of large-area nanowire resonator arrays," *Nature Nanotechnology*, vol. 3, no. 2, pp. 88–92, 2008.

[23] B. D. Gates, "Self-assembly: Nanowires find their place," *Nature Nanotechnology*, vol. 5, no. 7, pp. 484–485, 2010.

[24] B. Bhushan, *Springer Handbook of Nanotechnology*. Springer, 2004.

[25] V. Schmidt, J. V. Wittemann, S. Senz, and U. Gösele, "Silicon nanowires: A review on aspects of their growth and their electrical properties," *Advanced Materials*, vol. 21, no. 25-26, pp. 2681–2702, 2009.

[26] M. Law, J. Goldberger, and P. Yang, "Semiconductor nanowires and nanotubes," *Annual Review of Materials Research*, vol. 34, no. 1, pp. 83–122, 2004.

[27] R. S. Wagner and W. C. Ellis, "Vapor-liquid-solid mechanism of single crystal growth," *Applied Physics Letters*, vol. 4, pp. 89–90, Mar. 1964.

[28] Y. Wu, Y. Cui, L. Huynh, C. J. Barrelet, D. C. Bell, and C. M. Lieber, "Controlled growth and structures of molecular-scale silicon nanowires," *Nano Letters*, vol. 4, pp. 433–436, Mar. 2004.

[29] D. Tsivion, M. Schvartzman, R. Popovitz-Biro, P. v. Huth, and E. Joselevich, "Guided growth of millimeter-long horizontal nanowires with controlled orientations," *Science*, vol. 333, pp. 1003–1007, Aug. 2011.

[30] X. Duan and C. M. Lieber, "General synthesis of compound semiconductor nanowires," *Advanced Materials*, vol. 12, no. 4, p. 298–302, 2000.

[31] V. T. Renard, M. Jublot, P. Gergaud, P. Cherns, D. Rouchon, A. Chabli, and V. Jousseaume, "Catalyst preparation for CMOS-compatible silicon nanowire synthesis," *Nature Nanotechnology*, vol. 4, no. 10, pp. 654–657, 2009.

[32] Y. Ke, X. Weng, J. M. Redwing, C. M. Eichfeld, T. R. Swisher, S. E. Mohney, and Y. M. Habib, "Fabrication and electrical properties of si nanowires synthesized by al catalyzed vapor-liquid-solid growth," *Nano Letters*, vol. 9, pp. 4494–4499, Dec. 2009.

[33] Z. Dai, Z. Pan, and Z. Wang, "Novel nanostructures of functional oxides synthesized by thermal evaporation," *Advanced Functional Materials*, vol. 13, no. 1, p. 9–24, 2003.

[34] N. Wang, Y. Tang, Y. Zhang, C. Lee, I. Bello, and S. Lee, "Si nanowires grown from silicon oxide," *Chemical Physics Letters*, vol. 299, pp. 237–242, Jan. 1999.

[35] T. J. Trentler, K. M. Hickman, S. C. Goel, A. M. Viano, P. C. Gibbons, and W. E. Buhro, "Solution-liquid-solid growth of crystalline III-V semiconductors:

An analogy to vapor-liquid-solid growth," *Science*, vol. 270, pp. 1791–1794, Dec. 1995. ArticleType: research-article / Full publication date: Dec. 15, 1995 / Copyright © 1995 American Association for the Advancement of Science.

[36] D. S. Engstrom, V. Savu, X. Zhu, I. Y. Y. Bu, W. I. Milne, J. Brugger, and P. Boggild, "High throughput nanofabrication of silicon nanowire and carbon nanotube tips on AFM probes by stencil-deposited catalysts," *Nano Letters*, vol. 11, no. 4, pp. 1568–1574, 2011.

[37] L. Magagnin, V. Bertani, P. Cavallotti, R. Maboudian, and C. Carraro, "Selective deposition of gold nanoclusters on silicon by a galvanic displacement process," *Microelectronic Engineering*, vol. 64, pp. 479–485, Oct. 2002.

[38] D. Gao, R. He, C. Carraro, R. T. Howe, P. Yang, and R. Maboudian, "Selective growth of si nanowire arrays via galvanic displacement processes in water-in-oil microemulsions," *Journal of the American Chemical Society*, vol. 127, pp. 4574–4575, Apr. 2005.

[39] M. Fernández-Regúlez, J. A. Plaza, E. Lora-Tamayo, and A. S. Paulo, "Lithography guided horizontal growth of silicon nanowires for the fabrication of ultrasensitive piezoresistive strain gauges," *Microelectronic Engineering*, vol. 87, pp. 1270–1273, May 2010.

[40] D. Dávila, A. Tarancón, C. Calaza, M. Salleras, M. Fernández-Regúlez, A. San Paulo, and L. Fonseca, "Monolithically integrated thermoelectric energy harvester based on silicon nanowire arrays for powering micro/nanodevices," *Nano Energy*, vol. 1, pp. 812–819, Nov. 2012.

[41] M. Fernandez-Regulez, M. Sansa, M. Serra-Garcia, E. Gil-Santos, J. Tamayo, F. Perez-Murano, and A. San Paulo, "Horizontally patterned si nanowire growth for nanomechanical devices," *Nanotechnology*, vol. 24, p. 095303, Mar. 2013.

[42] D. E. Perea, E. R. Hemesath, E. J. Schwalbach, J. L. Lensch-Falk, P. W. Voorhees, and L. J. Lauhon, "Direct measurement of dopant distribution in an individual vapour–liquid–solid nanowire," *Nature Nanotechnology*, vol. 4, no. 5, pp. 315–319, 2009.

[43] Y. Cui, X. Duan, J. Hu, and C. M. Lieber, "Doping and electrical transport in silicon nanowires," *The Journal of Physical Chemistry B*, vol. 104, no. 22, pp. 5213–5216, 2000.

[44] X. Duan, Y. Huang, Y. Cui, J. Wang, and C. M. Lieber, "Indium phosphide nanowires as building blocks for nanoscale electronic and optoelectronic devices," *Nature*, vol. 409, pp. 66–69, Jan. 2001.

[45] S. Ingole, P. Aella, P. Manandhar, S. B. Chikkannanavar, E. A. Akhadov, D. J. Smith, and S. T. Picraux, "Ex situ doping of silicon nanowires with boron," *Journal of Applied Physics*, vol. 103, pp. 104302–104302–8, May 2008.

[46] G. S. Doerk, G. Lestari, F. Liu, C. Carraro, and R. Maboudian, "Ex situ vapor phase boron doping of silicon nanowires using BBr3," *Nanoscale*, vol. 2, no. 7, p. 1165, 2010.

[47] K. Byon, D. Tham, J. E. Fischer, and A. T. Johnson, "Synthesis and postgrowth doping of silicon nanowires," *Applied Physics Letters*, vol. 87, pp. 193104–193104–3, Nov. 2005.

[48] R. A. Beckman, E. Johnston-Halperin, N. A. Melosh, Y. Luo, J. E. Green, and J. R. Heath, "Fabrication of conducting si nanowire arrays," *Journal of Applied Physics*, vol. 96, pp. 5921–5923, Nov. 2004.

[49] M. Sansa, M. Fernández-Regúlez, l. San Paulo, and F. Pérez-Murano, "Electrical transduction in nanomechanical resonators based on doubly clamped bottom-up silicon nanowires," *Applied Physics Letters*, vol. 101, pp. 243115–243115–5, Dec. 2012.

[50] H. V. Jansen, M. J. de Boer, S. Unnikrishnan, M. C. Louwerse, and M. C. Elwenspoek, "Black silicon method: X. a review on high speed and selective plasma etching of silicon with profile control: an in-depth comparison between bosch and cryostat DRIE processes as a roadmap to next generation equipment," *Journal of Micromechanics and Microengineering*, vol. 19, p. 033001, Mar. 2009.

[51] "Ultrasil SOI wafer technology."

[52] l. San Paulo, N. Arellano, J. A. Plaza, R. He, C. Carraro, R. Maboudian, R. T. Howe, J. Bokor, and P. Yang, "Suspended mechanical structures based on elastic silicon nanowire arrays," *Nano Letters*, vol. 7, pp. 1100–1104, Apr. 2007.

[53] R. He, *Silicon Nanowires for Nanoelectromechanical Systems*. PhD thesis, University of California, Berkeley, 2006.

[54] J. E. Allen, E. R. Hemesath, D. E. Perea, J. L. Lensch-Falk, Z. Y. Li, F. Yin, M. H. Gass, P. Wang, A. L. Bleloch, R. E. Palmer, and L. J. Lauhon, "High-resolution detection of au catalyst atoms in si nanowires," *Nature Nanotechnology*, vol. 3, no. 3, pp. 168–173, 2008.

[55] L. Cao, B. Garipcan, J. S. Atchison, C. Ni, B. Nabet, and J. E. Spanier, "Instability and transport of metal catalyst in the growth of tapered silicon nanowires," *Nano Letters*, vol. 6, pp. 1852–1857, Sept. 2006.

Chapter 3

Electrical measurement of bottom-up silicon nanowire resonators

Contents

The building-up of functional systems based on one or several mechanical nanostructures has raised the field of nanoelectromechanical systems (NEMS). Physical and biochemical sensing are some of the areas where NEMS are showing significant advance, because they can provide enhanced sensitivity and resolution, specifically originated from their small dimensions. Nanomechanical resonators, for example, combine low mass and high operating frequency at the same time, which allows to achieve mass sensing resolution down to the yoctogram range [1]. However, their small dimensions pose a challenge for the measurement of these devices, entailing constraints such as small signals, low dynamic range and high oscillation frequency. In view of this, the development of efficient transduction methods is especially crucial for the future development of NEMS.

SiNWs present high gauge factors, thus providing an intrinsic transduction mechanism for electrical read-out. In the case of double-clamped SiNWs, the resistance change was proposed to be due to the non-vanishing longitudinal strain caused by the lengthening of the deflected wire, and consequently resulting in an oscillating signal which varies at doubled frequency, 2 , with respect to the mechanical oscillation (as explained in section 1.3.1). He and co-workers implemented an electrical detection scheme based in a frequency down-conversion circuit (two-source, 2 detection) that exploits this feature [2]. Also, frequency downmixing schemes based on a linear dependence of the resistance change with the displacement (two-source, 1 detection) have been used to characterize the frequency response of cantilevers [3], where a piezoresistor is integrated in the surface of the cantilever, and CNTs [4], where the transduction mechanism is based on the change of conductance induced by the variation of the gate-induced charge in the nanotube (detailed in section 1.3.2). Moreover, these same nanotubes have been measured using the frequency modulation (FM) detection technique [5], which provides advantages in terms of absence of parasitic signals and the simplicity of the measurement setup.

In this chapter, we demonstrate the usefulness of the frequency modulation (FM) transduction scheme for the electrical read-out of bottom-up nanomechanical resonators. The FM scheme enables the observation of the resonance mode-splitting effect of silicon nanowires resonators in the UHF range for the first time, as well as the detection of higher-order modes of the resonant structure, which is crucial for developing quantitative mass-sensor with spatial selectivity. Our results indicate that two transduction mechanisms co-exist in the electrical read-out of the oscillation of bottom-up grown silicon nanowires. In particular, the existence of a transduction mechanism that presents a linear dependence of the change of the conductivity as a function of the displacement is necessary to explain the experimental results.

The chapter is organised as follows: the first section presents a study of different

down-mixing methods applied to nanomechanical resonators (the FM and two variants of the two-source detection method). The second section presents measurement results of bottom-up silicon nanowire resonators using these different methods. The following section presents a study of the measurement methods, focused on their efficiency for the detection of transduction signals of different origin, which is then applied to the determination of the transduction mechanisms present in the measured SiNW resonators. Afterwards, the results of Finite Element Modelling (FEM) simulations are presented, which allow extracting additional information from the measurement of multiple modes of the resonators. Finally, the last section deals with the mode-splitting phenomena observed during the measurements.

3.1 Electrical measurement methods based on downmixing techniques

The small dimensions of the resonators used throughout this work bestow resonance frequencies in the range of 50-150 MHz for the first mode of resonance, and much higher resonance frequencies for higher modes. Moreover, small dimensions also imply that the transduction signals generated by their motion are vary small. Working with high frequency signals of small amplitude arises issues due to parasitic capacitances, mismatch with the RF components, etc. The detection methods used in this work are based on downmixing RF techniques, which alleviate the issues of working with high frequency signals. These techniques are an adaptation of methods used in radio-frequency, based in the transformation of a signal which carries information at a determined frequency to a different frequency which is more appropriate for its application. For example, in most radio-frequency techniques, such as analog radio, a low frequency signal (a voice or music) is modulated to high frequency in order to be transmitted at large distances using antennas. This high frequency signal is afterwards demodulated to obtain the original signal. In the case of nanomechanical resonators, the process is in some sense the inverse: the motion of the resonator generates a high frequency transduction signal, which is downmixed (moved to low frequencies) at device level, thus generating a low frequency measurement signal. This low frequency component carries information about the demodulator, and therefore of the motion of the resonator. This general principle can be implemented with different methods, corresponding to different modulation and demodulation techniques adapted to appropriate devices. In this work we use three different methods, as it is explained below.

With independence of the detection method, the measurement of the resonators is performed in a vacuum chamber, at a pressure of 10^{-6} mbar approximately, and ambient temperature. The major part of the measurements have been performed

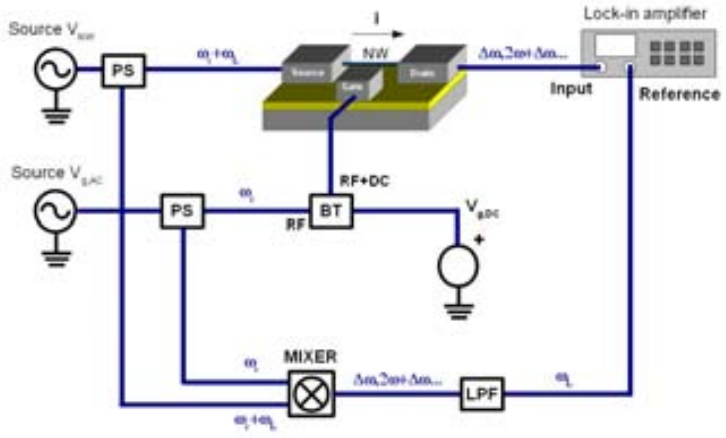

Figure 3.1: Measurement setup using the two-source, 1ω detection method. *PS* stands for power splitter, *BT* for bias tee and *LPF* for low-pass filter.

at the facilities of the group of Núria Barniol (ECAS group, Electronic Engineering department of the UAB).

3.1.1 Two-source, 1 measurement method

In this technique, voltage is applied to the resonator at a frequency with a small offset with respect to the resonance frequency. When the resonator is in resonance, its motion induces a resistance change proportional to its motion. Then, the multiplication of the applied voltage with the resistance of the device generates the low frequency measurement current, which is then detected using a lock-in amplifier. The reference signal is generated externally from the signals generated by the RF generators (the actuation voltage and the voltage through the wire) and and a mixer. The two-source, 1 detection technique has been previously used to detect the motion of carbon nanotube (CNT) resonators, in which the transduction signal is proportional to the motion of the resonator, originated by the conductance modulation caused by a change in the capacitance between the nanowire and the side-gate [4]. The measurements are performed using the setup of Figure 3.1.

A detailed description of the two-source, 1 method is presented. The voltage applied to the nanowire is:

$$V_{NW,2s1\omega}(t) = V_{NW}\cos((\ _c + \ _L)t) \tag{3.1}$$

where $_c$ is the high frequency carrier component and $_L$ the measurement frequency. The voltage applied to the side gate, which provides the electrostatic actuation, consists in a DC and an AC component, and takes the form:

$$V_{g,2s1\omega}(t) = V_{g,DC} + V_{g,AC}\cos(\ _c t) \tag{3.2}$$

The amplitude of vibration at the center of the resonator $x(t)$ can be expressed as a sinusoidal wave at the excitation frequency multiplied by the magnitude of the frequency response of the resonator $X(\ _c)$:

$$x(t) = X(\ _c)\ \cos(\ _c t) \tag{3.3}$$

In the general case, the transduction mechanism transforms this signal $x(t)$ to a change of resistance $\Delta R(t)$, so the resistance of the resonator vibrating at frequency $_c$ is:

$$R(t) = R_0 + \frac{R}{x}x(t) = R_0 + \frac{R}{x}\ X(\ _c)\ \cos(\ _c t) = R_0 + \Delta R(t) \tag{3.4}$$

where R_0 is the resistance at rest. Then, the current flowing through the nanowire is:

$$i_{NW}(t) = \frac{V_{NW,2s1\omega}(t)}{R(t)} = \frac{V_{NW,2s1\omega}(t)}{R_0(1+\frac{\Delta R(t)}{R_0})} \tag{3.5}$$

We develop this expression using Taylor expansions:

$$i_{NW}(t) \approx \frac{V_{NW,2s1\omega}(t)}{R_0}\quad 1 - \frac{\Delta R(t)}{R_0} + \left(\frac{\Delta R(t)}{R_0}\right)^2 + \tag{3.6}$$

The resistance change is only important when the nanowire is resonating at the resonance frequency $\ _0$–where the amplitude of motion is maximum–so $\Delta R(t)$ can be defined as $\Delta R(t) = \Delta R_0\cos(\ _0 t)$. Then, by expanding the expression, a multitude of frequency components are obtained. However, the measurement using the lock-in amplifier filters only the component at the measurement frequency $\ _L$. Then, the only term which provides information at the measurement frequency is the one that comes from the intermodulation of the NW voltage at frequency $\ +\ _L$ and the resistance at $\ _0$:

$$i_{NW}(t) \quad = \quad \frac{V_{NW}\Delta R_0}{R_0^2}\cos(\ _0 t)\cos((\ _0 + \ _L)t) + \tag{3.7}$$

$$i_{NW,\omega_L} \quad = \quad \frac{V_{NW}\Delta R_0}{2R_0^2}\cos(\ _L t) \tag{3.8}$$

where $\Delta R_0 = \ R\ \ x\ X(\ _0)$. Therefore, the output current measured at a low frequency $\ _L$ is proportional to the frequency response of the nanowire at the high actuation frequency $X\ _0$. Moreover, even when changing the frequency at which

the nanowire is actuated–and therefore, the frequency at which it oscillates–the measurement is always performed at the same low frequency. This is a general case, where no assumption is made about the transduction mechanism.

The expressions of the two-source, 1 detection method can be developed for the particular case of the conductance change due to charge modulation induced by the capacitance coupling with the side-gate, explained in section 1.3.2. The main difference with the general development is that, in this case, the conductance of the resonator presents three different components: a constant component of the conductance at rest, the conductance change due to the motion of the resonator at the actuation frequency $_c$ and another component at frequency $_c$, originated by the modulation of the conductivity of the resonator caused by the gate voltage. Therefore, this transduction mechanism includes a parasitic component which modifies the frequency response and hinders the detection of the resonance peak. The resistance change caused by this transduction mechanism has been developed in section 1.3.2:

$$\Delta R^{-1} = \Delta G = \frac{G}{q}\left(C_g(\quad t)V_{g,DC} + C_{g,0}V_{g,AC}(t)\right) \tag{3.9}$$

From this expression where $G \quad V_g = \quad G \quad q\, C_g$ is the transconductance, the amplitude of the current at the measurement frequency can be found:

$$I_{NW,\omega_L} = \frac{1}{2}\frac{}{\overline{2}}\frac{G}{V_g}\left(V_{g,AC} + V_{g,DC}\frac{C_g}{C_g}\right)V_{NW} \tag{3.10}$$

where $G \quad V_g$ is the transconductance of the nanowire and $C_g \quad C_g$ is the relative change of capacitance between the nanowire and the excitation side-gate due to its motion.

An estimation of the transconductance $G \quad V_g$ can be found from the parasitic signal, that corresponds to the first term of equation 3.10. When measuring the electrical background of the signal at a frequency , far away from resonance, the transconductance value is defined as:

$$\frac{G}{V_g} = \frac{1}{2}\frac{}{\overline{2}}\frac{I_{LIA,background}}{V_{g,AC}V_{NW}} \tag{3.11}$$

3.1.2 Two-source, 2 measurement method

The two-source, 2 technique has been previously used to measure the frequency response of piezoresistive silicon nanowires, in which the transduction signal is not proportional to its motion but quadratic (as seen in section 1.3.1). It is very similar to the two-source, 1 detection method presented above, but in this case it is

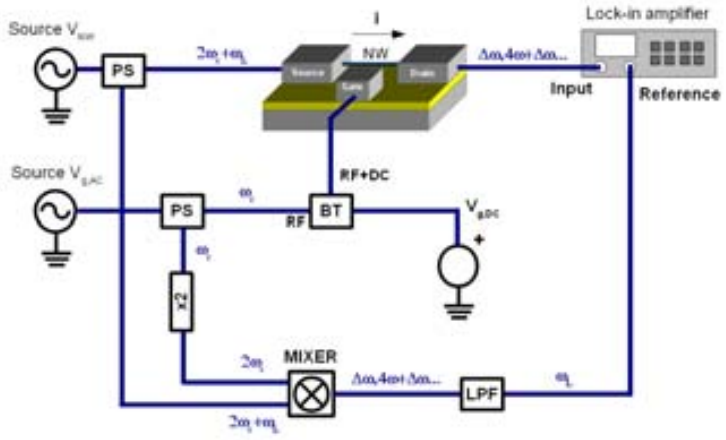

Figure 3.2: Measurement setup using the two-source, 2ω detection method.

adapted to a transduction signal occurring at twice the resonance frequency. The measurements are performed using the setup shown in Figure 3.2.

In this measurement technique, the actuation voltage is the same than for the two-source, 1 (equation (3.2)). On the contrary, the voltage passing through the nanowire operates at twice the resonance frequency with a small offset, and therefore it takes the form:

$$V_{NW,2s2\omega}(t) = V_{NW}\cos((2 \ _c + \ _L)t) \tag{3.12}$$

The nanowire has a resistance at rest R_0. Its motion causes a certain elongation, which in turn provokes a change in its resistance due to the piezoresistive effect. Following the analysis performed in section 1.3.1, this resistance change ΔR is described for the first mode of resonance as:

$$\frac{\Delta R(t)}{R_0} \approx 2\ 44 G_{PR}\frac{x^2(t)}{l_0^2} \tag{3.13}$$

where G_{PR} is the gauge factor and l_0 is the length of the resonator at rest. When $\Delta R(t) \ R_0 \ll 1$ (in our case, $\Delta R(t) \ R_0 < 10^{-3}$), then the expression for the current flowing through the resonator can be approximated as:

$$I_{NW} = \frac{V_{NW,2s2\omega}}{R_0 + \Delta R(t)} \approx \frac{V_{NW,2s2\omega}}{R_0}(1 - \Delta R(t) \ R_0) \tag{3.14}$$

This expression contains two terms: the purely electrical term due to the resistance of the resonator and a second term related to its motion. Discarding the high-frequency and DC components (which are filtered by the lock-in amplifier), the motional term provoked by the oscillation of the resonator is:

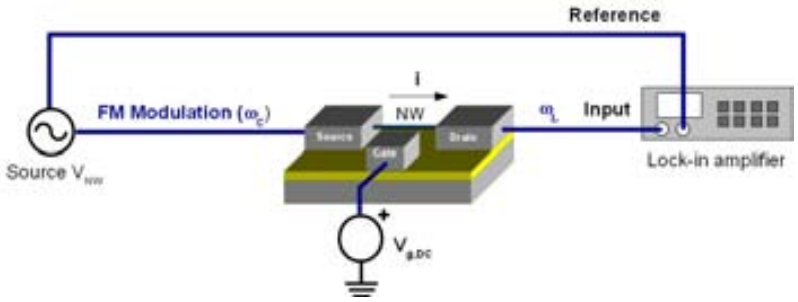

Figure 3.3: Measurement setup using the frequency modulation detection method.

$$
\begin{aligned}
I_{NW,motional} &= -\frac{V_{NW,2s2\omega}}{R_0}\frac{\Delta R(t)}{R_0} \\
&= 2\ 44 G_{PR}\frac{V_{NW}}{R_0}\frac{X(\ _c)^{\ 2}}{l_0^2}\cos^2(\ _c t)\cos((2\ _c + \ _L)t) \qquad (3.15) \\
& \qquad (3.16)
\end{aligned}
$$

And the measurement term at low frequency is:

$$
I_{NW,motional,\omega_L} = 0\ 61\frac{V_{NW}G_{PR}}{R_0}\frac{X(\ _c)^{\ 2}}{l_0^2} \qquad (3.17)
$$

Therefore, the measurement signal at low frequency $_L$ carries information about the response of the resonator at the actuation frequency $_c$. In the case of the two-source, 2 measurement technique there is no electric parasitic signal, that is, the measurement signal is due entirely to the motion of the resonator. Moreover, the amplitude of the measurement signal using this technique is proportional to the square of the displacement of the resonator $X(\ )^{\ 2}$.

3.1.3 Frequency modulation

The frequency modulation (FM) detection technique is based in introducing an FM-modulated voltage through the resonator. The FM signal consists in a high frequency carrier signal near the resonance frequency of the resonator $_0$, which modulates a low frequency reference signal at frequency $_L$. When the resonator is in resonance, the conductivity change induced by the motion of the resonator demodulates the high frequency FM signal, generating the reference signal at $_L$ which is then detected using a lock-in amplifier. A schematic of this detection method is shown in figure 3.3.

In this case, the FM signal causes both the actuation and downmixing. The electrostatic force is generated by the voltage difference between the resonator and the

side-gate, which is polarized at a DC voltage $V_{g,DC}$. The equation of the actuation voltage is:

$$V_{actuation,FM} = V_{NW} - V_{driving\_electrode} = V_{NW,FM} - V_{g,DC} \tag{3.18}$$

The FM modulated signal $V_{NW,FM}$ takes the form:

$$V_{NW,FM}(t) = V_{NW} \cos\left(\quad_c t + \frac{\Delta}{L} \cos \quad_L t \right) \tag{3.19}$$

This signal is centered at the carrier frequency $\quad_c$, and $\quad_\Delta$ is the frequency deviation. As this FM signal is also the actuation signal, it is useful to transform it into the frequency domain, to relate it with the frequency response of the resonator. In order to ease this transformation, the signal can be expressed as a sum of trigonometric functions using the Jacobi-Anger expansion:

$$V_{NW,FM}(t) = V_{NW} \left[J_0\left(\frac{\Delta}{L}\right) \cos(\quad_c t) \right.$$
$$\left. + \sum_{n=1}^{\infty} J_n\left(\frac{\Delta}{L}\right) (\cos((\quad_c - n \quad_L)t) + (-1)^n \cos((\quad_c - n \quad_L)t)) \right] \tag{3.20}$$

where J_n is the n^{th} Bessel function. In frequency domain, the FM signal consists in a series of peaks, the central one at the carrier frequency $\quad_c$ and the others surrounding it at intervals of frequency f_L. The relative amplitude of these peaks varies depending on the frequency deviation $\quad_\Delta$. Figure 3.4 shows the frequency response of the FM signal for different values of $\quad_\Delta \quad_L$ near the carrier signal at frequency f_0. For all the cases, these peaks can be considered negligible for frequencies far away from the carrier. It is interesting to note the opposite sign of the peaks adjacent to the excitation frequency, that is, at $\quad_0 + \quad_L$ and $\quad_0 - \quad_L$. Thanks to this particularity, the FM presents no parasitic signal at the low frequency $\quad_L$ due to intermodulation and other effects.

When the FM signal is applied to a SiNW resonator, the conductance change due to the motion generates a current I_{NW} with several frequency components at different frequencies, which have either electrical or mechanical origin. As the output signal is detected with a lock-in amplifier, tuned precisely at the reference frequency $\quad_L$, all of the components which are not at this measurement frequency are filtered and discarded.

Now, the expression of the current through the nanowire is developed, with the objective to find a term at frequency $\quad_L$ that contains information regarding the motion of the nanowire. This study was first reported by Gouttenoire et al. [5], and it is adapted here. We consider an oscillating cc-beam with a displacement at its

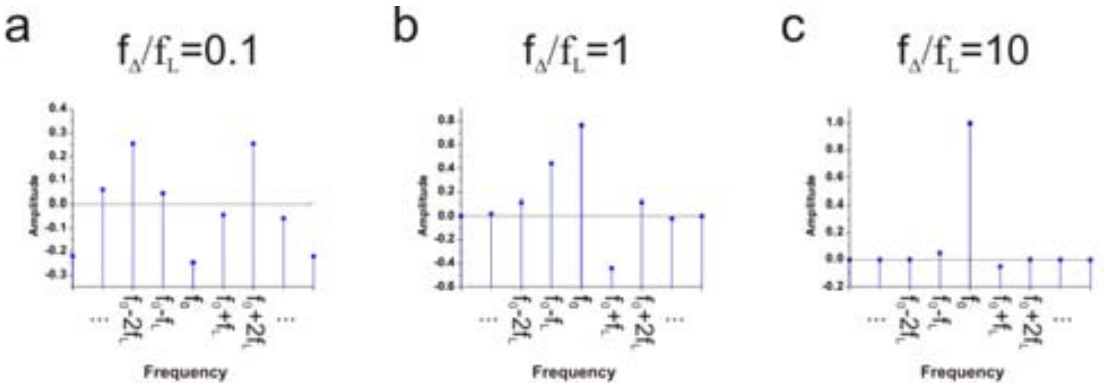

Figure 3.4: Frequency spectrum of a FM signal centered at frequency f_0 ($f_0 = \omega_0/2\pi$), for different values of f_Δ/f_L.

center $x(t)$, to which an FM voltage is applied. Developing the general expression of the current through this device using a Taylor expansion we obtain:

$$I_{NW}(V_{NW,FM}(t)\ x(t)\ V_{g,DC}) = I(0\ x_0\ V_{g,DC}) + \frac{I}{V_{sd}}(0\ x_0\ V_{g,DC})V_{NW,FM}(t) + \frac{I}{x}(0\ x_0\ V_{g,DC})x(t) + I_2 \tag{3.21}$$

where x_0 is the position of the resonator at rest (in our case, it is generally 0), V_{sd} is the voltage drop at the nanowire and I_2 contains higher order terms. In this expression, the first and third terms are zero, because there is no voltage drop in the nanowire (and therefore no current passing through it), and the second term contains high frequency purely electrical terms. By developing the higher terms of the Taylor expansion contained in I_2 we obtain:

$$I_2 \approx \frac{1}{2}\frac{^2I}{V_{sd}^2}V_{NW,FM}(t)^2 + \frac{^2I}{V_{sd}\ x}V_{NW,FM}(t)x(t) + \frac{1}{2}\frac{^2I}{x^2}x(t)^2 \tag{3.22}$$

Here, for the same reason as before, the last term is zero and the first term only contains high frequency signals. The second term, however, is the product of the motion of the nanowire with the excitation signal. These two high frequency signals originate a downmixing, similarly to the two-source techniques, and generate the low frequency component. Here, the transduction parameter $^2I\ \ x\ V_{sd}$ is kept generic, and therefore no assumptions are made about the transduction mechanism.

We now focus in the FM signal. The FM voltage can be expressed as $V_{FM} = V_{FM}\cos(\ \ (t))$. For a timescale Δt smaller than that of the resonator ($Q\ \ _0$), the

argument of the cosine can be rewritten as $(t+\Delta t) = (t) + \Delta t \quad t$. Also, when the frequency is much higher than the frequency deviation ($\gg$ $_{\Delta}$) and $_0 Q \gg \ _L$, we can consider that the resonator is exposed at each time t to an harmonic force of frequency $_i = \quad t = \ + \ _{\Delta}\cos(\ _L t)$, plus an additional phase which can be considered constant. Then the current through the nanowire is:

$$I(t) = \frac{^2 I}{x \ V_{sd}} V_{FM} \cos(\ _i \Delta t + \ (t)) x(t+\Delta t) \tag{3.23}$$

When the nanowire is actuated with a sinusoidal signal, its amplitude of motion can be found from its frequency response. In this case the motion of the nanowire can be written as:

$$x(t+\Delta t) = Re(X(\ _i)\cos(\ _i \Delta t + \ (t))) - Im(X(\ _i)\sin(\ _i \Delta t + \ (t))) \tag{3.24}$$

Substituting equation 3.24 into 3.23, we find an expression for the studied current component:

$$I(t) = \frac{1}{2}\frac{^2 I_{NW}}{x \ V_{NW}} V_{NW} Re(X(\ _i)) \tag{3.25}$$

We now develop the different terms of this expression. The one related with the frequency response of the nanowire, $Re(X(\ _i))$, can be expanded using Taylor series. After this expansion, the term at low frequency is:

$$Re(X(\ _i))_{\omega_L} \approx \frac{Re(X(\ _i))}{\ _{\Delta}\cos(\ _L t)} \tag{3.26}$$

During the modelling of the nanowire (section 1.1.2), its frequency response $X(\ )$ is explained in detail. This frequency response represents the amplitude and phase of vibration of the center of the nanowire as a result of an excitation force of frequency $\ $. The real part of this response is:

$$Re(X(\ )) = \frac{F}{m_{eff}} \frac{^2_0 - \ ^2}{(\ ^2_0 - \ ^2)^2 + \left(\frac{\omega\omega_0}{Q}\right)^2} \tag{3.27}$$

where F is the amplitude of the excitation force at the excitation frequency. Then, the derivative of this expression with respect to the frequency is:

$$\frac{Re(X(\ ))}{} = \frac{F}{m_{eff}} \frac{2Q^2 w\left(-\ ^4_0 + Q^2\left(w^2 - \ ^2_0\right)^2\right)}{\left(w^2 \ ^2_0 + Q^2\left(w^2 - \ ^2_0\right)^2\right)^2} = \frac{F}{m_{eff}} D(\ ) \tag{3.28}$$

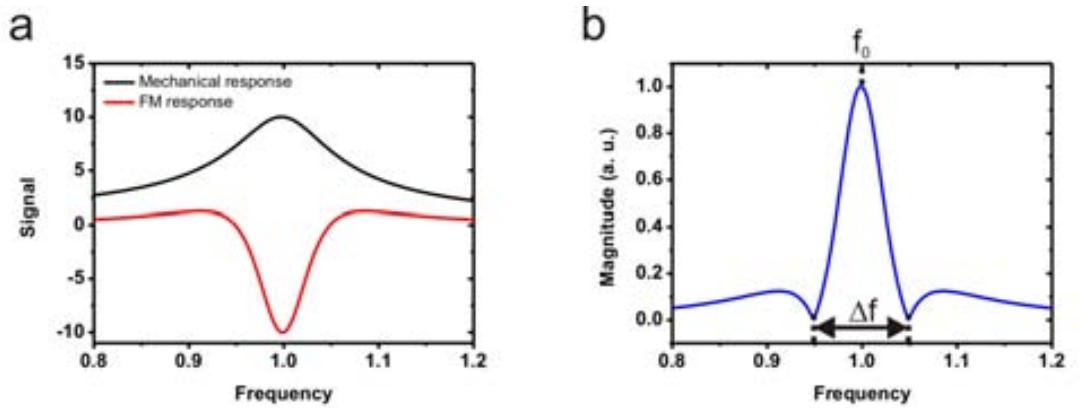

Figure 3.5: Detection of the frequency response of a resonator using the FM method. a) Different frequency responses: the mechanical response of the resonator and the FM response. The FM response is the derivative of the real part of the response of the resonator. b) Determination of the quality factor of the resonator from the frequency response: Q=$f_0/\Delta f$.

And finally, the complete expression of the low-frequency current detected by the lock-in amplifier is:

$$I_{FM,\omega_L}(t) = \frac{1}{2}\frac{^2I_{NW}}{x\ V_{NW}}V_{NW}\frac{F}{m_{eff}}D(\ )\ _\Delta cos(\ _L t) \tag{3.29}$$

The measurement current is a function of the transduction mechanism, contained in the term $^2I_{NW}\ \ x\ V_{NW}$. One of the interesting things that can be observed in this expression is that the detected signal as a function of the excitation frequency does not correspond to the frequency response of the resonator $X(\ )$, but to the real part of the derivative of that response $D(\ )$. This is illustrated in Figure 3.5a: the actual amplitude of motion at the center of the resonator with respect to the excitation frequency follows the response coloured in black, while the signal measured with the FM detection technique is described by the red shape. In this sense, the interpretation of the FM response is not straightforward.

Additionally, the FM detection technique has another particularity which is useful to simplify the study of the response of the resonator. When plotting the magnitude (which is the term that is actually measured with the lock-in amplifier), the bandwidth which determines the quality factor is enclosed by the two minima of the response (Figure 3.5b). This eases the process of extracting the quality factor from the frequency response obtained during the measurements.

Equation (3.29) shows that the output current is proportional to the frequency deviation $_\Delta$. However, this expression is only valid when $_\Delta \gg \Delta$, the width of the resonance peak. When this condition is not fulfilled, the measured response widens with respect to the real response of the resonator [5]. In our measurement conditions, due to the low signals and high quality factors of the studied devices,

there is a compromise between the amplitude of the detected signal and the bandwidth of the measured peak. This means that, for some measurement conditions, the measured quality factor does not correspond with the quality factor of the resonator, and instead the measured response peak widens with respect to the mechanical one as a consequence of the measurement method.

In conclusion, the FM demodulation method provides a measurement signal without electrical parasitic signals. However, its interpretation is not as straightforward as with the other studied detection techniques, in the sense that the measured signal is more difficult to relate with the mechanical response of the resonator. It is important to highlight that the FM measurement method requires a relatively simple measurement setup (composed of an RF source, a DC source and a lock-in amplifier).

3.1.4 Comparison of the measured response with different detection methods

The measurement of the mechanical response of a resonator yields a different electrical response for each detection method, as it is observed in equations (3.10), (3.17) and (3.29). For this reason, it is useful to perform a comparison of the mechanical response of the resonator compared with its measurement employing different detection methods. However, it is difficult to perform a quantitative comparison, because the different measurement methods have been developed for different transduction mechanisms, and therefore depend on different parameters. The relation between the measurement methods and transduction mechanisms is further studied in section 3.3.1.

Figure 3.6 shows a comparison of the mechanical response of the resonator and the results of its measurement with the different studied detection methods. This graph is obtained by calculating the mechanical response $X(\ )$ with a certain resonance frequency and a quality factor. Then, the shape obtained with the different measurement methods is obtained from equations (3.8), (3.17) and (3.28). All the equations are scaled for an easier comparison, and for the two-source, 1 method only the response of mechanical origin is shown, without the electrical parasitic signal. We observe that each detection method presents a characteristic frequency response, and the two-source, 1 is the only one that is proportional to the mechanical response of the resonator.

3.2 Electrical characterization results

In the last section several measurement methods for nanomechanical resonators based on downmixing techniques have been studied. In this section, we characterize

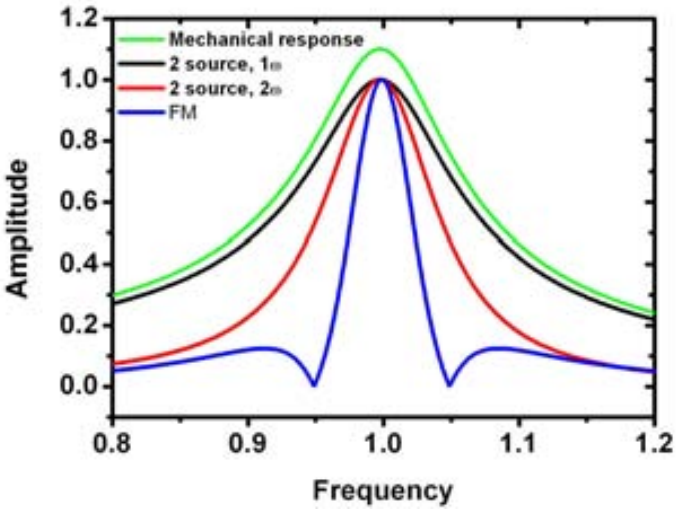

Figure 3.6: Comparison of the frequency response of a resonator and its measurement with different detection methods. The amplitude of the signals is arbitrary, chosen for comparison.

the frequency response of bottom-up silicon nanowires using different measurement methods, in order to compare their efficiency.

3.2.1 Frequency modulation measurement method

The FM detection technique had been previously used to characterize CNT resonators. It has been employed to measure devices with frequencies up to tens of gigahertzs [6], and it has allowed to use CNT resonators as mass sensors with yoctogram resolution [1]. However, to our knowledge, this technique had not been applied to the measurement of silicon nanowires before.

We find that the FM method allows the measurement of bottom-up silicon nanowire resonators with high efficiency. We measure the response of high order resonances (up to the third mode, with frequencies of 360 MHz), which had not been previously measured for this kind of devices. Moreover, we observe mode-splitting due to asymmetries in the cross section for both the fundamental and higher order modes. This effect had been previously observed for Si nanowires using optical methods [7], and had been electrically measured for semiconductor nanowires at low frequency [8, 9], but never at high frequency nor for other than the fundamental mode.

In this thesis, the FM method has been employed to measure a variety of bottom-up nanowires of different dimensions. Figure 3.7 shows the results of the measurement of three different nanowires, with diameters ranging from 52 to 100 nanometers and lengths of 2 to 3 micrometers. The fabrication method allows the side-gate to

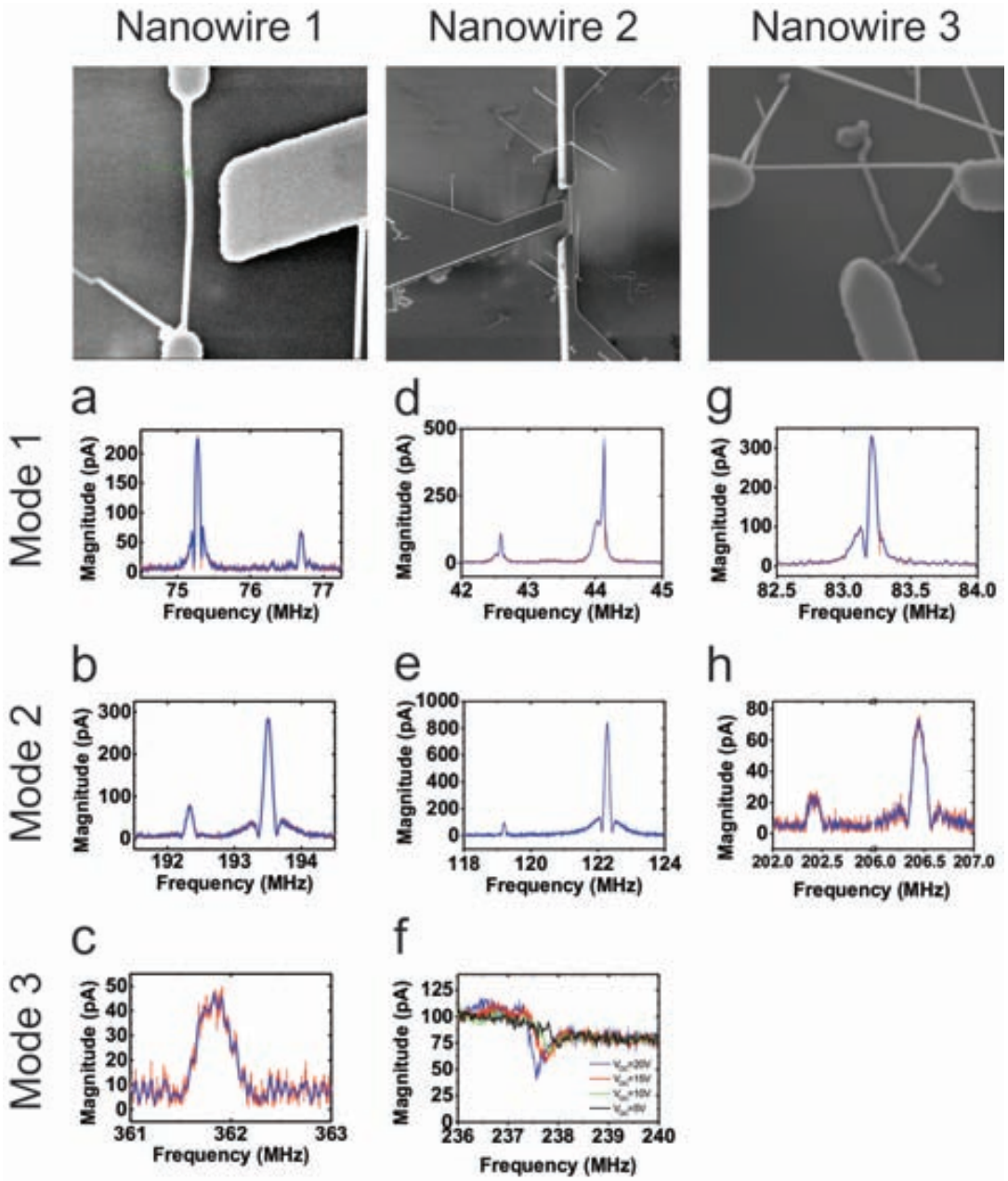

Figure 3.7: Electrical measurement of the frequency response of different SiNWs using the FM detection method. The thin line (ref) represents experimental data, and the thick line (blue) a smoothing for clarity. The first row presents SEM images of the different nanowires.
a-c) Silicon nanowire 100 nm wide and 3 μm long. Side-gate at 380 nm. a)V_{NW}=200 mV, $V_{g,DC}$=5 V. b) V_{NW}=350 mV, $V_{g,DC}$=18 V. c) V_{NW}=1125 mV, $V_{g,DC}$=25 V.
d-f) Silicon nanowire 70-85 nm wide and 3 μm long. Side-gate at 380 nm. d)V_{NW}=140 mV, $V_{g,DC}$=0.5 V. e) V_{NW}=800 mV, $V_{g,DC}$=10 V. f) V_{NW}=800 mV.
g-h) Silicon nanowire 52-64 nm wide and 2.3 μm long. Side-gate at 900 nm. g) V_{NW}=140 mV, $V_{g,DC}$=10 V. h) V_{NW}=140 mV, $V_{g,DC}$=20 V.

be positioned relatively close to the nanowire (less than 400 nanometers), providing good electrostatic coupling and facilitating the electrical actuation of the nanowire. For the first two nanowires (with diameter of 100 and 70-85 nanometers respectively, and a lengths of 3 μm) three different resonance modes are detected, corresponding to different modeshapes. Moreover, for the first two modes, additional resonance peaks are detected: these are caused by orthogonal vibration modes due to the breakage of the radial symmetry of the nanowire arising from small imperfections [7, 8, 9].

Moreover, nanowires of smaller dimensions can also be measured by the FM detection technique: a 52-65 nanometer wide nanowire with a length of 2.3 μm is measured, in this case up to the second mode of resonance (Nanowire 3, Figure 3.7g-h). The length is chosen in order to have resonance frequencies comparable to those of the thicker nanowires. However, due to technological constrictions of the fabrication process (explained in more detail in section 2.3.2) the side gate is located far away from the nanowire, at 900 nanometers, which worsens the electrostatic coupling and therefore the actuation efficiency. This is due to the resolution of the photolithography step, and in our case it is the main hindrance for the measurement of nanowires of small diameters.

Also, as detailed above, a trade-off exists between the amplitude of the detected signal and the apparent quality factor in the case of FM measurements, determined by the frequency deviation f_Δ. In Figure 3.7 this term is optimized for a maximum peak amplitude (and therefore, a maximum signal-to-noise ratio), and under these conditions the width of the resonance peaks is widened. However, by lowering the frequency deviation, we measure in the regime where the measured width of the resonance peak corresponds to that of the mechanical response of the resonator. Under these conditions, we find a quality factor of 3200 for the fundamental mode of Nanowire 1. This quality factor is comparable to those found for other works employing bottom-up nanowires [2, 10], and it is quite high taking into account the size of the resonators and that the measurements are taken at ambient temperature. Such high quality factors probably arise from the crystalline structure of the nanowire and its low number of surface defects [10].

In general, the shape of the measured resonance peak corresponds to the real part of the derivative of the response of the resonator, which is coherent with the analysis of the FM detection method. We confirm this by fitting the experimental response to the theoretical one, as it is shown in Figure 3.8. The fit is performed adjusting the measurement to the shape of the FM response (equation (3.28)), and therefore it does not account for the widening arising from the frequency deviation. Therefore, it does not provide information about the mechanical quality factor. This fit is performed for one of the peaks of the second mode of resonance, because it presents a good signal-to-noise ratio. In this particular response we observe that the agreement

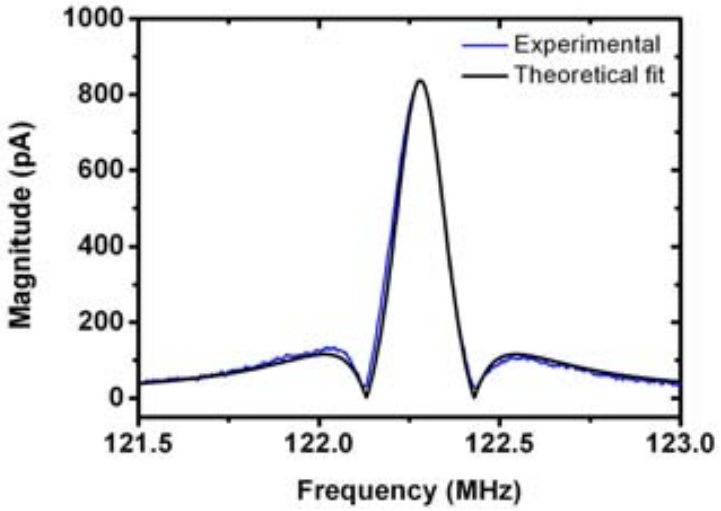

Figure 3.8: Fit of the experimental response of a nanomechanical resonator measured using the FM detection method. The experimental response corresponds to the measurements shown in Figure 3.7e. Resonance frequency f_0=122.28 MHz, Q=400.

between the measured response and the theoretical one is good. Furthermore, we detect a quality factor of 400, which is probably lower than the mechanical one due to the aforementioned widening of the response caused by the detection method.

In some cases however, the measured shape deviates with respect to the predicted one. This is the case, for example, of the fist mode of Nanowire 2 in Figure 3.7, in which one of the peaks presents an abnormal shape: this is caused by non-linearities in the response of the resonator. The detection of nonlinear resonators using the FM detection technique has been previously studied for CNTs [11]. In this case, the observed nonlinearities are probably related to the spring hardening effect, which occurs when the amplitude of motion of the resonator is sufficiently large with respect to its dimensions.

The apparition of nonlinear effects can be studied by observing the evolution of the response of the resonator as a function of the DC gate voltage. The increase of this gate voltage provokes an increase in the excitation force, and therefore, in the amplitude of motion. When this amplitude of motion is sufficiently large the response of the resonator is not a lorentzian any more, and for large DC values hysteresis appears in the response. This effect is shown in Figure 3.9: when increasing the voltage, the frequency of the peak shifts to higher frequencies, as the stiffness of the resonator increases due to the elongation of the wire. The figure shows two frequency sweeps for each DC voltage, from low to high frequency and its inverse. In the major part of the sweeps both responses coincide, but the one at the highest DC voltage (V_{DC}=2 V) presents an hysteresis in the response. Both the upwards shift

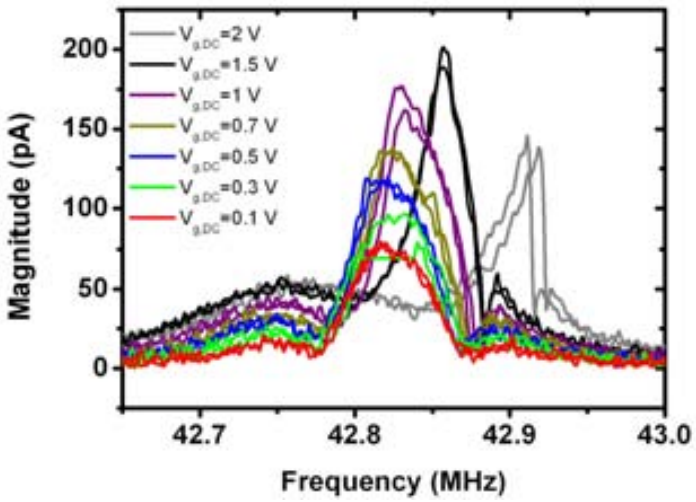

Figure 3.9: Evolution of the frequency response of a nanomechanical resonator detected by the FM method. The resonator has a diameter of 70-85 nm, and a length of 3 μm (it is the same device shown in Figure 3.7d-f). Measurement conditions: V_{NW}=80mV. The figure shows two sweeps for each DC voltage, from low to high frequencies and its inverse. When increasing the DC voltage, the amplitude of motion increases until the nanowire presents a non-linear response.

of the resonance frequency and the hysteresis are signs of a nonlinear mechanical response, possibly arising from the spring hardening effect described in section 1.1.3.

The issue of non-linearities is especially important for resonators of small dimensions [12]. In these devices, the transduction signals are typically small, while the noise background of the system does not necessarily get smaller. For this reason, it is not unusual to be forced to operate the resonator in a nonlinear mode (with a high amplitude of motion, which provides a higher transduction signal) in order to be able to detect its motion. Even in resonators in which the signal is clearly detectable in linear regime, operating the resonator with high amplitudes of motion, in order to obtain transduced electrical signals of higher amplitude, is desirable for many applications. For these reasons, the study on non-linearities in resonators is becoming a topic of interest in the field of nanomechanical resonators [11, 13, 14].

3.2.2 Two-source measurement methods

The two-source measurement method has been previously used to characterize the frequency response of nanowires and nanotube resonators. In the particular case of silicon nanowires, they have been reported to present high piezoresistive factors, providing a self-transducing method efficient at high frequencies. These devices have been measured using the two-source, 2 method, which has allowed the electrical

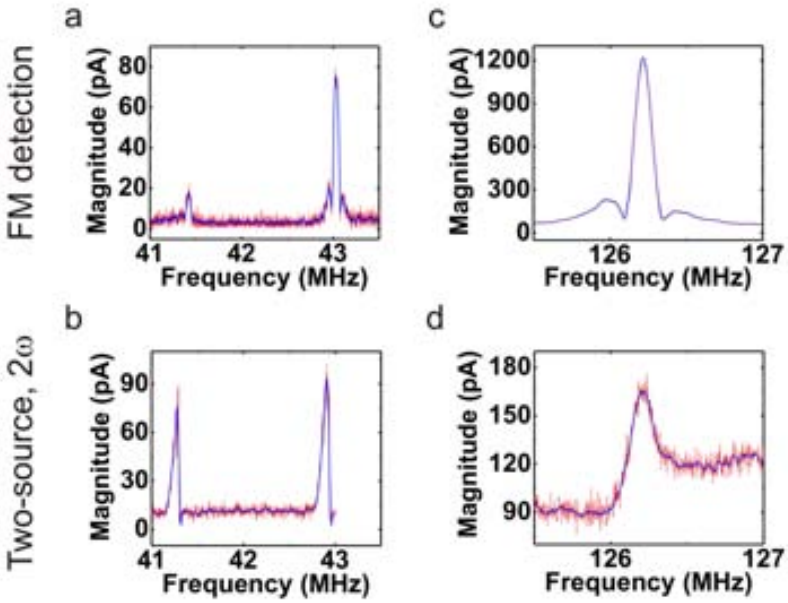

Figure 3.10: Measurement of the frequency response of a single nanowire 75 nm wide and 3μm long, using different detection techniques. The mode-splitting phenomena can be observed by both methods. The thin line represents experimental data, and the thick line a smoothing for clarity. a) FM detection technique, fundamental mode. V_{NW}=100 mV, $V_{g,DC}$=100 mV. b) Two-source, 2ω detection technique, fundamental mode. V_{NW}=200 mV, $V_{g,AC}$=280 mV, $V_{g,DC}$=500 mV. c) FM detection technique, second mode. V_{NW}=1.1 V, $V_{g,DC}$=8 V. d) Two-source, 2ω detection technique, second mode. V_{NW}=500 mV, $V_{g,AC}$=1.1V, $V_{g,DC}$=10 V.

measurement of nanowires with diameters of 30 nanometers at room temperature [2]. These nanowires are very similar to our devices both in material properties and geometry. It is interesting to measure our resonators using the two-source, 2 method, and afterwards compare the obtained results with the FM detection.

Figure 3.10 shows the frequency response of the same nanowire obtained by the FM (top) and by the two-source, 2 (bottom) methods. The measurements are performed for Nanowire 2 (Figure 3.7d-f), which has a diameter of approximately 75 nanometers and a length of 3μm. For the fundamental mode (Figure 3.10a-b) we obtain similar signal levels using both methods, but the actuation conditions–and hence the amplitude of motion–are much lower for FM detection. The FM method allows a linear measurement of the response of the fundamental mode, whereas with the two-source, 2 method the high amplitude needed for the measurement causes the resonator to behave nonlinearly. Remarkably, for the second resonance mode a very large output signal level is obtained by means of the FM detection scheme (Figure 3.10c-d), whereas the signal obtained using the two-source, 2 method is

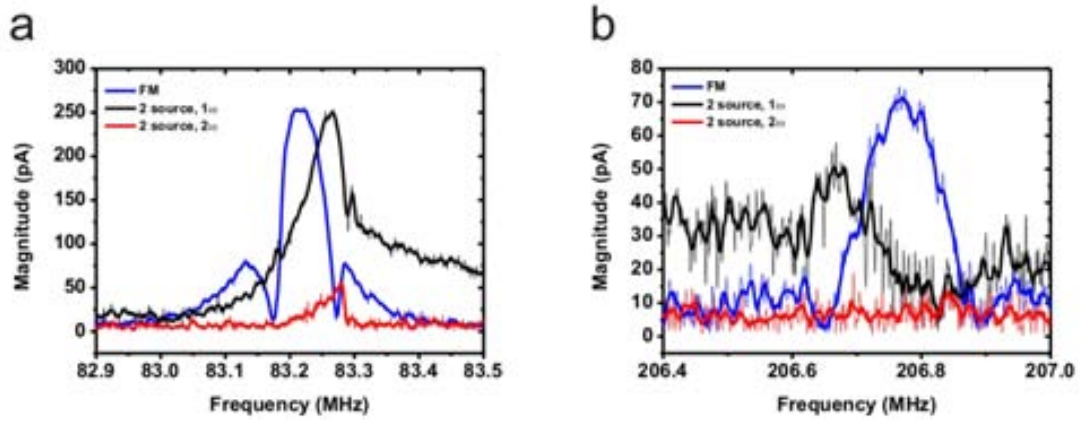

Figure 3.11: Measurement of the frequency response of a single nanowire 52-65 nanometers wide and 2.3 μm long, using different detection techniques. a) Fundamental mode. FM conditions: $V_{NW,FM}$=140 mV, $V_{g,DC}$=7 V. Two-source conditions: $V_{NW,2s}$=36 mV, $V_{g,DC}$=7 V, $V_{g,AC,2s}$=140 mV. b) FM conditions: $V_{NW,FM}$=140 mV, $V_{g,DC}$=22 V. Two-source conditions: $V_{NW,2s}$=80 mV, $V_{g,DC}$=22 V, $V_{g,AC,2s}$=140 mV.

much weaker even with higher excitation conditions. These results point out to a greater efficiency of the FM method for the measurement of silicon nanowires, specially for lower modes of resonance.

Additionally, the two-source, 1 detection method has been used to measure semiconductor nanowires of several materials [8, 9] and semiconductor nanotubes [4]. This detection technique is usually employed for devices in which the transduction mechanism is the conductivity modulation caused by induced charge in the resonator.

Figure 3.11 shows the results of the characterization of the frequency response of Nanowire 3 using the three different detection methods, for the first and second resonance modes. The excitation conditions ($V_{AC} + V_{DC}$) are the same for the three detection methods, so the motion of the resonator can be considered to have a similar amplitude for all of them. We observe that the signal amplitude is similar for the FM and the two-source, 1 detection techniques for both modes, and weaker for the two-source, 2 method, pointing out at the lower efficiency of this later method. Moreover, a parasitic signal of electrical origin is observed for the two-source, 1 detection technique.

3.3 Study of the transduction mechanisms

In the previous section the efficiency of the different detection methods in the measurement of bottom-up SiNWs has been studied. It has been observed that the FM and two-source, 1 methods are more efficient. To discern the origin of these differ-

Detection method	Transduction mechanism	
	linear	quadratic
Frequency modulation	good	null
Two-source, 1	good	weak
Two-source, 2	null	good

Table 3.1: Efficiency of the studied detection methods for the measurement of the signals originated by different transduction mechanisms.

ences, in this section a study of these detection methods is performed, by building and simulating an electromechanical model of the system. Afterwards, additional measurements are performed based on the information obtained by this model.

3.3.1 Simulation of the detection methods

In the last section, we have successfully applied different downmixing detection methods to the measurement of the same device in order to compare their efficiency. These downmixing methods had been previously applied to devices which present different transduction mechanisms. More concretely, the FM and two-source, 1 detection methods had been used to measure devices based on the conductivity modulation caused by induced charge, while the two-source, 2 method had been used to measure piezoresistive nanowires. From the transduction point of view, the most important difference between these two mechanisms is the frequency of the transduced signal in relation to the oscillation frequency of the resonator. When the conductance change is proportional to the motion of the resonator (such as in the case of conductance modulation, as seen in equation (1.65)) the transduced signal has the same frequency as the oscillation frequency of the resonator. We classify this transduction as linear transduction. On the other hand, when the conductance change is proportional to the square of the motion of the resonator (such as in the case of piezoresistive transduction (1.59)) the transduction signal has twice the oscillation frequency of the resonator: we classify this transduction as quadratic transduction. This classification is shown in Table 3.1.

Without getting into the physical origin, it is interesting to evaluate the effectiveness of the different detection methods for the two families of transduction mechanisms. With this objective, we have built an electromechanical model of the resonator and the actuation/detection setup using commercial software (MathWorks® Matlab [15] and Simulink R2007A [16]). This model is adapted for the three different detection methods, and for the two transduction mechanisms.

An example of the model is shown in Figure 3.12a, for the FM detection of a 1 transduction mechanism (and therefore, corresponding to the detection method

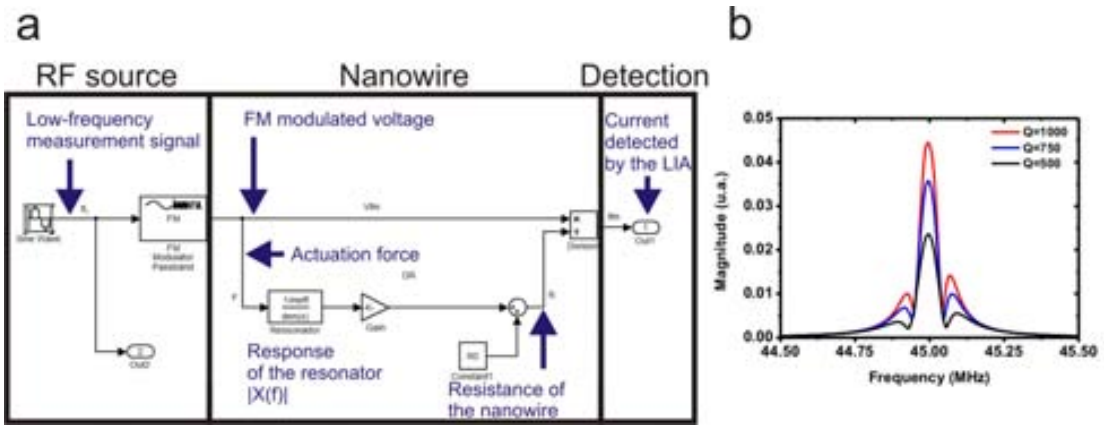

Figure 3.12: Simulation of the system comprising the resonator and the actuation/detection setup. a) Simulation schematic of the FM transduction method for a 1ω transduction, implemented using MathWorks Simulink. The model includes the electromechanical element, as well as the actuation and detection setup. The lock-in amplifier is not included in this model, and its behaviour is simulated afterwards using Mathworks Matlab [15]. b) Simulation of the detection of the response of a resonator using the FM setup, for different values of the quality factor Q.

shown in Figure 3.3). The schematic includes the actuation/detection setup and the response of the resonator, which is defined as a linear transference function based on the frequency response of the resonator (equation (1.29)). The software generates the low frequency measurement signal, modulates it and applies it to the resonator, modelled with its frequency response $X(\ )$ and a gain which represents the transduction efficiency. The resulting signal, which corresponds to the resistance change, is added to the resistance at rest. Afterwards, the voltage applied to the resonator is divided by the total resistance to obtain the current through the device. This current is the parameter which is then detected using the lock-in amplifier during the experiments. To simulate the lock-in amplifier, a Fourier transformation of the current is then performed, and the component at the readout frequency $_L$ is monitored.

Using this model, and varying the FM carrier frequency , a frequency sweep can be simulated. Figure 3.12b shows the result of one of such sweeps. It is obtained by detecting the amplitude of the output signal at the measurement frequency ($_L$) for each value of excitation frequency . The resulting shape corresponds to the FM detection of the mechanical response of the resonator, as described by equation (3.29). Moreover, during these series of sweeps the mechanical quality factor has been changed, and a widening of the response and a decrease in the peak is observed, as expected. These simulations are coherent with the behaviour observed during the experimental measurements and with the theoretical equations.

This model is also applied to evaluate the efficiency of the different detection methods for different transduction mechanisms. Therefore, the transduction ef-

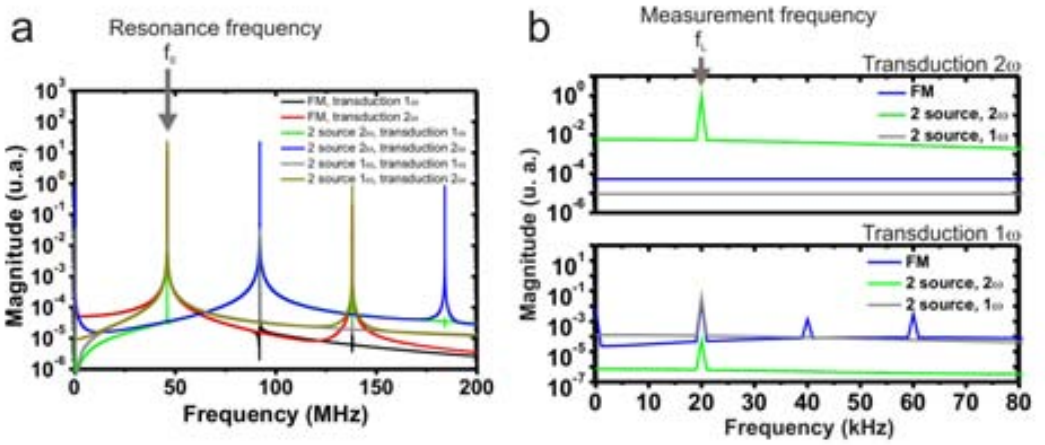

Figure 3.13: Simulation of the frequency spectrum of the current at the output of the nanowire in resonance, using different readout techniques and transduction principles: resonance frequency f_0=46 MHz; lock-in measurement frequency f_L=20 kHz. a) Wide frequency spectrum. b) Low frequency detail for the 2ω transduction mechanism (top) and for the 1ω transduction mechanism (bottom).

ficiency is analysed for each combination of detection method and transduction mechanism. In this case, instead of taking a full spectrum of the response as in the case of Figure 3.12b only one excitation frequency is used, corresponding to the resonance frequency of the resonator. Under these conditions, the motion of the resonator (and therefore, the resulting transduction signal) are highest, allowing to study the maximum obtainable transduction signal for each detection method. Then, a Fourier transformation of the output current is performed, in order to study the frequency components of the measurement signal for this single excitation frequency. The obtained frequency spectra are shown in Figure 3.13a for each of the different combinations of detection mechanism and transduction method. More importantly, a detail of this spectrum for low frequencies is shown in Figure 3.13b. The peaks at 20 kHz represent the detected transduction signal, and its amplitude relative to the rest of detection methods. Therefore, the efficiency of each detection setup for the 2 (3.13b, top) and 1 (3.13b, bottom) transductions can be evaluated.

From these simulations we confirm that a pure 2 transduction produces a detectable signal using the two-source, 2 detection. Moreover, a 1 transduction produces a detectable signal using the FM and two-source, 1 detection of comparable amplitude. More importantly, we observe that a pure 2 transduction does not provide a detectable signal using FM detection. Alternatively, if the transduction is entirely at 1 , the resulting output signal using the two-source, 2 method happens to be extremely small. From the simulations shown in Figure 3.13b, we have evaluated that for the same amplitude of motion of the nanowire and considering the experimental detection conditions, the measured signal would be approximately

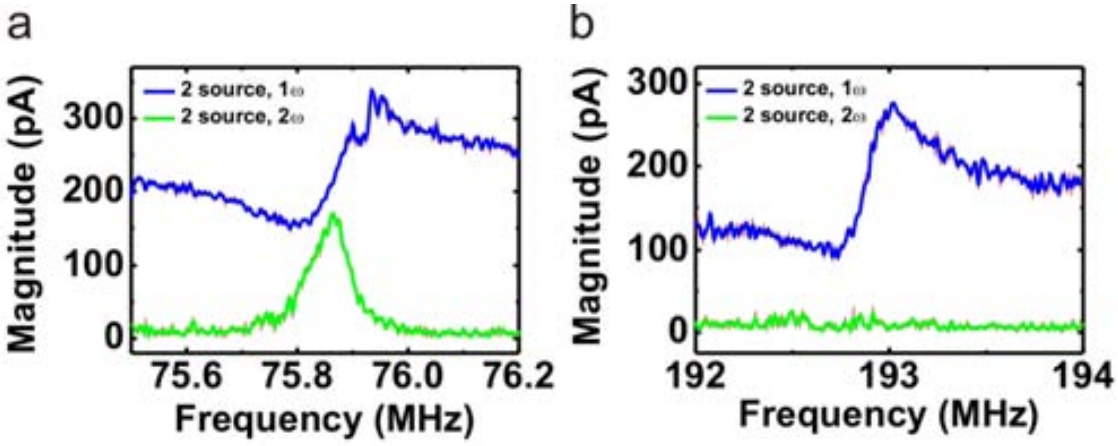

Figure 3.14: Comparison of the frequency response of a single nanowire 100 nm wide and 3 μm long using the two-source, 1ω and 2ω techniques for the same excitation conditions. The thin line represents experimental data, and the thick line a smoothing for clarity. a) Fundamental mode. V_{NW}=100 mV, $V_{g,AC}$=350 mV, $V_{g,DC}$=5 V. b) Second mode of resonance. V_{NW}=100 mV, $V_{g,AC}$=350 mV, $V_{g,DC}$=18 V.

400 times lower for the two-source, 2 than for the FM method in the case of pure 1 transduction. These conclusions are summarized in Table 3.1.

3.3.2 Comparison of 1 and 2 detection methods

During the experimental comparison of different detection methods we have observed that there are differences between the efficiency of each detection method, specially at higher resonance modes. Furthermore, the simulation of these detection methods has given us evidence that they are efficient for different transduction mechanisms. For this reason, the comparison between the different detection methods provides a good tool to discern the origin of the transduction mechanisms for bottom-up silicon nanowires.

The FM detection method provides excellent SNRs and allows the characterization of high order resonance modes occurring at high frequency. However, the correlation of the frequency response detected using this method and the mechanical response of the resonator is not straightforward. Therefore, this method is effective to detect and track the resonance frequency of the device, but it is complex to study the mechanical response of the resonator based on the information it provides. On the other hand, the two-source techniques do not provide such high SNRs, but present an easier understanding to correlate the electrical response with the mechanical response of the resonator.

Figure 3.14 shows a comparison of the measurement of the response of a nanowire using the two source detection methods. For the fundamental mode of resonance

(Figure 3.14a) we find that the signals have comparable amplitudes. In accordance to what has been discussed above, this a signature that transduction at 1 and 2 must co-exist: simulations reveal that the expected signal for the two-source, 2 method should be 30 times lower if a 1 transduction mechanism was the only existing mechanism. Remarkably, the frequency spectrum corresponding to the second resonance mode (Figure 3.14b) presents important differences: while it is readily detected using the two-source, 1 method, it is below the noise level for the two-source, 2 (by increasing the actuation signal, the second mode can also be detected, as it is shown in Figure 3.10). It points out to a greater efficiency of the 1 transduction mechanism at higher resonant modes.

In order to obtain more information of the behaviour of the different transduction mechanisms, we study the evolution of the detected response with a variation of the DC gate voltage for different detection methods. The evolution of the amplitude of motion with respect to the actuation voltage has been studied in section 1.2.1. For an oscillation amplitude of the resonator much smaller than the gap, and a DC voltage much higher than the AC voltage, the electrostatic actuation force is proportional to the DC voltage, and therefore the amplitude of motion of the resonator is proportional to the DC voltage too. However, if the amplitude of motion is too large, higher order effects appear and this relation no longer holds. According to the calculation of the electrostatic force in our case, the amplitude of motion of the resonator should be small compared to the gap. However, without having direct evidence of this amplitude we can't be sure that these approximations are correct.

Figure 3.15 shows the DC dependence of the response of the same resonator using the two-source, 1 (3.15a-c) and 2 (3.15d-f) detection methods. The AC actuation voltage is the same in both cases, as well as the amplitude of the voltage passing through the nanowire. First of all, we observe that, for low amplitudes of motion, the two-source, 1 detection method provides a better signal to noise ratio. More interestingly, by observing Figure 3.15c we find that the maximum amplitude of the resonance peak using this detection method scales linearly with the DC gate voltage, and moreover it is symmetrical with the DC actuation voltage. This symmetric behaviour is expected, because the actuation force depends on the square of the actuation voltage. On the other hand, in the case of the two-source, 2 detection method, the peak amplitude depends quadratically with the DC voltage (Figure 3.15f). This is in concordance with the different origins of the transduction mechanism: in the case of the two-source, 1 the transduction signal is proportional to the amplitude of motion of the nanowire (1 transduction), and in the case of the two-source, 2 it is quadratic with the oscillation amplitude (2 transduction).

Additionally, the shape of the frequency response can be fitted to the theoretical equations of each transduction mechanism. By comparing the frequency response of a resonator using the same excitation conditions and measuring it with the two

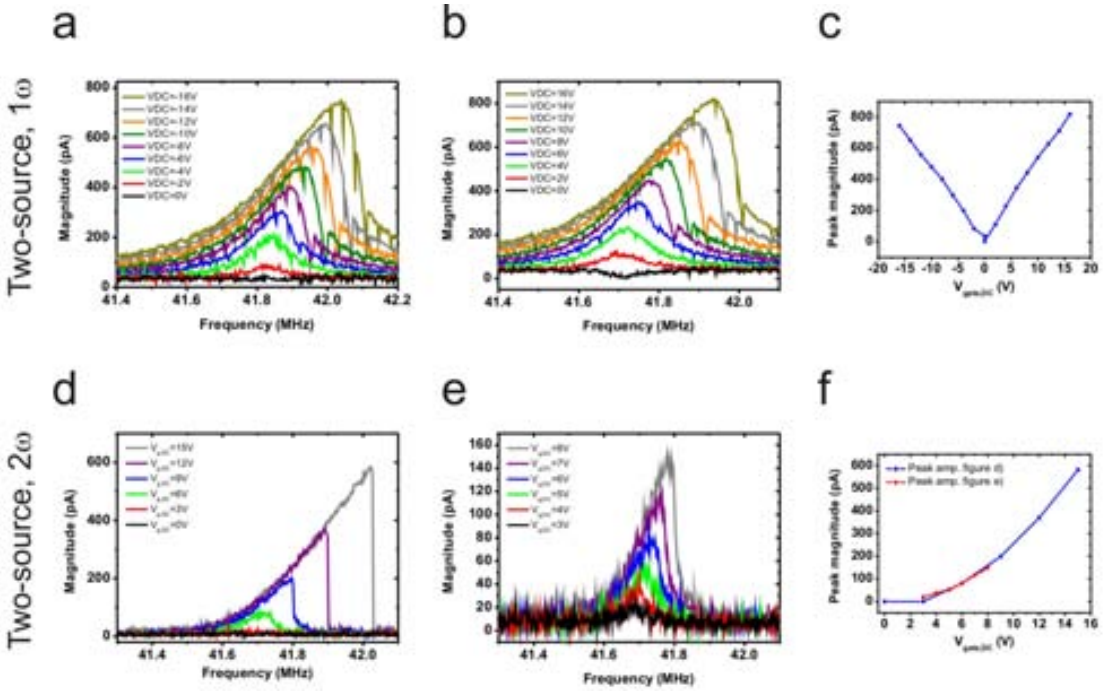

Figure 3.15: Evolution of the frequency response of a nanomechanical resonator detected by different two-source methods. The nanowire has a diameter of 80 nanometers and length of 3 μm. The side-gate is located at 700 nanometers. Measurement conditions: V_{NW}=36 mV, $V_{g,AC}$=140 mV. a-c) Dependency of the frequency response to a variation in the DC gate voltage using the two-source, 1ω detection technique, for positive (a) and negative (b) DC values. c) Maximum magnitude of the resonance peak as a function of the DC gate voltage. d-f) Dependency of the frequency response to a variation in the DC gate voltage using the two-source, 2ω detection technique, for positive DC values. e) Shows a detail for low DC voltages. f) Maximum magnitude of the resonance peak as a function of the DC gate voltage.

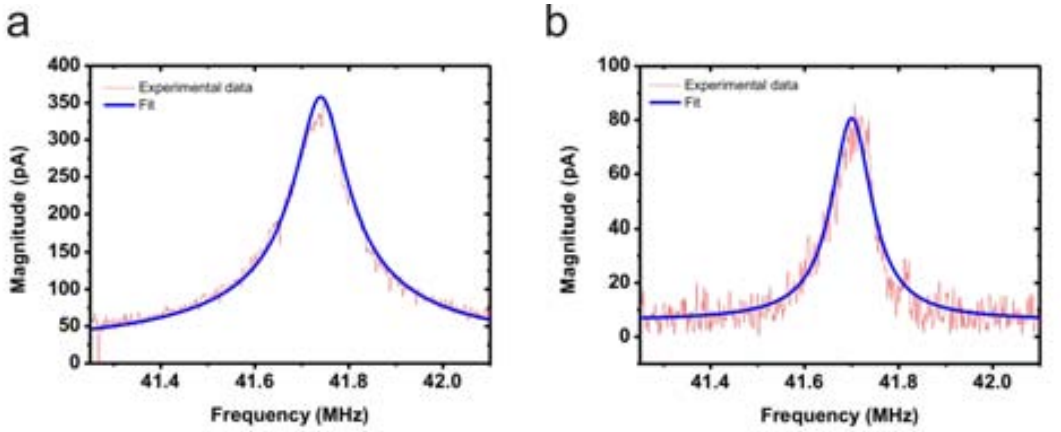

Figure 3.16: Fitting of the frequency response of a nanomechanical resonator detected by the different two-source methods. The nanowire has a diameter of 80 nanometers and length of 3 μm. The side-gate is located at at 400 nanometers. Measurement conditions: V_{NW}=36 mV, $V_{g,AC}$=140 mV, $V_{g,DC}$=6 V. a) Two,source, 1ω detection method. The experimental results are fitted to a function proportional to the mechanical response of the resonator, as corresponds to 1ω transduction. Fitting conditions: f_0=41.74 MHz, Q=400. a) Two,source, 2ω detection method. The experimental results are fitted to a function proportional to the square of the mechanical response of the resonator, as corresponds to 2ω transduction.Fitting conditions: f_0=41.7 MHz, Q=400.

different methods, we can observe if the results are consistent with 1 and 2 transduction. This comparison is shown in Figure 3.16, where the fittings are performed for two of the responses obtained in Figure 3.15. A good fitting is obtained using the same mechanical parameters (f_0=41.7 MHz, Q=400) and varying the shape of the adjusted response: for the case of two-source, 1 the measurement results fit well to a lorentzian proportional to the mechanical response of the resonator, whereas for the two-source, 2 the adjusted function is proportional to the square of the mechanical response (equations (3.8) and (3.17) respectively). This is also consistent with the different origin of the transduction signals, caused by 1 and 2 transduction mechanisms.

3.3.3 Discussion of the origin of the transduction signal

We have observed that there is experimental evidence that the different detection methods detect transduction signals of different origins. In this section the origins of these 1 and 2 transduction mechanisms are discussed.

The transduction originating the two-source, 2 detection is coherent with the 2 piezoresistive mechanism, originated by the elongation of the nanowire during the oscillation [2]. We can make an estimation of the gauge factor by estimating the oscillation amplitude of the nanowire from the electrostatic coupling with the side

gate. Then, from the peak current detected by the lock-in amplifier and equation (3.17), we obtain gauge factors in the order of 200 in the case of Figure 3.14. This gauge factor is consistent with to the dimensions and doping of the silicon nanowires [17].

We discuss now the possibilities for the transduction mechanism responsible for obtaining measurable signals for the FM and two-source, 1 detection schemes. One possibility is that the SiNW conductance change is due to the change of the gate-induced charge along the nanowire. Assuming this transduction principle, and using the two-source 1 detection technique, the magnitude of the signal detected by the lock-in amplifier has been previously studied. It can be described as the sum of two components, described in equation (3.10), which is reproduced here for clarity:

$$I_{NW,\omega_L} = \frac{1}{2}\frac{G}{\overline{2}}\frac{}{V_g}\left(V_{g,AC} + V_{g,DC}\frac{C_g}{C_g}\right)V_{NW} \tag{3.30}$$

As it is explained above, the first component corresponds to a purely electrical parasitic signal, from which the transconductance of the nanowires can be extracted, while the second is caused by the motion of the nanowire. We can apply this equation to Nanowire 1, which has a diameter of 80 nanometers, a length of 3 μm and a side-gate separated from the nanowire by 700 nanometers. From Figure 3.14 we can obtain the value of the transconductance from the signal level at a frequency far away from the resonance, in which the main contribution is the parasitic current. The obtained transconductance value is 16 nS/V, which is consistent with the high doping levels of the SiNWs.

In order to validate the transconductance value, this parameter can also be found in static mode by monitoring the resistance while varying the value of the gate voltage. We find that the change of resistance provoked by the charge induced by the gate voltage is small compared with the total resistance value. Moreover, a drift of the resistance is observed during the measurements, which further hinders the detection of the conductance change originated by the gate voltage. For these reasons, the transconductance in static is difficult to detect using a semiconductor analyser or similar methods. Therefore, we perform semi-static measurements, using the lock-in amplifier to monitor the resistance value of the nanowire when applying a voltage at 34 Hz. Using this method, and varying the gate voltage from -25 to 25 V, a transconductance value of 7-9 nS/V is obtained, in the same order of magnitude of that obtained with dynamic measurements.

By knowing the value of the transconductance and the amplitude of the resonance peak in the experimental response, we obtain the variation in capacitance of the resonator and the side-gate due to the motion of the resonator, C_g C_g, which is around 5 % in this case (Figure 3.14). In order to obtain the amplitude of motion from this parameter, a model of the capacitance change with respect to the distance between the nanowire and the side-gate is needed. Several models can be used, as

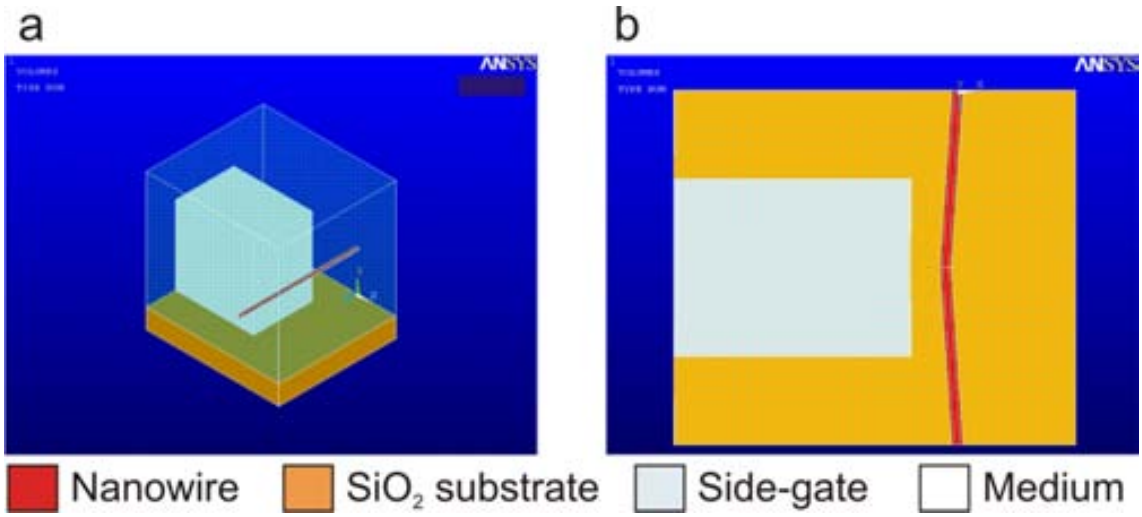

Figure 3.17: Ansys model of a nanowire near a side-gate for electrical actuation, based on the geometry of a real device as studied by scanning electron microscopy. The model is used to study the capacitance between the resonator and the side-gate. The nanowire is shown coloured in red, the side-gate in gray, and the SiO_2 substrate in orange. a) General view of the model for a nanowire at rest. b) Top view of a model representing a nanowire deflected towards the side-gate.

explained in section 1.2.1. By using two different models to calculate the capacitance between the nanowire and the side gate (a parallel plate capacitor and a wire parallel to an infinite plane), we estimate that the capacitance at rest has a value of 29 aF in the case of the wire-parallel plane model, and the motion necessary to cause the observed response should be around 50 nm.

Additionally, we use the Ansys software [18] to simulate this capacitance with Finite Element Modelling (FEM) simulations. We inspect the device with SEM, and then construct a geometry as similar as possible to the experimental one (Figure 3.17a). This geometry includes the nanowire, the side-gate, the substrate and a medium surrounding the elements. The capacitance simulations are performed using the CMATRIX command, which extracts the capacitance between two conductors of the model. The capacitance between the nanowire and the side-gate is simulated in this manner, yielding a value of 50 aF for the nanowire at rest. We observe that this value in not too far away from the one obtained with the wire-plane model. In order to estimate the capacitance of the nanowire during its motion, another model is built where the nanowire is deflected with respect to the side-gate (Figure 3.17b), and we extract its capacitance in this case. From these simulations we also find that an amplitude of motion higher than 50 nanometers is needed to justify the observed experimental response, similarly to the theoretical models.

As the diameter of the nanowire is 100 nm, such amplitude of motion is not possible without the nanowire showing a highly nonlinear response, which is not ob-

served during the measurements. Moreover, the studied case is quite conservative, and shows a strong background current which allows to extract the transconductance. In the case of Figure 3.15, for example, the background current is very low and the side-gate is located farther away from the nanowire, so a higher amplitude of motion would be necessary to justify the observed peak with this method. However, as the phenomenon of non-linearities is difficult to characterize, it is necessary to obtain a better estimation of the motion of the nanowire in order to evaluate the feasibility of this transduction mechanism.

Another candidate for the transduction at 1 is the static deflection of the nanowire caused by the DC voltage. This static deflection provokes an asymmetry in the motion of the nanowire, causing the piezoresistive signal to have an additional component at the excitation frequency, and therefore providing a transduction term at 1 . We have analysed this possibility by comparing the static deflection of the nanowire with the expected amplitude of motion x at resonance. As a first approximation we suppose that the response of the resonator can be described by the mass-spring model, and that the DC voltage applied to the gate is much larger than the AC component. In this case, the electrostatic actuation force takes the form described in section 1.2.1. In the case of static deflection, where only a DC component exists, the motion of the nanowire can be extracted from the electrostatic force by the spring constant:

$$F_{NW,DC} = -\frac{1}{2}\frac{C}{x}V_{g,DC}^2 = -kx \tag{3.31}$$

$$x_{NW,static} = \frac{C}{x}\frac{V_{g,DC}^2}{2k} \tag{3.32}$$

The same method can be applied to extract the dynamic amplitude of motion. In this case, the maximum amplitude of motion is extracted from the force using the value of the frequency response of the resonator at the resonance frequency.

$$F_{NW,AC} \approx \frac{C}{x}V_{g,AC}V_{g,DC} \tag{3.33}$$

$$x_{NW,resonance} = \frac{F_{NW,AC}Q}{k} \tag{3.34}$$

Therefore, the relationship between both amplitudes is:

$$\frac{x_{NW,resonance}}{x_{NW,static}} = \frac{2QV_{g,AC}}{V_{g,DC}} \tag{3.35}$$

Under typical actuation conditions, this relationship is in the range of 50-150 (for example, in the case of Figure 3.7a, $x_{NW,resonance}$ $x_{NW,static} = 80$), which means

that the asymmetry caused by the static deflection in resonance is negligible for the fundamental resonance mode.

In conclusion, our measurements indicate the co-existence of two different transduction mechanisms in the studied nanowires. More concretely, a linear (1) and a quadratic (2) mechanisms co-exist. While the quadratic transduction mechanism is consistent with piezoresistive transduction, previously reported for nanowires similar to the ones studied here, we have not fully resolved the origin of the linear transduction mechanism. In part, this is due to the lack of information of both the transduction method and the amplitude of motion of the nanowires at resonance. For this reason, more information regarding the amplitude of motion of the studied devices is needed for a complete study of the origin of the linear transduction mechanism.

3.4 FEM simulations of the mechanical frequency response of SiNW resonators

Finite element modelling (FEM) simulations have been performed using the Ansys software in order to study the theoretical resonance frequencies and the shapes of the resonance modes, and compare them with the experimental measurement results. The characterization of the SiNWs has allowed us to obtain information of the resonance frequency of several modes of resonance, which in turn can provide some hints about parameters such as the internal stress of the structure.

In this section, simulations of bottom-up resonators based on finite element modelling are presented. Based on these simulations, the influence of the geometry and stress on the resonance frequency of the nanowires is analysed, and a comparison with the experimental measurements allows to extract conclusions about the geometry and internal stress of the measured resonators.

A modal analysis provides the different frequencies and shapes of the resonance modes of a resonator from its geometry, material and clamping conditions. Each of the measured devices (shown in Figure 3.7) is modelled and simulated using this method. An example of these simulations is shown in Figure 3.18: in this case, the resonator is an hexagonal prism, with a length and diameter similar to the fabricated devices (a diameter of 90 nanometers and a length of 3 micrometers). It is important to note that, if the hexagonal prism is regular, the resonance frequency is the same for all of its radial directions (there is no appearance of orthogonal modes with different frequencies). In Figure 3.18 we observe the shape of the first three modes of the resonators, that corresponds to the modeshape $w(x)$ presented in chapter 1.

During the experimental measurements we have been able to detect multiple resonance frequencies of the studied resonators, which provide additional information

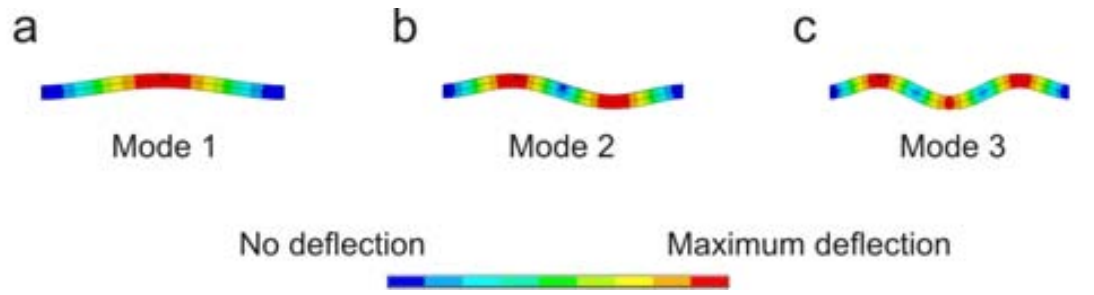

Figure 3.18: Shape of the resonance modes of an hexagonal silicon nanowire cc-beam. The first three modes are shown, from left to right. The amplitude of the motion is arbitrary. For these simulations, the diameter of the nanowire is 90 nanometers and its length is 3 micrometers

	Nanowire 1	Nanowire 2	Nanowire 3
Length (μm)	3	3.3	2.3
Diameter (nm)	100	70-85	52-65
f1 - simulated (MHZ)	88,7	49,3	88,4
f1 - experimental (MHZ)	72,3	43	83,5
f1 - diference	-22,88%	-14,75%	-5,85%
f2 - simulated (MHZ)	243,0	135,7	242,7
f2 - experimental (MHZ)	210,0	122,0	206,5
f2 - diference	-15,73%	-10,12%	-17,52%
f3 - simulated (MHZ)	472,3	265,6	473,5
f3 - experimental (MHZ)	413	238	-
f1 - diference	-14,35%	-11,58%	-

Table 3.2: Comparison between the experimental measurements and the simulated nanowires with the same dimensions, for multiple modes and three different nanowires.

about the dimensions and internal stress in the resonator. In this sense it is interesting to simulate the resonance frequency of the measured nanowires, based on the geometry obtained by SEM images. The resonance frequency of the devices shown in Figure 3.7 has been simulated and the results are shown in Table 3.2. There are important differences between the experimental and predicted frequencies, specially for the first mode of resonance. There are several factors that can account for this difference: inaccuracy in the dimensions of the nanowires (which are determined from SEM inspection), the appearance of stress during the fabrication process or defects in the structure of the nanowires.

From the results in Table 3.2, we observe that the experimental values are always lower than the theoretical ones. It is possible that this effect is caused by compressive stress accumulated during the fabrication process, due to the nanowire growing

longer than the trench where it is confined.

3.4.1 Simulation of the stress and buckling

One of the parameters which has an important effect in the resonance frequency of cc-beams is the stress accumulated in the structure. Contrary to other geometries, such as the cantilevers, in general cc-beams accumulate stress which is difficult to release because both edges are confined by side-walls. During the inspection of the fabricated devices we have observed some nanowires which present buckling, so we know that the fabrication process can induce some stress in the structure.

The effect of the stress can be introduced into modal FEM simulations. In order to evaluate the influence of this parameter in the resonance frequency of the resonators, modal simulations of a nanowire with different values of stress are performed. The simulated nanowire has a diameter of 90 nanometers and a length of 3 μm. In these simulations, the stress is on the longitudinal direction with respect to the nanowire, similar to that obtained when compressing or stretching it from its clamped edges. As both of these ends are fixed, the geometry of the wire is exactly the same for all the simulations, but the stress accumulated in the structure affects the mechanical characteristics of the resonator. By convention, a compressive stress is defined as negative, while a tensile stress is defined as positive. Figure 3.19 shows the effect of the stress in the resonance frequency of the resonator. More concretely, Figure 3.19a shows the influence of the stress on the absolute value of the resonance frequency, while Figure 3.19b, represents the deviation of the resonance frequency under stress f_d from the resonance frequency without stress f_0. We observe that compressive stress reduces the resonance frequency, while tensile stress increases it. For example, a compressive stress of 500 MPa introduces a reduction of around 30 % in the resonance frequency of the first mode (in absolute terms, a reduction from 69 to 48 MHz in this particular case).

A different geometric defect observed in the fabricated bottom-up silicon nanowires is the difference in diameter between its ends (tapering). In our case, this defect is present in the major part of the fabricated devices, and it is caused by effects particular to the fabrication method, as discussed in section 2.3.2.1. It is important to quantify the influence of this effect in the resonance frequency of the different modes. FEM simulations have been performed for different tapering values, where a conification of around 10 % of the diameter was observed. The results of these simulation are presented in Table 3.3. We observe that this difference in diameter does not have an important effect on the resonance frequencies of the resonator.

Another of the effects of the stress on cc-beams is the buckling of the structure, which has indeed been observed for fabricated devices. This buckling causes a displacement of the centre of the nanowire at rest. If this effect is important enough,

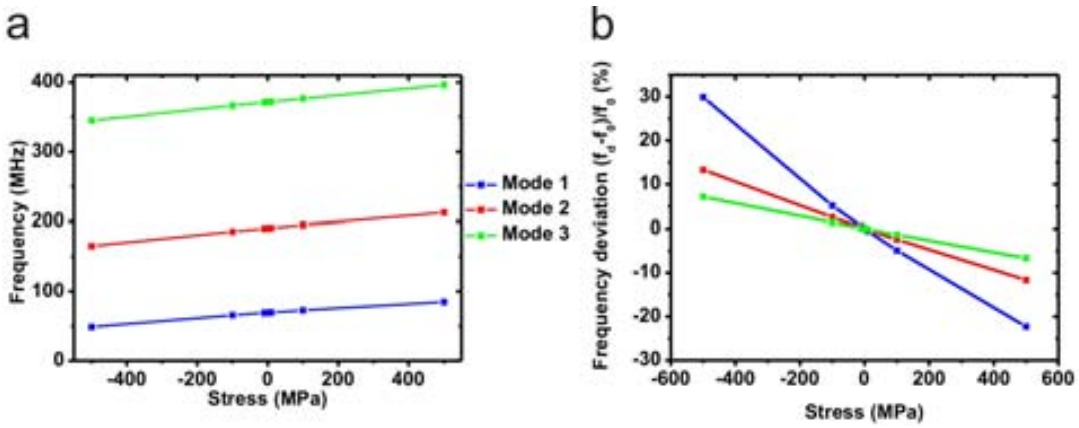

Figure 3.19: Effect of the stress in the resonance frequency of the first 3 modes of an hexagonal cc-beam resonator, for the particular case of a nanowire with a diameter of 90 nm and a length of length=3 μm. a) Results of the modal simulation of the resonator for different values of axial stress. b)Deviation of the resonance frequency of the resonator under stress f_d with respect to the resonance frequency of the unstressed resonator f_0.

	Frequency (MHz)		
Diameter	Mode 1	Mode 2	Mode 3
90 nm	69.35	190.49	371.73
88-92 nm	69.34	190.43	371.64
85-95 nm	69.31	190.28	371.29

Table 3.3: Simulation of the effect of tapering on the resonance frequencies of a cc-beam resonator. Length of 3 μm.

it can cause a modification of the mechanical response of the nanowire and explain the 1 transduction signal. However, the analysis of a buckled beam is not straightforward: when the beam buckles it releases accumulated stress, and the deformed structure and its internal stresses both modify the resonance frequency.

3.4.2 Fitting of the experimental results with FEM simulations

The effect of the stress on the resonance frequency of the measured nanowires can be evaluated, in order to try to find a stress that justifies the discrepancy between the experimental and simulated values. For these simulations we try to fit the experimental frequencies found for Nanowire 1 in Figure 3.7. Figure 3.20 shows the results of the simulations for different values of stress and three different diameters (100, 95 and 90 nanometers). We find that the values which are in better concor-

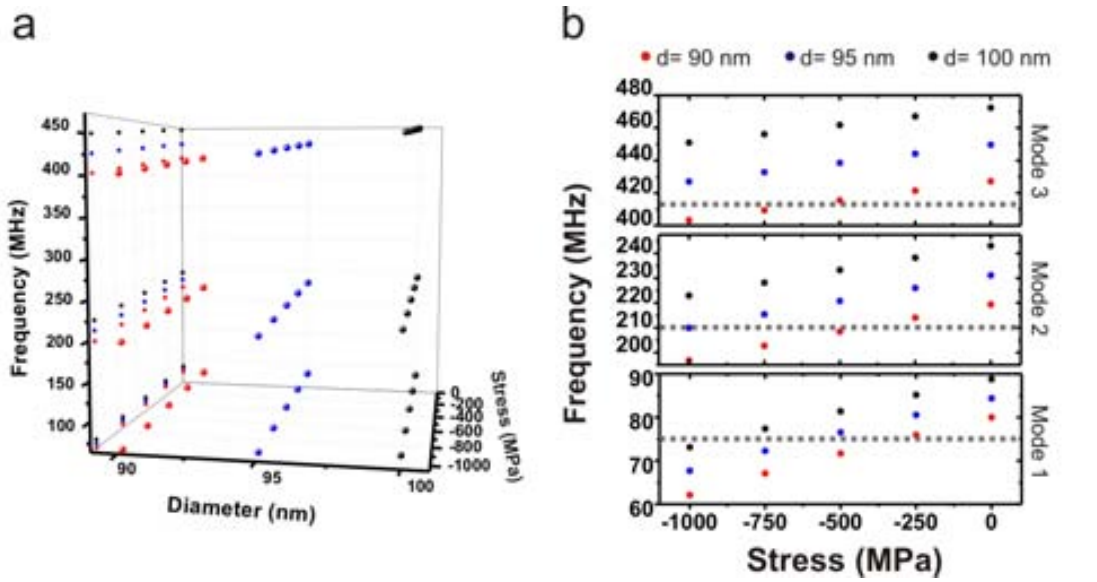

Figure 3.20: Simulation of the resonance frequency of the first three modes of an hexagonal cc-beam with a length of 3 μm, for several diameters and values of axial stress. a) Simulation results of the resonance frequencies of the first three modes of the resonator for different values of diameter and stress. b) Detail of the graph in a): projection in the frequency/stress plane, in order to ease the fitting of the experimental resonance frequencies. Each graph represents a different mode of resonance. The horizontal gray lines represent the experimental resonance frequency values for a beam of the studied dimensions: 75.25 MHz for the first mode, 210 MHz for the second mode and 413 MHz for the third. The point where the experimental and simulated values present the best concordance is for the 90-nanometers nanowire, with a stress between -250 and -500 MPa.

dance with the experimental measurements are a diameter of 90 nanometers and a compressive stress in the range of -250 and -500 MPa. Therefore, we can conclude that the simulations confirm the presence of compressive stress in the bottom-up nanowires.

3.5 Study of the mode splitting effect

During the measurements we detect different resonance peaks for each mode of resonance, caused by the mode splitting effect. In this section this effect is presented, and FEM simulations are performed in order to validate its origin.

During the measurements, the mode splitting effect is observed, for example, for all of the devices in Figure 3.7. These peaks correspond to the vibration of the nanowire in different orthogonal directions. Therefore, these orthogonal modes share the same modeshape with slightly different resonance frequencies. For this reason, in this work we refer to them as different directions of vibration of the same mode, instead of different modes.

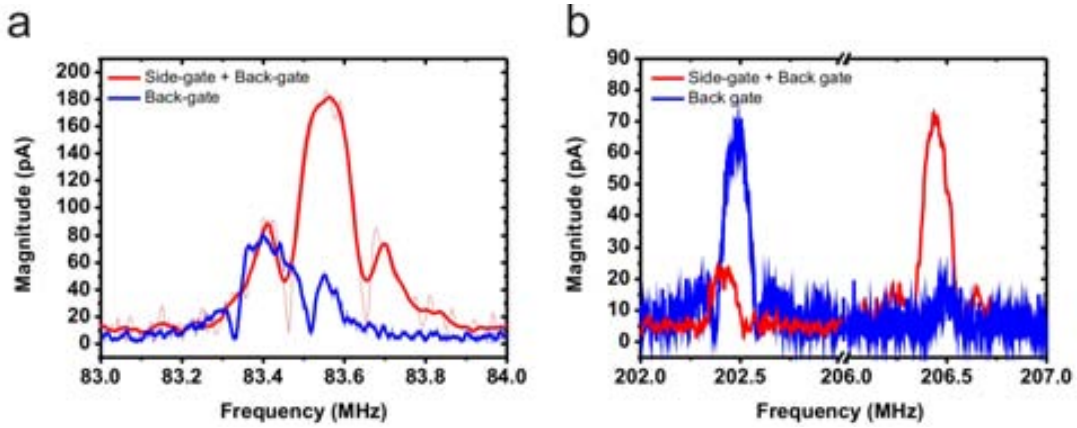

Figure 3.21: FM measurement of the frequency response of Nanowire 3, with a diameter of 52-65 nanometers, a length of 2.3 μm and at 900 nanometers from the side-gate. The excitation in each case is performed either by using the lateral side-gate and the back-gate at the same time, or using only the back-gate. a) First mode of resonance. Excitation conditions side-gate+back-gate (red): V_{NW}=140 mV, $V_{g,DC}$=5 V. Back-gate (blue): V_{NW}=250 mV, $V_{g,DC}$=20 V. b) Second mode of resonance. Measurement conditions: V_{NW}=250 mV, $V_{g,DC}$=20 V.

If the silicon nanowire was a perfect hexagon, the resonance frequency would be the same for all of the vibration directions. However, small defects in the nanowire break this asymmetry and localize the modes in determined directions. The mode splitting effect should be present for all of the resonance modes of the device. However, typically the amplitude of motion (and therefore the signal to noise ratio) is lower for higher modes. In the case of the measurement of the third mode of Nanowire 1 and Nanowire 2 (Figure 3.7c,f) only the dominant peak is detected, probably because the second peak is below the noise level.

In our measurements, we typically find the amplitude of one of the orthogonal modes is higher. The electrostatic force is applied in the direction of the side-gate. When the direction of vibration of the mode is aligned with the excitation direction, the actuation is more effective and therefore the amplitude of vibration is higher. In some particular cases, only one mode of resonance is found for low modes: in this case, it is possible that one of the modes is aligned to the excitation direction, so the other mode has a very inefficient actuation. Moreover, by changing the direction of excitation, the relative amplitude of the peaks switches. This is observed in Figure 3.21, in which different directions of excitation are used: the nanowire is excited using the side-gate (with which the direction of excitation is in-plane) and the substrate as a back-gate (with which the direction of excitation is out-of-plane). We observe that for the first mode, only one resonance peak appears: it is possible that the two orthogonal vibrations are too close together to be able to discern them separately. For the second mode of resonance, however, the orthogonal modes clearly appear. In this case, it is observed that the relative amplitude of the peaks varies

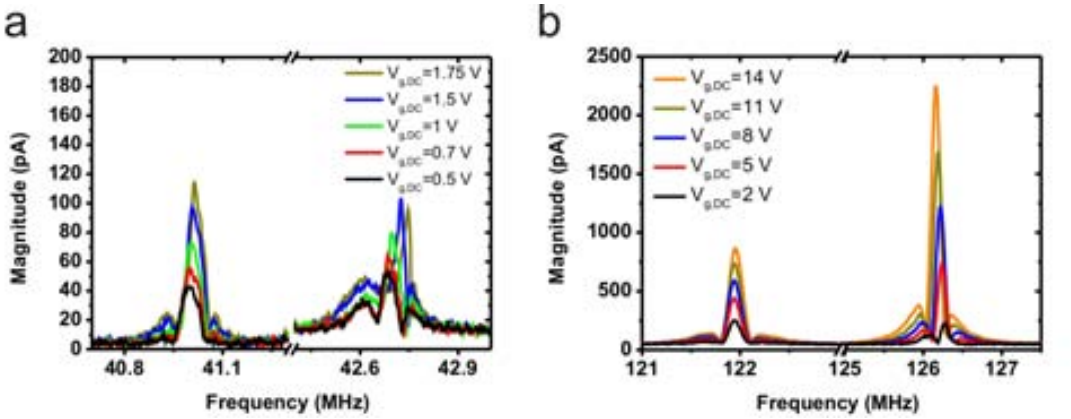

Figure 3.22: FM measurement of the evolution of the frequency response of the two modes of the resonator as a function of the DC actuation voltage. The studied silicon nanowire as a diameter of 70-85 nm and a length of 3 μm. The side-gate is located at 380 nm from the nanowire. a) Response of the orthogonal directions for the first mode of resonance. V_{NW}=80 mV. b) Response of the orthogonal directions for the second mode of resonance. V_{NW}=800 mV.

depending on the direction of actuation. We also observe that the electrostatic coupling is much worse in the case of the back-gate excitation: using SEM we have observed that the nanowire is farther from the substrate than from the side-gate, and therefore the electrostatic actuation is more inefficient in the former case. For this reason, higher excitation conditions are used to be able to electrically detect the response.

A control of the directionality of the excitation force can provide information of the direction of vibration, which is useful for mass sensing applications. A similar phenomena is used by Gil-Santos et al. [7], in which the determination of the direction of vibration is used to detect of the axial position of a punctual mass deposition. In their case, the vibration is caused by thermomechanical noise, so there is no preferential direction of vibration, but the transduction is performed by optical interferometry, which allow to determine the angle of the vibration planes with respect to the direction of the laser beam.

The different amplitudes of vibration in different directions also induce differences in the linearity of their respective response peaks for the same actuation conditions. Figure 3.22 shows the evolution of the response of the different modes during a variation of the DC gate voltage. As it is explained above, an increasing DC gate voltage provokes an increase of the amplitude of motion, so it is a useful method to study the evolution of the linearity of the response of the resonator. For the first mode of resonance (Figure 3.22a) the lower mode of resonance increases its amplitude with the DC voltage, and the resonance frequency and shape of the response change very little. However, in the case of the higher mode, the increase in the DC voltage provokes a variation of the resonance frequency and the response,

due to the nanowire entering a nonlinear regime. This higher mode is probably more aligned to the electrostatic direction of actuation, and therefore its amplitude of vibration is higher. For the second mode of resonance however (Figure 3.22b) the evolution of the response of the two orthogonal modes is more similar: the shape of the modes is linear for high voltages, but a slight shift in the frequency of the resonance peaks is observed in both cases. As amplitude of vibration of the resonator is typically lower for the second mode of resonance than for the first one, the absence of nonlinear effects in the measurement of the second mode is coherent.

Gil-Santos et al. propose the asymmetry factor Ω as a means to characterize the asymmetry of the nanowire, which is defined from the relative difference of resonance frequency of the two directions of vibration, defined as $_h$ and $_l$.

$$\Omega = \frac{_h - _l}{_l} \tag{3.36}$$

If the asymmetry factor is too low compared with the quality factor, the two resonance peaks will superpose (they will be too close together), and they won't be discernible from each other. We now consider an elliptical nanowire with a maximum radius R_{max} and a minimum radius R_{min}. In this case, $_h$ is located in the direction of the higher radius and $_l$ in the direction of the lower radius, and the resonance frequency of the n_{th} mode is defined as [7]:

$$_{n,l} = \frac{R_{min}(k_n l)^2}{2l^2}\sqrt{\frac{E}{\rho}} \qquad _{n,h} = \frac{R_{max}(k_n l)^2}{2l^2}\sqrt{\frac{E}{\rho}} \tag{3.37}$$

In this case, the asymmetry factor also corresponds to the difference in the radii of the elliptical nanowire:

$$\Omega = \frac{R_{max} - R_{min}}{R_{max}} \tag{3.38}$$

The resonance splitting phenomena has been validated using Ansys modal simulations, performed with two nanowires of different cross-sections: the first one presents regular hexagonal cross section with a distance between parallel sides of 100 nanometers. The second one presents an irregular hexagonal cross-section: it has a diameter of 100 nanometers, except for one side which has a thicker diameter of 110 nanometers. This irregularity introduces a radial asymmetry in the nanowire, in a manner similar to the elliptical nanowire described above with respect to a cylindrical nanowire. By simulating the resonance modes of these two structures, we observe that the regular nanowire presents the same resonance frequency for the different directions of vibration, and also that the nanowire does not vibrate in a preferential direction (i. e. it does not have localized vibration modes). However, for the case of the irregular nanowire, the directions of vibration are localized in

the thick axis and its orthogonal direction, and they present different resonance frequencies. The behaviour of the nanowire in the second case is similar to the one obtained during the experiments: two different resonance frequencies, close together, and vibrating in fixed directions. Therefore, these simulations confirm that the two different resonance peaks found during the measurements correspond to different directions of vibration, caused by imperfections in the section of the nanowire. We also confirm that if the section of the nanowire was a regular hexagon, only one resonance frequency would exist for each mode.

References

[1] J. Chaste, A. Eichler, J. Moser, G. Ceballos, R. Rurali, and A. Bachtold, "A nanomechanical mass sensor with yoctogram resolution," *Nature Nanotechnology*, vol. 7, pp. 301–304, Apr. 2012.

[2] R. He, X. L. Feng, M. L. Roukes, and P. Yang, "Self-transducing silicon nanowire electromechanical systems at room temperature," *Nano Letters*, vol. 8, pp. 1756–1761, June 2008.

[3] I. Bargatin, E. B. Myers, J. Arlett, B. Gudlewski, and M. L. Roukes, "Sensitive detection of nanomechanical motion using piezoresistive signal downmixing," *Applied Physics Letters*, vol. 86, pp. 133109–133109–3, Mar. 2005.

[4] V. Sazonova, Y. Yaish, H. Üstünel, D. Roundy, T. A. Arias, and P. L. McEuen, "A tunable carbon nanotube electromechanical oscillator," *Nature*, vol. 431, pp. 284–287, Sept. 2004.

[5] V. Gouttenoire, T. Barois, S. Perisanu, J.-L. Leclercq, S. T. Purcell, P. Vincent, and A. Ayari, "Digital and FM demodulation of a doubly clamped single-walled carbon-nanotube oscillator: Towards a nanotube cell phone," *Small*, vol. 6, no. 9, p. 1060–1065, 2010.

[6] E. A. Laird, F. Pei, W. Tang, G. A. Steele, and L. P. Kouwenhoven, "A high quality factor carbon nanotube mechanical resonator at 39 GHz," *Nano Letters*, p. 111202105855000, Dec. 2011.

[7] E. Gil-Santos, D. Ramos, J. Martínez, M. Fernández-Regúlez, R. García, l. S. Paulo, M. Calleja, and J. Tamayo, "Nanomechanical mass sensing and stiffness spectrometry based on two-dimensional vibrations of resonant nanowires," *Nature Nanotechnology*, vol. 5, no. 9, pp. 641–645, 2010.

[8] M. R. Nelis, L. Yu, W. Zhang, Y. Zhao, C. Yang, A. Raman, S. Mohammadi, and J. F. Rhoads, "Sources and implications of resonant mode splitting in silicon nanowire devices," *Nanotechnology*, vol. 22, p. 455502, Nov. 2011.

[9] H. S. Solanki, S. Sengupta, S. Dhara, V. Singh, S. Patil, R. Dhall, J. Parpia, A. Bhattacharya, and M. M. Deshmukh, "Tuning mechanical modes and influence of charge screening in nanowire resonators," *Physical Review B*, vol. 81, p. 115459, Mar. 2010.

[10] X. Feng, R. He, P. Yang, and M. Roukes, "Quality factors and energy losses of single-crystal silicon nanowire electromechanical resonators," pp. 1325–1326, IEEE, 2007.

[11] A. Eichler, J. Moser, J. Chaste, M. Zdrojek, I. Wilson-Rae, and A. Bachtold, "Nonlinear damping in mechanical resonators made from carbon nanotubes and graphene," *Nature Nanotechnology*, vol. 6, no. 6, pp. 339–342, 2011.

[12] H. W. C. Postma, I. Kozinsky, A. Husain, and M. L. Roukes, "Dynamic range of nanotube- and nanowire-based electromechanical systems," *Applied Physics Letters*, vol. 86, pp. 223105–223105–3, May 2005.

[13] N. Kacem, J. Arcamone, F. Perez-Murano, and S. Hentz, "Dynamic range enhancement of nonlinear nanomechanical resonant cantilevers for highly sensitive NEMS gas/mass sensor applications," *Journal of Micromechanics and Microengineering*, vol. 20, p. 045023, Apr. 2010.

[14] N. Kacem, S. Hentz, D. Pinto, B. Reig, and V. Nguyen, "Nonlinear dynamics of nanomechanical beam resonators: improving the performance of NEMS-based sensors," *Nanotechnology*, vol. 20, p. 275501, July 2009.

[15] "MATLAB - the language of technical computing. http://www.mathworks.com/products/matlab/."

[16] "Simulink - simulation and model-based design. http://www.mathworks.com/products/simulink/."

[17] R. He and P. Yang, "Giant piezoresistance effect in silicon nanowires," *Nature Nanotechnology*, vol. 1, no. 1, pp. 42–46, 2006.

[18] "ANSYS - simulation driven product development. http://www.ansys.com/."

Chapter 4

Fabrication of top-down silicon nanowire resonators

Contents

In the field of nanomechanical resonators, the tendency during the last years has been the study of structures of ever-decreasing dimensions. With this goal in mind, bottom-up fabricated nanostructures are ideal candidates thanks to their intrinsically small feature size. However, for the use of these devices beyond research, batch fabrication and good process repetitivity are indispensable, and at this point the integration of bottom-up and top-down structures is a major bottleneck. On the contrary, most top-down fabrication technologies present the necessary qualities for batch processing, but the reliable fabrication of structures of small dimensions

is still challenging. Therefore, the study of technologies capable of fabricating top-down structures of small dimensions is important to develop applications based on nanodevices.

This chapter presents the fabrication of top-down nanowires with dimensions comparable to the ones attained by bottom-up techniques. This means diameters as small as possible, ideally of less than 100 nanometers, and lengths in the orders of micrometers. Also, the fabrication is carried out using batch fabrication techniques, which enables the fabrication of a multitude of resonators in parallel.

The first section describes the state of the art in top-down nanomechanical resonators, more specifically those based on clamped-clamped nanowires. The second section presents several alternative steps for the fabrication of nanomechanical resonators based on top-down cc-beam nanowires. Finally, the fabrication process employed for the fabrication of top-down nanowires is presented, followed by an analysis of the fabrication results.

4.1 Introduction to resonators based on top-down cc-beam nanowires

The fabrication of top-down nanomechanical systems is based in the same technologies as traditional MEMS. As such, these technologies and their problems are an evolution of their larger counterparts, but at the same time they are well studied and controlled. However, the scaling of these techniques in the sub-100 nanometer range is challenging. A lot of work is being done in the fabrication of top-down structures of small dimensions, as well as in the increase of complexity of larger structures. This section contains a review of some works dealing with the fabrication of top-down nanomechanical resonators, and in order to limit the scope of this introduction, more specifically clamped-clamped beam nanowire resonators. So far, this kind of structures have presented the best sensitivity and resolution as nanomechanical mass sensors.

Often, the fabrication process is based on the deposition of thin films: there are a number of techniques capable of controllably fabricate thin layers of different materials (atomic layer deposition, evaporation, chemical vapour deposition,...). Therefore, when the resonator is patterned in one of these layers,its thickness is already inherently small. Afterwards, the patterning of this film can be defined using e-beam of FIB techniques, which also provide high resolution. Employing this this approach, many works use thin layers of silicon compounds deposited over silicon or SiO_2. The group of M. Roukes has studied the dynamics of top-down nanomechanical resonators, and many of their devices are based in silicon carbide (SiC) membranes patterned using e-beam lithography [1, 2, 3]. This approach yields de-

vices with sections around 100 nm (both in the in-plane and out-of-plane directions), and additionally the resonators can be coated with aluminium (Al) to allow electrical read-out (such as the device shown in Figure 4.1a). Another popular material is silicon nitride (SiN) [4, 5]: SiN resonators were used to demonstrate dielectric excitation, a method to detect the motion of non conductive resonators [6], with devices with lateral dimensions also in the order of 100 nm [7]. Furthermore, 50 nanometer thick resonators with widths of 16 nm have been fabricated by the group of S. Evoy using SiCN membranes (Figure 4.1b), and they have been characterized using optical methods [8].

Additionally, other approaches tackle the issues related with the fabrication of these top-down resonators. Some works are based in metal layers: the group of S. Evoy build NEMS resonators by patterning a 50 nanometer thick TiN layer deposited by Atomic-Layer Deposition (ALD) [9], and Nelson-Fitzpatrick et al. use thin Al layers [5] (although this technique does not allow them to reach thicknesses below 170 nm). Sulkko et al. present a method in which e-beam followed by FIB milling allow to achieve small gaps between a resonator and its side-gate, providing outstanding control over the electrostatic actuation of the resonator [10].

In some cases, the nanomechanical cc-beam serves as the transduction element of larger resonators. In this sense, Steeneken et al. use a thin Si beam to detect the motion of a larger cantilever [11]. An evolution of the same principle is used by Mile et al. which use two top-down SiNWs as straing gauges to piezoresistively transduce the motion of a larger Si beam [12], taking advantage of a differential geometry which inherently provides background suppression.

However, few works deal with the large scale fabrication of nanomechanical resonators. In this case, the pattern transfer step must be performed using standard photolithography, which entangles restrictions in terms of pattern resolution (see section 2.2.4.1). Fujii et al. circumvent this limitation by defining wires in a SOI wafer using photolithography and afterwards oxidizing them, obtaining devices of tens of nanometers [13, 14]. However, the main advances in this field have been performed using the CMOS-NEMS approach [15, 16, 17], in which the resonators are fabricated with standard CMOS technologies (in some cases, adding some post-processing steps). The CMOS-NEMS technology has the advantage that the resonators can be fabricated alongside circuitry to perform signal treatment on-chip, such as signal amplification or the building of closed loop systems. However, the use of CMOS technologies also implies severe limitations on the materials and processes, which have to be accommodated to the existing CMOS fabrication process. Outside the CMOS-NEMS field, Bargatin et al. from the CEA/LETI (Grenoble) have reported the large scale fabrication of resonator arrays using photolithography, and their characterization using optical methods [18]. In their work, the characterization method allows to determine the resonance frequency of all of the devices, permitting

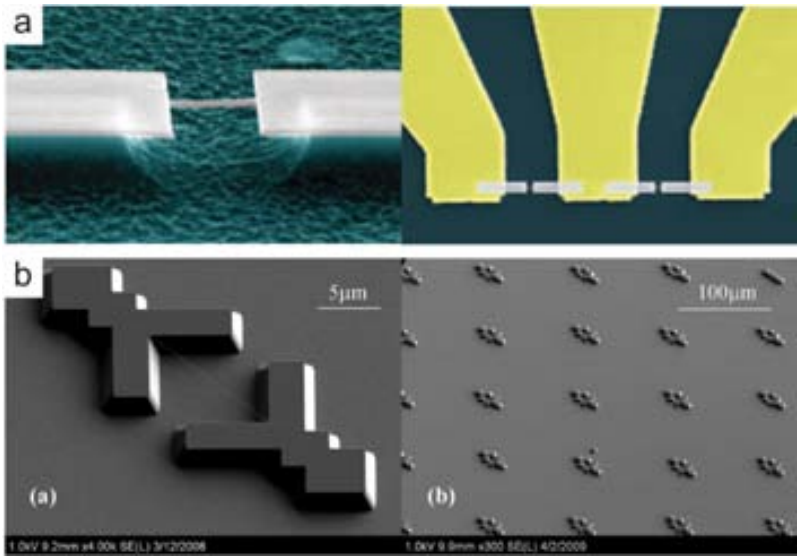

Figure 4.1: Nanomechanical resonators fabricated by top-down approaches. a) SiC beam of lateral dimensions around 100 nm. It is located near a reference beam in order to facilitate its electrical read-out. Extracted from [19]. b) SiCN beam with a cross-section of 50x16 nm, which is characterized using optical methods. Extracted from [8].

the study of the repeatability of the fabrication method.

4.1.1 Challenges in the fabrication of top-down nanomechanical resonators

The main challenges in the fabrication of top-down nanomechanical resonators are the technological issues arising from the fabrication of structures of small dimensions. While most fabrication techniques rely on standard photolithography to transfer patterns to the substrate, this technique does not provide enough resolution to transfer patterns in the order of 100 nanometers or below. In this case, the use of alternative lithography techniques (such as e-beam of FIB) or pattern reduction methods (such as oxidation) is necessary to correctly define the resonators. Even with the correct patterning techniques, obtaining a stable fabrication process which is effective at these scales can be also an issue, which can result in a poor repetitivity and throughput of the process.

The aforementioned issues become even more important for the batch fabrication of nanomechanical resonators: in this case parallel techniques (such as standard photolithography) have to be used, and throughput and repetitivity become more important. In general, the batch fabrication of this kind of devices is still a challenging technological enterprise.

4.2 Fabrication technologies

As described above, a common approach for the fabrication of top-down nanomechanical resonators is taking advantage of thin layers and high resolution patterning for the fabrication of small structures. Based on this approach, this section studies some of the technological steps involved in the fabrication of top-down resonators. An overview of thin layer technologies is first presented, followed by a description of high-resolution photolithography techniques. Afterwards, several techniques aimed at the reduction of dimensions of existing structures are presented. One of the critical steps in the fabrication, dry etching, is not addressed here as it is studied in detail in section 2.2.4.2.

4.2.1 Thin film deposition for the fabrication of nanomechanical resonators

Many top-down resonators of small dimensions are fabricated from a thin layer of material deposited on a substrate. Several fabrication techniques allow the controllable deposition of thin layers (in some cases, even of single atomic layers): taking advantage of this techniques, one of the dimensions of the resonator (its thickness) can be controlled. Different deposition techniques exist based on different principles and effective for different kinds of materials. This section will briefly present the chemical vapor deposition and evaporation techniques.

One of the most common deposition techniques is Chemical Vapor Deposition (CVD), in which the process is performed by the reaction of chemicals in gas phase. These reactions are generally performed at high temperatures in order to supply energy for the deposition reaction to occur. Some of the most common variants of these technique are low-pressure CVD (LPCVD) and plasma-enhanced CVD (PECVD). In LPCVD the reaction occurs at low pressure (0.1-1 mbar) and high temperature (500-900 ^{o}C). This approach can be used for polysilicon, silicon nitride or silicon oxide, and yields materials with good mechanical qualities and good selectivities in etching processes. However, the materials deposited by LPCVD usually have a high level of stress due to the high temperatures of the process. In contrast, PECVD relies in plasma to supply the energy necessary for the reaction, and therefore can operate at lower temperatures (150-350^{o}C). In general, materials deposited with this technique have worse mechanical properties but also a lower level of stress. For NEMS fabrication, where stress and mechanical properties both play an important role in the fabrication and the properties of the resonator, all these parameters have to be evaluated when choosing the fabrication method.

Another method to deposit thin films, which is widely used in metals, is evaporation. This technique consists in heating up a material source to a temperature to which evaporation occurs. This process is performed in a vacuum chamber with the

substrates in line of vision of the evaporation source, so that the evaporated material deposits on them. The heating of the substrate can be performed by several methods, such as surrounding the source material with coils and inducing a high current through them, or bombarding the source material with an electron beam. The evaporation process yields a conformal layer of deposited material on the substrate, but it is very susceptible to shadow effects provoked, for example, by irregularities on the substrate. Nevertheless, nanostencil lithography takes advantage of this shadow effects to selectively deposit materials through a stencil on a substrate [20, 21, 22].

Two other widely used thin film deposition methods are sputtering and Atomic Layer Deposition (ALD). The sputtering process is based in the bombardment of a target material with high energy inert ions, causing parts of this material to be removed from the target and ejected towards the substrate. Due to its physical nature, this process can be performed with a wide variety of materials, and presents a good step coverage. In contrast, ALD is a chemical process alternative to CVD. However, ALD is based in self-limiting surface reactions, providing an outstanding control over the deposited thickness (even to the atomic level–0.1Å). The process consists in the sequential reactions by two chemicals in gas phase: one of them is in charge of the self-limiting material deposition reaction, while the other one reactivates the surface for the next deposition step. The main disadvantages of ALD are its slowness and the limited choice of materials compatible with this technique.

Silicon-on-Insulator (SOI) wafers are also used for the fabrication of NEMS resonators based on thin films. These wafers consist in a silicon handle wafer covered by a layer of SiO_2 and a top silicon layer on top of them. The fabrication process of a SOI wafer is based in the oxidation of the handle wafer, and the subsequent fusion bonding with the silicon device layer. This process allows controlling the thickness of both the silicon and oxide layers, and additionally the wafers are commercially available with a wide selection of parameters (doping, thickness of the different layers, etc.). SOI wafers provide a good platform for the fabrication of NEMS resonators from the top Si layer, which can be doped to become conductive, and furthermore it is isolated from the substrate by the SiO_2 layer.

4.2.2 High resolution nanolithography

One critical step in the fabrication of top-down resonators is the pattern definition of the resonator itself. In opposition to bottom up techniques, in this case the resonator is patterned directly in the substrate by using lithography techniques. In consequence, the minimum feature size of the lithography technique defines the minimum size of the resonator in the in the planar direction. In section 2.2.4.1 a general overview of some photolithograpic techniques has been given. The present section is centered in high-resolution techniques, capable of delivering patterns in the orders of tens of nanometers. More concretely, e-beam, nano-imprint, scanning-

probe assisted lithographies and nanostencil lithography are discussed.

E-beam lithography consists in the exposition of an electron-sensitive resist using a beam of electrons. The resist can be positive or negative, and this process can be performed in an adapted SEM of TEM equipment. The resolution of the process is limited by the backscattering of the electrons in the resist (not by the beam width itself), and it can reach 10 nanometers with the adequate exposition conditions. E-beam lithography is a serial technique, which means that it is slow and not adequate for exposing large areas or patterns. However, it can be combined with a step of optical photolithography in order to circumvent this limitation. Therefore, e-beam lithography is widely used for the fabrication of a large number of nanostructures.

Another serial alternative for the transfer of high resolution patterns is the use of scanning probe techniques. Scanning probe techniques are based on controlling the motion of an atomically sharp tip in contact or near a substrate. The motion of this tip can be controlled with sub-nanometer accuracy, providing a high degree of control over its operation. These techniques are widely used for microscopy, manipulation and machining applications at the nanoscale. One example of scanning-probe assisted lithography is the scanning-probe induced oxidation technique, which consists in the local oxidation of a material by supplying a high voltage between the probe and the substrate [23]. At ambient humidity conditions, a water meniscus is formed at the contact point of the tip, oxidizing a small region of the surface. This oxidized region can be later used as a mask for an etching process. The main disadvantage of this technique is that the material of substrate must be suitable for oxidation in this conditions (such as silicon, or some metals like Ti or Al). Additionally, if the tip is operating in contact with the substrate, it changes its shape due to the wearing, and introduces reproducibility issues. This can be avoided by operating the cantilever in non-contact mode.

Nanoimprint lithography (NIL) is a parallel technique capable of attaining high resolutions , which is based in employing a hard material master to stamp and deform a polymeric resist. The deformed resist can be then used as a mask for pattern transfer techniques (such as dry etching). The stamp can be fabricated by high-resolution techniques such as e-beam combined by RIE and it is reusable, so a single stamp can be used to fabricate a high number of nanostructures. There are two main variants of NIL: Thermal NIL (T-NIL) and UV-NIL. In T-NIL the material film is thermoplastic, which is deformed with the help of high temperature. In contrast, UV-NIL uses a liquid photoresist at room temperature, which is hardened after the stamping process using UV-exposure. NIL is capable of defining high resolution patterns (few nanometers) in parallel, and at low cost compared with other parallel techniques providing similar resolutions.

Finally, Nanostencil Lithography is a shadow-masking method, based on the selective deposition of material by evaporation through micro- and nano-apertures

realized in a thin membrane. It is a clean and parallel fabrication method, which requires no use of photoresists and no contact with the substrate whatsoever. Furthermore, resolutions down to 50 nanometers have been demonstrated [24], and it is applicable at chip or wafer level [25, 21]. Nanostencil Lithography has been used in this work for the metallization of electrical contacts in silicon electrodes (see Appendix A).

4.2.3 Reduction of beam dimensions: oxidation and wet etching

In some cases, the parallel fabrication of nanomechanical resonators of small dimensions is desirable. In this case, high-resolution serial techniques cannot be used due to their long processing times, and optical photolithography does not provide enough resolution for the pattern transfer. To circumvent these limitations, one alternative is to reduce the dimensions of a resonator patterned with standard photolithography by using a techniques such as oxidation or etching, until it has the desired dimensions. If the reduction method is well controlled, beams of several nanometers can be fabricated [26]. This section is centered in the reduction of the dimensions of silicon beams by means of oxidation and wet etching processes.

The oxidation of silicon is generally used to grow a thin film of silicon oxide on its surface, with a very good control of the oxide thickness and a low density of defects. During the oxide growth part of the silicon is consumed, so this technique can also be used to controllably thin a silicon layer. An illustration of the oxidation of a silicon surface is shown in Figure 4.2a: during the oxidation process, roughly half of the oxide grows below the initial layer of silicon, and the other half above. This oxidation reaction already takes place at ambient temperature and humidity, but in this case the process self-passivates with an oxide thickness of about 2 nanometers.

The oxidation of silicon is typically carried out at temperatures from 900 °C to 1200 °C. There are two different kinds of oxidation: dry oxidation, which takes place in the presence of O_2, and wet oxidation, in the presence of H_20. Typically, wet oxidations provide higher oxidation rates, but the oxide quality obtained with this technique is lower. The oxidation process of silicon is well studied due to its importance in the fabrication of ICs, and can be reliably controlled by varying the temperature, time and gas flow in the furnace during the process. Several works have been published which use an oxidation process to reduce the dimensions of Si beams [26, 27, 28, 29, 30].

Another approach to reduce the dimensions of Si beams is the use of wet etching methods. During a wet etching, the Si surface is dipped into a etchant chemical in liquid form witch dissolves its surface. In general, the wet etching of silicon is more effective for some crystallographic directions than for others, resulting in

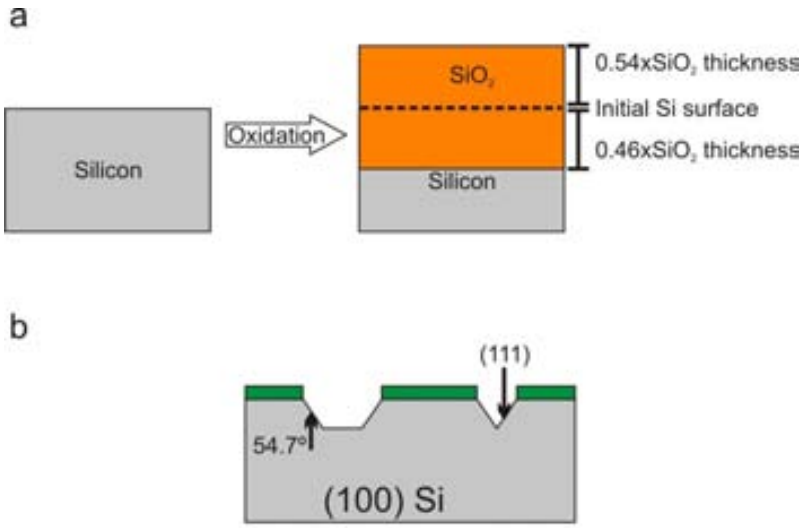

Figure 4.2: Effect of etching and oxidation processes in a silicon substrate. a) Geometry of the Si oxidation process: the SiO_2 grows from the Si surface. b) Anisotropic wet etching of a (110) silicon substrate, with some parts protected by a mask (green).

an anisotropic etch profile. For example, for some common silicon etchants such as potassium hydroxide (KOH) and tetramethyl ammonium hydroxide (TMAH), the etching process is slowest for the (111) plane: Figure 4.2 shows typical etch profiles for a (100) Si substrate with some areas protected by a mask. The etch rate depends on the temperature of the process, the etch time, and the concentration of the etchant. Several works make use of wet etching techniques to define and reduce dimensions of Si beams [30, 29, 31]. The disadvantage of this method for the reduction of beams is that eventually the beam is reduced to a triangular cross-section confined by (111) planes; at this point, the etch rate is too slow for the reduction to be very effective. For this reason, in general this method is combined with thermal oxidations.

4.3 Fabrication of top-down resonators

The fabrication process of nanomechanical resonators based on top-down silicon nanowires developed in this work is based in standard photolithography and oxidation to reduce the dimensions of the resonator. This process allows parallel fabrication, and the final pattern dimensions are only limited by the control over the oxidation process. Therefore, this process potentially allows to obtain a high number of devices per chip, contrary to the few which were obtained using bottom-up methods, and at the same time small dimensions in the sub-100 nanometer scale. This section deals with the fabrication of nanomechanical resonators using top-down

methods. First, a detailed description of each step of the fabrication process is given, and afterwards the geometry of the fabricated devices is studied.

4.3.1 Fabrication process

The different processes for the fabrication of top-down nanomechanical resonators are carried out in the clean room facilities of the Institut de Microelectrònica de Barcelona (IMB-CNM, CSIC). The main steps of the fabrication process are shown in Figure 4.3, along with an illustration of the section of the beam during each step of the fabrication. A SOI wafer is used as a substrate for the process (Figure 4.3a). The patterns are defined using optical photolithography, with a minimum feature size of 350 nm. These patterns are then transferred to the silicon device layer using reactive ion etching (Figure 4.3b). Then, the structures are oxidized in order to reduce the dimensions of the patterned beams (Figure 4.3c), and afterwards the oxide is removed using a dip in a solution with HF followed by critical point drying (Figure (Figure 4.3d). Finally, the nanowires are doped using the same ex-situ technique used for the bottom-up nanowires–an annealing in close proximity to a SiN wafer. This section describes in detail the different steps involved in the fabrication process.

4.3.1.1 Patterning of the substrates

The substrates used for the fabrication of top-down nanomechanical resonators are four-inch SOI wafers with a thin silicon layer, of approximately the same thickness as the resolution of the photolithography process (340 nm). This silicon layer is chosen in order to fabricate resonators of a unitary width to thickness ratio. In this case, the top silicon layer does not have low resistivity, but it is not necessary due to the doping process which is performed afterwards. The buried oxide layer has a thickness of 400 nm, which acts as an insulator between the silicon contacts and the substrate. The wafers used during this work are provided by Soitec Corporation, and their specific characteristics are shown in table 4.1. The crystalline orientation of the silicon device layer is not critical in this case. However, the resonators are oriented along the <011> direction, which is the direction in which the bulk piezoresistive coefficient of silicon is higher [32], maximizing the piezoresistive response. However, to our knowledge, there is no certainty that this fact holds true for nanowires of small dimensions.

The patterns in the substrates are defined using optical photolithography. In order to achieve the best possible resolution (the smallest pattern, as well as the best uniformity of these patterns) the process is carried out in the NIKON NSR 1505-G7 equipment, which uses an i-line high pressure mercury lamp with a resolution of 0.35 μm. The photolithography process is the same as described for the higher-resolution

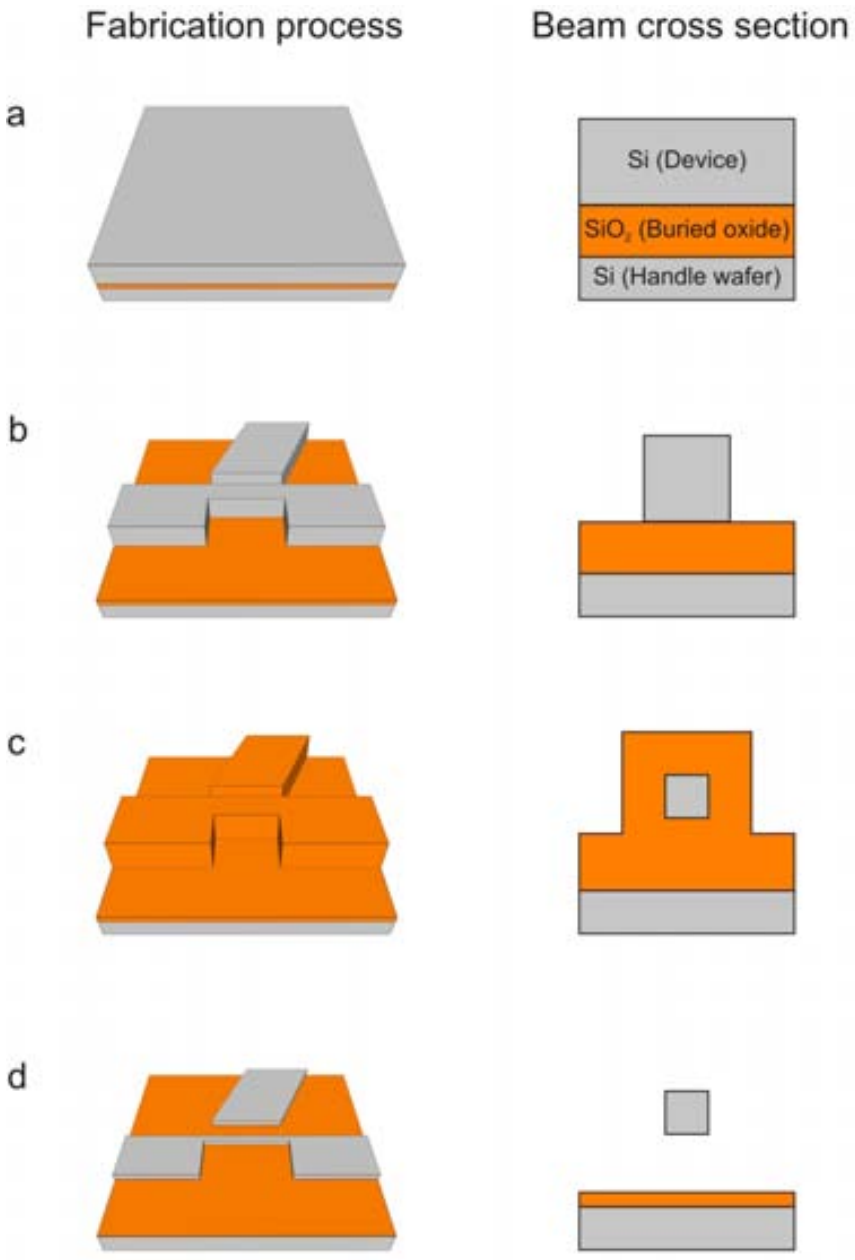

Figure 4.3: Top-down fabrication of nanomechanical resonators. Left column: steps of the fabrication process. Right column: Detail of the cross section of the resonator during the different steps of the fabrication process. a) SOI substrate. b) Definition of patterns in the silicon device layer (resonator and electric contacts) by photolithography and dry etching. c) Oxidation to reduce the dimensions of the section of the resonator. d) Release of the resonator using HF.

Device Layer	
Orientation	<100>
Thickness	340 ± 40 nm
Dopant	P/Boron
Resistivity	14-22 ohm $\times$ cm
Buried oxide (BOX)	
Thickness	400 nm
Handle Wafer	
Dopant	P/Boron
Resistivity	14-22 ohm $\times$ cm

Table 4.1: Specifications of the SOI wafers used during the fabrication of top-down nanomechanical resonators (source: Soitec Corporation).

patterns in bottom-up nanowires (section 2.3.1.1). Roughly, in order to achieve the higher possible resolution, the exposition parameters have to be adjusted and afterwards validated using a SEM inspection. This process yields photoresist patterns defining resonators with lateral dimensions of 500 or 350 nanometers, situated near a side-gate.

The next step in the fabrication is the transference of these photoresist patterns to the top silicon layer. This process is carried out using reactive ion etching. However, a new RIE process has to be calibrated in order to correctly pattern the resonators. In this case, the surface of the side-walls must be smooth, and the scalloping effect present in time-multiplexed RIE recipes (described in section 2.2.4.2) is too important to correctly define the 350 nm wide patterns. A non-pulsed RIE recipe has been optimized for this fabrication process, with the objective to obtain smooth and vertical side-walls for the resonator.

The dry etching process is carried out in the Alcatel AMS-110 DE equipment. The tests to calibrate the etching recipe consist in using an existing recipe as a base, and varying its parameters until we reach fabrication conditions adequate for our devices. The gases used for this recipe are the same that for the bottom-up process (C_4F_8 and SF_6), but in this case the recipe uses a constant flow of both of these gases at the same time to etch the silicon layer. The results of the optimization process can be seen in Figure 4.4, using the conditions shown in Table 4.2.

The actual dry etching process is as follows: immediately prior to the silicon RIE, a short SiO_2 dry etch is performed in order to eliminate the native silicon oxide layer. Afterwards, the dry etching of the silicon layer is performed, until the silicon layer is completely removed. Finally, the photoresist remaining after the dry

RIE Recipe	
Parameter	Value
SF_6 flow (sccm)	20
C_4F_8 flow (sccm)	20
ICP RF power (W)	220
Plate LF power (W)	20
Pressure (Pa)	2
Time (s)	240

Table 4.2: Conditions of the optimized RIE process for the definition of top-down nanomechanical resonators.

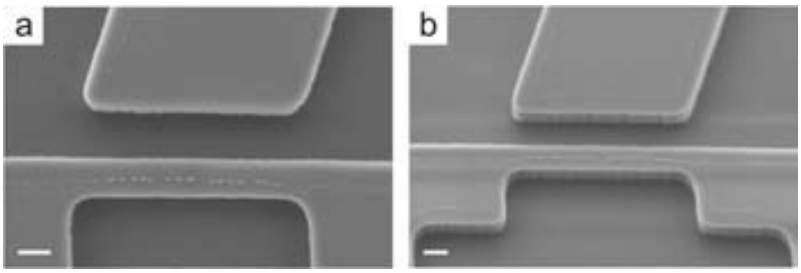

Figure 4.4: Results of the reactive ion etching to fabricate resonators based on a top-down approach. a) SEM image of a 500 nanometers wide resonator after the RIE process. Some photoresist traces can be seen on top of the resonator. Scale bar: 400 nm. b) SEM image of a tilted (30°) resonator after the RIE process. The side-walls are smooth and vertical, with some defects due to irregularities in the photoresist edges. Scale bar: 400 nm.

etching process is removed by processing the chip in an oxygen plasma equipment for 15 minutes, followed by 10-15 minutes of stripper and afterwards a dip in hot acetone.

After the dry etching, beams with a width of 350 or 500 nm are obtained (depending on the pattern size), and a thickness of 340 nm (defined by the thickness of the Si device layer). Figure 4.4 shows images of the fabricated devices. The surface of the beams is relatively smooth, with some roughness caused by the irregularity of the photoresist edges and the RIE process (as seen in Figure 4.4b).

4.3.1.2 Oxidation

As explained above, the photolithography and RIE processes allow the definition of beams of sections of 340×350 nanometers. To further reduce this section and obtain dimensions in the order of 100 nanometers, an oxidation process is performed. Using this process, the section of the beams can be reduced to the desired dimensions, and afterwards the oxide can be eliminated by an HF dip.

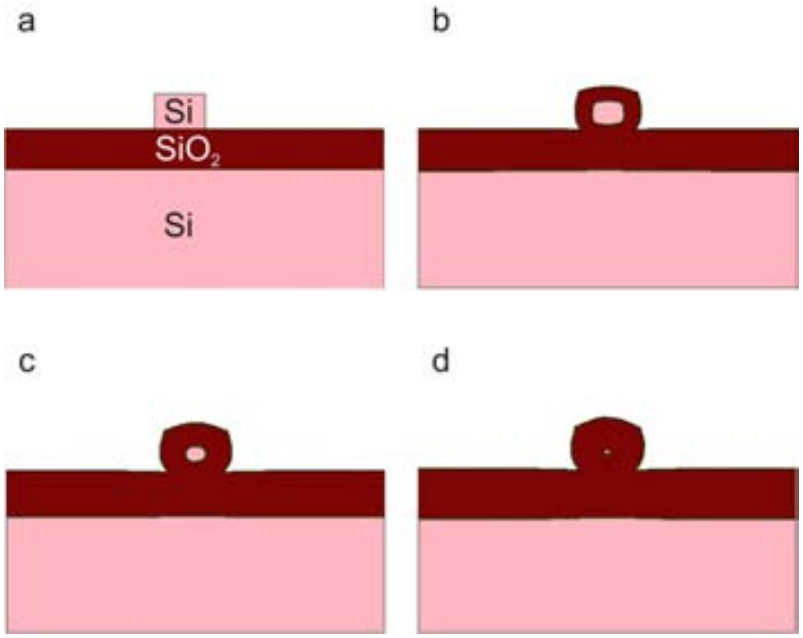

Figure 4.5: Simulation of the oxidation process using the Sentaurus software. a) Initial structure: beam of 500x340 nanometers over a SiO_2 software. b) Oxidation time: 300min. c) Oxidation time: 600min. d) Oxidation time: 900 min.

The oxidation process in the clean room of the IMB-CNM is performed in the BTU-Bruce diffusion furnace. The oxidation process is as follows: before the oxidation, the chips are chemically cleaned to eliminate organic or metallic contaminants. The oxidation process itself consists in several steps. First, the chips are charged into the furnace at 150°C, and afterwards stabilized to a temperature of 400°C under a flow of N_2. Then the temperature is ramped from 400-1000 °C for 2 hours under a flow of 6000 sccm N_2 and 1000 sccm of O_2. The main oxidation process is carried out at 1000°C, under a flow of 7500 sccm of O_2, during a variable time which depends on the required amount of oxidation. Then the temperature is ramped down again to 600 °C during 1:30 hours under a flow of nitrogen, and finally down to 400°C again.

This process is simulated using the Sentaurus simulator (Synopsis Inc.) [33] in order to determine the amount of oxidation time needed for the reduction of dimensions of the resonator. The simulations are based on the oxidation process described above, varying the time of the oxidation step. Figure 4.5 shows the results of these simulations, which determine that an oxidation time of around 15 hours would be necessary to achieve the desired dimensions (section around 100 nanometers).

Nevertheless, the available dry oxidation equipment is not able to perform oxidations of more than 100 nm, which is not enough for the reduction process. For this reason, we perform a series of oxidations followed by SiO_2 removal by wet etch-

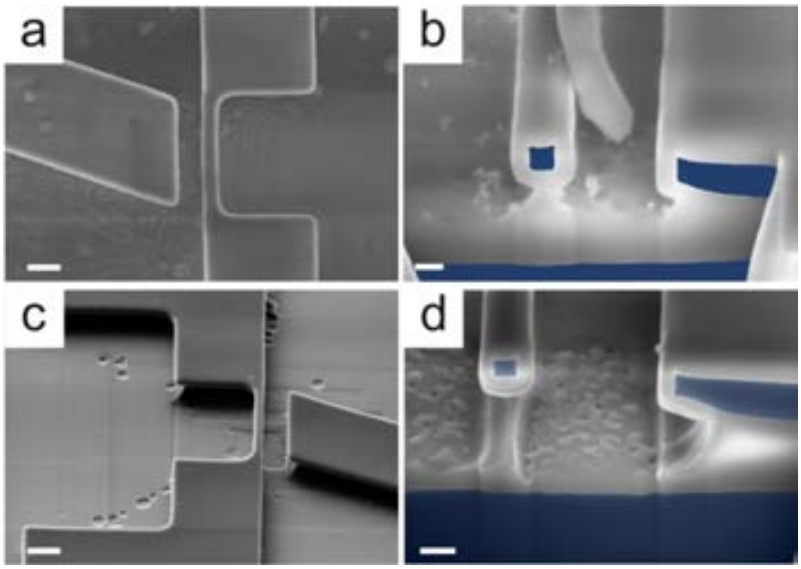

Figure 4.6: Results of the oxidation process to reduce the dimensions of nanomechanical resonators. a) SEM image of a nanowire near a side gate after the second oxidation, covered in SiO_2. Scale bar: 1 μm. b) SEM image of the cross-section of a nanowire after the second oxidation. The section has been performed using FIB milling. In this case the diameter of the resonator is roughly 170 nm. The silicon parts (nanowire, side-gate and substrate) are coloured in blue for easier identification. Scale bar: 200 nm. c) SEM image of a nanowire after the third oxidation, still covered by SiO_2. Scale bar: 1 μm. d) SEM image of the cross-section of a nanowire after the third oxidation (the same device as in (c)). The section has been performed using FIB milling. The diameter of the resonator in this case is roughly 125 $\times$ 100 nm. The silicon parts (nanowire, side-gate and substrate) are coloured in blue for easier identification. Scale bar: 200nm.

ing. In order to get an indication of the oxidation times adequate to the particular geometry of the beams, this new process is also simulated using the Sentaurus Process simulator, and the results are shown in Figure 4.5. These simulations provide an indication of the oxidation times, but we have found that the actual oxidation results present some differences with respect to the simulated ones.

The full process finally used to reduce the dimensions of the resonators is as follows: first, the chips are cleaned in order to eliminate the native oxide and other impurities present in the surface of the chips. Then, an oxidation of 100 nm of SiO_2 is performed (using the oxidation process described above), followed by a dip in HF to eliminate the grown oxide. The oxidation process is then repeated, and then beams are then examined by performing FIB milling and inspection using SEM (Figure 4.6a), in order to validate their section in detail. Finally, another HF followed by a short oxidation is performed to define the final dimensions of the beam. After this oxidation, an HF followed by critical-point drying is performed in order to release the resonators.

After the last oxidation process, the section of the nanowires is inspected by

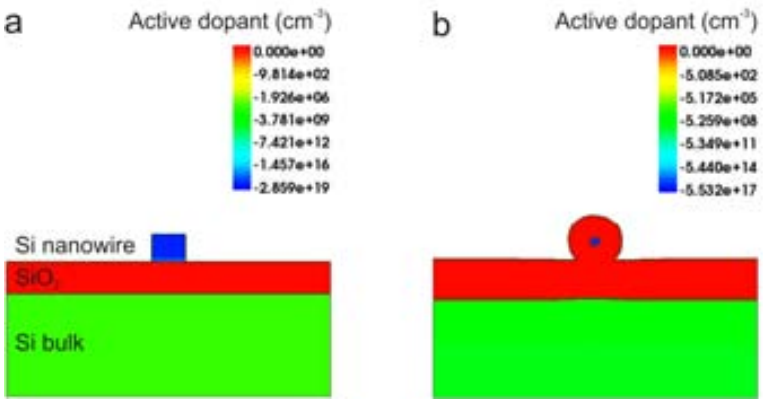

Figure 4.7: Evolution of the active dopant concentration during the oxidation of Si beams. The figure shows a cross-section of the Si beam patterned in the device layer of a SOI wafer. The dimensions of the beam are 340 × 500 nanometers, and the thickness of the oxide layer 400 nanometers. a) Active dopant concentration after the patterning of the Si beam. In this case, the beam presents a doping concentration around -2×10^{19}. b) Active dopant concentration after the oxidation process. We observe a decrease of two orders of magnitude on the doping of the beam, which in this case is around -5×10^{17}

FIB milling and SEM (Figures 4.6b,c), before the HF release of he resonators. This inspection shows that in most cases the nanowires present rectangular cross-sections with straight side-walls. The nanowires are located at a distance of approximately 900 nm of the side-gate, and around 650 nm from the back-gate: the same oxidations that reduce the section of the resonator separate the resonator from the electrical actuation electrodes. The oxidation process has made possible to fabricate nano-mechanical resonators of sections in the range of 100 × 100 nanometers, around the same size as some of the bottom-up fabricated nanowires. The section of these nanowires is limited by the control over the oxidation process, the variability of the thickness of the silicon device layer, and the variability of the photolithography process.

4.3.1.3 Doping

The doping method for the top-down silicon nanowires is the same as for the bottom-up ones. A doping process by ionic implantation before the oxidation is not possible, because the dopant diffuses into the SiO_2 during the oxidation process. This has been observed in some fabricated devices, by measuring their electric properties before and after oxidation, and has been further validated using simulations. Figure 4.7 shows the results of simulations using Sentaurus, showing the concentration of active dopant before and after the oxidation. It is observed that this concentration decreases in two orders of magnitude, and also (not shown in the figure) that part of the dopant diffuses to the oxide around the nanowire.

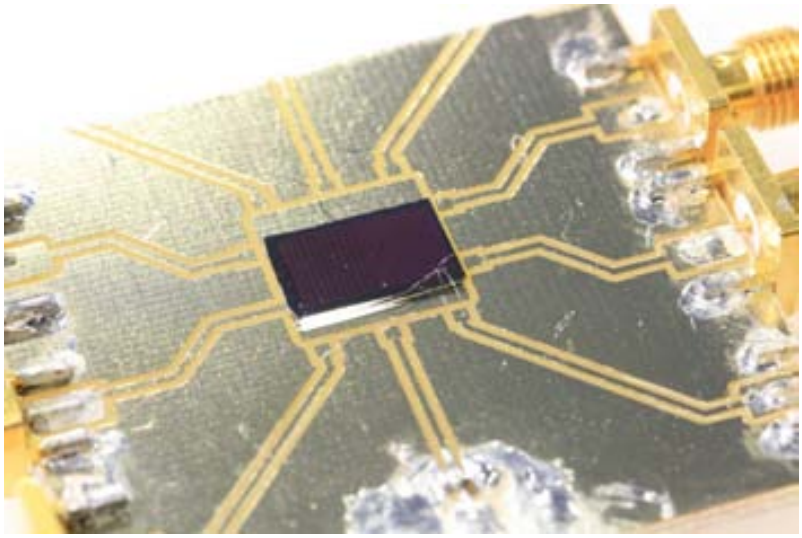

Figure 4.8: Packaging of the top-down nanomechanical resonators using wire-bonding to a PCB. Chip with a resonator and its side-gate wire-bonded to a PCB.

The ex-situ doping method and conditions are exactly the same that for bottom-up nanowires. The chips with top-down nanowires are annealed from 850-1000 °C in proximity to a boron nitride wafer, under a mild flow of nitrogen. This process allows the boron of the wafer to diffuse into the nanowire and electrodes, and the same annealing serves as an activation step for the dopant. See section 2.3.1.4 for a more thorough explanation of the process and its conditions.

The doped nanowires present resistances of 3-10 kΩ, depending on their section. These resistance values correspond to resistivities in the order of 1×10^{-4} ohm·m, similar to those of the bottom-up nanowires.

4.3.1.4 Packaging of the chips

The packaging of the chips is performed in the same way as their bottom-up counterparts. Once the nanowires are doped, they are stuck in a PCB with conductive silver paste and the individual resonators are wire-bonded to a PCB. The voltage of the substrate is controlled by an independent pad in the PCB (Figure 4.8). Due to their sections, slightly larger than those of the fabricated bottom-up nanowires, these resonators are not so sensitive to ESD issues. However, electrostatic protection measures are still observed during the packaging and measurements.

4.3.2 Fabrication results

The fabrication process described above has permitted the fabrication of nanomechanical resonators based on top-down nanowires. The fabricated devices have sections

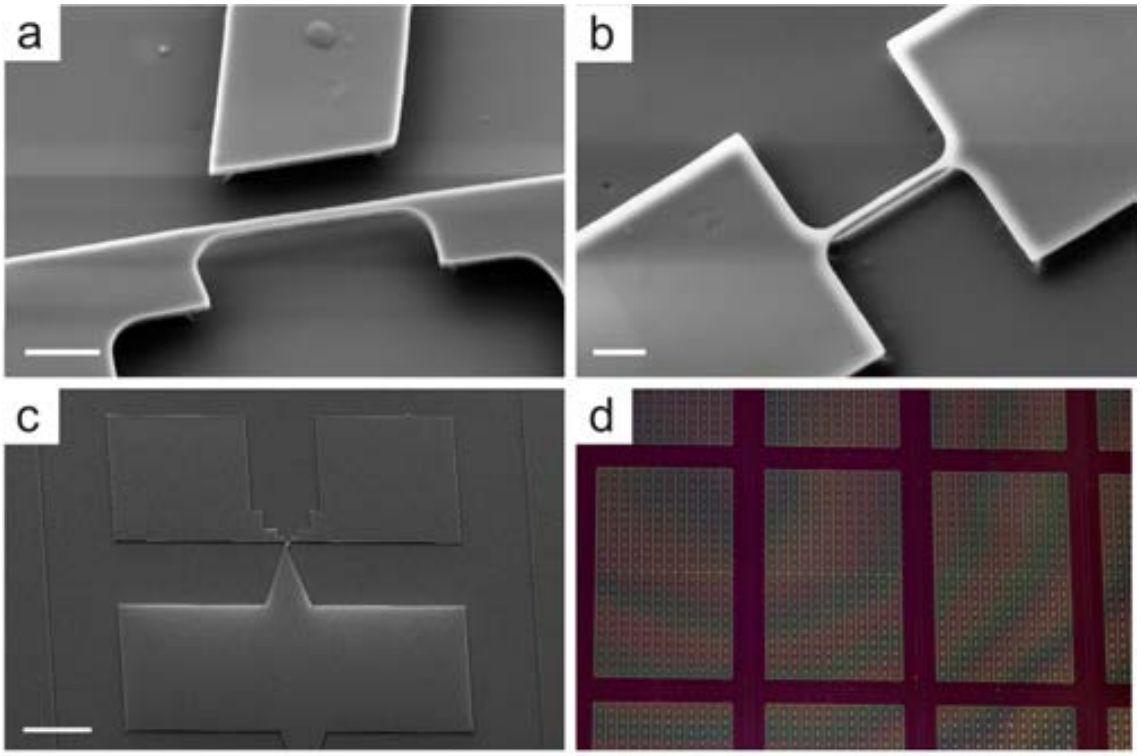

Figure 4.9: Fabrication results of top-down nanomechanical resonators. a) SEM image of a top-down resonator with a side-gate in close proximity. Scale bar: 1 μm. b) SEM image of a top-down resonator designed for back-gate actuation. Scale bar: 1 μm. c) SEM image of the electrodes individually contacting the nanomechanical resonator and its side-gate. Scale bar: 50 μm. d) Detail of a wafer containing chips with fabricated top-down nanomechanical resonators.

ranging from 110 $\times$ 145 nanometers to 60 $\times$ 70 nanometers. The length of the devices is approximately 3 μm, although due to the fabrication process it is not constant, but has a widening near the clampings. The dimensions of the resonators are comparable to some of the fabricated bottom-up silicon nanowires (which had diameters of 100 nanometers and lengths of 3 micrometers), which allows to compare the different fabrication approaches. Also, the fabricated devices have good conductivity to allow their electrical measurement. Moreover, they are located at approximately 900 nanometers from a side-gate for electrostatical actuation, and 600 nanometers from the bulk silicon layer which can also act as a back-gate. Some examples of the fabricated devices are shown in Figure 4.9.

One of the main differences between the bottom-up and top-down fabrication approaches that are used in this work is the number of functional devices: while the bottom-up fabrication technique yielded few resonators per chip, due to the random nature of the catalyst deposition method, the top-down approach can potentially yield hundredths of functional resonators per chip. Using our current designs, 480

devices per chip are fabricated, which represent about 40800 devices per wafer. Moreover, each resonator is addressable individually, i. e. readout contacts are patterned for each of them.

Even if the design of the chip and the fabrication technology are suitable for the parallel fabrication of a large number of resonators, the actual designs only contain a small percentage of the devices adequate for measurement (that is, with an appropriate geometry). Moreover, as the oxidation has to be tuned for each particular geometry, most of the devices of the chip are not correctly fabricated. Even if the number of fabricated devices is more than enough for a proof of concept, it is not enough to perform adequate statistics of the fabrication process. However, as an orientative figure, the diameter of a number of resonators of a chip was measured using SEM. Of 32 devices, 27 of them (an 85%) were functional, meaning that the resonator seemed adequate for measurement (no broken parts, no fabrication issues). The measurement of the diameter of the functional resonators had a median of 179 nanometers, with a standard deviation of 15.8 nanometers. This high deviation value is caused by drifts of the different technological processes in different geometric areas of the chip. That is, the resonators located nearby had similar diameters, but the difference in diameter gets larger the farther apart the resonators are located.

From the study of the fabrication process, we identify several sources of variance in the fabrication results. The device layer of the SOI wafer presents a less than ideal uniformity. Nominally, the thickness of this layer is 340 $\pm$ 40 nanometers, and this has been confirmed by using interferometry measurements. This variability in thickness of the device layer causes deviations in the fabrication process, more specially in the oxidation step. Moreover, some variability was observed in the photolithography process, although it was not quantified. Also, we observe different oxide thickness for the devices in the border of the chips than for those in the center. This last issue can be alleviated by performing the oxidations at full wafer scale, using the appropriate fabrication equipments.

4.3.2.1 Geometry of the resonators

It is important to study the geometry of the structures in order to predict their behaviour as nanomechanical resonators. The resonance frequency of a structure is affected by its geometry and internal strains, so their study is important in order to predict the behaviour of the structure. During the modelling of the frequency response of beam resonators (section 1.1) perfect beams have been studied, with regular cross-sections for the whole beam and perfect clampings (rigid and immobile). It is readily observable that the geometry of the fabricated resonators does not completely correspond to a perfect beam: its section is not regular for its whole length, but it widens near the clampings. Moreover, the clampings to the silicon contacts are not ideal, in the sense that there is an important overetching of the

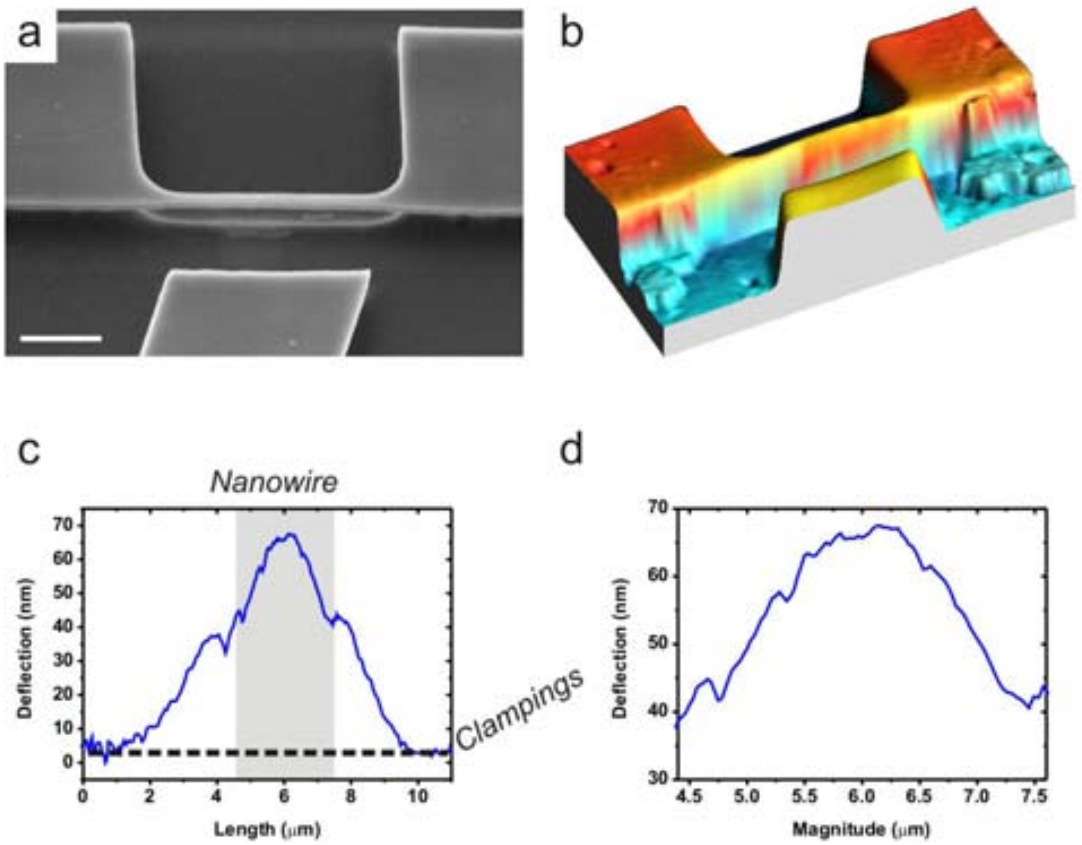

Figure 4.10: Geometry of the top-down fabricated resonators. a) SEM image of the resonator. The deflection of the beam due to the accumulation of stress during the oxidation is observable. Scale bar: 1 μm. b) AFM image of the resonator and side-gate. c) Deformation of the clampings and the nanowire, extracted from the AFM measurements. The portion of the length corresponding to the nanowire is highlighted in gray. d) Detail of the curve in *c)*, containing only the deformation of the wire.

SiO_2 that provokes an overhang in the silicon contacts (as observed in Figure 4.9a). These overhangs provide some mobility and curvature to the beam at the position of the clampings. These two effects must be taken into the account when studying the structures from a mechanical point of view.

Another geometric effect which is observed is a deformation of the whole structure in the out-of-plane direction. This deformation has been observed in the SEM images, and further studied using AFM measurements in tapping mode. The results of these measurement are shown in Figure 4.10. Both the nanowire and the silicon overhangs (i. e. the parts of the Si device layer that are not subject to the substrate by the SiO_2) are deformed "upwards" (in the out-of- plane direction, and away from the substrate). The nanowire itself is deformed about 30 nanometers from the clampings to the center of the nanowire. Moreover, the side-gate is also slightly

deformed and deviated from the center of the nanowire: this allows to electrically excite the motion of the nanowire in different directions. This is useful to measure the resonance modes of the nanowire corresponding to different vibration directions (in-plane and out-of-plane), which otherwise would be difficult to study.

Another important point about the deformation of the structure is not the geometry itself, but that it is a symptom of internal stress in the structure. A similar effect has been observed by Pennelli et al. for similarly fabricated structures [30]. They attribute this deformation to surface strain accumulated during the oxidation, which is released in the form of deformation when the oxide covering the nanowire is removed. However, this deformation causes an internal stress in the resonator which modifies its stiffness, affecting its resonance frequency. Pennelli et al. estimate the internal stress of the resonator relating its longitudinal deformation (as measured by AFM) and their stiffness. This deformation and its associated stress are taken into account when studying the response of the resonator in the following chapters.

References

[1] X. M. H. Huang, X. L. Feng, C. A. Zorman, M. Mehregany, and M. L. Roukes, "VHF, UHF and microwave frequency nanomechanical resonators," *New Journal of Physics*, vol. 7, pp. 247–247, Nov. 2005.

[2] Y. T. Yang, C. Callegari, X. L. Feng, K. L. Ekinci, and M. L. Roukes, "Zeptogram-scale nanomechanical mass sensing," *Nano Letters*, vol. 6, pp. 583–586, Apr. 2006.

[3] X. L. Feng, C. J. White, A. Hajimiri, and M. L. Roukes, "A self-sustaining ultrahigh-frequency nanoelectromechanical oscillator," *Nature Nanotechnology*, vol. 3, pp. 342–346, May 2008.

[4] P. A. Truitt, J. B. Hertzberg, C. C. Huang, K. L. Ekinci, and K. C. Schwab, "Efficient and sensitive capacitive readout of nanomechanical resonator arrays," *Nano Letters*, vol. 7, no. 1, pp. 120–126, 2006.

[5] T. Larsen, S. Schmid, L. Grönberg, A. O. Niskanen, J. Hassel, S. Dohn, and A. Boisen, "Ultrasensitive string-based temperature sensors," *Applied Physics Letters*, vol. 98, pp. 121901–121901–3, Mar. 2011.

[6] Q. P. Unterreithmeier, E. M. Weig, and J. P. Kotthaus, "Universal transduction scheme for nanomechanical systems based on dielectric forces," *Nature*, vol. 458, pp. 1001–1004, Apr. 2009.

[7] J. Rieger, T. Faust, M. J. Seitner, J. P. Kotthaus, and E. M. Weig, "Frequency and q factor control of nanomechanical resonators," *Applied Physics Letters*, vol. 101, pp. 103110–103110–4, Sept. 2012.

[8] C. Guthy, R. M. Das, B. Drobot, and S. Evoy, "Resonant characteristics of ultra-narrow SiCN nanomechanical resonators," *Journal of Applied Physics*, vol. 108, pp. 014306–014306–10, July 2010.

[9] N. Nelson-Fitzpatrick, C. Guthy, S. Poshtiban, E. Finley, K. D. Harris, B. J. Worfolk, and S. Evoy, "Atomic layer deposition of TiN for the fabrication of nanomechanical resonators," *Journal of Vacuum Science & Technology A: Vacuum, Surfaces, and Films*, vol. 31, no. 2, p. 021503, 2013.

[10] J. Sulkko, M. A. Sillanpaa, P. Hakkinen, L. Lechner, M. Helle, A. Fefferman, J. Parpia, and P. J. Hakonen, "Strong gate coupling of high-q nanomechanical resonators," *Nano Letters*, vol. 10, pp. 4884–4889, Dec. 2010.

[11] P. G. Steeneken, K. Le Phan, M. J. Goossens, G. E. J. Koops, G. J. a. M. Brom, C. van der Avoort, and J. T. M. van Beek, "Piezoresistive heat engine and refrigerator," *Nature Physics*, vol. 7, pp. 354–359, Apr. 2011.

[12] E. Mile, G. Jourdan, I. Bargatin, S. Labarthe, C. Marcoux, P. Andreucci, S. Hentz, C. Kharrat, E. Colinet, and L. Duraffourg, "In-plane nanoelectromechanical resonators based on silicon nanowire piezoresistive detection," *Nanotechnology*, vol. 21, p. 165504, Apr. 2010.

[13] H. Fujii, S. Kanemaru, T. Matsukawa, H. Hiroshima, H. Yokoyama, and J. Itoh, "Fabrication of a nanometer-scale si-wire by micromachining of a silicon-on-insulator substrate," *Japanese Journal of Applied Physics*, vol. 37, no. Part 1, No. 12B, pp. 7182–7185, 1998.

[14] H. Fujii, S. Kanemaru, T. Matsukawa, and J. Itoh, "Air-bridge-structured silicon nanowire and anomalous conductivity," *Applied Physics Letters*, vol. 75, pp. 3986–3988, Dec. 1999.

[15] J. Arcamone, G. Rius, G. Abadal, J. Teva, N. Barniol, and F. Pérez-Murano, "Micro/nanomechanical resonators for distributed mass sensing with capacitive detection," *Microelectronic Engineering*, vol. 83, pp. 1216–1220, Apr. 2006.

[16] J. Verd, M. Sansa, A. Uranga, F. Perez-Murano, J. Segura, and N. Barniol, "Metal microelectromechanical oscillator exhibiting ultra-high water vapor resolution," *Lab on a Chip*, vol. 11, no. 16, p. 2670, 2011.

[17] J. Verd, A. Uranga, G. Abadal, J. Teva, F. Torres, F. Pérez-Murano, J. Fraxedas, J. Esteve, and N. Barniol, "Monolithic mass sensor fabricated using a conventional technology with attogram resolution in air conditions," *Applied Physics Letters*, vol. 91, pp. 013501–013501–3, July 2007.

[18] I. Bargatin, E. B. Myers, J. S. Aldridge, C. Marcoux, P. Brianceau, L. Duraffourg, E. Colinet, S. Hentz, P. Andreucci, and M. L. Roukes, "Large-scale integration of nanoelectromechanical systems for gas sensing applications," *Nano Letters*, vol. 12, no. 3, pp. 1269–1274, 2012.

[19] A. K. Naik, M. S. Hanay, W. K. Hiebert, X. L. Feng, and M. L. Roukes, "Towards single-molecule nanomechanical mass spectrometry," *Nature Nanotechnology*, vol. 4, no. 7, pp. 445–450, 2009.

[20] J. Arcamone, M. A. F. van den Boogaart, F. Serra-Graells, J. Fraxedas, J. Brugger, and F. Pérez-Murano, "Full-wafer fabrication by nanostencil lithography of micro/nanomechanical mass sensors monolithically integrated with CMOS," *Nanotechnology*, vol. 19, p. 305302, July 2008.

[21] O. Vazquez-Mena, G. Villanueva, V. Savu, K. Sidler, M. A. F. van den Boogaart, and J. Brugger, "Metallic nanowires by full wafer stencil lithography," *Nano Letters*, vol. 8, no. 11, pp. 3675–3682, 2008.

[22] J. Brugger, J. Berenschot, S. Kuiper, W. Nijdam, B. Otter, and M. Elwenspoek, "Resistless patterning of sub-micron structures by evaporation through nanostencils," *Microelectronic Engineering*, vol. 53, pp. 403–405, June 2000.

[23] F. Pérez-Murano, G. Abadal, N. Barniol, X. Aymerich, J. Servat, P. Gorostiza, and F. Sanz, "Nanometer-scale oxidation of si(100) surfaces by tapping mode atomic force microscopy," *Journal of Applied Physics*, vol. 78, pp. 6797–6801, Dec. 1995.

[24] O. Vazquez-Mena, T. Sannomiya, L. G. Villanueva, J. Voros, and J. Brugger, "Metallic nanodot arrays by stencil lithography for plasmonic biosensing applications," *ACS Nano*, vol. 5, pp. 844–853, Feb. 2011.

[25] V. Savu, M. A. F. v. d. Boogaart, J. Brugger, J. Arcamone, M. Sansa, and F. Perez-Murano, "Dynamic stencil lithography on full wafer scale," in *52nd International Conference on Electron, Ion, and Photon Beam Technology and Nanofabrication*, vol. 26, pp. 2054–2058, AVS, 2008.

[26] H. I. Liu, D. K. Biegelsen, F. A. Ponce, N. M. Johnson, and R. F. W. Pease, "Self-limiting oxidation for fabricating sub-5 nm silicon nanowires," *Applied Physics Letters*, vol. 64, pp. 1383–1385, Mar. 1994.

[27] J. Kedzierski, J. Bokor, and C. Kisielowski, "Fabrication of planar silicon nanowires on silicon-on-insulator using stress limited oxidation," in *Papers from the 41st international conference on electron, ion, and photon beam technology and nanofabrication*, vol. 15, pp. 2825–2828, AVS, 1997.

[28] K.-N. Lee, S.-W. Jung, K.-S. Shin, W.-H. Kim, M.-H. Lee, and W.-K. Seong, "Fabrication of suspended silicon nanowire arrays," *Small*, vol. 4, no. 5, p. 642–648, 2008.

[29] G. Pennelli, "Top down fabrication of long silicon nanowire devices by means of lateral oxidation," *Microelectronic Engineering*, vol. 86, pp. 2139–2143, Nov. 2009.

[30] G. Pennelli, M. Totaro, and A. Nannini, "Correlation between surface stress and apparent young's modulus of top-down silicon nanowires," *ACS Nano*, vol. 6, pp. 10727–10734, Dec. 2012.

[31] S. Chen, J. G. Bomer, W. G. van der Wiel, E. T. Carlen, and A. van den Berg, "Top-down fabrication of sub-30 nm monocrystalline silicon nanowires using conventional microfabrication," *ACS Nano*, vol. 3, pp. 3485–3492, Nov. 2009.

[32] Y. Kanda, "A graphical representation of the piezoresistance coefficients in silicon," *Electron Devices, IEEE Transactions on*, vol. 29, no. 1, pp. 64–70, 1982.

[33] "Synopsis - sentaurus process. http://www.synopsys.com/."

Chapter 5

Electrical measurement of top-down silicon nanowire resonators

Contents

In the last chapters the fabrication of nanomechanical resonators based on top-down and bottom-up silicon nanowires has been presented. The nanowires fabricated using both approaches are similar in many aspects: both of them are fabricated from crystalline silicon, although the bottom-up nanowires are grown along the <111> direction while the top-down ones are fabricated following the <011> direction in order to maximize their piezoresistive coefficients. Furthermore, their dimensions are comparable: the resonators fabricated using both methods have lengths in the order of micrometers and diameters in the order of 100 nanometers–the bottom-up resonators present diameters from 50 to 100 nanometers, while the thinnest top-down resonators of 60-72 nanometers–. The development of both fabrication methods

allows measuring and comparing the characteristics of similar devices fabricated with different technologies.

This chapter presents the electrical measurement of top-down silicon nanowire resonators. Similarly to the measurement of their bottom-up counterparts, several different detection techniques are used, and a comparison of the efficiency of these methods and its relation with the transduction mechanisms is performed. The first section of the chapter presents the electrical measurement of top-down resonators using the FM and the two-source techniques. The second section extends the discussion of the transduction mechanisms initiated in Chapter 3 to the top-down resonators, and presents a method to estimate the amplitude of vibration at resonance based on SEM inspection. Afterwards, FEM simulations of the top-down resonators are performed, with the objective of fitting the electrically measured resonance frequencies with the simulated ones, which provides additional information about the dimensions and stress of the resonators. Finally, a comparison between the bottom-up and top-down fabricated resonators is performed.

5.1 Electrical characterization results

This section presents the electrical measurement of top-down silicon nanowire resonators. These measurements are based in the downmixing detection methods studied in section 3.1: the frequency modulation, the two-source, 1 and the two-source, 2 detection methods. The efficiency of these different techniques for the measurement of the frequency response of top-down resonators is studied.

Similarly to the bottom-up nanowires, the top-down resonators are actuated electrostatically by means of a side-gate. The detection of its motion is performed by taking advantage of the conductivity change which occurs in the resonator due to its motion, caused by a certain transduction mechanism. The readout of this transduction signal is performed using electrical downmixing methods, in which the high frequency response of the resonator is detected by its contribution to a low-frequency measurement signal, which is detected using a lock-in amplifier. The major part of the measurements are taken at room temperature at a pressure of approximately 10^{-6} mbar. Most of these measurements have been performed at the facilities of the group of Núria Barniol (ECAS group, Electronic Engineering department of the UAB).

5.1.1 Frequency modulation measurement method

The frequency modulation (FM) detection method has been used in Chapter 3 to electrically measure the frequency response of bottom-up nanowires with outstanding results. Besides, this method had been previously used to measure the frequency

response of top-down resonators. More concretely, Koumela et al. employ it to measure the response of top-down resonators fabricated by EBL lithography [1, 2]. In their work, only the first mode of the resonator is characterized, at frequencies from 50 to 300 MHz.

We use the FM method to measure the frequency response of several top-down nanomechanical resonators, in order to find and study their resonance modes. Some of the obtained results are shown in Figure 5.1: in this particular case, the characterized resonator has a width of 137 nanometers (characterized by SEM) and its thickness is estimated to be of around 110 nanometers. However, this thickness is difficult to characterize by SEM, and the only reliable method to do it is by studying its section using FIB+SEM, which destroys the resonator. The length of the resonator is 2.5 micrometers approximately. We find that the FM method provides an efficient detection of the response of the resonator, allowing the characterization of high modes of resonance at frequencies close to 600 MHz. For the particular case of Figure 5.1 we detect 6 different peaks, located in three different groups of relatively close frequencies. They are identified as the frequencies of vibration of the resonator for the in-plane and out-of-plane directions of each mode of resonance. Similarly to the bottom-up nomenclature, here we identify a mode of resonance with a particular modeshape, independently of the direction of vibration. Therefore, we detect the response of the first three resonance modes for the in-plane and out-of-plane directions. The out-of-plane direction is identified with the peak at lower frequency, because the thickness of the resonator is smaller than its width. The detection of both orthogonal modes is possible due to the fact that the side-gate is slightly displaced in the out-of-plane direction with respect to the resonator, so that there is a component in the excitation force in each of the directions of vibration. As discussed above, in this case the geometry of the top-down resonators does not correspond to that of an ideal double clamped beam: for this reason, instead of studying the resonance frequencies using the theoretical equations, all of these assumptions are validated afterwards using FEM Ansys simulations.

During most of these measurements we observe that the shape of the frequency response of the resonator fits well with the derivative of the real part of the expected mechanical response of the resonator, which is coherent with the FM detection method. This means that the mechanical response of the resonator is linear for most of the detected modes. For some of the measurements, however, the response does not seem to correspond exactly to the mentioned shape (the second in-plane mode of Figure 5.1, for example). The FM detection technique presents a complex response, and care must be taken when interpreting the results (as explained in section 3.1). In this case, more than a mechanical nonlinear behaviour, it is more probable that it is the electrical detection which modifies the measured response of the resonator. Therefore, it is possible that by varying the detection parameters

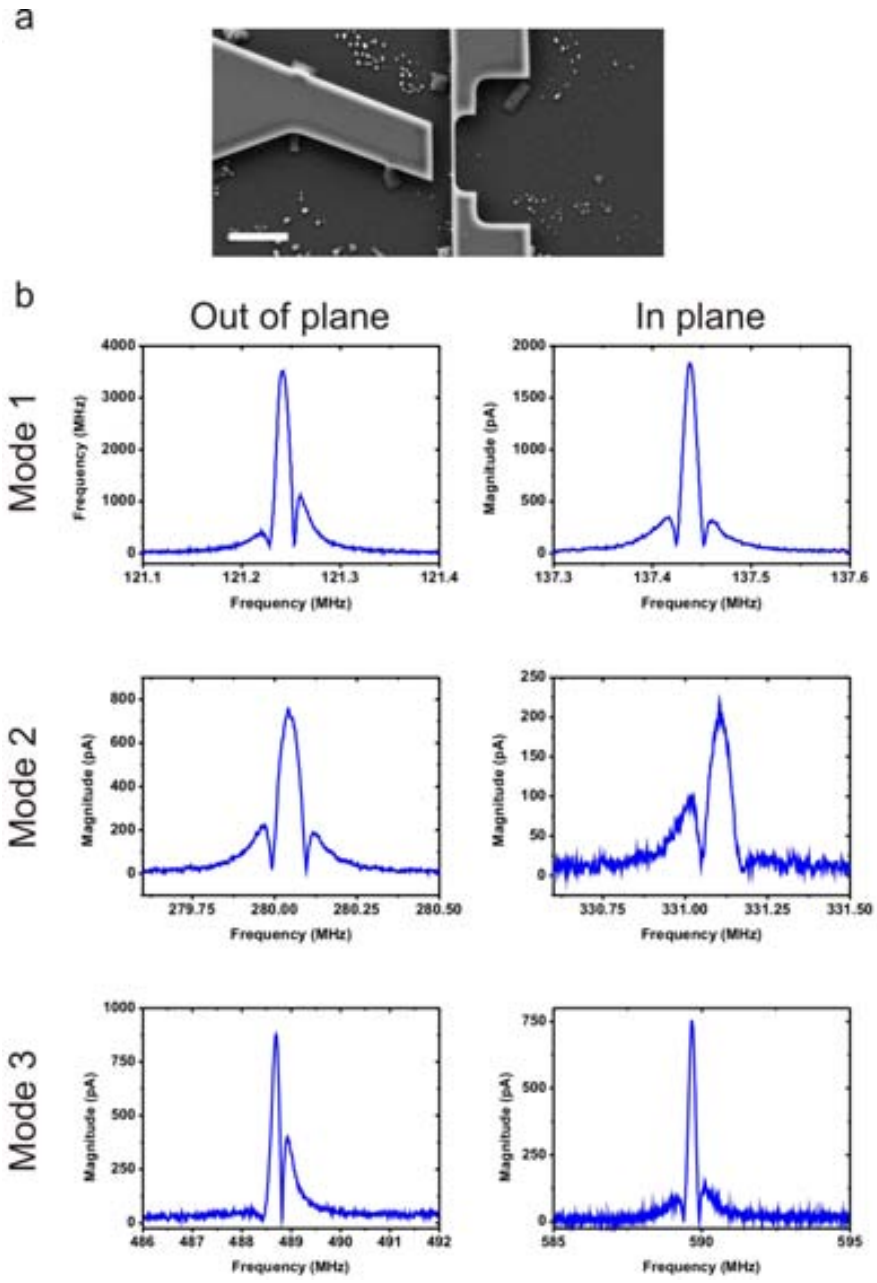

Figure 5.1: Electrical Measurement of the frequency response of a top-down nanomechanical resonator using the frequency modulation detection method. a) SEM image of the resonator. The nanowire has a diameter of 137 × 110 nanometers approximately, with a length of 2-3 micrometers. Scale bar: 3 μm. b) The first three modes of resonance are detected, for different directions of vibration. Measurement conditions for the first mode of resonance: $V_{NW} = 140$ mV, $V_{g,DC} = 10$ V. Measurement conditions for the second mode of resonance: $V_{NW} = 250$ mV, $V_{g,DC} = 15$ V. Measurement conditions for the third mode of resonance: $V_{NW} = 250$ mV, $V_{g,DC} = 15$ V.

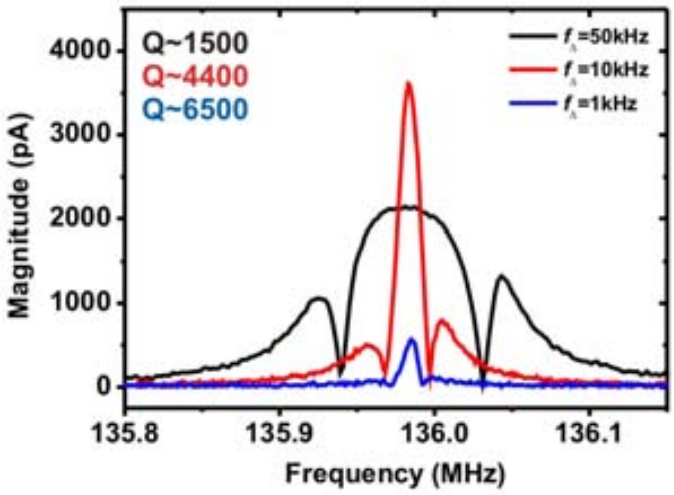

Figure 5.2: Evolution of the measured frequency response of a resonator when changing the value of the frequency deviation f_Δ. The measured quality factor varies with respect to the mechanical one as a consequence of the widening of the electrically measured response, for some values of f_Δ.

(such as the frequency deviation f_Δ) we would be able to recover the expected response.

During the measurement of the bottom-up nanowires, we observed that there is a compromise between the SNR and the amplitude of the detected response, due to particularities of the FM detection. This phenomenon is also observed for the top-down resonators. An example of the influence of the measurement conditions over the detected response if shown in Figure 5.2, where a resonator is measured using different values of frequency deviation f_Δ. We assume that this parameter does not strongly affect the efficiency of the actuation of the resonator, and therefore the changes observed in the response are due exclusively to the detection method. Of the three studied values of f_Δ, we observed that one of them presents an optimal SNR, where the amplitude is highest with respect with the other two. Additionally, in this case the detected response corresponds to the one expected for FM detection. When the value of the frequency deviation is lowered, the amplitude of the measured response decreases, which is also consistent with the detection equations of the FM method (3.29). Moreover, when increasing the frequency deviation above the optimal value, the amplitude of the detected signal decreases and the width of the detected peak increases (that is, the measured quality factor decreases). This effect is not contemplated in the studied equations, but it is indeed expected of the FM detection method for certain measurement conditions [3]. When the frequency deviation is not much smaller than the width of the measured resonance peak, a widening of the detected resonance response with respect to the mechanical one is

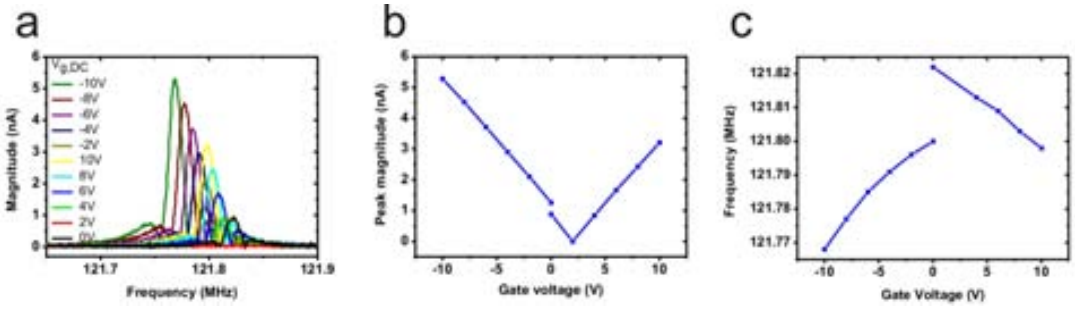

Figure 5.3: Evolution of the measured frequency response of a resonator when changing the value of the DC gate voltage. Measurement conditions: $V_{NW} = 0.1$ V.

observed, and for high values of frequency deviation the detected amplitude peak decreases. Therefore, an accurate choice of the frequency deviation is needed for the measurement of these resonators, specially when studying the mechanical quality factor. In the case of Figure 5.2 we detect quality factors in the order of 4400-6500 with the optimum measurement conditions.

The evolution of the measured response to a variation of the DC gate voltage is also studied. As discussed in section 1.2.1, this parameter affects the amplitude of vibration of the resonator, and additionally in most cases it does not affect the efficiency of the transduction. Moreover, an increase in the electrostatic potential can also induce a change in the resonance frequency of the device, caused by the spring softening effect (explained in section 1.1.3). Figure 5.3 shows the measurement of the evolution of the response of the resonator when varying the gate voltage. To obtain the graphs, two different sets of sweeps were measured: one for positive DC gate voltages and one for negative voltages. For this reason, there is a slight offset between the values of amplitude and resonance frequency for positive and negative values, caused by the temporal drift of the response of the resonator. We observe a linear increase of the amplitude of the resonance peak with an increasing gate voltage, both for positive and negative values (Figure 5.3b) with a slope of 395 pA/V. This effect is consistent with electrostatic actuation and a 1 detection. However, we have observed that correlating the detected response using the FM method with the mechanical response is not straightforward, and therefore this is not the ideal method to study the evolution of the mechanical response of the resonator. We also observe a decrease in the resonance frequency of the resonator, which seems to vary with a quadratic dependence with the DC gate voltage. This is consistent with the spring softening effect, and it is frequently observed in resonators with electrostatic actuation [4, 5]. In this case, it is safe to assume that the value of the resonance frequency as measured with the FM method is the same as the mechanical one.

Additionally, in Figure 5.3 we observe that the maximum signal amplitude is not lowest at 0 V as expected, but somewhere around 2 V: this effect is probably caused

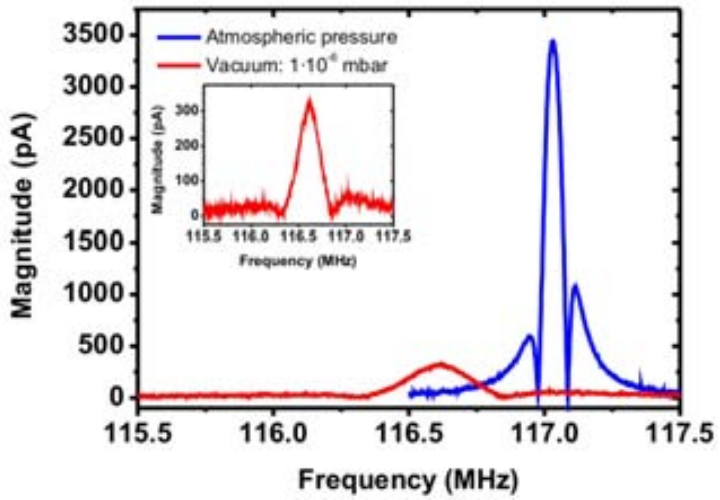

Figure 5.4: Measurement of the frequency response of the resonator in air and vacuum conditions. The approximate section of the nanowire is 125 × 90 nanometers, and its length is 3 - 3.7 micrometers. Measurement conditions: $V_{NW} = 250$ mV, $V_{g,DC} = 15$ V. The inset shows a detail of the response of the resonator in air conditions. $f_{0,air} = 116.6$ MHz, $Q_{air} = 1500$, $f_{0,vacuum} = 117$ MHz, $Q_{vacuum} = 200$.

by charge accumulated in the silicon oxide which covers the substrate below the resonator, which induces an unknown potential and therefore modifies the DC voltage applied to the resonator. We have confirmed this by monitoring the response of the resonator before and after exposing the device to SEM inspection, during which negative charges become trapped in the substrate. We observe that the minimum peak signal as a function of DC gate voltage shifts as a result of this exposition, confirming that the electric field induced by these charges affects the behaviour of the resonator.

Although the optimum medium for the measurement of nanomechanical resonators is at vacuum, it is also interesting to study their behaviour in air conditions. Figure 5.4 shows the frequency response of a resonator in vacuum and ambient pressure for the same actuation conditions. The inset shows a detail of the response in air, with a smaller vertical scale. We observe different effects arising from the change of medium: the most important one is the decrease of the quality factor due to damping arising from collisions with the air molecules. In practice this affects the amplitude of vibration of the resonator and the width of the mechanical response. We observe that the peak amplitude descends in a factor of 10, while the quality factor decreases in a factor of 7.5 approximately. According to the theoretical frequency response of the resonator, the maximum amplitude of oscillation is proportional to the quality factor. Therefore, the evolution of the amplitude and the quality fac-

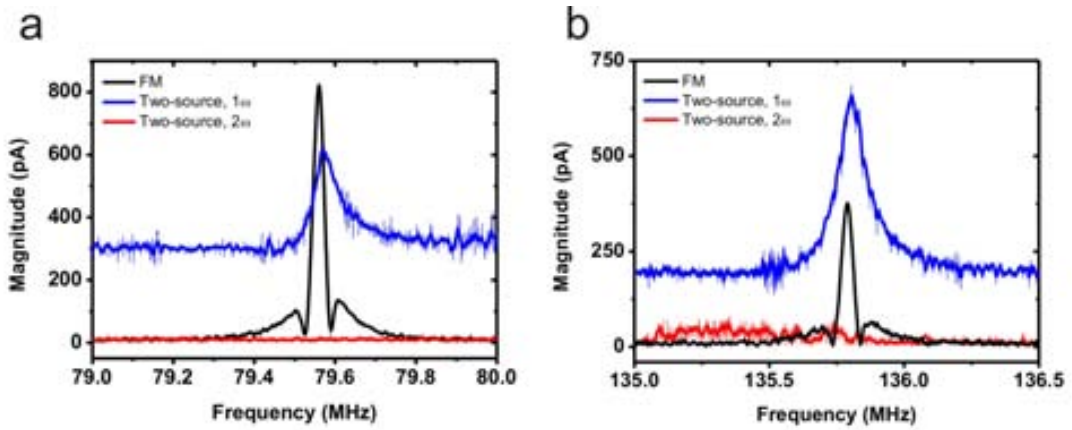

Figure 5.5: Comparison of the electrical measurement of the response of a resonator using the FM, the two-source, 1ω and the two-source, 2ω methods. The first out-of-plane (a) and in-plane (b) modes are shown. The device has a section of 110×80 nanometers approximately and a length of 3 μm. a) FM measurement conditions: $V_{NW,FM} = 140$ mV, $V_{g,DC} = 10$ V; Two-source measurement conditions: $V_{NW,2source} = 80$ mV, $V_{g,DC} = 10$ V, $V_{g,AC} = 140$ mV. b) FM measurement conditions: $V_{NW,FM} = 140$ mV, $V_{g,DC} = 15$ V; Two-source measurement conditions: $V_{NW,2source} = 80$ mV, $V_{g,DC} = 15$ V, $V_{g,AC} = 140$ mV.

tor is in a relatively good concordance with the theory, taking into consideration the uncertainty in the determination of the quality factor in the case of the FM measurement method and the poor knowledge of the transduction mechanisms (and therefore, the relation between the electrical and mechanical responses). The second observed effect is the decrease of the resonance frequency, which recovers its original value once the vacuum conditions are restored. This effect has also been observed by Peng et al. during the measurement of CNT resonators [6], and it may be caused by the adsorption of molecules present in the air to the surface of the resonator.

5.1.2 Two-source measurement methods

In the last section we have validated the usefulness of the FM detection method to measure the response of top-down nanomechanical resonators. Now, we compare the efficiency of this method with the different two-source techniques.

Figure 5.5 shows the measurement of the first out-of-plane and in-plane modes of a top-down nanowire using the different detection techniques. The measured nanowire has dimensions comparable to those of the studied bottom-up nanowires: it has a diameter of 110×80 nanometers approximately, while some of the measured bottom-up nanowires have a diameter of 90-100 nanometers. We employ the same actuation conditions for the different detection methods, so we can consider that the amplitude of motion of the resonator is similar. We observe that the amplitude of the detected response is similar for the FM and the two-source, 1 methods,

for both directions of vibration. The exact amplitude using both methods is not comparable, because some parameters in the FM method influence the amplitude of the detected signal. Moreover, it is notable that the resonance is not detected using the two-source, 2 detection technique for none of the directions of vibration. Furthermore, the 2 signal is not detected either for higher modes of resonance. This indicates a difference in the transduction mechanisms present in bottom-up and top-down nanowires: this is studied in depth in the next section.

Therefore we conclude that the FM and the two-source, 1 detection methods are effective for the measurement of the fabricated top-down nanowires. The FM method allows the measurement of high modes of resonance with frequencies close to 600 MHz. Moreover, the FM method presents no parasitic electric signals, and its measurement setup is simpler than that of the two-source techniques.

5.2 Study of the transduction mechanisms

As we have studied in section 3.3.1, different transduction mechanisms contribute differently to the signal detected by the various detection methods. We concluded that the two-source, 2 detection method is effective when the transduction signal is caused by a quadratic transduction mechanism (2 transduction), such as a piezoresistive change of conductance due to the elongation of the beam. In contrast, the two-source, 1 and the FM detection methods are efficient transducing linear transduction signals (1 transduction), such as those originated by the conductance modulation due to charge capacitively induced by the side-gate. The results of Figure 5.5 indicates that a linear transduction mechanism is present in the case of the fabricated top-down nanowires, and it is effective to measure higher modes of resonance. On the other hand, the measurements show that a 2 transduction signal is not detected, and therefore a quadratic transduction mechanism is either not present or very weak.

We now study the evolution of the response of the resonator when changing the DC gate voltage using the two-source, 1 method. The variation of this voltage provides a good tool to study the electrical response as a function of mechanical parameters (the amplitude of vibration), because the change of the DC voltage in most cases does not induce changes in the transduction mechanisms or detection parameters. The obtained results are shown in Figure 5.6. We observe that, similarly to analogous measurements with bottom-up nanowires, the amplitude of the resonance peak escalates linearly with the DC voltage. As explained above, this is expected from a linear transduction mechanism, where the transduced signal is proportional to the amplitude of motion of the resonator. Furthermore we observe that the minimum amplitude is not centered at 0 V: this phenomenon was also observed in the FM measurements, and it may be due to charge accumulated on the

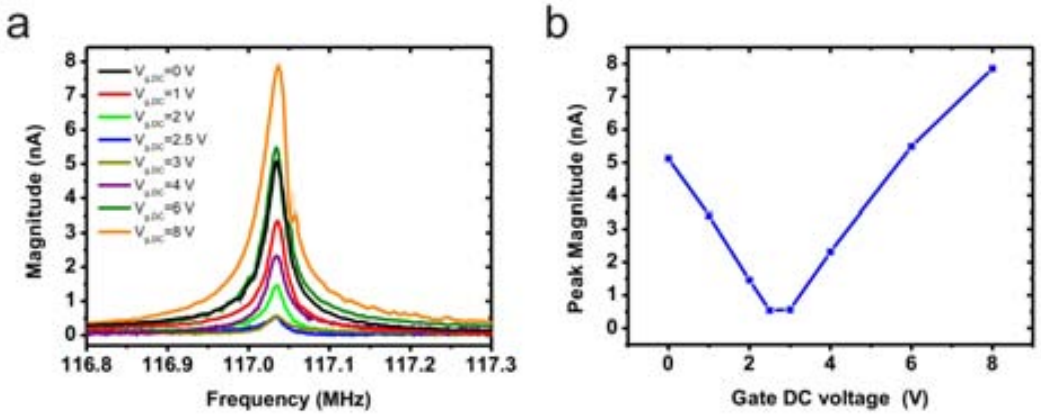

Figure 5.6: Evolution of the frequency response of a nanomechanical resonator detected by the two-source, 1ω method. Measurement conditions: $V_{NW} = 80$ mV, $V_{g,AC} = 200$ mV.

substrate.

Similarly to the case of the bottom-up nanowires, we study the possibility that the 1 transduction is caused by conductance modulation due to charge induced in the resonator by capacitive coupling to the side-gate. The current measured at low frequency $_L$ using this measurement method is described by equation (3.10). In order to evaluate the possibility that the transduction signal is caused by this effect, we study the measurement of a nanowire using the two-source, 1 detection method, shown in Figure 5.7. We first obtain the value of the transconductance from the purely electrical signal measured at a frequency far away from resonance, by fitting it to the first term of expression (3.10). With this method, we find a value for the transconductance of 20 nS/V, which is similar to that found for bottom-up nanowires. In this case, we obtained no information from the static measurement of the transconductance (based on monitoring the resistance while changing the gate DC voltage), due to resistance fluctuations and noise which hinder the measurement. However, from the uncertainty of these DC measurements we determined that the static transconductance should be lower than 200 pS/V, which otherwise is below the value found dynamically.

From the transconductance value extracted from the dynamic measurements (20 nS/V) and applying it to the equation of the detected current we find that the relative change of capacitance at resonance C_g C_g should be of 0.2 approximately (a 20%). For a nanowire of with a width around 100 nanometers and located at 900 nanometers from the side-gate, such a capacitance change would mean a huge amplitude of motion: as an example, according to FEM simulations (detailed in section 5.3), an amplitude of motion of 50 nanometers implies a capacitance change of only 1%.

Taking into account these difficulties, the origin of the 1 signal is still not clear.

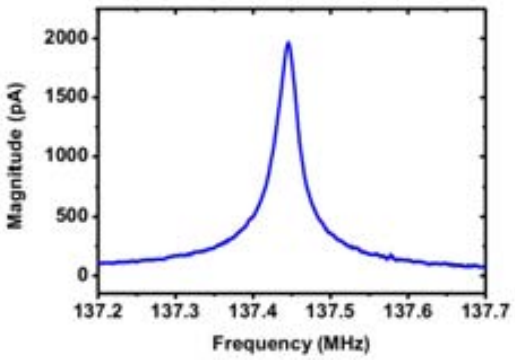

Figure 5.7: Electrical measurement of the frequency response of a resonator using the two-source, 1ω measurement method. The nanowire has a diameter of 137×110 nanometers approximately, with a length of 2-3 micrometers. Measurement conditions: $V_{NW,2source} = 120$ mV, $V_{g,DC} = 10$ V, $V_{g,AC} = 200$ mV.

Another option is that the deflection of the nanowire at rest, provoked by the stress accumulated during the fabrication process, affects the transduction signal. The idea is that, if the nanowire is sufficiently deflected, the elongation signal which usually takes place at 2 would appear at 1 , due to the nanowire not reaching its rest position (the piezoresistive transduction signal appears at the square of the amplitude of motion). This is illustrated in Figure 5.8, specially in the latest case (c): when the nanowire is deflected, it does not elongate twice per cycle, originating a 2 signal, but instead it alternates between elongation and compression during vibration.

The described effect would "translate" the 2 piezoresistive signal at frequency 1 , in some cases entirely. Furthermore, it would also explain the absence of a piezoresistive signal in the case of the studied top-down nanowires, which present an important static deflection. However, in the case of the fabricated devices, we observe a deflection in the out-of-plane direction, but not in the in-plane one. Therefore, this effect would only appear when the direction of motion is aligned with the static deflection of the nanowire. Nonetheless, during the measurements of top-down resonators the 2 signal is not detected neither in the in-plane nor in the out-of-plane directions. In any case, a deep study of this effect should be performed using FEM simulations in order to evaluate its feasibility.

5.2.1 Estimation of the amplitude of motion using scanning electron microscopy

One of the difficulties when analysing the transduction mechanisms of the resonators is the lack of information about the amplitude of vibration at resonance. With no

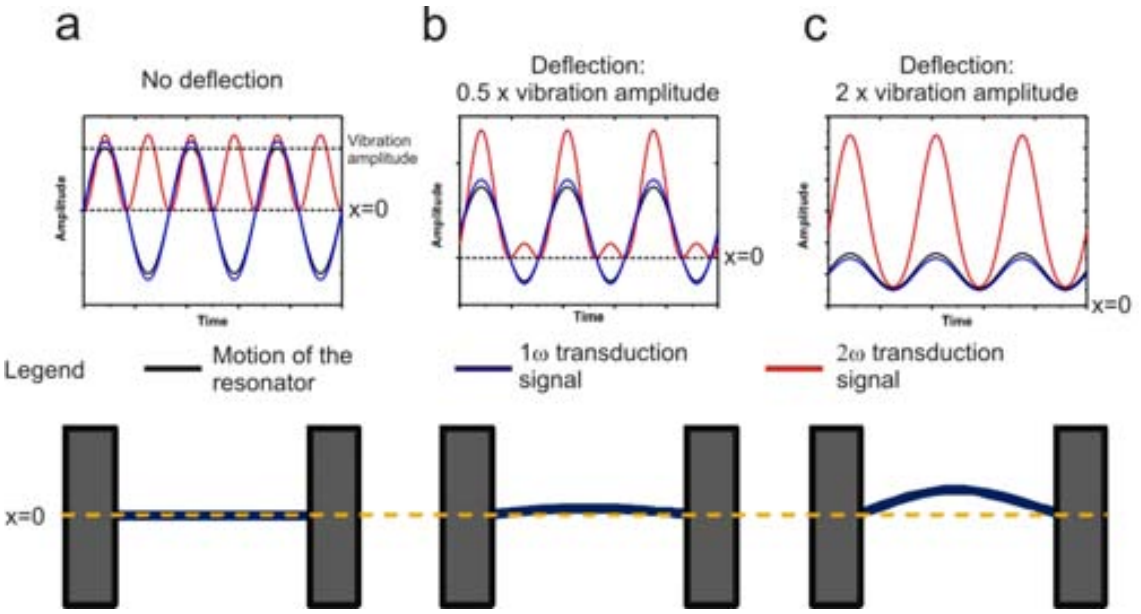

Figure 5.8: Evolution of the linear and quadratic transduction signals when the nanowire is deflected with respect to the rest position. The higher row shows the shape of the motion at the center of the resonator and the two transduction signals, while the lower row depicts the deflected resonator. a) No deflection. b) The deflection at the center of the nanowire is half of its amplitude of vibration. c) The deflection at the center of the nanowire is twice its amplitude of vibration.

information about neither the transduction mechanism nor the vibration amplitude, it is not possible to make an estimation of the transduction efficiency of the readout system. In order to estimate the amplitude of motion of the resonators, we attempt to image the resonator while it is in resonance using SEM. Furthermore, to confirm that the nanowire is in resonance, we first locate its resonance frequency electrically, and then we measure it at the same time that we inspect it with the microscope. This work has been performed in collaboration with Jordi Llobet, using the Zeiss 1560XB Cross Beam equipment located in the clean room of the IMB-CNM.

The measurement of the resonators is performed inside the vacuum chamber of the SEM equipment. The measurements are performed on chip, using low current measurement probes. The probes are connected to triaxial cables, which transport the signal through feedthroughs in the vacuum chamber to the measurement system outside. The FM detection method is employed to measure the resonators.

The measurement process is as follows. First the chips with top-down resonators are fixed to a holder inside the SEM chamber. Then the devices to be measured are located, and the SEM image is aligned with precision to the resonator using the same imaging conditions that will be used for the experiments. This step is critical, because the stage which provides motion to the sample with respect to the SEM column can not be moved once the probes are connected. Once the resonator is

aligned, the probes are positioned to the electrodes on the chip, and the lock-in is used to measure the resistance of the resonator and the electrical stability of the contacts. Once everything is correctly set-up, a frequency sweep is performed in order to find the resonance frequency of the resonator.

It is important to ensure that the detected resonance mode is in the in-plane direction, so that its motion can be observed with the microscope. During the measurements, we detect two different resonance peaks, corresponding the first mode of the resonator in the two orthogonal directions. Then, the peak corresponding to the in-plane mode is chosen from the theoretical resonance frequencies extracted from the dimensions of the nanowire. Also, the direction of the resonance mode is confirmed applying changes to the DC voltage of the side-gate and the substrate: the in-plane mode is very sensitive to changes in the voltage of the side-gate, while the out-of-plane mode is more sensitive to changes of the DC voltage of the substrate. After these measurements, the substrate of the chip is connected to ground during the rest of the experiments, to avoid the accumulation of charges provoked by the electron beam.

Once the in-plane mode is located, the excitation frequency is set to match the resonance frequency of the resonator, so that the detected current is maximum. We have found that exposing the resonator to the electron beam of the SEM increases the resonance frequency of the resonator, so during the exposition the excitation frequency has to be continuously adjusted so that the output current is maximum. Then we take high resolution images of the resonator while maintaining it in resonance.

Figure 5.9 shows SEM images taken during the experiments, using the same imaging conditions but under different electrical measurement conditions: 1) with the actuation signals applied to the resonator at the resonance frequency, while the nanowire is at resonance; 2) with the actuation signals applied to the resonator but with an excitation frequency far away from the resonance (i. e. the nanowire is not at resonance); 3) and without electrical signals applied to the resonator. We observe that under condition 3 (with no electric signals) the image has the best quality. When we turn on the actuation signals (2) a deformation appears in the image, due to the voltage applied to the nanowire and to the side-gate. However, we observe very little difference between the nanowire in resonance (1) and out of resonance (2): the width of the wire seems to be the same, with only some minor differences in the shape of diagonal lines at the edge of the structure. The image in Figure 5.9b shows a detail of the center of the nanowire (where the amplitude of vibration should be maximum) under the different conditions. The red marks have the same dimensions in all three cases, for ease of comparison.

From the imaging experiments we don't observe a widening of the resonator when it is in resonance. Moreover, from the noise of the images in conditions (1) and (2),

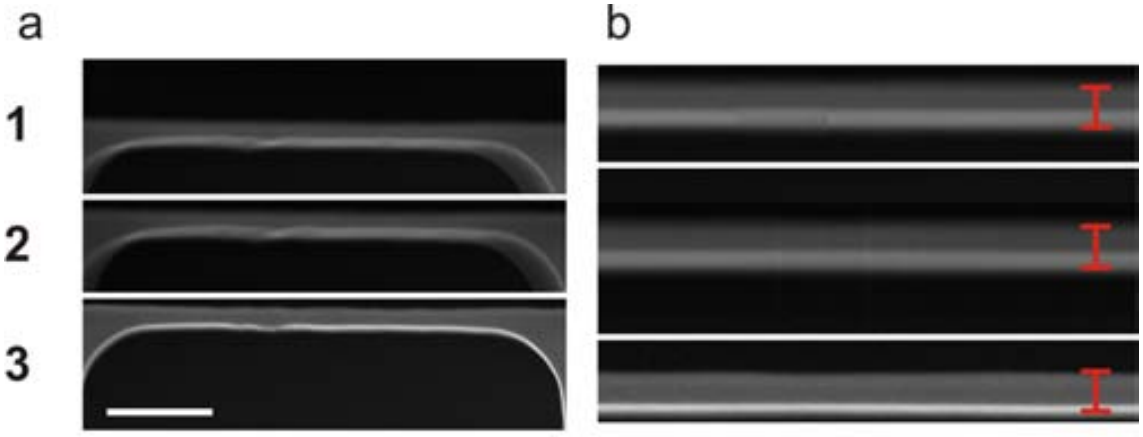

Figure 5.9: SEM images of the resonator while applying different actuation signals, using the same imaging conditions. The resonator has a width of 120 nanometers. Scale bar: 500 nm. Actuation conditions: $V_{g,DC} = 15$ V, $V_{NW} = 3.5$ V. 1) nanowire in resonance, actuation signals applied. 2) nanowire out of resonance, actuation signals applied. 3) nanowire out of resonance, actuation signals not applied. a) General view of the resonator. All of the images are taken with the same magnification. b) Detail of the image at the center of the resonator, where the oscillation amplitude is maximum. The red marks have the same dimensions in all three conditions, for ease of comparison. All of the images are taken with the same magnification.

we estimate that their resolution in the direction of motion is around 10 nanometers, that is, from these images we wouldn't be able to detect an amplitude of vibration lower than 10 nanometers. This imaging resolution allows us to establish an upper limit to the amplitude of vibration of the resonator, and therefore a minimum value for the actuation efficiency using the current measurement conditions. The peak current detected during the experiments, when the amplitude of vibration is maximum, is around 6 nA. Therefore, taking the amplitude of motion of the resonator as the resolution of the image, we establish a lower value for the transduction efficiency of 0.6 $\mathrm{A{\cdot}m^{-1}}$, or 0.6 $\mathrm{nA{\cdot}nm^{-1}}$.

In conclusion, these experiments confirm that the amplitude of motion of the nanowire at resonance is below 20 nanometers. This result also confirms that the transduction is not caused solely by conductance modulation due to accumulated charge in the side-gate: during the simulations performed to evaluate this transduction mechanism, we arrived to the conclusion that huge amplitudes of motion would be needed to justify the detected signals, and now we have confirmed that this is indeed not the case. Therefore, another mechanism or combination of mechanisms must be responsible for the transduction of the motion of the resonator.

5.3 FEM simulations of the frequency response of top-down resonators

The top-down resonators studied in this work have a complex geometry, in the sense that they present some particularities which differ from the ideal cc-beam theoretical model. Therefore, their study using the beam theory presented in Chapter 1.1 is of limited use. In section 4.3.2 we have observed that their geometry and internal stress are affected by the high-temperature oxidations which take place during their fabrication. Therefore it is important to build and simulate a model of the resonators based on finite elements which takes into account the particularities of these resonators, in order to study their behaviour and compare it with the experimental results. In this section, this model and its simulations are presented, and the obtained results are compared with the experimental characterization results.

The geometry of the resonators is studied using SEM images and AFM, as explained above. The fabrication process presents some variability, so it is important to characterize each individual chip and, if possible, each studied resonator in order to obtain information as accurate as possible. One of the terms which is difficult to characterize is the underetch of the electrodes fabricated from the silicon device layer: this effect is caused by the release of the resonators from the thermal silicon oxide grown during the oxidation, using a wet etching. This underetch is visible in Figures 5.10a-b. The position of this underetch makes it difficult to characterize it using SEM, and moreover it varies importantly from chip to chip. For this reason, in order to reliably characterize it, we perform FIB milling in the clamping regions of a measured resonator and inspect its shape by SEM (Figure 5.10b). The underetch worsens the quality of the clampings (lowering their rigidity and increasing the clamping losses) and reduces the resonance frequency of the resonator.

Due to the effects explained above–and contrary to the case of bottom-up nanowires, where the clampings could be considered perfect–the model of the top-down resonators must include the particular geometry of the clampings. We build a model of the resonator based on the information obtained from the SEM images, which is shown in Figure 5.10c superimposed to a SEM image of the resonator. The resonator and clampings are modelled as a layer of silicon with some fixed areas, which represent the regions where the layer is in contact with the buried silicon oxide. Therefore, this silicon oxide layer is considered to remain immobile and present a perfect adhesion to the silicon. As these clamping regions are not well characterized, they are one of the parameters adjusted during the simulations. Furthermore, the resonator is modelled as a rectangular beam of constant cross-section, with rounded sections which connect it to the silicon layer at both its ends.

The modelled resonators are simulated using the Ansys software [7]. Modal simulations of the structures are performed in order to obtain the resonance frequencies

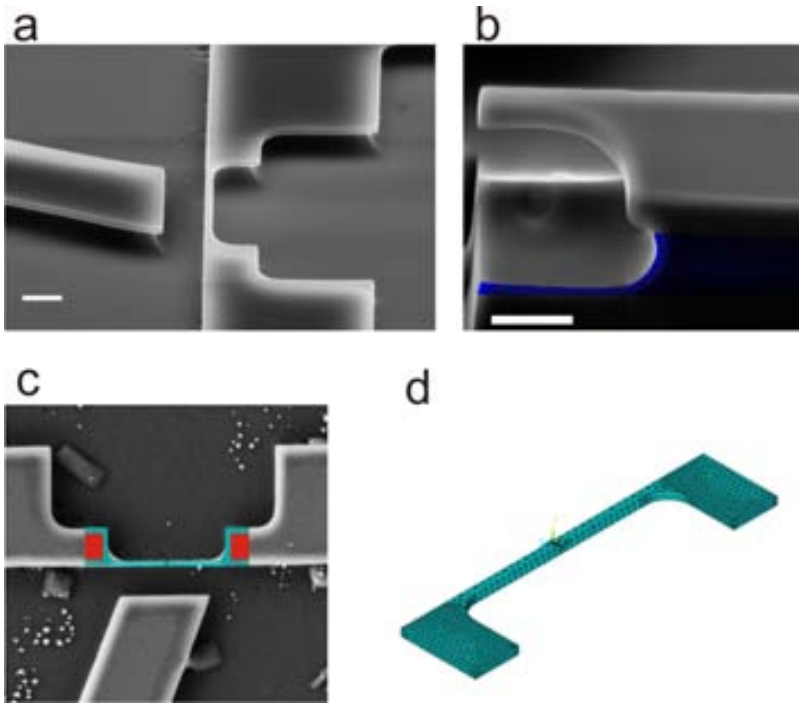

Figure 5.10: Modelling of the top-down nanomechanical resonators for FEM simulations. a) SEM image of a top-down resonator. The underetch of the silicon layer caused by the wet etching is visible. Scale bar: 1 μm. b) SEM image of a transversal cut on the clamping are of the resonators. The buried oxide layer which provides the clamping is coloured in blue. In this image, an underetch of 100 nanometers approximately is observed. Scale bar: 0.5 μm. c) Top view of the model superimposed to a SEM image of a real resonator. The clamping areas used during the simulation are marked in red. d) Tilted view of the model used for FEM simulations.

and shapes of the different modes, similar to those performed for bottom-up nanowires. Some results of these modal simulations are presented in Figure 5.11, showing the shape of the first modes of resonance. We find that these modes correspond to the first three in-plane and out-of-plane modes, as expected from beam theory. In addition, the figure reproduces the experimental measurements of Figure 5.1, in order to relate each detected peak with its particular modeshape. We observe that the amplitude of the in-plane and the out-of-plane peaks are in the same order of magnitude, even though the excitation force presumably has its main component in the in-plane direction. Another interesting conclusion of the simulations is that the in-plane and out of plane modes are found alternated (the peaks at the lowest resonance are the first out-of-plane and the first in-plane modes respectively, followed by the second out-of-plane and in-plane modes, and so on).

Besides the modeshape, the modal simulations also provide the value of the different resonance frequencies of the structure. During these simulations, we try to adjust different geometric parameters and the axial stress along the beam, in order

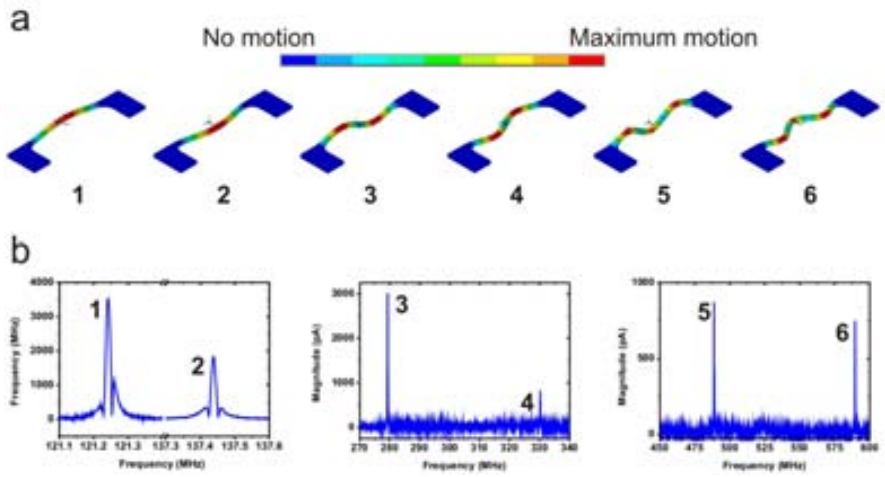

Figure 5.11: Ansys modal simulations of the top-down nanomechanical resonators, using a geometry base on that found on the measured devices. The first 6 modes of the resonator are simulated, corresponding to the first three modeshapes in different directions. a) Image of the shape of these modes, sorted from lower to higher frequency. The scale bar represents the amplitude of motion of each part of the structure for each mode. b) Correspondence between the simulated modeshapes and the resonance peak obtained during the measurement of a resonator (with a diameter of 137 × 110 nanometers approximately, with a length of 2-3 micrometers). An exact fitting of the frequencies is not performed in this case. Modes 1,3,5 are out-of-plane, and modes 2,4,6 are in-plane.

to fit the simulated values to the experimental ones, following the same procedure that for the bottom-up nanowires. However, we are not able to correctly fit the frequencies of all of the modes with only these parameters. This is probably due to the fact that the stress present in the structure is more complex than a simple axial value, as the deformation of the structure suggests. Also, the curvature found during the AFM characterization is not included in the simulations. It must also be noted that simulating the frequency of the modes of the resonator with a good agreement with six different modes is a complex task, specially with a structure with such particularities.

A good fitting of the resonance frequencies can be achieved by adjusting the geometry (width and thickness) of an undeflected resonator, and afterwards each component of the stress separately. Although this method yields good results, it is difficult to evaluate if these levels of stress are in good concordance to those found in the structure, specially when the deflection present in the nanowire is not simulated. The simulation results, and their concordance with the measurement results are presented in Table 5.1.

The Ansys FEM simulations are also used to study the capacitance between the resonator and the side-gate. Similarly to the bottom-up simulations, the capacitance is studied using the CMATRIX environment, which allows to extract

Mode (n)	Simulated f_n	Experimental f_n	Difference
1	121.1×10^6	121.2×10^6	-
2	137.4×10^6	137.5×10^6	-
3	278.2×10^6	279.4×10^6	0.4%
4	329.4×10^6	330.3×10^6	0.3%
5	483.6×10^6	488×10^6	0.9%
6	597.02×10^6	589×10^6	1.4%

Table 5.1: Comparison between the experimental measurements and the simulation results for a top-down resonator. The geometry of the model is based on SEM inspection, with some adjustments in order to fit the experimental frequencies: the thickness of the resonator, which is difficult to characterize using SEM, has been slightly modified. An overhang of the silicon layer of 100 nanometers due to the wet etching is also adjusted for these simulations. The final model of the resonator has a section of 137×125 nanometers and a length of 2.8-3.6 μm. The numbering of the modes follows that of Figure 5.11 (modes 1,3,5 are out-of-plane, and modes 2,4,6 are in-plane). Different stresses perpendicular to the axial direction are introduced to fit the different resonance modes, more concretely an in-plane stress of 600 MPa and out-of-plane stress of 830 MPa.

the capacitance between two different parts of the model surrounded by a certain medium. The capacitance value obtained with this method is then used to evaluate the proposed transduction mechanisms, more concretely the conductance modulation due to charge accumulated in the resonator by coupling with the side-gate. As this transduction mechanism is heavily influenced by the capacitance between both elements, the correct determination of this parameter is critical for its study, and more concretely for the determination of the capacitance change during the vibration of the resonator C_g C_g. For the evaluation of this parameter, the capacitance between the nanowire and the side-gate is simulated for the nanowire at rest, and for different levels of deflection of the beam, in order to simulate the behaviour of the capacitance during the motion of the resonator. From these series of simulations, the change of capacitance during the motion C_g C_g is extracted. The model employed for the evaluation of the capacitance between the resonator and the side-gate is shown in Figure 5.12, and includes the simulated resonator with a side-gate nearby and the surrounding medium (not shown).

5.4 Comparison between top-down and bottom-up silicon nanowire resonators

During this thesis we have fabricated and characterized nanomechanical resonators based on bottom-up and top-down nanowires. These different approaches yield devices of comparable dimensions and material, and the same methods have been

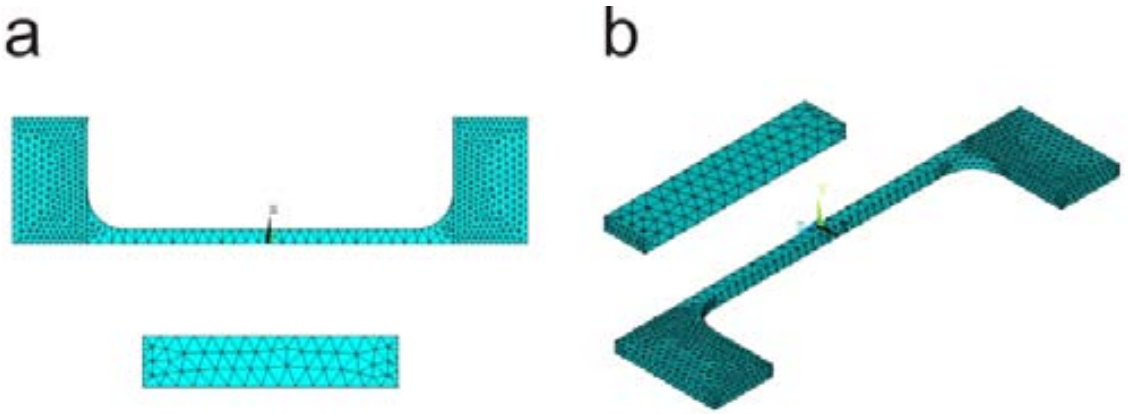

Figure 5.12: Ansys model used for the simulation of the capacitance between the resonator and the side-gate. The model also includes a medium which surround both elements (not shown).

used to characterize them. For this reason, this work presents a good basis to compare bottom-up and top-down technologies, from the device point of view as well as its fabrication. This section presents a study of the differences between the resonators fabricated using both approaches, some of them which have already been mentioned in other parts of this work. The study is divided in two parts: the fabrication and geometry of the resonators, and the electrical characterization of their frequency response. At the end of each part, a table summarizing the most important points is included.

5.4.0.1 Fabrication results and geometry

The fabrication of the bottom-up nanowires is based on the use of a VLS synthesis method, in which the nanowires grow in Si crystalline substrates (which can be pre-patterned with other structures) from a reaction catalysed by gold nanoparticles. These nanoparticles can be fabricated with small diameters (down to nanometers) and with a good control over the variability of their dimensions, allowing the relatively simple fabrication of nanowires of small diameters, which grow only in the areas where the catalyst is present and along a certain crystalline direction of the substrate. However, the controlled placement of this catalyst is currently the limiting step in this technological approach: it is complex to place these nanoparticles in specific positions of the chip, and in order to reliably fabricate nanomechanical resonators, their placement is a key issue. Despite these problems, using a random deposition technique, we succeed in fabricating resonators based on bottom-up nanowires with diameters close to 50 nanometers, positioned near a side-gate for electrical actuation.

On the other hand, top-down technologies are very well studied and controlled, because they have been used for decades for the fabrication of ICs. These techniques

provide a reliable fabrication approach, but their resolution is limited by the photolithography step, which is used to define patterns on the substrates. In most cases, this step presents a resolution of hundredths of nanometers, which is insufficient for the desired dimensions. We circumvent this limitation by using photolithography followed by oxidation steps, which are used to reduce the dimensions of the fabricated structure. Using this approach, we are able to fabricate nanowires of dimensions comparable to those fabricated by the bottom-up method (with diameters from 72 to 140 nanometers) and moreover using batch fabrication methods, yielding a high number of devices per chip.

As we can see, both approaches have their advantages and disadvantages: the bottom-up approach provides a relatively controlled method to fabricate nanowires of small diameter with little control over their placement, while with the top-down approach a well controlled batch fabrication is possible but the fabrication of structures with small dimensions is a complex issue. In this work, we have fabricated nanowires with both approaches, succeeding in fabricating resonators of comparable dimensions using both techniques: clamped-clamped beams with diameters in the order of tens of nanometers and lengths in the order of micrometers. The material of the devices is also very similar, crystalline silicon in both cases, albeit with different crystalline orientation. We have also exploited the particular advantages of each individual technique, fabricating nanowires of 50 nanometers with the bottom-up approach, and taking advantage of the batch fabrication to pattern a high number of devices per chip using the top-down approach.

The different fabrication methods also have an impact in the geometry of the fabricated resonators, beyond their specific dimensions. Using the bottom-up method, the obtained nanowires are hexagonal prisms with low surface roughness with a slight tapering in their section. Furthermore they present excellent clampings at both of their ends, rigid and immobile. In the case of top-down nanowires, they are rectangular beams but their section is not completely constant, presenting an important widening towards their ends. Moreover, they exhibit a certain deflection, provoked by the accumulation of stress during the fabrication process. Also, their clamping are not completely rigid, but present a certain mobility caused by overhangs caused by the fabrication process.

5.4.0.2 Electrical measurement

The objective of this work is the study of the frequency response of the nanomechanical resonators, and more specifically their modes of resonance. The resonators fabricated using both approaches have been electrically measured using the same techniques, the downmixing of the high frequency transduction signal to a low frequency measurement signal, which carries information about the motion of the resonator. More concretely, they have been measured using the FM and two-source

Fabrication		
	Bottom-up	Top-down
Fabrication method	grown (VLS)	etched (photolitho.) + oxidation
Minimum cross-section	50 nm (hexagonal)	72 × 60 nm
Control over diameter	good	limited by control over oxidation
Control over placement	poor (random)	good
Orientation	Si <111>	at choice
Fabrication throughput	low	high
Geometry	hexagonal prism	rectangular prism
Diameter's symmetry	high	low
Clamping	fixed and epitaxial	not completely rigid, underetch
Stress	compressive	complex

Table 5.2: Comparison of the fabrication method and results with the employed bottom-up and top-down methods.

techniques. For both fabrication approaches, the FM technique has been demonstrated to provide an outstanding method to characterize the frequency response of the resonators, permitting the characterization of high order modes of resonance, with high SNRs compared to other methods and presenting signals of mechanical origin, without contribution of purely electrical components which hinder the characterization. Moreover, the FM technique has permitted the characterization of the frequency response of both bottom-up and top-down resonators up to the third resonance mode for different directions of vibration.

One of the differences between the measurement of these different kinds of devices is the SNR, and more specifically the signal levels provided by the resonators at resonance. We find that the top-down resonators present much higher signal levels, finding resonance peaks with amplitudes up to 8 nA. On the contrary, the bottom-up resonators typically present much lower signal levels, of 1 nA of amplitude at most. However, when comparing resonators of similar diameters, we find that the signal levels are also comparable: therefore, this is probably not provoked by intrinsic differences due to the fabrication methods, but due to the disparity of the typical dimensions of the measured nanowires, which are larger for the top-down than for the bottom-up resonators. During the measurements we find the same noise levels for top-down and bottom-up nanowires, because in our case this parameter is probably limited by the noise in the readout instrumentation.

Another difference found during the measurement of the top-down and bottom-up nanowires is their dynamic range, that is, the difference between the minimum detectable signal and the maximum linear signal level. We find that bottom-up nanowires, specially for small diameters and for the first mode of resonance, tend to

behave nonlinearly even for low excitation signals. This yields low signal-to noise ratios, derived from the limited linear range of the device, which restricts the amplitude of the obtained signals. On the contrary, top-down nanowires behave linearly in most cases, allowing to increase the magnitude of excitation and transduction signals and obtaining better signal-to-noise ratios. This behaviour is again expected taking into account the difference in lateral dimensions of the resonators. In all of the cases, the detected nonlinear effects are possibly caused by spring hardening, originated by an excessive elongation of the resonator during its motion which causes changes to its rigidity. This effect is important when the amplitude of vibration is large with respect to the diameter of the resonator. Therefore, resonators with thicker diameters (in our case, top-down resonators) allow higher linear amplitudes of vibration than resonators with smaller diameters (bottom-up). Additionally, in our system the noise is limited by the measurement system. Therefore, the dynamic range is probably the origin of the higher SNRs and signal levels found in top-down nanowires, derived from their thicker diameters.

The quality factor of the resonators is also an important parameter, specially for their use as sensors. In devices of our characteristics, the FM method presents some particularities that make it difficult to measure the quality factor of the resonators, arising from a widening of the electrical response in relation to the mechanical one. Another of the used measurement methods, the two-source, 1 , presents a parasitic electrical signal which generally distorts the shape of the resonance and also hiders the determination of the quality factor. For these reasons, we have not been able to perform an exhaustive study of the quality factor in all of our devices. However, for the measured bottom-up nanowires we have found quality factors in the order of 2000 to 3000 for the fundamental mode. On the other hand, during the measurement of top-down nanowires the obtained quality factors are in some cases of 4500 or more. Again, this difference in quality factor can be attributed to several facts, with the dimensions of the resonators being one of them. One of the important contributions to dissipation in the case of nanomechanical resonators are surface defects, specially for resonators fabricated with materials with low density of bulk defects (such as crystalline silicon). Beams of smaller diameters present higher surface-to-volume ratios, and therefore the importance of surface defects increases. Some studies have pointed out that the tendency in nanomechanical resonators is to have decreasing quality factors with decreasing dimensions for this reason [8]. In general, we have found lower quality factors when measuring nanowires of smaller dimensions: therefore it is possible that the dimensions have an influence in the difference of the measured quality factors. Additionally, a multitude of factors have been found to intervene in the energy dissipation in a nanomechanical resonators, such as clamping losses, the stress, surface and bulk defects, etc. For this reason, it is difficult to perform a more detailed study of this factor.

Measurement results

	Bottom-up	Top-down
Detected modes	1st to 3rd modes	1st to 3rd modes
Range of frequencies	50-413 MHz	80-590 MHz
Detected directions of vibration	2 (1st and 2nd modes)	2 (all modes)
Peak signal level	1 nA (max.)	8 nA (max.)
SNR	lower	higher
Linearity of the measured response	important non-linearity	mostly linear
Dynamic range	lower	higher
Quality factor	3000 (max.)	4500 (max.)

Table 5.3: Comparison of the measurement results for bottom-up and top-down resonators.

One of the important geometrical differences between the resonators fabricated using both approaches is the shape of their cross-section. Bottom-up nanowires have a regular hexagonal cross-section, while the top-down typically present a rectangular or even oval cross-section. One direct consequence of this fact is the relation between the resonance modes of the resonators in different directions. In the case of bottom-up nanowires, the difference in the resonance frequency of the modes in different directions is caused by imperfections in its section. Therefore, the modes corresponding to orthogonal directions are generally at frequencies close together. This provokes an interesting behaviour in mass sensing applications, because a small deposited mass can then easily affect the relative frequencies and directions of vibration of these modes. On the other hand, the section of the top-down resonators causes two orthogonal modes at two very different frequencies, due to a high difference of diameter in the different directions of vibration. This renders the resonator more insensitive to the mentioned mode rotation effects, which add an additional layer of complexity to the response of the resonator in mass sensing applications. This is not in itself an advantage, but it can be useful depending on the application of the resonator.

The characterization of high modes of resonance of the bottom-up and top-down resonators allow to extract additional information of complex effects such as the stress of the structure. FEM simulations have been performed based on the geometry of the resonators, in order to study the correspondence between the theoretical and the measured resonance frequencies. The model of the bottom-up resonators is easy to build and simulate, thanks to their simple geometry. We find that the measured resonance frequencies are always below the ones predicted based on their dimensions. During the simulations we found that this divergence is probably due to compressive stress in the structure, accumulated during the fabrication process. This is compatible with the buckling observed in some of the nanowires inspected

Measurement methods and transduction mechanisms

	Detection method	Transduction mechanism	Efficiency
Bottom-up	FM	linear	good
	Two-source, 1	linear	good
	Two-source, 2	quadratic (piezoresistive)	weak, only 1st mode
Top-down	FM	linear	good
	Two-source, 1	linear	good
	Two-source, 2	-	null

Table 5.4: Measurement methods and transduction mechanisms for bottom-up and top-down resonators.

with SEM. However, the structure of the top-down resonators is not so simple, and presents some particularities which are difficult to characterize using SEM (the deflection of the beam due to accumulated stress, the overhangs caused by the underetch of the silicon layer,...). For this reason, the building of a geometrical model of the resonator is more complex than for the case of the bottom-up devices. During the simulation we find some discrepancies between the predicted values and the measured ones, which can not be explained solely by geometrical effects or axial stress in the structure. This leads us to believe that the deflection of the beam and the associated stress effects have an important effect on the resonance frequencies of the structure. Therefore, we find that the two fabrication approaches present different particularities associated with accumulation of stress, which affect the behaviour of the two families of devices in different ways.

The employment of different two-source techniques also allow the study of the origin of the transduction mechanisms in the measured resonators. We find that there are two families of transduction methods which transform the motion of the resonator in measurable electric signals: linear transduction (1) which provides a transduced signal proportional to the motion of the resonator, and quadratic (2), which generates a transduced signal at twice the resonance frequency. The FM technique, which is used for the measurement of both bottom-up and top-down nanowires, relies in the 1 transduction mechanism. Therefore, thanks to the measurement results, we can assert that this is the dominating transduction mechanism for the two types of devices. Also, bottom-up nanowires had previously measured using a piezoresistive downmixing scheme based on 2 transduction. We have reproduced these results and confirmed the existence of a 2 transduction mechanism for bottom-up nanowires. However, this 2 transduction signal has been found to be weaker that the one at 1 , specially for higher modes, hinting at a higher efficiency of the 1 transduction mechanism. Interestingly, we have not observed 2

transduction in top-down nanowires in any case. One possible explanation for this absence is that the deflection of the top-down nanowires "translates" the 2 signal into 1 , due to the nanowire never reaching its neutral position during resonance. Nonetheless, the exact origin of the 1 transduction signal is still not clear: we have trouble relating the experimental results to some of the known linear transduction mechanisms. This is, in part, due to a lack on knowledge of the exact amplitude of motion of the resonators during oscillation.

In conclusion, the fabrication and characterization of nanomechanical resonators based on different approaches provides a good platform for the evaluation of the different fabrication methods. In this work we have evaluated the advantages and disadvantages of these fabrication approaches. Moreover, during their characterization and simulation we found that the differences between their behaviour could be attributed to geometrical and stress effects arising from their fabrication.

References

[1] A. Koumela, D. Mercier, V. Gouttenoire, C. Marcoux, S. T. Purcell, and L. Duraffourg, "Silicon nanowire resonator with integrated electrostatic actuation," *Procedia Engineering*, vol. 25, pp. 1649–1652, 2011.

[2] A. Koumela, D. Mercier, C. Marcoux, L. Duraffourg, and S. Purcell, "Performances of suspended silicon nanowire resonators for time reference applications," in *Frequency Control Symposium (FCS), 2012 IEEE International*, pp. 1–4, 2012.

[3] V. Gouttenoire, T. Barois, S. Perisanu, J.-L. Leclercq, S. T. Purcell, P. Vincent, and A. Ayari, "Digital and FM demodulation of a doubly clamped single-walled carbon-nanotube oscillator: Towards a nanotube cell phone," *Small*, vol. 6, no. 9, p. 1060–1065, 2010.

[4] J. Verd, G. Abadal, J. Teva, M. Gaudo, A. Uranga, X. Borrise, F. Campabadal, J. Esteve, E. Costa, F. Perez-Murano, Z. Davis, E. Forsen, A. Boisen, and N. Barniol, "Design, fabrication, and characterization of a submicroelectromechanical resonator with monolithically integrated CMOS readout circuit," *Journal of Microelectromechanical Systems*, vol. 14, pp. 508 – 519, June 2005.

[5] J. Arcamone, G. Rius, G. Abadal, J. Teva, N. Barniol, and F. Pérez-Murano, "Micro/nanomechanical resonators for distributed mass sensing with capacitive detection," *Microelectronic Engineering*, vol. 83, pp. 1216–1220, Apr. 2006.

[6] H. B. Peng, C. W. Chang, S. Aloni, T. D. Yuzvinsky, and A. Zettl, "Microwave electromechanical resonator consisting of clamped carbon nanotubes in an abacus arrangement," *Physical Review B*, vol. 76, p. 035405, July 2007.

[7] "ANSYS - simulation driven product development. http://www.ansys.com/."

[8] H. W. C. Postma, I. Kozinsky, A. Husain, and M. L. Roukes, "Dynamic range of nanotube- and nanowire-based electromechanical systems," *Applied Physics Letters*, vol. 86, pp. 223105–223105–3, May 2005.

Chapter 6

Mass sensing based on nanomechanical resonators

Contents

In the last years, the field of mass sensing based on nanomechanical resonators has experienced an impressive evolution, fuelled by the decreasing dimensions of NEMS. This kind of mass sensing is based on monitoring the resonance frequency of a mechanical structure, which changes when a mass is deposited on its surface. Generally, decreasing the dimensions of nanomechanical resonators brings about a decrease of their mass and an increase of their resonance frequency, and both parameters provoke an improvement of their characteristics as mass sensors. Because of

this, the miniaturization of the resonators has derived in unprecedented sensitivities in the last years, with an increasing interest on the deep study of these systems.

This chapter deals with the use of nanomechanical resonators as mass sensors. The first part of the chapter conforms an introduction to the field of mass sensing based on nanomechanical resonators, including an introduction to the field and the state of the art and the theory of mass sensors based on nanomechanical resonators. The second part of the chapter deals with the evaluation of nanomechanical resonators as mass sensing devices. First, a numerical evaluation of the maximum attainable mass resolution using nanomechanical resonators is performed. Then, the implementation of a close-loop topology for the real time tracking of their resonance frequency is described, which is used to monitor changes in the response of the resonator and to study the frequency stability and mass resolution of the system. Finally, an evaluation of the performance of the fabricated nanowires as mass sensors is performed.

6.1 Introduction to mass sensing based on NEMS

The small dimensions of electromechanical systems provide advantages on a high number of applications. In the case of nanomechanical resonators, they present low masses and high resonance frequencies, which makes them outstanding candidates as mass sensing devices. The sensing principle is the dependence of the resonance frequency of these structures to changes on their mass: therefore, by tracking the resonance frequency, changes to the mass of the resonator (such as those provoked by deposited particles or films) can also be monitored. In this sense, the mass of the resonator is one crucial parameter in mass sensing: the lower the mass of the resonator, the higher the relative change of mass provoked by the deposition of a determinate mass, and therefore the higher the change in the resonance frequency. Similarly, when depositing a determinate amount of mass on the resonator, the resulting absolute frequency shift is larger the higher is the resonance frequency of the resonator. Hence, low masses and high resonance frequencies are desirable characteristics in a nanomechanical resonator acting as a mass sensor.

In the last years, the field of mass sensing based on nanomechanical resonators has experienced simultaneous improvements in two of its aspects: on the one hand, the miniaturization of the resonators, allowing increased mass sensitivity and resolution, and on the other hand advances in the understanding of the mass sensing principle, which have originated an improvement of the sensing methods. These evolutions have led this field to a situation where it is applicable to mass spectrometry [1, 2, 3, 4].

The evolution of top-down fabrication techniques and the introduction of bottom-up technologies, specially CNT-based resonators, have enabled an increasing minia-

Author & year	Resolution	Responsivity	Conditions
Yang, 2006 [5]	7 zg	0.96 Hz/zg	TD-NEMS, T=4.2 K
Verd, 2008 [6]	80 zg	1.1 Hz/ag	CMOS-NEMS, T=300 K
He, 2008 [7]	0.5 zg *	15 Hz/zg	SiNW, T=300 K
Jensen, 2008 [8]	1 zg	100 kHz/zg	CNT, T=300 K
Lassagne, 2008 [9]	25 zg	11 kHz/zg	CNT, T=300 K
Feng, 2008 [10]	50 zg	-	TD-NEMS, T=22 K
Chiu, 2008 [11]	0.2 zg	-	CNT, T=6 K
Naik, 2009 [2]	1.7 zg	12 Hz/zg	TD-NEMS, T=40 K
Chaste, 2012 [4]	1.7×10^{-3} zg	-	CNT, T=58 K
This work, bottom-up	-	6.6 Hz/zg	SiNW, T=300 K
This work, top-down	6 zg	3.7 Hz/zg	TD-NEMS, T=300 K

* Estimated value

Different configuration: cantilever, not integrable

The responsivity represents the best value obtained with the technology; the mass resolution is extracted from the experimental frequency stability tests.

Table 6.1: State of the art in mass sensors based on nanomechanical resonators. For comparison, only the optimum mass responsivities and resolutions are shown. The resolution and responsivity are defined in zeptograms (1 zg=1×10^{-21} g). The term TD-NEMS denotes a top-down resonator, and CMOS-NEMS a resonator monolithically integrated with CMOS technology.

turization of the resonators, and hence an improvement of the maximum attainable mass sensitivity and the minimum resolution in mass sensors based on NEMS. Table 6.1 presents a summary of some of the works in mass sensing of the last years, including the most significant mass sensing parameters: the minimum detectable mass (Δm) and the responsivity (the shift of the resonance frequency as a function of the deposited mass). We observe that the major part of the devices are fabricated using top-down approaches: although this technology typically presents a better repetitivity and control over the fabrication, the obtained resonators do not present the best characteristics as mass sensors, due to their typically larger dimensions. On the other hand, we observe that bottom-up devices, specially CNTs, present much larger mass sensitivities: the hollow structure presented by these structures confers them a very low mass, therefore making them more sensitive to external masses deposited on their surface. The mass resolution depends on the sensitivity of the resonator and the noise of the system: therefore, a high sensitivity is crucial to obtain a good resolution, but low noise levels and good frequency resolution are equally important. We observe that the sensitivity of the devices fabricated during this work are in the range of the state of the art for bottom-up nanowires and top-down NEMS:

a detailed discussion of their performance as mass sensors is performed in section 6.3.3.

In parallel to the improvement of the intrinsic characteristics of the resonators as mass sensors, the study of mass sensing principles and the application of these sensors in real systems has been studied. One of the issues of these resonators for the detection of punctual masses is the dependence of the response of the sensor (i. e. the resonance frequency shift) on the position of the deposited mass. This effect, which was well know, has been further studied in the last years [11, 12, 13]. Therefore, a precise determination of the amount of mass deposited on the sensor involves knowing the position where this mass lands. This difficulty has been circumvented in some studies by performing statistical analysis. The idea is depositing a determinate type of particles with fixed mass (such as atoms or molecules) and monitoring a high number of frequency shifts in the response of the resonator [11, 2, 4]: a statistical analysis of these frequency shifts allows to determine the value of the mass of the deposited particles with precision. The downside of this method is that this analysis can not be performed in real time. More recently, an alternative to monitor the position and mass of accreted particles in real time has been demonstrated. It is based on the monitoring of the resonance frequency of several modes at the same time, which are affected differently by the position of the mass deposited on the resonator. By correlating the frequency shift of different resonance modes it is possible to decouple the effects of the mass and the position, and therefore the measurement of the deposited amount mass in real time is possible. This approach has been used by Hanay et al. for the real-time detection and weighing of proteins [3].

6.2 Characteristics of mass sensors based on nanomechanical resonators

In this section the main parameters that define the performance of mass sensors based on nanomechanical resonators are presented. Afterwards, the scaling of these parameter with the dimensions of the resonator are shown, followed by a study of the effect of the position of the deposited mass on the response of the sensor and the definition of the dynamic range. The study is centred in the cc-beam topology, which is the one employed for all of the resonators fabricated in this work.

6.2.1 Mass sensing parameters

During the theoretical study of nanomechanical resonators (section 1.1) we determined that the resonance frequency depends on the mass of the resonator, and

therefore a change of this mass provokes a shift of the resonance frequency. Particularly, the resonance frequency depends on the mass and the stiffness on the resonator. These contributions have opposite effects in the resonance frequency: an increase in stiffness provokes an increase in the resonance frequency of the resonator, while an increase in the effective mass provokes a decrease of the resonance frequency. In practice, a particle or mass deposited on the resonator provokes a change on both parameters. However, for a mass much lower than the mass of the resonator, the stiffness effects can be neglected, and the main contribution corresponds to the deposited mass. Throughout this section the deposited mass is considered to produce a negligible change in the stiffness of the resonator, and therefore its only contribution is a modification of its mass.

The two most important parameters to characterize the performance of a sensor are its sensitivity and resolution. The sensitivity is defined as the ratio between the measured quantity and the response of the sensor, and its inverse is called the responsivity. Therefore, in the present case the sensitivity S_m is the ratio between the deposited mass and the frequency shift of the resonator. The second term, the resolution, is defined as the minimum change a sensor can detect in the quantity it is measuring: in the case of a mass sensor, it is the minimum detectable mass Δm. We study these parameters as a function of the characteristics of the resonators.

In the simplest case we consider a punctual mass Δm deposited at the centre of a cc-beam resonator. The resonator has an initial resonance frequency f_n, an effective mass m_{eff} and an elastic constant k. In this case, the deposited mass provokes a frequency shift Δf_n:

$$f_n - \Delta f_n = \frac{1}{2\pi} \sqrt{\frac{k}{\Delta m + m_{eff}}} \tag{6.1}$$

The mass responsivity of the resonator can be defined as:

$$R = \left| \frac{f_n}{m} \right| \approx \frac{f_n}{2m_{eff}} \quad (Hz \;\; kg) \tag{6.2}$$

A more widely employed term in the case of mass sensors is the sensitivity, which is the inverse of the responsivity:

$$S_{m,punctual} = \frac{\Delta m}{\Delta f} \approx -\frac{2m_{eff}}{f_n} \quad (kg \;\; Hz) \tag{6.3}$$

Another common situation is the deposition of a uniformly distributed film of material over the resonator. In this case, we consider that the deposition surface (on top of the beam) is $A = length \times width$. In this situation, the mass sensitivity is:

$$S_{m,area} = \frac{S_{m,punctual}}{\alpha A} \quad (kg\ \ m^2 Hz) \tag{6.4}$$

where α is the factor relating the effective mass of the resonator to its real mass $m_{eff,cc-beam} = \alpha m_{beam}$, which has been previously defined.

The resolution of a mass sensor is the minimum detectable mass Δm_{min}. In mass sensors based on nanomechanical resonators, this parameter is determined by the mass sensitivity and the minimum detectable shift of the resonance frequency Δf_{min}:

$$\Delta m_{min} = \Delta f_{min}\, S_{m,punctual} \tag{6.5}$$

Therefore,an accurate measurement the resonance frequency of the resonator is critical in order to increase the mass resolution of the system.

6.2.1.1 Effect of the scaling of the resonator on the mass sensing performance

The field of mass sensors based on nanomechanical resonators has experimented an evolution in the last years regarding the decrease of the size of the mass sensors, in order to achieve better mass sensitivity. It is interesting to study exactly how the different parameters of the resonator scale as a function of its dimensions, and how this affects the mass sensitivity.

With this objective, the different parameters involved in mass sensing (and described in section 1.1) are developed as a function of the geometrical parameters of the resonator. The study is performed for the particular case of a cc-beam, but the development for other geometries is straightforward. Following the same nomenclature used in section 1.1, the resonator has a length l, a section $b \times h$ and its motion is along the h direction. The expressions of the different parameters of the resonator as a function of its dimensions can be seen in Table 6.2.

Resonance frequency	$f_n = \frac{(k_n l)^2}{2\pi} \quad \sqrt{\frac{E}{12\rho}} \frac{h}{l^2}$	f_n	l^{-2}
Effective mass	$m_{eff,n} = \frac{192\, b\, h\, l\, \rho}{(k_n l)^4}$	$m_{eff,n}$	l
Mass sensitivity	$S_{m,punctual} = \pi \frac{1536\sqrt{3}}{(k_n l)^6} \frac{\rho^{3/2}}{\sqrt{E}} b l^3$	$S_{m,punctual}$	l^3

Table 6.2: Development of the mass sensing parameters of a cc-beam resonator with rectangular cross-section as a function of its geometrical dimensions. The length of the resonator is l, its section $b \times h$ and its motion is along the h direction. The scaling of the different parameters as a function of the length of the resonator is shown in the last column.

The same expressions can be developed for the case of a cc-beam resonator with an hexagonal cross-section, with a distance between parallel sides d. With this geometry, it is also useful to study the dependence of the sensor as a function of the diameter, as it is shown in Table 6.3.

Resonance frequency	$f_n = \frac{(k_n l)^2}{2\pi}\frac{\sqrt{10}}{12}\quad\overline{\frac{E}{\rho}}\frac{d}{l^2}$	f_n	d
Effective mass	$m_{eff,n} = 96\quad\overline{3}\frac{d^2\, l\, \rho}{(k_n l)^4}$	$m_{eff,n}$	d^2
Mass sensitivity	$S_{m,punctual} = \pi\frac{1152\sqrt{3}}{\sqrt{10}}\frac{d\, l^3\, \rho^{3/2}}{\sqrt{E}(k_n l)^6}$	$S_{m,punctual}$	d

Table 6.3: Development of the mass sensing parameters of a cc-beam resonator with hexagonal cross-section as a function of its geometrical dimensions. The length of the resonator is l, and the distance between parallel sides d. The scaling of the different parameters as a function of the diameter d is shown in the last column.

As we observe in the tables, the mass sensitivity has a strong dependence on the dimensions of the resonator, and specially on its length. A decrease of the length of the resonator increases its resonance frequency and decreases its mass, the parameters which determine the mass sensitivity of the resonator. Moreover, we also observe a strong dependence of the mass sensitivity on the $(k_n l)$ parameter, which depends on the mode of resonance. However, this does not mean that, in general, the use of higher modes of resonance provides increased punctual mass sensitivity. For the determination of this mass sensitivity, we supposed that the whole amount of deposited mass contributes to the effective mass of the resonator: for the first mode of resonance and in the case of cc-beam resonator, this only happens when the mass lands at the center of the beam. However, this condition is not the same for all of the modes of the resonator: for example, the second mode has a node at its center, and therefore a punctual mass deposited at this position does not affect its resonance frequency at all. A more extensive exposition of this effect is performed later in this chapter.

A graphical representation of the scaling of the resonance frequency and the mass sensitivity for the particular case of a cc-beam with hexagonal cross-section (the geometry of the fabricated bottom-up nanowires) is shown in Figure 6.1. We observe the strong dependency on the length of the resonator, which affects both parameters, and specially the mass sensitivity. The dimensions studied in the graph are in the order of those attainable with bottom-up fabrication technologies: the studied bottom-up nanowires have a length of 2-3 μm and a diameter of 50-100 nanometers.

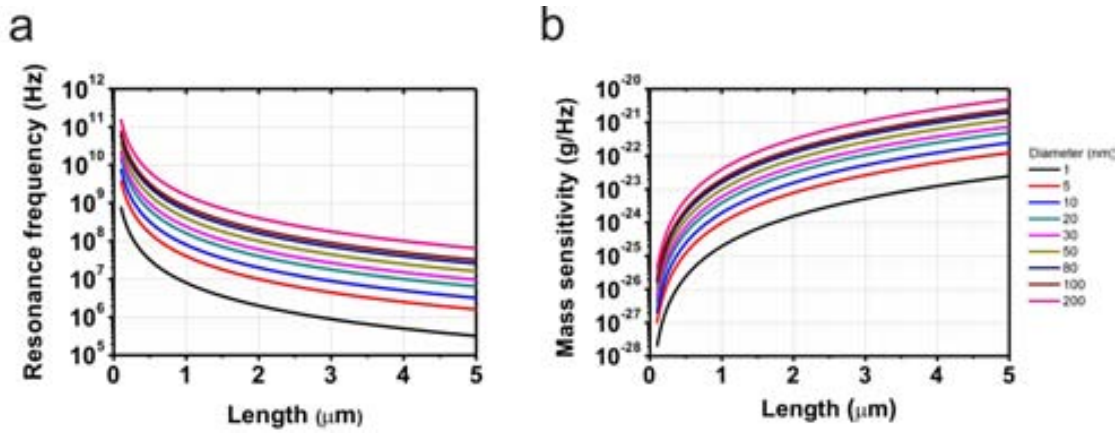

Figure 6.1: Scaling of the parameters of a nanomechanical resonator as a function of its dimensions, for the particular case of an hexagonal cc-beam. The diameter is the distance between two parallel sides of the hexagon. a) Resonance frequency. b) Punctual mass sensitivity.

6.2.2 Decoupling of the position and mass of deposited particles

Up to this point, the study of the mass sensing parameters has been mostly centered in a punctual mass deposited at the center of a the cc-beam resonator. In real applications, however, particles in general deposit at random positions along the whole length of the resonator, provoking a certain frequency shift depending on this position. We now study the effects of the position of the deposited mass on the resulting resonance frequency shift, and how to circumvent them in mass sensing.

During the modelling of the resonators the effective mass m_{eff} was presented, which is related with the real mass of the resonator m_{beam} as $m_{eff} = \alpha_n m_{beam}$. This term represents the contribution of the mass of each part of the resonator to its motion, and is particular for each mode. The α_n coefficient can be obtained by integrating the modeshape of the n_{th} mode of the resonator $w_n(x)$, shown in equation (1.15).

$$\alpha_n = \int_0^l w_n'(x)^2 \, \mathrm{d}x \tag{6.6}$$

In this case, $w_n'(x)$ is the modeshape scaled such as that $\max(w_n(x)) = 1$. analogously, a punctual particle deposited on the resonator with mass Δm affects the effective mass of the mode differently, depending on the particular deposition position along the beam x_d. This effect also implies that the resulting frequency shift depends on the particular position of the deposited particle. More concretely, the frequency shift Δf resulting from a mass deposition at a particular longitudinal position of the beam x_d is:

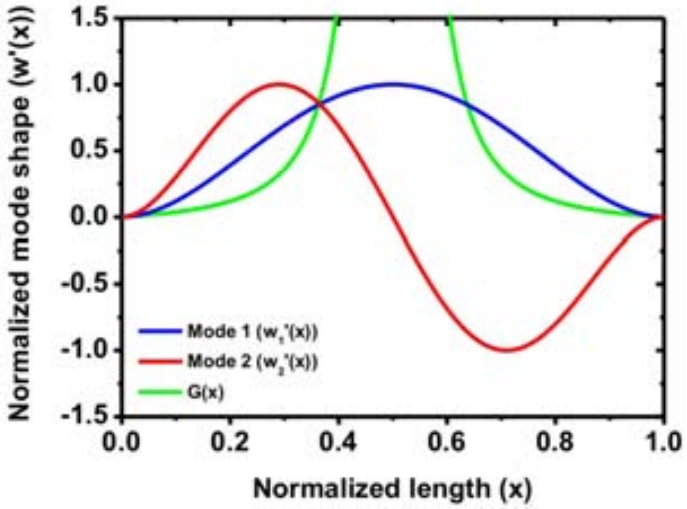

Figure 6.2: Normalized shape of the first two modes of resonance, and the G(x) function with respect to the length of the resonator, for the particular case of a double clamped beam.

$$\Delta f = -\frac{f_n}{\alpha_n \, m_{beam}} \Delta m \, w_n' \, (x_d)^2 \tag{6.7}$$

where f_n is the initial resonance frequency of the studied mode. We observe that the mode shape appears in equation (6.7), and therefore a punctual mass deposited at a particular longitudinal position along the resonator will contribute differently to the resonance frequency of each mode: for example, the modeshape of the first mode w_1 has a maximum at the center of the resonator ($x_d = l\ 2$), while that of the second mode w_2 has a node at that position (this is observed in Figure 6.2). This means that a punctual mass deposited at that position results in a maximum frequency shift for the first mode, and null for the second. Taking advantage of this, by correlating the frequency shifts of these different modes the mass and position effects can be decoupled, allowing the measurement of the mass of the deposited particle. For the first two modes of a resonator, we can define a relation between the modeshapes, the position of the deposited particle and the resulting frequency shifts:

$$G(x_d) = \frac{w_1(x_d)^2}{w_2(x_d)^2} = \frac{\alpha_1 \, \delta f_1}{\alpha_2 \, \delta f_2} \tag{6.8}$$

$G(x_p)$ can be calculated for any combination of modes, but it has a single solution only for some combinations. This function is plotted in Figure 6.2 for the particular case of a cc-beam resonator, obtained from its first 2 modes. In this case $G(x)$ is symmetric with respect the centre of the beam, which means that it has multiple

solutions: more concretely two solutions for the position of the deposited particle exist. However, as the functions $w_n(x)$ are also symmetric with respect to the centre of the beam, in this case it is still possible to resolve the deposited mass by choosing one of the two possible candidates. This principle is used by Hanay et al. to perform real-time detection of proteins [3].

6.2.3 Dynamic Range

The dynamic range is a widely used parameter in the field of electronic amplifiers as a measurement of their range of operation. Analogously, in the field of nanomechanical resonators, it can be defined as the ratio of the maximum vibration amplitude at the onset of nonlinearity to the rms displacement noise floor within the operation bandwidth [14]. Therefore, it is the range of vibration amplitudes at which the operation of the resonator is optimal, limited by the minimum detectable vibration amplitude and the range at which the resonator behaves nonlinearly. The dynamic range of nanomechanical resonators is a critical parameter in sensing applications, because it defines the maximum attainable signal-to-noise ratios. As it is explained below, this in turn limits the minimum detectable frequency shift, and therefore the resolution in mass sensing. In practice, the dynamic range of the whole sensing system may be different than that of the resonator, because the noise floor and levels of nonlinearity can be limited by the different parts of the system (for example, the noise of the readout system may be larger than the intrinsic noise of the resonator). However, in this study we suppose that the actuation/readout methods are sufficiently well designed, and therefore the ultimate limiting factor is the resonator itself. A complete study of the resonator/readout system can be found in reference [14].

Consequently, the dynamic range is defined by two different factors: the noise floor of the resonator and its maximum amplitude of vibration x_c. The noise can be defined as the spectral density of random fluctuations of the resonator $S_X(\ )$, which are studied in detail in the next section. In this case, the dynamic range is defined as:

$$DR = 10\log\frac{x_c^{\ 2}}{\int_{2\pi B} S_X(\ )\mathrm{d}} \tag{6.9}$$

where the noise is integrated over a bandwidth B. Also, as a convention arising from the parallelism with the dynamic range of electronic amplifiers, it is often considered that the onset of nonlinearity is the point at which the amplitude of motion is 1dB lower than it should when considering a totally linear response (also called 1dB compression point) [14]. The critical amplitude of motion of the resonator can be limited by several parameters. In general, the limiting factor in the case of

clamped-clamped beams is the variation of the rigidity of the structure caused by the elongation during its vibration, also called the spring hardening effect (studied in Section 1.1.3).

Several works have studied this mechanical onset on nonlinearity of cc-beam resonators, limited by the non constant stress on the beam, such as Postma et al. [15] and Matheny et al. [16]. When increasing the driving amplitude of an ideal cc-beam, at some point its response reaches a point where it presents hysteresis. This hysteresis appears at a certain amplitude of the response, called the critical amplitude of nonlinearity x_{nl} (which is different from the 1dB compression point), which can be calculated from the expression:

$$x_{nl} = {}_0\frac{l^2}{\pi^2}\overline{\frac{\rho\ \overline{3}}{EQ}} \tag{6.10}$$

From the modelling of the nonlinear response, and the reference level established by the amplitude x_{nl}, the 1dB compression point can be established as $x_c = 0\ 745x_{nl}$. This expressions gives an estimation of the mechanical onset of nonlinearity in cc-beam resonators. As an example, applying these expressions to one of the measured bottom-up nanowires (Figure 3.7a-c) with a length of 3 μm and a diameter of 100 nm, the critical amplitude stands in the order of 2 nanometers.

6.3 Evaluation of the performance of nanomechanical resonators as mass sensors

This section deals with the performance of nanomechanical resonators as mass sensors. First, a numerical evaluation of the mass resolution of nanomechanical resonators based on different noise sources is presented. Then, a closed loop system for the monitoring of the resonance frequency is presented and applied to the fabricated resonators. Finally, an evaluation of the performance of the fabricated SiNW resonators as mass sensors is presented, and compared with the state of the art.

6.3.1 Numerical evaluation of the mass resolution

We have asserted that the noise in the oscillation of the resonator affects its performance as mass sensor. On the one hand it affects its dynamic range, setting the lower level of detectable signal, and on the other hand it adds uncertainty on the determination of the resonance frequency of the resonator, and therefore it affects its mass resolution. In this section, the limits to the mass resolution imposed by the different noise sources are studied, and their scaling as a function of the dimensions of the resonator.

We consider a system in which the resonance frequency of the resonator has fluctuations $\delta\ _0$ provoked by the noise. Moreover, we consider that the minimum detectable frequency shift is comparable to these frequency fluctuations: this means that a resonance frequency shift is only detected when this shift is higher than the resonance frequency fluctuations.

The fluctuations of the resonance frequency can be represented in the frequency domain by the spectral density of frequency fluctuations $S_\omega(\ )$. In a mass sensing system, the resonator is not operated in open loop, but integrated in a close loop which detects its resonance frequency in real time. Therefore, the response of the closed loop also affects the resolution. Then, in this case, the detected resonance frequency fluctuations can be obtained from the spectral density of frequency fluctuations and the transfer function of the feedback loop $H(\ )$.

$$\delta\ _0 \approx \left[\int_0^\infty S_\omega(\ )H(\ )\mathrm{d}\ \right]^{1/2} \tag{6.11}$$

The most simple way to model the feedback loop is taking into account the measurement averaging time τ, which limits the bandwidth of the system ($B \approx 1\ \ 2\pi\tau$). A longer measurement time decreases the measurement bandwidth and filters more noise, but it also slows the response time of the system. The measurement averaging time is fixed taking into account both factors, as a compromise between response time and accuracy of the measurement. Then, the frequency fluctuations are limited by the noise comprised only in the measurement bandwidth:

$$\delta\ _0 \approx \left[\int_{\omega_0-\pi B}^{\omega_0+\pi B} S_\omega(\ )\mathrm{d}\ \right]^{1/2} \tag{6.12}$$

Therefore, in order to characterize the frequency fluctuations, a model of their spectral density $S_\omega(\ )$ is needed.

6.3.1.1 Modelling of noise sources in nanomechanical resonators

In order to study the mass resolution of sensors based on nanomechanical resonators, an evaluation of the different noise sources which affect the resonator is needed, and more specifically, of the spectral density of resonance frequency fluctuations $S_\omega(\ )$ provoked by these noise sources. Here different noise sources are considered, which have a different effect on the behaviour of the resonator; some of them directly modify the resonance frequency of the resonator–such as frequency fluctuations due to absorption-desorption of molecules on the resonator, which change its effective mass–while others act on parameters which indirectly affect the determination of the resonance frequency–such as thermomechanical noise, which modifies the motion of the resonator and hinders the measurement of its resonance frequency–. A model of

different noise sources which affect the measurement of the resonance frequency of the resonator is presented here, based on the study of Ekinci et al. [17].

Thermomechanical fluctuations

Thermomechanical fluctuations are caused by thermally driven random motion of the nanomechanical resonator, and they are the fundamental noise limit for these devices. To begin the study of this noise, we define the mean square displacement fluctuations at the center of mass of the resonator (the centre of the resonator in case of a cc-beam), which can be deduced by the fluctuation-dissipation theorem:

$$x_{th}^2 = \frac{k_B T}{m_{eff}\ \ _0^2} \tag{6.13}$$

The spectral density of these random fluctuations $S_x(\ )$ can be modelled from the thermomechanical force spectral density, which has a white spectrum (that is, a flat spectrum) and the modulus of the transfer function of the nanomechanical resonator which has been described previously:

$$S_x(\ ) = \frac{1}{m_{eff}} \frac{S_F(\ )}{(\ ^2 - \ _0^2)^2 + \ ^2\ _0^2\ Q^2} \tag{6.14}$$

where $S_F(\ )$ is the thermomechanical force spectral density, given by

$$S_F(\ ) = 4 m_{eff}\ \ _0 k_B T\ Q \tag{6.15}$$

In a typical measurement scheme, the resonator is driven at a constant amplitude (considering a noiseless carrier), and the frequency shift is measured using a phase-locked loop (PLL) topology. Supposing a tracking of the resonance frequency using the phase information, the effective spectral density of frequency fluctuations $S_\omega(\ )$ can be described from the phase fluctuations as:

$$S_\omega(\ ) = \frac{S_\phi(\ )}{(\delta\partial\ \delta\ )^2} \approx \left(\frac{_0}{2Q}\right)^2 \frac{S_x(\ )}{x_c^2} \tag{6.16}$$

$$\approx \frac{_0^5}{Q^3} \frac{k_B T}{E_c} \frac{1}{(\ ^2 - \ _0^2)^2 + \ ^2\ _0^2\ Q^2} \tag{6.17}$$

where $S_\phi(\ )$ is the spectral density of phase fluctuations, given by $S_\phi(\ ) = S_x(\ )\ \ x_c^2$. The carrier level is characterized by an energy $E_c = m_{eff}\ \ _0^2\ x_c^2$, where x_c is the beam's center displacement. Substituting expression (6.17) into (6.12), and integrating for the case where $Q \gg 1$ and $2\pi B \ll \ _0\ Q$ (both conditions are fulfilled in experimental conditions), the resonance frequency fluctuations are obtained:

$$\delta \ _0 \approx \left[\frac{k_B T}{E_c} \frac{_0 B}{Q}\right]^{1/2} \tag{6.18}$$

The mass resolution is obtained by substituting this equation into (6.5).

$$\delta m \approx 2 m_{eff} \left(\frac{E_{th}}{E_c}\right)^{1/2} \left(\frac{B}{Q \ _0}\right)^{1/2} \tag{6.19}$$

Where $E_{th} = k_B T$ is the thermal energy. This expression can also be rewritten as a function of the dynamic range and mass sensitivity

$$\delta m \approx S_m \left(B \frac{_0}{Q}\right)^{1/2} 10^{(-DR/20)} \tag{6.20}$$

Scaling of the thermomechanical-limited mass resolution

In the last section, we have observed that the dimensions of the resonator affect its mass sensitivity, specially in the case of its length. In order to design the resonators with the objective of maximizing the mass resolution, it is also useful to deduce the evolution of expression (6.19) with the diameter of the resonator. In the case of an hexagonal beam, scaling (reducing) the distance between parallel sides d by a factor K the following relations are found:

$$x_{c,fin} = K^{-1} x_{c,ini} \tag{6.21}$$

$$E_{c,ini} = m_{eff,ini} \ \ _{0,ini}^{2} \ x_c^2 \qquad E_{c,fin} = K^{-6} E_{c,ini} \tag{6.22}$$

$$\delta m_{ini} = 2 m_{eff,ini} \left(\frac{E_{th}}{E_{c,ini}}\right)^{1/2} \left(\frac{B}{Q \ _{0,ini}}\right)^{1/2} \qquad \delta m_{fin} = K^{3/2} \delta m_{ini} \tag{6.23}$$

In this case, the subscript ini represent the unscaled parameters, and fin the scaled ones. To approximate the maximum lineal oscillation amplitude x_c , the expression 6.10 has been used. We observe that the mass resolution improves when the resonator's thickness increases. However, there are several considerations that must be taken into account: firstly, the expressions used in this study hold when the lateral dimensions of the resonator (d in this case) are much smaller than its length l. Also, here the quality factor Q has a fixed value, but in practice it has been observed to change with the dimensions of the resonator.

Temperature fluctuations

The resonator's dimensions and material parameters are temperature dependent, and therefore changes in the temperature also provoke changes in the resonance

frequency. Due to its small dimensions, nanomechanical resonators have a small heat capacitance and are subject to large temperature fluctuations. This section presents an estimation of the mass resolution limited by temperature fluctuations caused by the fluctuation-dissipation theorem, when the ambient temperature is considered constant. The dependence of the resonance frequency upon long-term temperature variations is not studied here. Clealand and Roukes propose an estimation for the spectral density of frequency fluctuations arising from temperature fluctuations of a NEMS resonator for the case of a doubly clamped beam of constant cross section.

$$S_\omega(\quad) = \left(-\frac{22\ 4c_s^2}{{}_0^2 l^2}\alpha_T + \frac{2}{c_s}\frac{\delta c_s}{\delta T}\right)\frac{{}_0^2 k_B T^2}{\pi g(1+(\quad - \quad{}_0)^2\tau_T^2)} \tag{6.24}$$

Where $c_s = \quad \overline{E\ \rho}$ is the temperature dependent speed of sound, $\alpha_T = (1\ \ l)\delta l\ \ \delta T$ is the thermal expansion coefficient and g and τ_T are the thermal conductance and the thermal time constant for the nanostructure. Integrating this expression over the measurement bandwidth, the resonance frequency fluctuations can be obtained.

$$\delta\quad{}_0 = \left[\frac{1}{2\pi^2}\left(-\frac{22\ 4c_s^2}{{}_0^2 l^2}\alpha_T + \frac{2}{c_s}\frac{\delta c_s}{\delta T}\right)\right] \tag{6.25}$$

In this case, the mass resolution limited by temperature fluctuations can be approximated as

$$\delta m \approx 2\, m_{eff}(1\ 26\times 10^{-4}\ \ K)\left[\frac{k_B T^2 \Delta f}{\pi g}\right]^{1/2} \tag{6.26}$$

Adsorption-desorption noise

Gas molecules can adsorb upon the resonator's surface, changing its mass and therefore its resonance frequency. This way, random adsorption-desorption of molecules induces fluctuations on the resonance frequency, and therefore reduces the mass resolution of the sensor.

The adsorption-desorption cycle can be modelled through the adsorption and desorption rates, r_a and r_d respectively.

$$r_a = \frac{2}{5}\frac{p}{\overline{mk_B T}}s \tag{6.27}$$

$$r_d = \nu_d \exp\left(-\frac{E_b}{k_B T}\right) \tag{6.28}$$

Where p and T are the gas pressure and temperature respectively, and E_b is the binding energy between the surface and the adsorbate atom, and m the mass of

the adsorbates. The adsorption rate depends upon the sticking coefficient s where $0 < s < 1$. r_d depends upon the desorption attempt rate ν_d, where $\nu_d \sim 10^{13} Hz$.

The surface of the resonator can be modelled as comprising N_a sites for adsorption. We can then define σ^2_{occ} as the variance in the occupation probability of a site, and τ_r as the correlation time for an adsorption-desorption cycle. These terms can be described as a function of r_a and r_d as $\sigma^2_{occ} = r_a r_d \ (r_a + r_d)^2$ and $\tau_r = 1 \ (r_a + r_d)$. The frequency fluctuations arising from the adsorption-desorption processes can be described as

$$S_\omega(\ ) = \frac{2\pi \ {}^2_0 N_a \sigma^2_{occ} \tau_r}{(1 + (\ - \ {}_0)^2 \tau_r^2)} \left(\frac{m}{m_{eff}} \right)^2 \tag{6.29}$$

Here, the surface is modelled as comprising N_a sites for adsorption. σ^2_{occ} represents the variance in the occupation probability of a site, and τ_r is the correlation time for an adsorption-desorption cycle. Integrating the expression (6.29) upon the measurement bandwidth, the frequency fluctuations can be obtained as:

$$\delta \ {}_0 = \frac{1}{2\pi} \frac{m \ {}_0 \sigma_{occ}}{m_{eff}} [N_a \arctan(2\pi B \tau_r)]^{1/2} \tag{6.30}$$

And the mass sensitivity can be approximated as

$$\delta m \approx \frac{1}{2\pi} m \sigma_{occ} [N_a \arctan(2\pi B \tau_r)]^{1/2} \tag{6.31}$$

Momentum exchange noise

In a gaseous environment, there is a momentum exchange between the nanomechanical resonator and the molecules that impringe upon it. This noise source is specially important at high pressures, that is, when there is a higher density of gas molecules. These fluctuations can be modelled by an expression very similar to that of the intrinsic noise, but instead of using the intrinsic quality factor Q of the device using the quality factor due to gas damping $Q_{viscous}$. Assuming that the intrinsic intrinsic losses of the resonator are much higher to those provoked by the viscous environment ($Q_{intrinsic} \gg Q_{viscous}$), Ekinci and Roukes deduce an expression for the mass resolution limited by the momentum exchange noise:

$$\delta m \approx 2 m_{eff} \left(\frac{E_{th}}{E_c} \right)^{1/2} \left(\frac{B}{Q_{viscous \ \ 0}} \right)^{1/2} \tag{6.32}$$

6.3.1.2 Numerical evaluation of the mass resolution of silicon nanowire resonators

In order to evaluate the mass resolution for nanomechanical resonators, we now calculate the contributions of the different noise sources to nanomechanical resonators with dimensions based on experimental values. Two different nanowires of different dimensions are studied: the first nanowire (NW1) has a length of 2 μm and a distance between parallel sides of 50 nm: these are approximately the dimensions of the smallest SiNW that we have measured in this work. The second nanowire (NW2) has length of 0.5 μm, a distance between parallel sides of 30 nm and a resonance frequency of 1 GHz approximately, which is considered the maximum resonance frequency which can be detected using the current measurement system. The measurement conditions will be the same for both of them: a measurement bandwidth $B = 1$ kHz, measurements in vacuum conditions (10^{-3} mbar, approximately 10^{-3} Torr), a temperature of $T = 270$ K, and a quality factor $Q = 1000$.

Noise source	δ**m NW1 (g)**	δ**m NW2 (g)**
Thermomechanical noise	$5\,76 \times 10^{-22}$	$9\,69 \times 10^{-24}$
Temperature fluctuations	$6\,42 \times 10^{-24}$	$5\,77 \times 10^{-25}$
Momentum exchange noise	$2\,32 \times 10^{-24}$	$1\,63 \times 10^{-26}$

Table 6.4: Influence of the different noise sources in the mass resolution of two silicon nanowires with different dimensions, under the same conditions. NW1 has a length of 2 μm and a distance between parallel sides of 50 nm; NW2 has length of 0.5 μm and a distance between parallel sides of 30 nm.

Table 6.4 shows the mass resolution limited by each noise contribution. We find that, for both nanowires, the thermomechanical noise is the limiting factor in the current measurement conditions, while the other noise sources are at least one order of magnitude smaller in all cases. For this reason, we now study the evolution of the mass resolution of thermomechanical noise as a function of different parameters of the resonator.

Figure 6.3 shows the dependence of the mass resolution of the resonator on its dimensions and measurement bandwidth, in a graphical representation of the equation (6.23). In Figure 6.3a we observe that the best theoretical mass resolution is obtained with short nanowires of wide diameter, basically due to the fact that they present the best relation between dynamic range and mass sensitivity. However, in practice these nanowires are also difficult to actuate, and some of the dimensions shown in the graph do not respect the conditions of the analysis in beam theory ($d \ll l$). Also, these results do not include the effects of the transduction mechanism or other experimental issues. Despite all of this, these graphs show a clear tendency, which holds at least for resonators with similar geometries. The evolution of the

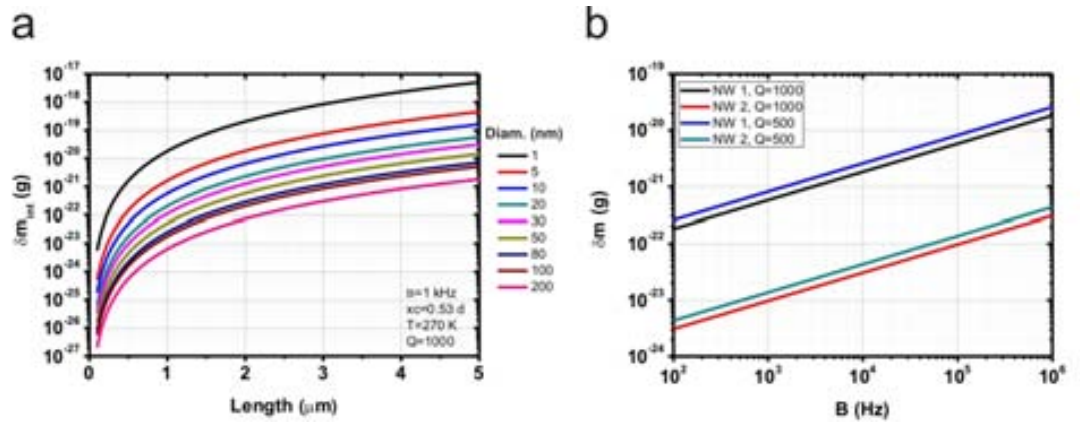

Figure 6.3: Evolution of the mass resolution limited by thermomechanical noise when varying parameters of the resonator. a) Dependence of the mass resolution on the dimensions of the resonator. b) Dependence of the mass resolution on the measurement bandwidth. NW1 has a length of 2 μm and a distance between parallel sides of 50 nm. NW2 has a length of 0.5 μm and a distance between parallel sides of 30 nm.

mass resolution with the measurement bandwidth is shown in Figure 6.3b. In this case, a higher bandwidth implies a worse mass resolution, due to the fact that more noise is integrated into the measurement. Also, a narrower bandwidth usually implies a higher integration time: this relation is expected of most sensing systems, and represents a trade-off between the measurement time and the resolution of the mass sensor.

6.3.1.3 Determination of the frequency resolution

As it is explained above, the resolution of a nanomechanical resonator acting as a mass sensor is determined by the stability of the resonance frequency of the device. In an ideal mass sensor (without noise or dissipation), the output would be a perfect sine wave at this frequency. In practice however, noise introduces deviations in both the amplitude and phase of the sine wave, which affect the stability of the measured signal. The frequency stability can be defined as the fluctuations of the output frequency in a determined time interval [18].

In order to study the frequency stability, we define the output of the mass sensor $V(t)$ as a sine wave with a certain error in its amplitude and phase:

$$V(t) = (V_0 + \epsilon(t)) \sin(2\pi f_0 t + \partial(t)) \tag{6.33}$$

where $\partial(t)$ is a statistical process which represents the phase noise, V_0 and f_0 are the nominal amplitude and frequency of the signal respectively and $\epsilon(t)$ is the amplitude noise, which is not important in this application. We define the instantaneous frequency as:

$$\nu(t) = f_0 + \frac{1}{2\pi}\frac{df(t)}{dt} = f_0 + \Delta f(t) \tag{6.34}$$

In equation (6.34), $\Delta f(t)$ is identified with the frequency noise of the system, which modifies its nominal frequency. From this term, the instantaneous fractional frequency $y(t)$ is defined, which is widely used to characterize frequency stability:

$$y(t) = \frac{\Delta f(t)}{f_0} \tag{6.35}$$

There are two approaches to characterize the resonance frequency noise. The first one is spectral analysis, which evaluates the noise in frequency domain using the spectral density of frequency and phase fluctuations (phase noise). The second one is the temporal analysis, which characterize the stability of the resonator in a certain time interval using statistical methods.

One of the most widely used methods to characterize frequency stability is the Allan variance, which is a temporal method. It is based on the relative stability of the measured resonance frequency of the device with respect to its own nominal resonance frequency. The main advantage of the Allan variance is that it provides a numerical value for the frequency stability, which is easy to interpret and compare, in contrast to other methods such as phase noise in which the interpretation can be more complex.

The method of the Allan variance was proposed by David Allan in 1966 [19], and was proposed as the recommended standard for the measurement of frequency stability of oscillators in 1971 by the IEEE [20]. The Allan Variance is based in the variance between adjacent samples of a set of measurements of resonance frequency [19]. This method was developed to characterize the frequency stability of oscillators, where the measurement of the standard deviation in some cases provides less accurate information due to temporal drifts in its output.

For the study of the Allan variance we start with an infinite set of resonance frequency samples $f(t)$, taken during a determined integration time τ. The the frequency drifts can be defined as:

$$y(t) = \frac{\Delta f(t)}{f_0} = \frac{f(t) - f_0}{f_0} \tag{6.36}$$

In this case, the variance between adjacent samples is defined as [21]:

$$\sigma_f^2 = \frac{1}{2}\ (\overline{y}_2 - \overline{y}_1) \tag{6.37}$$

This equation is applicable to measurements with infinite samples. In practice, however, we have a finite set of m samples. In this case, and considering that the

samples have been taken with an integration time τ, the Allan variance can be approximated as:

$$\sigma_y^2(\tau\ m) = \frac{1}{2\,(m-1)} \sum_{i=1}^{m-1} \left(\overline{y}_{i+1} - \overline{y}_i\right)^2 \tag{6.38}$$

From the expression (6.38), we can obtain the expression of the Allan variance for a finite set of frequency samples $f(t)$:

$$\sigma_f^2(\tau\ m) = \frac{1}{2\,(m-1)\,f_0^2} \sum_{i=1}^{m-1} \left(f_{i+1} - f_i\right)^2 \tag{6.39}$$

The integration time used to measure the frequency samples is a critical parameter, which affects the noise and the stability of these samples. An increase in the integration time implies a longer averaging of the frequency, and therefore a reduction of the noise. On the other hand, for large average times, the frequency drifts can affect the measurement (such as thermal drifts). For this reason, it is a common practice to evaluate the Allan variance for different integration times in order to better characterize the frequency stability. Another widely used variant of this term is the Allan deviation, which is the square root of the variance.

6.3.2 Closed-loop tracking of the resonance frequency

In order to apply the fabricated nanomechanical resonators as mass sensors, a method to track their resonance frequency is needed. The simplest way to perform mass sensing is to obtain the resonance spectrum of the device, then deposit the mass, and obtain another spectrum in order to compare the responses. This method has several disadvantages: the most important one is that it is time-consuming, as measuring one frequency spectrum typically takes minutes; also, this difference between different frequency spectra does not account for possible temporal drifts of the resonance frequency due to parameters not related with mass deposition. By performing a real-time tracking of the resonance frequency, these drifts appear as a continuous frequency shift, and the mass deposition as more abrupt changes in the frequency response, specially if individual deposition events are detected (such as deposition of atoms, molecules, etc.). For these reasons, have we implemented a feedback loop in order to monitor the resonance frequency of the resonator in real time.

In order to take advantage of the current measurement system, we have implemented a closed-loop system based on software feedback. The main advantages of this approach are its simplicity and flexibility. On the other hand, this approach requires an intensive communication between the computer and the instrumentation, and the communication time as well as the response time of the instruments

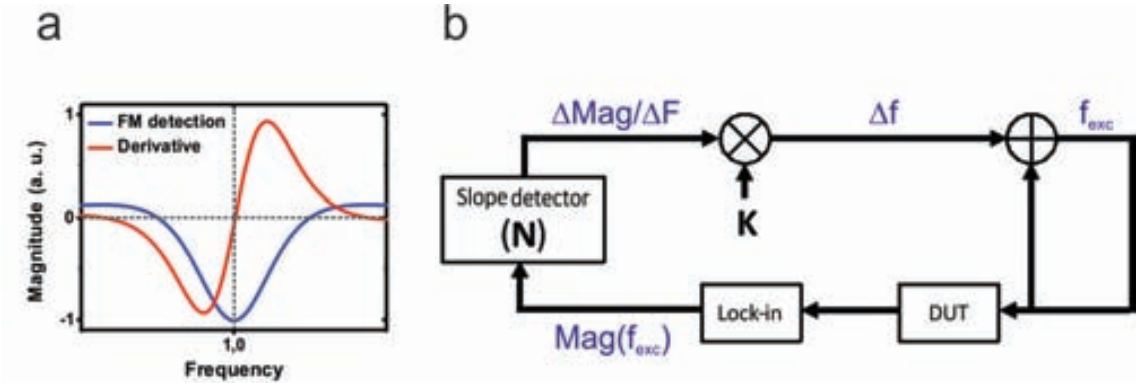

Figure 6.4: Closed loop system for the real time monitoring of the resonance frequency, using the FM detection method and software feedback. a) Theoretical response of the resonator measured using the FM response and its derivative. The resonance frequency is 1, and the amplitudes are arbitrary and scaled for comparison. b) Schematic of the closed loop implementation using the slope detection method.

causes this feedback loop to be slower than other approaches based on hardware components. More concretely, these two factors limit the response time of the system tens of milliseconds. The implementation of the control software has been performed by Fabrice Terry, an under-graduate student performing an internship at the IMB-CNM.

Most feedback loops are based on a Phase-Locked Loop (PLL) topology, in which the tracking of the resonance frequency is made through the phase of the frequency response at resonance. This parameter does not depend on the magnitude of of the frequency response, and therefore this method is insensitive to changes in the amplitude of motion of the resonator. However, the frequency modulation detection method does not provide phase information (that is, the phase is constant during the resonance peak), and therefore a PLL can not be used in this case. Another option is performing a tracking of the magnitude at some fixed point of the frequency response, but this method is very sensitive to changes of the amplitude of motion of the resonator, which would be translated into apparent changes of the resonance frequency. For these reasons, we have implemented a tracking of the maximum of the response, which corresponds to the resonance frequency of the resonator, and where its derivative is zero independently of its peak value.

Figure 6.4a shows the shape of the FM signal and its derivative. We observe that the derivative is zero at the resonance peak, and it is linear for a range of frequencies near the resonance. The feedback loop is based on monitoring the slope of the response of the resonator in this range, and correct the excitation frequency to bring this slope to zero. Is is important to note that this range of linear slope is enclosed by a maximum and a minimum: upon reaching one of these two positions, the feedback will not work correctly.

During the operation of the resonator, in general there is difference between the excitation frequency and the resonance frequency. In this situation, the feedback loop applies a correction Δf to the excitation frequency in order to bring it closer to the resonance frequency. This correction can be computed from the value of the slope around the excitation frequency $\Delta Mag\ \ \Delta F$:

$$\Delta f = K\frac{\Delta Mag}{\Delta F}\ \ (\mathrm{Hz}^2\ \ \mathrm{A}) \tag{6.40}$$

Where K is the factor relating the slope and the frequency correction. The slope is calculated from the values of magnitude and frequency of the last N measurements. If we define Δf_i as the frequency correction of the last i_nth measurement, the slope is calculated in a range of frequencies ΔF which is:

$$\Delta F = \sum_{i=1}^{N} \Delta f_i \tag{6.41}$$

If we consider that we operate in a narrow range of frequencies, the slope and the frequency correction can be considered be constant, and then $\Delta F = N\Delta f$.

The implementation of the feedback loop is shown in Figure 6.4b. The resonator is measured using the FM detection technique, and actuated at a certain measurement frequency f_{exc}. The magnitude of its response $Mag(f_{exc})$ is detected using a lock-in amplifier, during a measurement time t, and acquired by the software. Using the information of the excitation frequency and a certain number of previous measurements N, the slope $\Delta Mag\ \ \Delta F$ is detected using a least-squares algorithm. This detected slope is then multiplied by the proportionality constant K in order to calculate a frequency correction Δf, which is then added to the excitation frequency. As the loop depends on previous measurements at different frequencies to work, at the beginning of its operation it is initialized by taking a range of values of magnitude at a number of different frequencies.

We have validated this tracking method by tracking the resonance frequency of a top-down nanowire. We have monitored its resonance frequency during 9 hours, and the results are shown in Figure 6.5. Different values of the tracking parameters are tested, and for this measurement $N = 8$, $K = 1 \times 10^{15}$ Hz^2 A and t=200 ms are used. During the tracking period, we observe that the magnitude of the detected current is kept constant around 3.35 nA, while the resonance frequency presents a maximum shift of around 25 kHz.

6.3.2.1 Tracking of changes in the frequency response of the resonator

During the operation of the system in sensing applications, it is used to track variations of the frequency response of the resonator caused by environmental parameters.

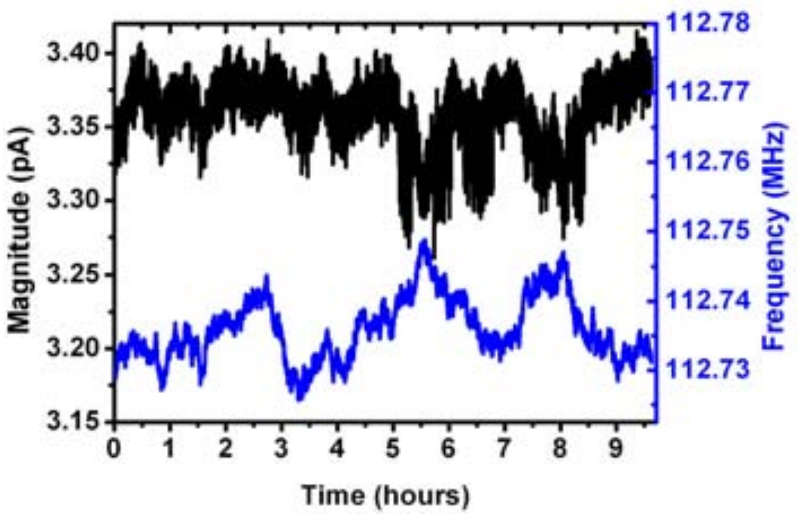

Figure 6.5: Tracking of the resonance frequency of a top-down resonator during 9 hours, using the FM measurement method and the closed loop system. Tracking conditions: $N = 8$, $K = 1 \times 10^{15}$ Hz^2/A, time constant of the lock-in amplifier t=200 ms. Measurement conditions: $V_{NW} = 350$ mV, $V_{g,DC} = 10$ V.

Therefore, besides the tracking of the resonance frequency in static conditions, it is also important to study the response of the closed loop system to changes in the response of the resonator. To simulate the detection of mass, the response of the closed loop system has been studied when changing the excitation conditions of the resonator, and tracking its changes in magnitude and resonance frequency. The tracking set-up is used to measure the changes in the response of a top-down resonator provoked by a change of the DC gate voltage. In Chapter 5 we observed that a change in the DC voltage of the gate provokes an important change in the magnitude of the detected response, and also a small shift of the resonance frequency of the resonator. The tracking of these two effects allows us to study the response of the closed loop system to sudden changes in the response of the resonator.

Figure 6.6 shows the response of the closed loop to variations in the DC gate voltage, for a number of samples $N = 15$ and an integration time of the lock in of 100 ms. In Figure 6.6a, the response of the detected magnitude and frequency is shown for different values of the proportionality constant K. We observe that for lower proportionality constants ($K = 1 \times 10^{16}$ Hz^2 A), the system takes a longer time to reach the new stable position after a step in the DC voltage. On the other hand, for too large constants ($K = 1 \times 10^{18}$ Hz^2 A) the response of the system becomes unstable, and its frequency and magnitude start oscillating. We find that the optimum proportionality constant in this case is around $K = 1 \times 10^{17}$ Hz^2 A: a detail of the tracking of the DC steps for this particular constant is shown in

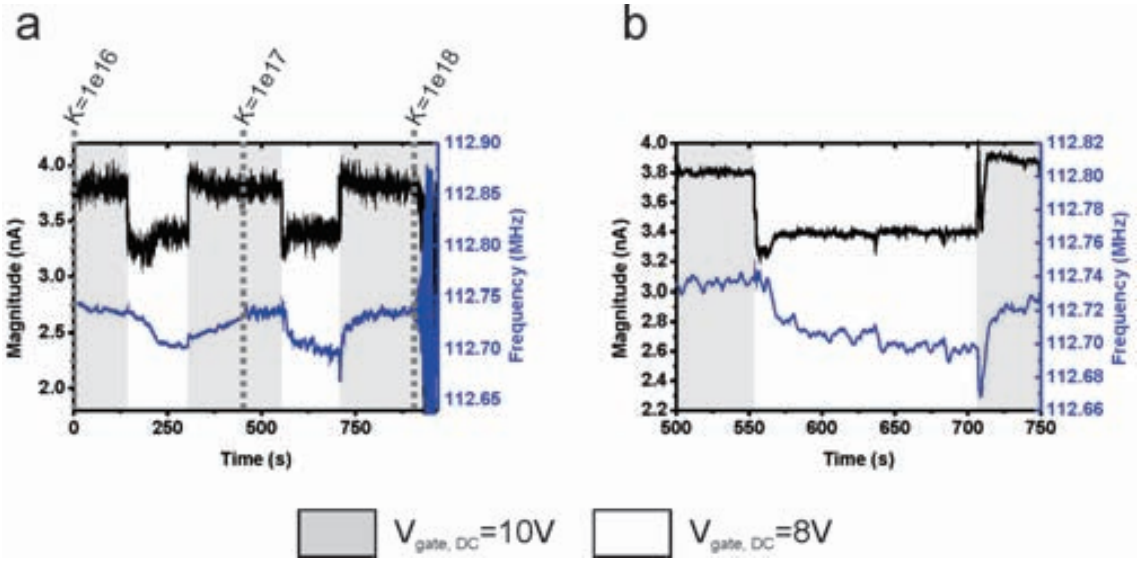

Figure 6.6: Tracking of the changes of the response of the resonator caused by variations in the DC gate voltage. In these experiments the number of samples N is 15, and the time constant of the lock-in is 100 ms. a) Response of the feedback loop to steps in the DC voltage, for different K values. b) Detail for a K of 1×10^{17} Hz^2/A.

Figure 6.6b. We observe that, under these conditions, the system takes less than five seconds to track the changes in the magnitude of the response, and a little longer to completely track the changes in the resonance frequency.

6.3.2.2 Measurement of the frequency stability

The frequency stability of the system limits the minimum detectable resonance frequency shift, and therefore the minimum detectable mass in sensing applications. For this reason, it is important to study and characterize the frequency stability of the closed loop system. In this section, the different parameters which affect the behaviour of the feedback loop are explored, and the frequency stability of the system under different conditions is studied with the help of the Allan deviation and the open loop response of the resonator.

There are several parameters in the loop which must be studied in order to get optimal results: the integration time of the lock-in amplifier t, the number of samples in the least squares array N and the proportionality constant K. The integration time of the lock-in amplifier is the factor which in general limits the response time of the loop. This parameter controls the measurement time of the magnitude of the resonator: therefore, the longer the integration time, the better the measurement of this magnitude. In our system, it is usually set to 100-200 ms. The second parameter is the number of samples in the least squares array. This is the number

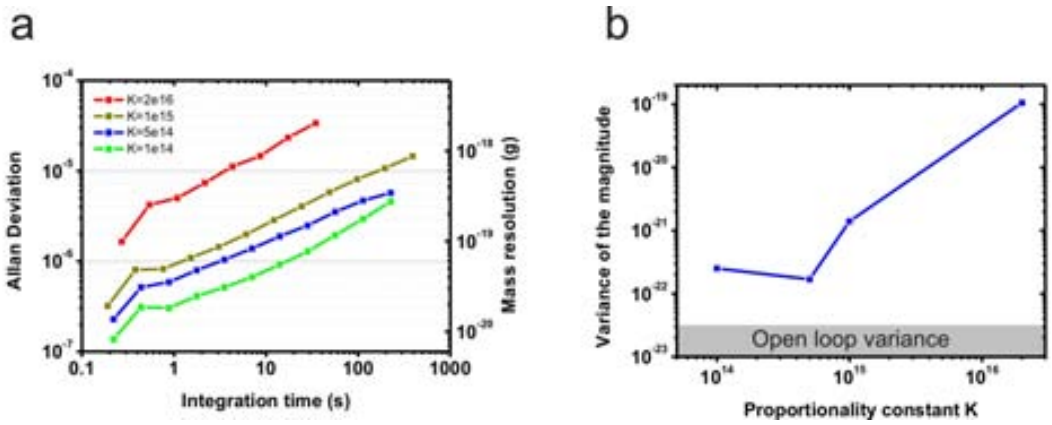

Figure 6.7: Measurement of the frequency stability of a top-down resonator, with a resonance frequency of 112.7 MHz. Measurement conditions: $V_{g,DC} = 10$ V, $V_{NW} = 350$ mV. Close loop conditions: number of samples $N = 8$, and integration time of the lock-in amplifier $t = 100$ ms. The measurements are taken for different values of K. The Allan deviation is calculated from samples of frequency taken during 20 minutes, and the magnitude measured for each frequency is also recorded. a) Allan deviation and the associated mass resolution for different values of K. The mass resolution has been calculated from the theoretical effective mass ($m_{eff} = 3 \times 10^{-14}$ g). b) Variance of the magnitude values recorded during the frequency tracking, for each value of K. For comparison, the variance of the open-loop magnitude taken at a fixed frequency using the same measurement time (20 minutes) is shown in gray.

of points that are used to calculate the slope of the magnitude as a function of frequency. A low number of points provides an unreliable measurement of the slope, which results in a system which unlocks easily from the resonance frequency. On the contrary, a large number of points makes the system more stable, but it also makes it slower to respond to changes in the resonance frequency, and causes a tendency to oscillate around the resonance peak. An adequate value must be found for this parameter, which in our system ranges from 8 to 14. The third studied parameter is the proportionality constant K. A low constant allows the system to accurately measure small oscillations of the resonance frequency, and is therefore ideal for a stable resonance frequency, but also causes the system to react slowly to sudden changes of the resonance frequency. This parameter must be therefore adjusted experimentally, taking into account the stability and expected changes in the value of the resonance frequency.

Figure 6.7 shows the measurements of the frequency resolution of a top-down nanowire measured in a closed-loop configuration. The resonator has a resonance frequency of 112.77 MHz, and it is measured using the FM method. For these measurements, the number of samples for the least-squares algorithm is fixed to 8, and the integration time to 100 ms. The resonance frequency is tracked during 20 minutes using these conditions, and for different values of the proportionality constant K. The magnitude measured during each point is also recorded. The Allan

deviation of the measurements is calculated from the obtained resonance frequency values (Figure 6.7a). Then, and from this deviation, the resonance frequency and the theoretical effective mass of the resonator, the associated mass resolution is calculated. The Allan Deviation measurements show that the best results are obtained for lower values of K, specially for $K = 1 \times 10^{-14}$ Hz^2 A, where the maximum attainable mass resolution is 6×10^{-21} g or 6 zg.

In the evaluation of the mass resolution we observed that the ultimate attainable deviation is limited by the noise affecting the resonator. However, in this system, continuously decreasing the K value would yield ever decreasing values of frequency resolution: in the extreme case, a value of $K = 0$ Hz^2 A would yield a deviation of zero. In this situation, however, the resonance frequency of the device would not be tracked correctly, and therefore the obtained deviation would not correctly reflect that of the resonator. In order to evaluate if the resonance frequency of the resonator is correctly tracked during the measurements, we use additional information from the measured magnitude. When the resonance frequency is correctly tracked, the amplitude of motion of the resonator is always maximum, and therefore so is the measured current. However, if the frequency is not tracked correctly, the amplitude of motion (and therefore the detected current) has a certain amount of deviations, due to the fact the the resonator is not operated at its resonance peak, and therefore the measured current is not maximum. For this reason, a correct tracking also implies better stability in the amplitude of the measured current.

In order to validate the frequency stability measurements, we calculate the variance of the magnitude for the measurements taken at each value of K (Figure 6.7b). If this variance decreases when increasing the K value, it means that we are tracking the resonance frequency of the device with more precision, and as a result the measured current values are also more stable. We observe that this is the situation for the major part of our measurements: a decreasing value of K also brings about an increased stability in the magnitude. In the lowest K values, however, the measured stability values are similar. For this reason, we deduce that the measurements reflect a real increase in the frequency stability of the system.

For comparison, in Figure 6.7b we also plot the variance of the magnitude for an open loop measurement (that is, at a fixed frequency) with the same measurement time and conditions. We observe that the variance of this measurement is even lower than in the best case of the tracking. This means that the deviation between the excitation frequency and the resonance frequency of the device is lower in open loop than in the closed loop configuration, and consequently that the frequency deviation values calculated from the closed-loop measurements are not limited by the noise of the resonator, but by the tracking system. Therefore, there is still room for an improvement of the frequency stability of the system, because we have not reached the ultimate limit imposed by the frequency stability of the resonator.

6.3.3 Evaluation of the mass sensing performance of SiNW nanomechanical resonators

In the last chapters we have presented the fabrication and measurement of nanomechanical resonators, using top-down and bottom-up fabrication approaches. The fabricated resonators have diameters ranging from 50 to 150 nanometers, and lengths of 2-3 micrometers. In this section, the performance of bottom-up and top-down nanowires as mass sensors is evaluated. Table 6.5 shows a comparison of the mass responsivity and resolution of bottom-up and top-down nanowires.

The values of mass sensitivity shown in the table is obtained from the measured resonance frequency and a modelling of their effective mass, performed by the information obtained by SEM imaging. The mass resolution is obtained from the measurement of the frequency stability of the closed-loop system with a top-down nanowire, which presents an Allan deviation of 1 4×10^{-7}. By supposing this value of frequency stability, we estimate the mass resolution from the responsivity of the resonators.

From the table, we observe that the responsivity of bottom-up devices is in the range of 1-6 $\times 10^{-21}$ Hz/g, and that of the top-down devices is of 1-6 $\times 10^{-21}$ Hz/g. The best performance is obtained from the bottom-up nanowire with smaller dimensions, which has a responsivity of 6.6 Hz/zg, in the range of previous measurements performed with bottom-up SiNWs [7]. However, this responsivity is also orders of magnitude below those presented by CNT resonators, which have small diameters and a very low effective mass. We also observe that the theoretical mass sensitivity is in the same order of magnitude for the top-down and bottom-up nanowires. The main difference between these approaches is the diameter of the resulting nanowires, which tends to be lower for the bottom-up ones. At the same time, however, due to the compressive stress, the bottom-up nanowires also have lower resonance frequencies than predicted: these two effects compete with one another, and cause the mass sensitivity not to vary a lot between top-down and bottom-up devices. The table also shows a comparison the the sensitivity of the fabricated devices with the state of the art of different fabrication technologies. We observe that in the case of top-down resonators and bottom-up SiNWs, the best obtained sensitivities are similar to those of the respective state of the art devices.

We observe that the best predicted mass resolution is around 1.6 zg for the smallest bottom-up nanowire, and of 2.8 zg for the smallest top-down resonator. The best mass resolution results reported in the literature at room temperature are those of He et al. [7], which are an estimation based on the frequency resolution of differently trasduced devices. Therefore, we conclude that our results represent the best mass resolution reported until now for cc-beam resonators at room temperature.

Bottom-up					
Device	d (nm)	l (μm)	f_0 (MHz)	R_m (Hz/zg)	Δm (zg)
NW1 (Fig. 3.7)	100	3	76.5	1.65	6
NW2 (Fig. 3.7)	70-85	3	44	1.60	4.9
NW3 (Fig. 3.7)	52-65	2.5	83	6.62	1.6
Top-down					
Device	$w \times t$ (nm)	l (μm)	f_0 (MHz)	R_m (Hz/zg)	Δm (zg)
NW1 (Fig. 5.1)	137x110	2.5	137.5	2.03	8.7
NW2 (Fig. 5.4)	110x90	3.2	117	2.07	7.4
NW3	72x60	2.8	80.4*	3.72	2.8
State of the art					
Work	Technology			R_m (Hz/zg)	Δm (zg)
He, 2008 [7]	Bottom-up SiNW, T=300 K			15	0.5
Naik, 2009 [2]	Top-down, T=40 K			12	1.7
Chaste, 2012 [4]	Bottom-up CNT, T=58 K			$3\,1 \times 10^{6}$	$2\,8 \times 10^{-3}$

* Theoretical value
Value calculated from the information provided in the work
Estimated value

Table 6.5: Estimation of the effective mass and mass responsivity of different nanowires measured throughout this work. All of the calculations are performed for the first mode of resonance. For the bottom-up nanowires, d is the distance between parallel sides. For the top-down nanowires, the section of the beam is $w \times t$, where w is the in-plane direction which is considered the direction of operation. The responsivity is shown in Hz/zg (1 zg is 1×10^{-21} g). The mass responsivity is calculated from the theoretical effective mass and the experimental resonance frequency. The mass resolution is calculated for a frequency deviation of 1.4×10^{-7}, which is experimentally obtained from the feedback loop using a top-down resonator. The last rows provide a comparison with several recent works, representative of different fabrication technologies.

References

[1] A. Boisen, "Nanoelectromechanical systems: Mass spec goes nanomechanical," *Nature Nanotechnology*, vol. 4, no. 7, pp. 404–405, 2009.

[2] A. K. Naik, M. S. Hanay, W. K. Hiebert, X. L. Feng, and M. L. Roukes, "Towards single-molecule nanomechanical mass spectrometry," *Nature Nanotechnology*, vol. 4, no. 7, pp. 445–450, 2009.

[3] M. S. Hanay, S. Kelber, A. K. Naik, D. Chi, S. Hentz, E. C. Bullard, E. Colinet, L. Duraffourg, and M. L. Roukes, "Single-protein nanomechanical mass spectrometry in real time," *Nature Nanotechnology*, vol. 7, pp. 602–608, Sept. 2012.

[4] J. Chaste, A. Eichler, J. Moser, G. Ceballos, R. Rurali, and A. Bachtold, "A nanomechanical mass sensor with yoctogram resolution," *Nature Nanotechnology*, vol. 7, pp. 301–304, Apr. 2012.

[5] Y. T. Yang, C. Callegari, X. L. Feng, K. L. Ekinci, and M. L. Roukes, "Zeptogram-scale nanomechanical mass sensing," *Nano Letters*, vol. 6, pp. 583–586, Apr. 2006.

[6] J. Verd, A. Uranga, G. Abadal, J. Teva, F. Torres, J. Lopez, E. Perez-Murano, J. Esteve, and N. Barniol, "Monolithic CMOS MEMS oscillator circuit for sensing in the attogram range," *IEEE Electron Device Letters*, vol. 29, pp. 146 –148, Feb. 2008.

[7] R. He, X. L. Feng, M. L. Roukes, and P. Yang, "Self-transducing silicon nanowire electromechanical systems at room temperature," *Nano Letters*, vol. 8, pp. 1756–1761, June 2008.

[8] K. Jensen, K. Kim, and A. Zettl, "An atomic-resolution nanomechanical mass sensor," *Nature Nanotechnology*, vol. 3, pp. 533–537, July 2008.

[9] B. Lassagne, D. Garcia-Sanchez, A. Aguasca, and A. Bachtold, "Ultrasensitive mass sensing with a nanotube electromechanical resonator," *Nano Letters*, vol. 8, pp. 3735–3738, Nov. 2008.

[10] X. L. Feng, C. J. White, A. Hajimiri, and M. L. Roukes, "A self-sustaining ultrahigh-frequency nanoelectromechanical oscillator," *Nature Nanotechnology*, vol. 3, pp. 342–346, May 2008.

[11] H.-Y. Chiu, P. Hung, H. W. C. Postma, and M. Bockrath, "Atomic-scale mass sensing using carbon nanotube resonators," *Nano Letters*, vol. 8, no. 12, pp. 4342–4346, 2008.

[12] S. Dohn, S. Schmid, F. Amiot, and A. Boisen, "Position and mass determination of multiple particles using cantilever based mass sensors," *Applied Physics Letters*, vol. 97, pp. 044103–044103–3, July 2010.

[13] E. Gil-Santos, D. Ramos, J. Martínez, M. Fernández-Regúlez, R. García, l. S. Paulo, M. Calleja, and J. Tamayo, "Nanomechanical mass sensing and stiffness spectrometry based on two-dimensional vibrations of resonant nanowires," *Nature Nanotechnology*, vol. 5, no. 9, pp. 641–645, 2010.

[14] K. L. Ekinci and M. L. Roukes, "Nanoelectromechanical systems," *Review of Scientific Instruments*, vol. 76, pp. 061101–061101–12, May 2005.

[15] H. W. C. Postma, I. Kozinsky, A. Husain, and M. L. Roukes, "Dynamic range of nanotube- and nanowire-based electromechanical systems," *Applied Physics Letters*, vol. 86, pp. 223105–223105–3, May 2005.

[16] M. H. Matheny, L. G. Villanueva, R. B. Karabalin, J. E. Sader, and M. L. Roukes, "Nonlinear mode-coupling in nanomechanical systems," *Nano Letters*, Mar. 2013.

[17] K. L. Ekinci, Y. T. Yang, and M. L. Roukes, "Ultimate limits to inertial mass sensing based upon nanoelectromechanical systems," *Journal of Applied Physics*, vol. 95, pp. 2682–2689, Mar. 2004.

[18] N. US Department of Commerce, "National institute of standards and technology." National Institute of Standards and Technology.

[19] D. W. Allan, "Time and frequency (time-domain) characterization, estimation, and prediction of precision clocks and oscillators," *IEEE Transactions On Ultrasonics Ferroelectrics And Frequency Control*, vol. 34, p. 647–654, Nov. 1987.

[20] J. A. Barnes, A. R. Chi, L. S. Cutler, D. J. Healey, D. B. Leeson, T. E. McGunigal, J. A. Mullen, W. L. Smith, R. L. Sydnor, R. F. C. Vessot, and G. M. R. Winkler, "Characterization of frequency stability," *IEEE Transactions on Instrumentation and Measurement*, vol. IM-20, pp. 105 –120, May 1971.

[21] J. Rutman and F. Walls, "Characterization of frequency stability in precision frequency sources," *Proceedings of the IEEE*, vol. 79, pp. 952 –960, July 1991.

General conclusions

This thesis has contributed to the field of nanomechanical resonators by generating new advances in fabrication technology and electromechanical transduction in silicon nanowire based resonators, focused towards the development of nanomechanical sensors that can provide ultimate mass resolution.

The main specific contributions to these areas are summarized next.

Fabrication technology of SiNW mechanical resonators

- A novel technology **based on the combination of bottom-up and top-down** fabrication processes for the realization of nanomechanical resonators based on single silicon nanowires have been developed. Bottom-up nanowires of diameters in the range of 50-100 nanometers have been synthesized using the CVD-VLS method. The technology allows to fabricate multiple silicon nanowire resonators at chip level with high dimensional control and very good clamping properties.

- **A novel top-down fabrication technology** has been designed based on optical lithography and sequencial oxidation/etching processes: it **allows the parallel fabrication of resonators with lateral dimensions of tens of nanometers**: the technology potentially allows to obtain hundreds of functional devices per chip and even at wafer level.

- Both technologies have allowed to fabricate SiNW based mechanical resonators of comparable dimensions. A comparative study of their performance has been realized.

- A novel doping method has been developed, based on submitting finished devices to an annealing in close proximity to a doping wafer in an atmospheric furnace. This method can be performed ex-situ, and it is non-destructive: it requires no aggressive implantation process and no contact with the devices. In this way, doping and growing conditions can be optimized separately.

Electromechanical transduction in SiNW mechanical resonators

We have applied advanced electrical detection schemes based on frequency down-mixing techniques for the characterization of the frequency response of the devices.

- **We have demonstrated that the frequency modulation (FM) detection method provides outstanding mechanical to electrical transduction for the characterization of the frequency response of bottom-up and top-down silicon nanowire mechanical resonators**: This method has enabled the detection of multiple resonance modes at frequencies up to 590 MHz.

- Using FM detection, the vibration of the nanowires in different orthogonal directions has been detected for bottom-up and top-down nanowires for the first and second modes of resonance, and for the highest resonance frequencies observed up to now.

- By combining the information obtained from the characterization of multiple resonance modes of the resonator with FEM simulation, the stress present in the structures has been quantified: bottom-up nanowires present a compressive stress of hundreds of MPa, while top-down nanowires present a complex stress in different directions.

We have studied **the electromechanical transduction mechanisms in SiNW resonators** by the comparative performance of three electrical detection methods: the aforementioned FM and two more detection techniques (namely the two-source, 1 and the two-source, 2).

- We have proved that **two different transduction mechanisms co-exist in bottom-up grown SiNWs**: linear (in which the transduced signal is proportional to the motion of the resonator) and quadratic (in which the transduced signal is proportional to the square of the motion of the resonator). Previously to this work, it was accepted that only the quadratic transduction mechanism was efficient for the electrical read-out of SiNW mechanical resonators.

- The mechanical to electrical transduction efficiency is much higher for the linear transduction mechanism than for the quadratic linear transduction mechanism.

- The quadratic transduction mechanism is only observed in bottom-up grown silicon nanowires and it is attributed to the presence of the giant piezoresistive effect. We have estimated a piezoresistive gauge factor of 200 for our nanowires, four times larger than for bulk silicon, and which is in accordance with previous studies of piezoresistance in silicon nanowires (He et al., 2006).

- We have found that in top-down nanowires only the linear transduction mechanism is efficient for electrical read-out. By simultaneously performing electrical characterization and real-time visual observation by SEM, we have quantified that the mechanical to electrical linear transduction mechanism provides and efficiency better than 0.6 nA/nm. This extremely high transduction efficiency can not be explained by only considering conductivity modulation by capacitive coupling as the only physical origin of the linear transduction mechanism.

Evaluation of the performance of SINWs for sensing applications

- From the experimental characterization of the frequency response of the SiNW mechanical resonators and modelling their effective mass from SEM imaging, we have found that bottom-up resonators fabricated during this thesis present mass responsivities in the range of 6 Hz/zg, while for the ones fabricated using only top-down methods the best obtained responsivity is of 3.7 Hz/zg. The better responsivity obtained in bottom-up grown SiNW resonators is due to the fact that SiNW with smaller dimensions have been successfully fabricated in this case.

- A novel closed loop system configuration based on the FM detection method and a slope detection algorithm has been designed and implemented, in view of the realization of mass-sensing experiments and the evaluation of the mass sensing resolution.

- The frequency stability of the closed-loop system using a top-down resonator has been characterized using the Allan deviation method, and we have obtained **a mass resolution of 6 zg** (6×10^{-21} g). From the stability of the feedback system, we have estimated **a mass resolution of 1.6 zg** (6×10^{-21} g) for the bottom-up nanowires.

- The mass resolution that can be achieved with these devices can be considered as the best one reported up to now at room temperature for mechanical resonators in a double-clamped configuration.

Final remark / Outlook

The results obtained during this thesis are a step forward for the application of silicon nanowire mechanical resonators as ultimate mass sensors operating at room temperature. Follow-up of this thesis in the short term will be devoted to the clarification of the physical origin of the linear transduction mechanism responsible

of the electromechanical response observed in the FM detection scheme, and to performing mass measurement to validate the established mass resolution

Appendices

Appendix A

Metallization of electrical contacts by Nanostencil lithography

One of the problems of the technologies employed for the fabrication of the top-down and bottom-up nanowires is that the electrical contacts are fabricated from silicon. These silicon contacts oxidise when exposed to air, and therefore they present a small layer of native oxide. This layer hinders the electrical measurement of the resonators, specially when contacting the electrodes using a probe station instead of wire-bonding. This issue can be mitigated by performing an HF dip just before the measurements, but this solution is not ideal: the resulting measurements are little repetitive (presumably to the oxide growing again after the HF), and repeating the process eventually leads to problems with the cleanliness of the chips.

Both in the top-down and bottom-up fabrication approaches, it is not possible to deposit metals on the chip before the fabrication process finishes, due to the high-temperature processes which take place during the last steps of the fabrication: the last step in all the cases is the high temperature annealing of the chips to dope the nanowires. After the fabrication process, performing a lift-off involves covering the whole substrate with photoresist (which can lead to damage or contamination of the samples), and moreover it should be performed at chip level, which entangles additional issues. One possible alternative to solve these problems is employing stencil lithography to selectively deposit metal only on the desired parts of the substrates [1, 2].

Nanostencil lithography is a high-resolution shadow-masking technique, based on the selective deposition of material by evaporation through micro- and nano-apertures realized in a thin membrane. Therefore, using this technique it is possible to deposit a layer of metal only on the silicon contacts of the substrates, without using photoresist and in a non-destructive way (presumably, without affecting the nanowires at all). In this appendix, the fabrication of stencils and their application in the selective deposition of metal contacts is presented. This work has been performed

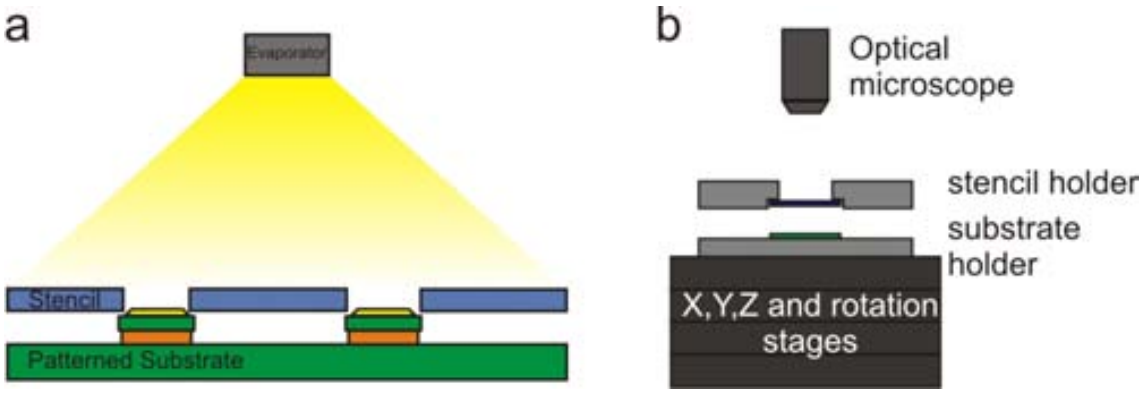

Figure A.1: Use of nanostencil lithography to selectively deposit metal layers on a substrate. a) Evaporation of metals on a pre-patterned substrate through the apertures of a stencil. b) Alignment between stencil and substrate. The stencil holder is fixed, while the substrate holder is connected to several positioners (x, y, z, rotation). The microscope can be manually moved to inspect different locations in the stencil-substrate.

as a part of a two months internship in the group of Jürgen Brugger (Microsystems Laboratory, EPFL, Lausanne).

Figure A.1a shows a schematic of the selective deposition of metal layers on a substrate employing nanostencil lithography. The stencil and the substrate are placed in close proximity in order to ensure the best possible resolution [3]. The deposition takes place inside an evaporator, where the metal covers the substrate only through the holes in the shadow mask. It is possible to perform this process at chip or full wafer level [4], and also to make the deposition in pre-patterned substrates: in the latter case, and additional alignment step is needed [5].

A.1 Fabrication of the stencils

The fabrication of the stencils is performed in the clean room of the CMI (Center of Micro an Nanotechnology) at the EPFL. The fabrication process is based on the definition of low-stress silicon nitride (SiN) membranes with apertures, which act as a shadow mask.

The main steps of the fabrication process of a stencil is shown in Figure A.2. The process starts with doubly polished silicon wafers, with a layer of 500 nm of low-stress silicon nitride covering both sides (Figure A.2a). Then, a layer of approximately 1 μm of Al is deposited in the back-side (Figure A.2b). Next, the apertures of the stencil are patterned in the SiN layer of the components side, using photolithography and dry etching (Figure A.2c-d). The next steps are aimed at defining the SiN membranes: first a dry etching of the back-side aluminium and SiN layers is performed. Then a deep RIE of the silicon wafer is performed using the Al

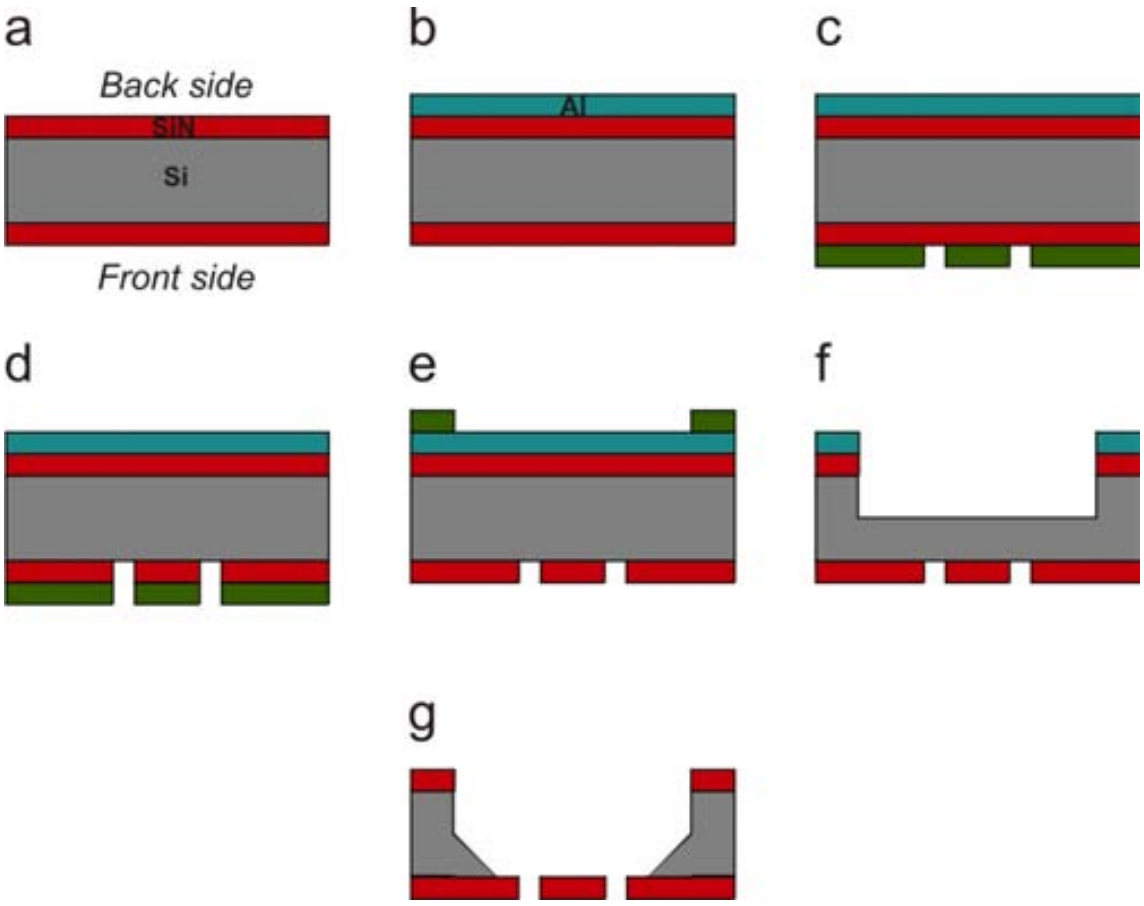

Figure A.2: Stencil fabrication process. a) Silicon substrate, with a thin layer of silicon nitride deposited on both sides. b) Deposition of a 1 μm Al layer on the back-side. c) Front-side photolithography for the definition of the membrane holes. d) Dry etching of the front side SiN layer to defines the holes of the membrane. e) Back-side photolithography for the definition of the membranes. f) Definition of the membranes: dry etching of the SiN layer, followed by a dry etching of the Al layer. Afterwards a deep RIE of the bulk Si is performed, until a Si layer with a thickness of around 100 μm remains. g) Silicon wet etching using KOH to release the SiN membranes.

layer as a mask, until a thickness of approximately 100 μm of Si remains until the SiN membrane (Figure A.2e-f). Finally, the membranes are released from the bulk silicon using a KOH wet etching (Figure A.2g).

The resulting stencil consists in several membranes of SiN with holes patterned in them. The size of the membranes and the hole density must be carefully chosen, in order to have sufficiently stable membranes. The membranes fabricated in this work consist in arrays of square holes of 90×90 μm (the size of the pre-patterned electrodes is 100×100 μm) and only 50 % of the electrodes are covered during each deposition, in order to have small membranes which are stronger. Alignment holes with special shapes are also included in the designs, which are used as alignment marks in order to ease the alignment of the membrane with the substrate.

After the internship, the stencil fabrication technology has been successfully transferred to the clean room of the IMB-CNM. This fabrication technology has been adapted to the equipments of the clean room of the CNM, and stencils based on this technology have been fabricated.

A.2 Selective deposition of metal electrodes

The fabricated stencils are employed for the deposition of metal covering the silicon electrodes, in chips with fabricated SiNW resonators. The substrates consist in arrays of silicon electrodes and silicon stripes, and some of these electrodes are connected by silicon nanowire resonators (Figure A.3b shows a fragment of the chip after the deposition process). The particular substrates used for these experiments contained bottom-up nanowires, although the technology can be also applied to the top-down fabrication approach, using exactly the same stencils. The complete selective metallization process consists in three steps: first, a buffered HF is performed to the substrates in order to eliminate the native SiO_2; then, the stencil and substrates are aligned and stuck together, and finally they are brought into a metal evaporator in order to deposit the electrodes.

For this application, a chip-level alignment method has been developed. The alignment resolution between the stencil and the substrate needs to be below 10 μm, and a rotation error as low as possible is also needed. A schematic of the alignment system is shown in Figure A.3b. The stencil and substrate are fixed to two different holders respectively. The substrate holder is connected so several stages (x,y,z and rotation) which allow to move it with respect to the stencil one, which is fixed. The alignment is performed using an optical microscope: the SiN membranes are translucent, and therefore by using the microscope the apertures of these membranes with the Si contacts can be aligned. Once the stencil and the substrate are aligned, they are brought in contact, and then their respective holders are fixed together using UV-glue. Afterwards, this whole piece is brought into an

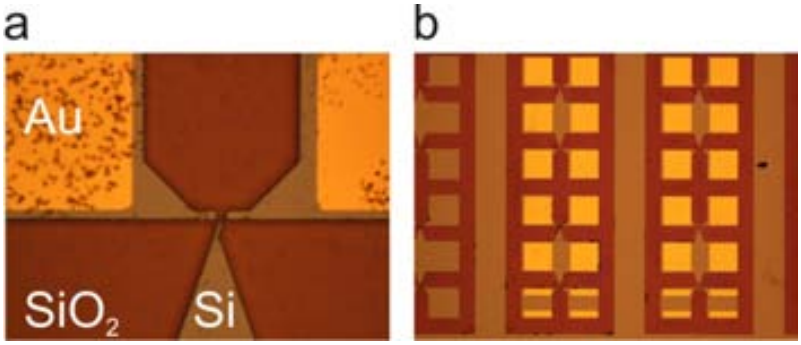

Figure A.3: Deposition of metal on top of the pre-patterned Si electrodes. a) Close view of a nanowire connecting two electrodes, near a side-gate for electrical actuation. Only the contacts are covered by a gold layer. b) View of a portion of the chip with the Si electrodes (size of the square electrodes: 100×100 μm) covered by a gold layer. The electrodes at the bottom of the image are partially covered by alignment marks.

evaporator and the contacts are deposited.

The results of this fabrication step are shown in Figure A.3. The metallization of two electrodes connected by a SiNW is shown in Figure A.3a, while an overview of multiple metallized electrodes is shown in Figure A.3b. The apparent contamination present in both images are in fact silicon nanowires, which grow over all the silicon surfaces of the chip due to the random deposition of the catalyst. After the deposition of the metal electrodes, we observe that the alignment is successful in the whole chip. A critical parameter is the rotation between the stencil and the substrate: even a very small rotation angle can misalign the patterns at the edges of the chip. This rotation error is also the most difficult to correct, because it requires performing a series of alignments at different parts of the chip.

After the deposition of the contacts, electrical measurements are performed to confirm the electrical continuity between the contacts and the Si substrate. Before the deposition of the metal contacts, the electrical measurements of a highly doped Si strip yield non-linear and non-repetitive results, which are coherent with an oxidized silicon substrate. During the evaporation, metal pads are deposited on the Si stripe, and then the measurements are repeated. In this case resistive I-V curves are obtained, as is expected from the metal contacts and the highly doped silicon substrate. The measured resistance is also consistent with the dimensions and doping of the measured silicon stripe. Therefore, we conclude that the selective deposition of metal electrodes eases the electrical measurement process, and alleviated the issues arising from the Si contacts.

References

[1] M. M. Deshmukh, D. C. Ralph, M. Thomas, and J. Silcox, "Nanofabrication using a stencil mask," *Applied Physics Letters*, vol. 75, no. 11, p. 1631–1633, 1999.

[2] J. Brugger, J. Berenschot, S. Kuiper, W. Nijdam, B. Otter, and M. Elwenspoek, "Resistless patterning of sub-micron structures by evaporation through nanostencils," *Microelectronic Engineering*, vol. 53, pp. 403–405, June 2000.

[3] O. Vazquez-Mena, L. G. Villanueva, V. Savu, K. Sidler, P. Langlet, and J. Brugger, "Analysis of the blurring in stencil lithography," *Nanotechnology*, vol. 20, p. 415303, Oct. 2009.

[4] O. Vazquez-Mena, G. Villanueva, V. Savu, K. Sidler, M. A. F. van den Boogaart, and J. Brugger, "Metallic nanowires by full wafer stencil lithography," *Nano Letters*, vol. 8, no. 11, pp. 3675–3682, 2008.

[5] J. Arcamone, M. Sansa, J. Verd, A. Uranga, G. Abadal, N. Barniol, M. van den Boogaart, J. Brugger, and F. Pérez-Murano, "Nanomechanical mass sensor for spatially resolved ultrasensitive monitoring of deposition rates in stencil lithography," *Small*, vol. 5, no. 2, p. 176–180, 2009.

Appendix B

Software

B.1 Control software for the instrumentation

In this work the electrical measurement of nanomechanical resonators using different setups has been performed. All of these setups are based on downmixing methods, and use a lock-in amplifier to read the measurement results. Typically in this kind of systems, the different instruments must work in a coordinated way. Moreover, the measurement time is long–due to the response time of the different components of the system, which must reach a stationary regime for each point of the measurement–, and the measurement conditions must be changed for each point of the measurement. For these reasons, a centralized software control of this kind is systems is indispensable.

In this work, the measurement software controls the different instruments using the GPIB communication bus (Figure B.1a). A series of libraries were designed and implemented for each particular measurement setup, as wall as a graphical interface to control the measurements and view the results in real time. Initially these software was implemented using National Instruments Labview [1], and later it was migrated to Python which offers greater adaptability.

The structure of the developed Python software is shown in Figure B.1b. The design of the different parts of the software make it easy to modify (adding or changing instruments, for example), and to add additional functionality. For example, the feedback software implemented by Fabrice Perry was built as additional libraries in top of the existing ones. Moreover, the libraries allow controlling the instruments and performing measurements using different methods (such as Python scripts), not only using the graphical user interface.

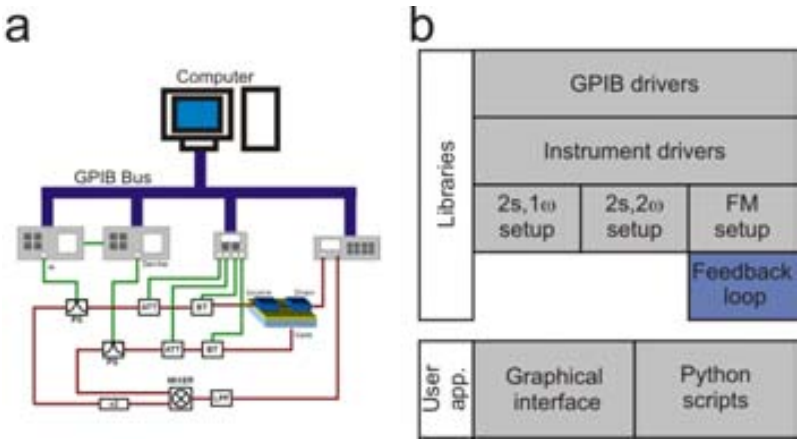

Figure B.1: Software developed for the measurement of nanomechanical resonators. a) Schematic of the 2-source, 2ω measurement setup including the software interface, which controls the instruments using the GPIB bus. b) Structure of the Python software. The feedback loop libraries have been implemented by Fabrice Perry.

B.2 List of open source software

During the development of this work open source software has been employed in a a variety of situations. This software, developed generally under the different versions of the GPL license, has its code available for inspection, modification and redistribution by the general public. Also, in some cases, this software is developed by volunteers with no financial interests.

A list of some of the employed open source software is now supplied, as a means of acknowledging its importance in the development of this work.

Ubuntu Linux Operating system based on the Linux kernel [2]

Mozilla Firefox Web browser [3]

Mozilla Thunderbird E-mail manager [4]

Libreoffice Office suite based on Open Office [5]

Zotero Reference management software [6]

Python General purpose programming language [7]

Scipy Python libraries for mathematics, science and engineering [8]

GTK+ Toolkit for creating graphical user interfaces [9]

Glade GUI design software for GTK [10]

Texlive Software distribution for the Tex typesetting system [11]

Texmaker LaTeX editor [12]

Jabref Bibliography manager [13]

References

[1] "NI LabVIEW -national instruments. http://www.ni.com/labview/esa/."

[2] "Ubuntu. http://www.ubuntu.com/."

[3] "Mozilla firefox web browser - mozilla.org."

[4] "Mozilla thunderbird. http://www.mozilla.org/en-US/thunderbird."

[5] "LibreOffice 4. http://www.libreoffice.org/."

[6] "Zotero - home. http://www.zotero.org/."

[7] "Python programming language - official website. http://www.python.org/."

[8] "SciPy. http://www.scipy.org/."

[9] "The GTK+ project. http://www.gtk.org/."

[10] "Glade - a user interface designer. http://glade.gnome.org/."

[11] "TeX live - TeX users group. http://tug.org/texlive/."

[12] "Texmaker (free cross-platform latex editor). http://www.xm1math.net/texmaker/."

[13] "JabRef reference manager. http://jabref.sourceforge.net/."

Appendix C

List of publications and contributions to scientific events

C.1 Peer-reviewed publications

M. Fernandez-Regulez, **M. Sansa**, M. Serra-Garcia, E. Gil-Santos, J. Tamayo, F. Perez-Murano and A. San Paulo
"Horizontally patterned Si nanowire growth for nanomechanical devices"
Nanotechnology, vol. 24, num. 9, p. 095303, 2013.

M. Sansa, M. Fernández-Regulez, Á. San Paulo, and F. Pérez-Murano
"Electrical transduction in nanomechanical resonators based on doubly clamped bottom-up silicon nanowires"
Applied Physics Letters, vol. 101, num. 24, p. 243115-243115-5, 2012.

J. Verd, **M. Sansa**, A. Uranga, F. Perez-Murano, J. Segura, and N. Barniol
"Metal microelectromechanical oscillator exhibiting ultra-high water vapor resolution"
Lab on a Chip, vol. 11, num. 16, p. 2670, 2011.

I. Martin-Fernandez, **M. Sansa**, M. J. Esplandiu, E. Lora-Tamayo, F. Perez-Murano, and P. Godignon
"Massive manufacture and characterization of single-walled carbon nanotube field effect transistors"
Microelectronic Engineering, vol. 87, num. 5-8, p. 1554-1556, 2010.

J. Arcamone, **M. Sansa**, J. Verd, A. Uranga, G. Abadal, N. Barniol, M. van den Boogaart, J. Brugger, and F. Pérez-Murano
"Nanomechanical Mass Sensor for Spatially Resolved Ultrasensitive Monitoring of Deposition Rates in Stencil Lithography"

Small, vol. 5, num. 2, p. 176–180, 2009.

C.2 Participation in scientific events

M. Sansa, M. Fernandez-Regulez, M. Serra-Garcia, A. San Paulo, and F. Perez-Murano
"Bottom-up silicon nanowire resonators for nanomechanical sensong: controlled fabrication technology and high-sensitivity frquency modulation transduction"
Poster presentation
17th International Conference on Solid-State Sensors, Actuators and Microsystems (Transducers' 2013), Barcelona (Spain), 2013 - *Accepted*.

M. Sansa, A. San Paulo, and F. Perez-Murano
"Fabrication and electrical characterization of bottom-up silicon nanowire resonators"
Poster presentation
IEEE Sensors, Taipei (Taiwan), 2012.

M. Sansa, A. San Paulo, and F. Perez-Murano
"Fabrication and electrical characterization of bottom-up silicon nanowire resonators"
Poster presentation
38th International Micro & Nano Engineering Conference (MNE 2012), Toulouse (France), 2012.

M. Sansa, A. San Paulo and F. Perez-Murano
"Silicon nanowires for ultrasensitive mass sensing"
Poster presentation
International seminar on Nanomechanical Systems, Toulouse (France), 2011.

M. Sansa, A. San Paulo and F. Perez-Murano
"Silicon nanowires for ultrasensitive mass sensing"
Poster presentation
8th International Workshop on Nanomechanical Sensing, Dublin (Ireland), 2011.

M. Sansa, J. Verd, A. Uranga, F. Perez-Murano, J. Segura, and N. Barniol
"Ultrasensitive humidity sensor based on a metal CMOS-NEMS oscillator"
Poster presentation
8th International Workshop on Nanomechanical Sensing, Dublin (Ireland), 2011.

M. Sansa, J. Arcamone, J. Verd, A. Uranga, G. Abadal, N. Barniol, V. Savu, M. A. F. van den Boogaart, J. Brugger, and F. Perez-Murano

"NEMS/CMOS sensor for monitoring deposition rates in stencil lithography"
Poster presentation
Eurosensors XXIII Conference, Lausanne (Switzerland), 2009.

M. Sansa, J. Arcamone, J. Verd, A. Uranga, G. Abadal, E. Lora-Tamayo, N. Barniol, M. A. F. van den Boogaart, V. Savu, J. Brugger, and F. Perez-Murano
"Nanomechanical test structure for optimal alignment in stencil-based lithography"
Oral presentation
IEEE International Conference on Microelectronic Test Structures, Oxnard (USA), 2009.

J. Arcamone, M. Sansa, J. Verd, A. Uranga, G. Abadal, N. Bamiol, M. A. F. van den Boogaart, J. Brugger, and F. Perez-Murano
"Nanomechanical mass sensor for monitoring deposition rates through confined apertures"
Oral presentation
4th IEEE International Conference on Nano/micro Engineered and Molecular Systems, Shenzen (China), 2009.